UNIVERSITÀ
DEGLI STUDI
DI PADOVA

Sede Amministrativa: Università degli Studi di Padova

Dipartimento di Ingegneria Civile, Edile e Ambientale

SCUOLA DI DOTTORATO DI RICERCA IN : Scienze dell'Ingegneria Civile e Ambientale

CICLO XXIV

MESOSCALE MODELLING OF CONCRETE AS A MULTIPHASE MATERIAL

Direttore della Scuola: Ch.mo Prof. Stefano Lanzoni

Supervisori: Ch.mo Prof. Carmelo Majorana
Dott. Ing. Valentina Salomoni

Dottorando: Giovanna Xotta

Abstract

In recent years, thanks to upgraded computational resources, concrete has started being modeled as porous medium at 3D meso level, distinguishing in the multiphase system the role of aggregates, cement paste and interfacial transition zone (ITZ). A deep knowledge on the behaviour of concrete materials at the mesoscale level requires, as a fundamental aspect, to characterize aggregates and specifically, their thermal properties if fire hazards (e.g. spalling) are accounted for. The assessment of aggregates performance (and, correspondingly, concrete materials made of aggregates, cement paste and ITZ) is crucial for defining a realistic structural response as well as damage scenarios.

A meso-scale approach has been here followed to study concrete behaviour under normal and high temperatures via the 3D fully coupled thermo-hydro-mechanical model developed at Padua University, called NEWCON3D. Particularly, it is assumed that concrete creep and damage are associated to cement paste and ITZ only and that creep of concrete obeys to the B3 model proposed by Bažant and Baweja, instead damage obeys to the Mazars' damage law with non-local correction.

Therefore several numerical analyses at the mesolevel have been carried out: firstly the role of the ITZ and of the aggregates on the hygro-thermal response of concrete have been investigated, highlighting the barrier effect covered by aggregates towards the flux of humidity; subsequently the visco-damaged behaviour of concrete at the meso level is investigated, to understand the influence of ITZ and aggregates on the overall mechanical behaviour at medium temperatures. Indeed, these two components are crucial for defining a realistic structural response as well as damage scenarios allowing to define an appropriate concrete mixture to withstand spalling. Finally, the study of concrete under high temperature conditions, to catch the "shape effect", comparing columns of different section at the macro level, and the crucial role of the aggregates and the ITZ on the real evolution of cracking, have been performed.

Abstract

Negli ultimi anni, grazie alle attuali risorse di calcolo, si è iniziato a modellare il calcestruzzo come un mezzo poroso al meso livello, distinguendo nel sistema multifase il ruolo degli aggregati, della pasta di cemento e dell'interfacial transition zone (ITZ). Una profonda conoscenza del comportamento del calcestruzzo al mesoscala richiede, come aspetto fondamentale, la caratterizzazione degli aggregati ed, in particolare, delle loro proprietà termiche, nel caso in cui vi siano rischi di incendio (e quindi di spalling). La valutazione delle prestazioni degli aggregati (e conseguentemente, di calcestruzzi come composti da inerti, pasta di cemento ed ITZ) è cruciale per la definizione sia di una risposta realistica strutturale, sia degli scenari di danno.

In questo lavoro si è quindi seguito un approccio al mesoscala per studiare il comportamento del calcestruzzo, in condizioni di temperatura normale ed elevata, tramite un modello tridimensionale igro-termo-meccanico totalmente accoppiato sviluppato presso l'Università di Padova, chiamato NEWCON3D. Nello specifico, si è assunto che i fenomeni di viscosità e di danno fossero associati solo alla pasta di cemento e all'ITZ (per gli aggregati si assume un comportamento elastico) e che il creep obbedisse al modello B3 proposto da Bažant e Baweja, invece il danno alla legge di Mazars con la correzione non locale.

Si sono pertanto condotte numerose analisi numeriche al meso livello: in primo luogo si è esaminato il ruolo dell'ITZ e degli aggregati sulla risposta igro-termica del calcestruzzo, mettendo in evidenza l'effetto barriera esercitato dagli aggregati sui flussi di umidità; successivamente si è indagato il comportamento visco-danneggiato del calcestruzzo al mesoscala, al fine di comprendere l'influenza dell'ITZ e degli aggregati sulla risposta meccanica globale a temperature medie. In realtà, come già detto precedentemente, queste due componenti sono molto importanti per ottenere una risposta realistica strutturale e per l'individuazione dei possibili scenari di danno, permettendo quindi di definire una miscela di calcestruzzo appropriata, in grado di resistere allo spalling. Infine, vi è uno studio del calcestruzzo in condizioni di temperatura elevata, al fine di catturare l '"effetto forma", confrontando due colonne di sezione differente al macro scala, ed il ruolo cruciale degli aggregati e dell'ITZ sull'evoluzione reale del danno.

SUMMARY

1 INTRODUCTION

Although traditional engineering studies consider concrete as a homogeneous material, idealized as an infinitesimal continuum medium with average properties (macroscopic approach), concrete is a highly heterogeneous material and its composite behaviour is exceedingly complex. In the early 80s Wittmann proposed three levels of observations for concrete, from lower to higher: the microscopic level at the micro-meter scale, the mesoscopic level at the mm-cm scale and the macroscopic level at the metric level.

With regard to the macroscale, most of the work proposed in literature consider phenomenological relationships based on macroscopic observations. Although this approach implies a simplification, through the use of continuum-type constitutive models, it has led to a satisfactory description of the basic features of the mechanical behaviour of concrete.

To obtain a deeper understanding of the macroscopic constitutive behaviour of concrete, material models, in which the structure of concrete at lower levels is explicitly represented, have been developed in recent decades thanks to upgraded computer resources.

Specifically, as for the level of observation lower than the macroscopic one, i.e. the mesoscale, it provides a more realistic description of concrete at the macro scale, influenced by the geometry and the properties of its components, and a better comprehension of several concrete phenomena, such as creep, damage and spalling. This could be expected, being the macroscopic behaviour observed macroscopically a direct consequence of the phenomenon which take place at the level of the material heterogeneities. Concrete at this level is a mixture of cement paste, aggregates of different size and a thin layer of matrix material between these two components called interfacial transition zone (ITZ). The models considered in this work, are included in this category.

A third level of analysis is the microscale, in which the internal structure of the hardened cement paste or the ITZ are studied. At this level chemical processes during hydration and drying are important features. Moreover, thanks to new development techniques such as nanoindentation or TEN (transmission electron microscope), concrete can be studied at a fourth level, i.e. the nanoscale.

Several mesoscopic models of concrete structure have been developed for studying the influence of material composition on the overall behaviour: truss models [1]; continuum models, where each phase of concrete is simulated by finite elements [2]-[5]; lattice models and particle model in which the continuum model is replaced by a system of discrete elements [6]-[13] and lattice particle discrete models, that simulate the concrete mesostructure by a system of interacting particle connected by a lattice [14].

It’s important to note that most of the models at the meso level are applied to the analysis of mechanical problems and only few of them have extended their applicability to the analysis of coupled degradation problems such as thermo-mechanical problems [15] and hygral gradients[16].

As regards this thesis, it have been adopted mesoscopic continuum models, since through this approach mechanical and nonmechanical properties can be more realistically simulated for concrete with different compositions. The novelty is that each single composite constituent itself can be approached as a multi-phase material, fully described and characterized via the coupled thermo-hydro-mechanical model ([17]-[19]).

One of the main problems that can be encountered in concrete are the long-term effects, such as creep, which is conventionally defined as the difference between the time-dependent deformations of a specimen under load and an identical unloaded control specimen in the same environment. This phenomenon, introduced by Woolson in 1905 [20], has been investigated historically by Glanville [21], L'Hermite [22]. Several creep models have been proposed by Bažant et al.; in particular Model B3 ([23]-[26]), which is the update of the earlier BP and BP-KX models ([27],[28]), can be successfully used even to model the single phases of concrete subjected to creep [29],[30] (i.e. cement paste and ITZ) .

One another phenomenon studied in the last decades, because of exceptional actions such as fires in concrete structures, is spalling ([31],[32]) which corresponds to the separation of pieces of concrete from the surface of a structural element when it is exposed to high and rapidly rising temperatures. Many information on this phenomenon, particularly on the explosive spalling, have been obtained after damage caused by the fire in the tunnels, such as the Danish Great Belt one, the Channel Tunnel, Mont Blanc and Tauern tunnels.

To simulate this phenomenon is no longer possible to use a linear constitutive law of the material, as concrete has a brittle behaviour; numerically the softening branch of the material can be described through several theories such as the fracture and damage. At the mesoscale, different models have been developed; for the simulation of fracture process for example there exist the models by Bažant [1], Schlangen et al. [6], Eckardt [33], instead as regards damage there exist the continuum models by Krajcinovic [34] and Mazars and Pijaudier Cabot [35],[36].

Therefore in this thesis work, concrete at the meso scale is considered as a three phase material made of aggregates, cement paste and the interfacial transition zone. For the numerical modelling of concrete (at the macro and meso scale level), it has been adopted a 3D fully coupled thermo-hygro-mechanical model of heated concrete developed at Padua University called NEWCON3D. When considering creep and damage respectively Model B3 and Mazars' damage law with non-local correction have been chosen and implemented in this code.

As regards the numerical analyses, in the first part the role of the ITZ on the hygro-thermal response of concrete at medium temperatures is investigated, comparing the results obtained at the macro and meso scale level. Subsequently the visco-damaged behaviour of concrete at the meso level is investigated, in order to understand the influence of ITZ and aggregates on the overall mechanical behaviour at medium temperatures. In fact, these two components are crucial for defining a realistic structural response as well as damage scenarios that allows for defining an appropriate concrete mixture to withstand spalling. Finally there is the study of concrete under high temperature conditions, in order to catch the "shape effect", comparing the behaviour of columns of different sections at macro level, and the crucial role of aggregates and ITZ for spalling predictions, one of the main objectives of this thesis. Moreover in APPENDIX is described an upgraded version of the F.E. code NEWCON3D so to innovatively couple creep, shrinkage and damage with unconventional plasticity. The unconventional elasto-plastic model chosen is the Subloading surface model ([37]-[39]) and several analyses are carried out to verify the correct numerical implementation.

REFERENCES

[1] Bazant Z.P., Tabbara M.R., Kazemi M.T. and Pijaudier-Cabot G. (1990), Random particle model for fracture of aggregate or fiber composites, J. Engrg. Mech., 116(8), pp. 1686-1705.

[2] Roelfstra P.E., Sadouki H., Wittmann F.H. (1985), Le béton numerique, Mater Struct, 18, pp.309-317.

[3] Wittmann F.H., Roelfstra P.E. and Kamp C.L. (1988), Drying of concrete: an application of the 3L-approach, Nucl. Eng. Des., 105, pp. 185-198

[4] Carol I., Lopéz C.M. and Roa O. (2001), Micromechanical analysis of quasi-brittle materials using fracture-based interface elements, Intern. J. Numer. Methods Engrg, 15, pp. 120- 133.

[5] Wriggers P. and Moftah S.O. (2006), Mesoscale models for concrete: Homogenisation and damage behaviour, Finite El An Des 2006, 42, pp. 623-636.

[6] Schlangen E and van Mier J.G.M (1992), Simple lattice model for numerical simulation of fracture of concrete materials and structures, Materials and Structures, 25(153), pp. 534-542.

[7] Schlangen E., (1993), Experimental and numerical analysis of fracture process in concrete, PhD Thesis, Delft University of Technology, Delft, The Netherlands.

[8] Schlangen E. (1995), Computational aspects of fracture simulations with lattice models, Fracture Mechanics of Concrete Structures, F.H. Wittmann ed., pp. 913-928.

[9] van Mier J.G.M., Vervuurt A. and Schlangen E. (1994), Boundary and size effects in uniaxial tensile tests: A numerical and experimental study, Fracture and damage in quasi brittle structures, Z.P. Bazant, Z. Bittnar, M. Jirasek and J. Mazars eds., E&F Spon, London.

[10] Lilliu G. and van Mier J.G.M. (2003), 3D lattice type fracture model for concrete, Engineering Fracture Mechanics, 70, pp. 927-941.

[11] Bolander J.E. and Saito S. (1998), Fracture analysis using spring networks with random geometry, Engineering Fracture Mechanics, 61, pp. 569-591.

[12] Bolander J.E., Yoshitake K. and Thomure J. (1999), Stress analysis using elastically uniform rigid-body-spring networks, Journal of Structural Mechanics and Earthquake Engineering, JSCE, No. 633/I-49, pp. 25-32.

[13] Bolander J.E., Hong G.S. and Yoshitake K. (2000), Structural concrete analysis using rigid-body-spring networks, Computer-Aided Civil and Infrastructure Engineering, 15, pp. 120-133.

[14] Cusatis G., Pelessone D., Mencarelli A. and Baylot J.T. (2011), Lattice Discrete Particle Model (LDPM): Formulation, Calibration, and Validation.

[15] Willam K.J,, Rhee I. and Xi J. (2005), Thermal degradation of heterogeneous concrete materials, Journal of Materials in Civil Engineering, ASCE, 17, No. 3, pp. 276-285.

[16] Sadouki H. and Wittmann (2001), Damage in a composite material under combined mechanical and hygral load, Continuous and Discontinuous Modelling of Cohesive-Frictional Materials, Edited by P.A. Vermeer, S. Diebels, W. Ehlers, H.J. Herrmann, S. Luding, E. Ramm, Lecture Notes in Physics, vol. 568.

[17] Majorana C.E., Salomoni V.A. and Schrefler B.A. (1998), Hygrothermal and mechanical model of concrete at high temperature, Mat Struc, 31(210), pp. 378-386.

[18] Schrefler B.A., Simoni L. and Majorana C.E. (1989), A general model for the mechanics of saturated-unsaturated porous materials, Mat Str, 22, pp. 323-334.

[19] Majorana C.E., Salomoni V. and Secchi S. (1997), Effects of mass growing on mechanical and hygrothermic response of three-dimensional bodies, J Mat Proc Tech, PROO64/1-3, pp. 277-286.

[20] Woolson I. H. (1905), Some Remarkable Tests Indicating 'Flow' of Concrete Under Pressure, Engineering News, 54, pp. 459.

[21] Glandville W.H. (1933), Creep of concrete under load, The Journal of the Institution of Structural Engineers.

[22] L'Hermite R. (1957), What do we know about the plastic deformation and flow of concrete?, Annales de L'Institute Technique du Batiment et des Travany Publics, Paris, 117, pp. 778-809. (In French)

[23] Bažant Z.P. and Baweja S. (1995), Creep and shrinkage prediction model for analysis and design of concrete structures - Model B3, Materials and Structures, 28, pp. 357-365, 415-430, 488-495.

[24] Bažant Z.P. and Baweja S. (1995), Creep and shrinkage prediction model for analysis and design of concrete structures: Model B3, The Adam Neville Symposium: Creep and Shrinkage Structural Design Effects, SP-194, A. Al-Manaseer, ed., American Concrete Institute, Farmington Hills, MI, pp. 1-83.

[25] ACI Committee 209 (2008), Guide for Modeling and Calculating Shrinkage and Creep in Hardened Concrete, ACI Report 209, 2R-08, Farmington Hills.

[26] Bažant Z.P., Yu Q., Li G.-H., Klein G.J. and Kristek V. (2010), Excessive deflections of record-span prestressed box-girder. Lessons learned from the collapse of the Koror-Babeldaob bridge in Palau, ACI Concrete International, 32(6), pp. 44-52.

[27] Bažant Z.P. and Panula L. (1978-1979), Practical prediction of time-dependent deformation for concrete, Materials and Structures, (RILEM, Paris). Part I and II , 11, N. 65, (1978), pp. 302-327; Part III and IV, 11, N. 66, (1978), pp. 415-434; Part V and VI, 12, N. 69, (1979), pp. 169-183.

[28] Bažant Z.P., Kim Joong-Koo and Panula L. (1991-1992), Improved prediction model for time dependent deformations of concrete, Materials and Structures, Part I and II , 24, (1991), pp. 327-345, 409-442; Part III, IV and IV, 25, (1992), pp. 21-28, 84-94, 163-169.

[29] Granger L. and Bažant Z.P. (1995), Effect of composition on basic creep of concrete and cement paste, Journal of engineering mechanics, 121.

[30] Baweja S., Dvorak G.J. and Bažant Z.P. (1998), Triaxial composite model for basic creep of concrete, Journal of Engineering Mechanics, pp. 959-965.

[31] Khoury G.A. and Anderberg Y. (2000), Concrete Spalling Review, Fire Safety Design.

[32] Majorana C.E., Salomoni V.A., Mazzucco G. and Khoury G.A. (2010), An approach for modeling concrete spalling in finite strains, Mathematics and Computers in Simulation (Special Issue), 80(8), pp. 1694-1712.

[33] Eckardt S, Hafner S. and Konke C. (2004), Simulation of the fracture behaviour of concrete using continuum damage models at the mesoscale, Proceedings of ECCOMAS 2004.

[34] Krajcinovic D. (1979), Distributed damage theory of beams in pure bending, ASME Journal of Applied Mechanics, 46, pp. 592-596.

[35] Mazars J. and Pijaudier–Cabot J. (1989), Continuum Damage Theory – Application to Concrete, J Engrg Mech, ASCE, 115, pp. 345-365.

[36] Majorana C.E. (1989), Influenza del danno sul comportamento termoigrometrico e meccanico del continuo, Giornale del Genio Civile, 7-9, pp. 211-236.

[37] Hashiguchi K. (1989), Subloading surface model in unconventional plasticity, Int. J. Solids Structures, 25, pp. 917-945.

[38] Salomoni V. A., Fincato R. (2011a), Subloading surface plasticity model algorithm for 3D subsidence analyses above gas reservoirs, Int. J. Geomech. (in press).

[39] Salomoni V. A., Fincato R. (2011b), "3D subsidence analyses above gas reservoirs accounting for an unconventional plasticity model", Int. J. Num. An. Meth. Geomech. (in press).

2 CONCRETE AT THE MESO SCALE LEVEL

2.1 Mesoscopic models of concrete

Many mesoscopic models of concrete can be found in literature for the study of the influence of material composition on the overall behaviour; each of them has its own advantages and disadvantages.

The first meso-scale model was the continuum model by Roelfstra et al. [1] (this model, named "Numerical Concrete" describes concrete very realistically by means of a two-phase material comprising large aggregates in a mortar matrix, see Fig. 2.1).

It is surprising that this model had already proposed to study the drying behaviour of composite at this scale; indeed most of the recent models at the meso-level focus their attention on the study of crack patterns and stress-strain curves under purely mechanical loading of concrete specimens and only a few of them have extended their applicability to the analysis of coupled degradation problems such as thermo-mechanical problems (see Ref.[2]) and hygral gradients (see Ref. [3]).

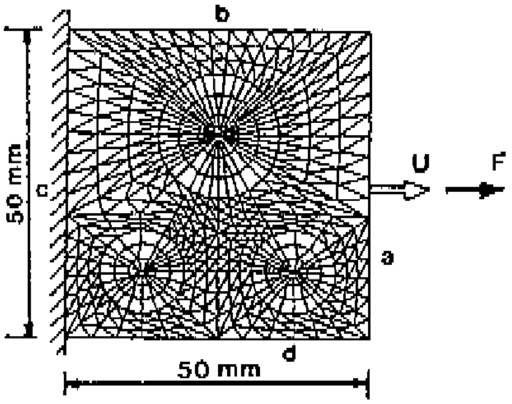

Fig. 2.1 Finite element mesh of "Numerical concrete".

In the continuum models (see also Wittmann et al. [4], Carol et al. [5], Wriggers and Moftah [6]) concrete is modelled as a three-phase material and each phase is discretized through finite elements with appropriate material properties. One of the main advantages of these models is that they represent composite materials more realistically, considering continuum fields of the state variables outside the cracking zone; this is an important feature as compared to other mesoscopic models, especially when chemical reactions and diffusion-driven phenomena are analysed. So these models describe with great accuracy the interaction between matrix and inclusions but critics of continuum models often argue that, from a computational point of view, the cost is too high to be used in large-scale simulations.

Bažant et al. [7] developed a truss model to simulate realistically the spread and its localisation (in Fig. 2.2 is reported a randomly generated specimen and its corresponding mesh of truss elements).

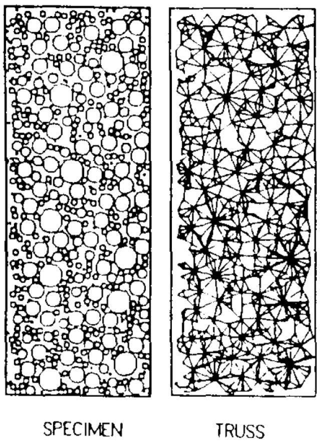

Fig. 2.2 Typical randomly generated specimen and its corresponding mesh of truss elements.

Schlangen and van Mier [8], Schlangen [9],[10] and van Mier et al. [11] first developed a lattice model for concrete. They used regular and irregular lattices in which each element was an elastic-brittle beam; these beam elements were able to transfer moment, axial and shear forces (see Fig. 2.3). The mechanical properties of the lattice beams were obtained by mapping the concrete mesostructure. This approach gives very realistic crack pattern under various loading conditions but one of the main disadvantages is that it doesn't satisfactory predict the load-displacement response as well as compression failure (these defects have been partially removed in a three-dimensional version of the model, Lilliu and van Mier [12]). Moreover, the element removal strategy usually employed to simulate cracking doesn't take into account a possible crack closure and that the length of the beam elements has to be smaller than the smallest aggregate represented in the mesh (this fact increase considerably the number of degrees of freedom in the calculation).

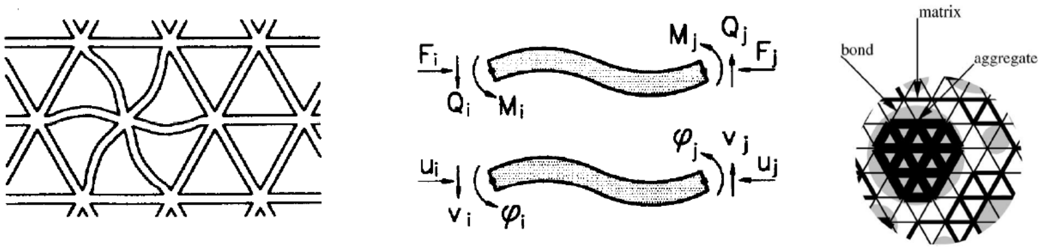

Fig. 2.3 Regular triangular lattice of beams, the external forces and deformations on a single element and the distinction between aggregate, matrix and bond phase.

Bolander and Saito [13], Bolander et al. [14],[15] formulated an irregular random lattice model in which the geometry of the model is based on the subdivision of the problem domain by means of Voronoi tessellation. They applied successfully to the simulation of fracture propagation in concrete.

Cusatis et al. [16] recently developed the Lattice Discrete Particle model (LDPM), which is a synthesis of two independent efforts, the Confinement Shear Lattice Model (CSL) and the Discrete Particle Model (DPM). This model can describe tensile cracking and continuous fracture as well as the nonlinear uniaxial, biaxial and triaxial response in compression, including the post-peak softening and strain localization. Three-dimensional conforming Delaunay triangulation and a dual domain tessellation define the topology and the geometry of the connection among the particles. The mechanical interaction among particles is characterized by axial and shear forces (shear behaviour exhibits friction and cohesion) (see Fig. 2.4).

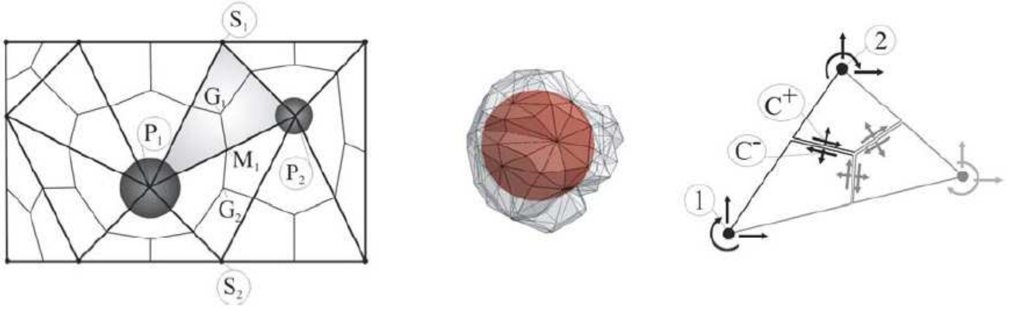

Fig. 2.4 Meso-structure tessellation, three-dimensional discrete particle and the definition of nodal degrees of freedom and contact facets in two dimensions.

As regards this thesis work, the mesoscale model adopted is the continuum one which represents more realistically composite materials such as concrete; therefore it is considered as a three-phase material and each phase is discretized through finite elements (HEXA20 for the three-dimensional case and HEXA 8 for the bi-dimensional one) with appropriate material properties. In Fig. 2.5 are reported the meshes adopted in the F.E. code NEWCON to study concrete at the meso level, respectively for the 2D and 3D cases.

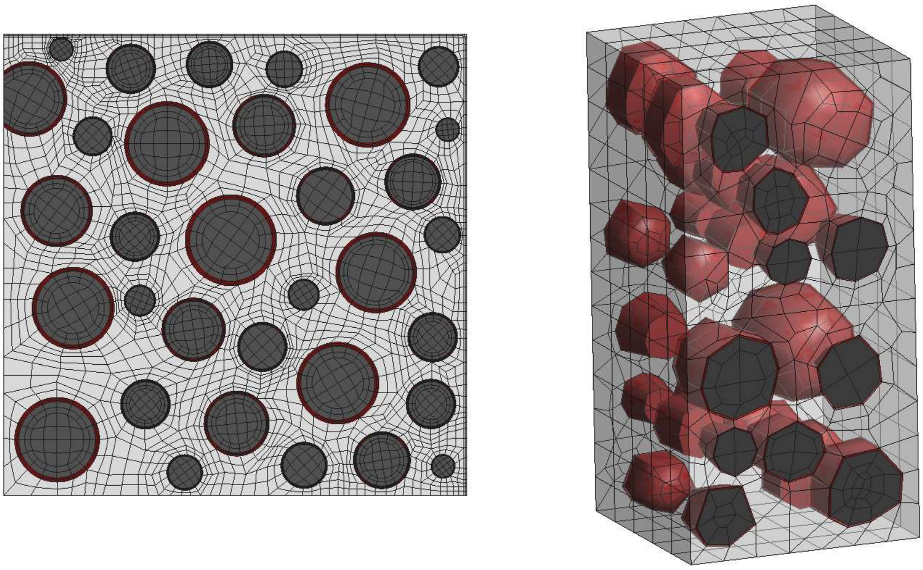

Fig. 2.5 Two examples of finite element mesh in 2D and in 3D, adopted in the F.E. code NEWCON to study the concrete behaviour at the meso level.

2.2 Concrete as a three-phase material

As composite material (see Fig. 2.6), concrete is a mixture of cement paste with aggregates inclusions of various sizes. Aggregates generally occupy 60-80% of the volume of concrete and greatly influence its properties, mix proportion and economy. Aggregates can be divided in two distinct categories: fine (often called sand) and coarse aggregates; the latter represents around the 40-50% of concrete volume.

However concrete is not just a two phase composite; it has been found that, the presence of grains in the cement paste, causes a thin layer of matrix material surrounding each inclusion to be more porous than the bulk of the surrounding cement paste matrix. This layer is named interfacial transition zone (ITZ) (see Refs. [17]-[22]) and has important effects on the properties of concrete, because it tends to act as the “weak link in the chain” when compared to the bulk cement paste and the aggregate particles.

In the following three subsections is presented a characterization and description of the properties of the three main components of concrete; this description is here focused on normal temperatures, indeed the changes of the properties behaviour at high temperatures will be treated in Section 4.2.

Fig. 2.6 Concrete sample at the mesoscale level.

2.2.1 Cement paste

The hydrated cement paste is a composite matrix of crystals of Calcium hydroxide, some minor components, unhydrated cement, pores of different sizes known as capillary pores and hydrates of various compounds (referred to collectively as gel) [23]. The gel itself has interstitial voids called gel pores, which are one or two order finer than the capillary pores. During the hydration process, the capillary pores represent that part of the volume not filled by the hydration products; therefore this volume reduces with the progress of hydration. Thus the capillary porosity depends by the water cement ratio of the mix (for w/c higher than 0.38, all cement can hydrate but capillary pores will also be present) and the degree of hydration.

These pores create an interconnected system distributed in the cement that is mainly responsible of the permeability of the hardened cement paste. In fact, for a mature paste, the permeability is not simply a function of its porosity, but it depends also by the distribution, shape, tortuosity, size and continuity of pores. Moreover it is lower the lower is the w/c ratio of the paste and with the progress of hydration (see Fig. 2.7).

If we analyse the stress-strain relations of the hardened cement paste and of the aggregates, individually under compression loading, they exhibit brittle elastic behaviour, that is to say linear, reversible deformation up to a limit, followed by sudden failure.

In contrast concrete, the composite material, shows significant quasi ductile behaviour (see Fig. 2.8). The load bearing capacity continues to increase beyond the linear elastic limit and there is a progressive decrease in load bearing capacity after the peak load. This behaviour that has important practical consequences, is due to the development of multiple microcracking predominantly in the ITZ.

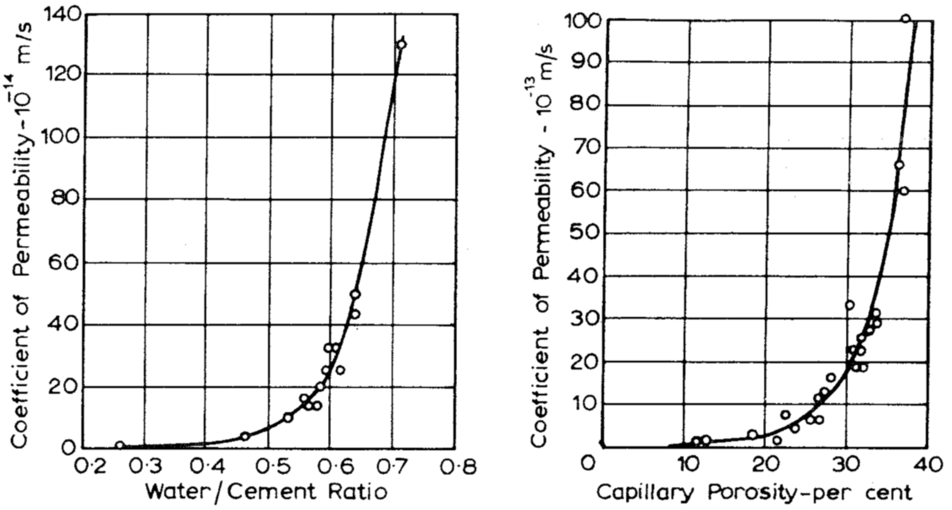

Fig. 2.7 Relation between permeability and water cement ratio and between permeability and capillary porosity of cement paste [23].

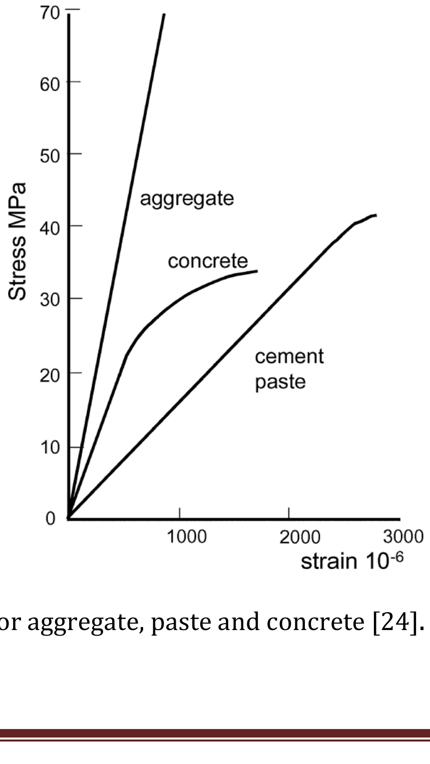

Fig. 2.8 Stress-strain relations for aggregate, paste and concrete [24].

As regards the modulus of elasticity of the cement paste, for normal weight concretes the hydrated cement has a smaller modulus of elasticity than aggregates. Therefore Young modulus of concrete is affected by the modulus of elasticity of the aggregates and by their volume proportion in concrete. Moreover also the quality of the bond, between the aggregates and the hardened cement paste, is important and may affect the modulus of elasticity value of concrete when it is strong, as in high performance concretes [23].

The thermal conductivity of concrete, that is a measure of the ability of the material to conduct heat and is defined as the ratio of heat flow rate to temperature gradient, depends on its composition and the moisture content at the time of heating [23], [25]. The degree of saturation is an important factor because the conductivity of air is lower than that of water (0.0034 W/m°C vs. 0.515 W/ m°C). On the other hand, the conductivity of water is less than half that of the hydrated cement paste, therefore the lower the water content the higher the conductivity of the hardened cement paste. As reported in [26] the thermal conductivity of saturated cement paste ranges between 1.1 and 1.6 W/m°C.

In any case the thermal conductivity of cement paste, it is less than for most aggregates; thus the conductivity of concrete will be greater if is greater the volume of the aggregates.

As regards the coefficient of thermal expansion [23], concrete has a positive value but it depends on the composition of the mix and on its hygral state at the time of heating, as the thermal conductivity.

The influence of the mix proportions is due to the fact that cement paste and aggregate have different coefficients. For the hydrated cement paste the values varies from 11×10-6 to 20×10-6 per °C and is higher than the coefficient of aggregate.

The influence of the moisture condition applies to the cement paste and is due to the fact that the thermal coefficient is made up of two parts: the true kinetic coefficient and the swelling pressure. The second part is due related to a decrease in the capillary tension of water held by the hydrated cement paste and in the absorbed water in it, with an increase of temperature.

2.2.2 Aggregates

Aggregates in concrete occupy at least three quarter of its volume and they account for the 70-85% of the weight of concrete; even if originally aggregate was viewed as an inert material, dispersed throughout the cement paste mainly for economic reasons, its physical, thermal and sometimes also chemical properties influence the performance of concrete.

Aggregates can be divided in two size groups: fine aggregates and coarse aggregates. Coarse aggregate is any particle (gravels constitute the majority of coarse aggregate used in concrete, with crushed stone making up most of the remainder) usually greater than 4.75mm in diameter, while fine aggregates generally consist of natural sand or crushed stone with most particles passing through a 4.75-mm sieve.

All natural aggregate particles originally formed a part of a larger mass, which has been fragmented by natural processes or artificially by crushing, Thus, many properties of the aggregate depend on the properties of the parent rock (such as chemical and mineral composition, strength, pore structure, etc…); on the other hand there are some properties possessed by the aggregate, but absent in the original mass (such as particle size, shape, etc…).

As regards the porosity of the aggregates, there are some pores wholly within the solid and other open onto the surface of the particle. Usually these pores are discontinuous; moreover, the cement paste envelops aggregate particles so that the pores in the aggregate do not contribute to the permeability of concrete. If the aggregate has a very low permeability, its presence reduces the effective area over which flow can take place. Furthermore, because the flow path in concrete has to circumvent the aggregate particles, the path becomes considerably longer, so that the effect of the aggregate in reducing the permeability may be considerable [23].

Regarding the strength and the elastic modulus of aggregates, in general they depend on its composition, structure and texture; then a low strength may be due to the weakness of constituent grains or if they are not well cemented together. As already said in the previous section, generally the normal weight aggregates have a higher Young modulus than the cement paste; therefore their volume and their modulus influence the modulus of the concrete composite.

The thermal conductivity, as previously introduced, is influenced by the conductivity of the aggregates (in general higher than for hardened cement paste) and by their volume proportion in concrete. The mineralogical character of the aggregates greatly affects the conductivity of the composite material; basalts and dolerites have a low conductivity, limestones and granites are in the middle range while siliceous and quartz aggregates exhibit the highest conductivities (see [23], [25]). In Table 2.1 are reported the thermal conductivities for saturated concrete in presence of different types of aggregates.

Table 2.1 Thermal conductivity for saturated concretes at temperature between 5 and 25 °C [27].

Aggregate type	Thermal conductivity for concrete [W/m°C]
Siliceous rocks e.g. quartzite and sandstone)	2.4-3.6
Igneous crystalline, e.g. granites and gneisses Sedimentary carbonate, e.g. limestone and dolomite	1.9-2.8
Igneous amorphous, e.g. basalts and dolerites	1.0-1.6

As regards the coefficient of thermal expansion, as previously advanced, it influences the coefficient of thermal expansion of concrete; the higher the coefficient of the aggregate the higher the coefficient of the concrete, which depends also on the aggregate content in the mix (see Table 2.2) and on the mix proportions in general. The coefficient of thermal expansion for the aggregates varies with the type of parent rock (Table 2.3) [23].

Table 2.2 Influence of aggregate content on the coefficient of thermal expansion.

Cement/sand ratio	Thermal coefficient of linear Expansion at the age of 2 years [10^{-6} per °C]
Neat cement	18.5
1:1	13.5
1:3	11.2
1:6	10.1

Table 2.3 Linear coefficient of thermal expansion for different rock types.

Rock Types	Thermal coefficient of linear expansion [10^{-6} per °C]
Granite	1.8-11.9
Diorite, andesite	4.1-10.3
Gabbro, basalt, diabase	3.6-9.7
Sandstone	4.3-13.9
Dolomite	6.7-8.6
Limestone	0.9-12.2
Chert	7.3-13.1
Marble	1.1-16.0

2.2.3 Interfacial Transition Zone

Cement grains size ranges from less than a micron up to 100 microns, while the aggregates are several orders of magnitude larger. This difference of size means that the aggregate particle is an obstacle which disrupts the packing of cement grains, resulting in the so called "wall effect" [24] (see Fig. 2.9). The origin of the ITZ lies in this "wall effect" of packing against the relatively flat aggregate surface[24]. In fact, as shown in this figure if a large object was placed in a random assembly of grains it would cut through many grains. As this is physically impossible in the case of aggregate particles in cement paste the normal packing of the grains is disrupted. The result is that the zone closest to the aggregate contains small grains and has a significantly higher porosity, while larger grains are found further out.

This means that the size of the ITZ is comparable with the size of cement grains and that, since packing is a random process, each individual region of ITZ will be different.

Anyway its thickness is typically in the range of 15-50 µm [28], according to numerous researchers. One reason for this large range is that there is no clear cut-off transition from

ITZ paste to matrix paste. Generally the ITZ can be considered to end when the porosity is within the 10% of the bulk value.

The packing of the anhydrous cement grains is the origin of the ITZ, but its eventual structure is also determined by the way in which the hydration products are deposited in this region [24]. During hydration, the microstructural development of Portland cement is dominated by the formation of the two major hydrate phases: the C-S-H (calcium silicate hydrate) and the CH (calcium hydroxide). After the first few seconds, the concentration of silicate in solution remains very low and consequently the C-S-H phase is mostly deposited around the cement grains. In contrast the concentration of calcium in solution is much higher in solution and calcium hydroxide is mainly deposited in the open pores.

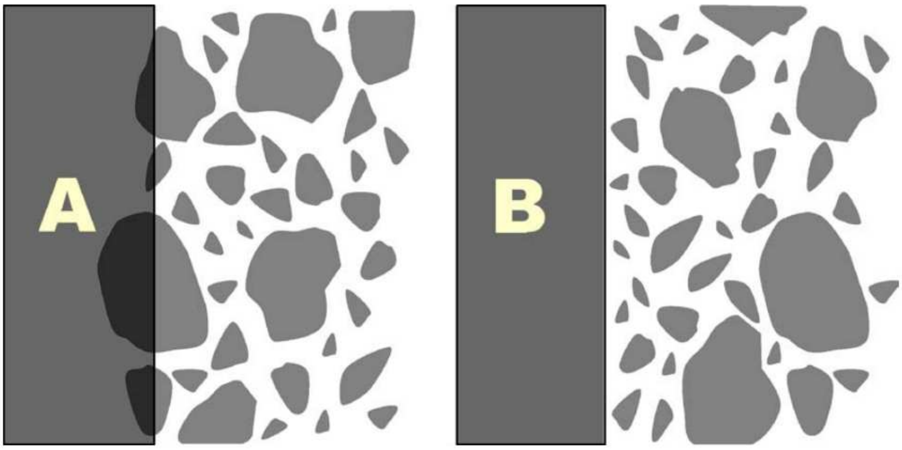

Fig. 2.9 Illustration of the “wall” effect. (see Ref. [24]).

As mentioned above, the packing of cement grains leaves an initially more porous zone around the aggregate. This favours the deposition of more calcium hydroxide in this zone, as can be seen in Fig. 2.10 on the left; on the right it is reported the redistribution of calcium hydroxide in the ITZ. The distribution of C-S-H and its redistribution is show in Fig. 2.11.

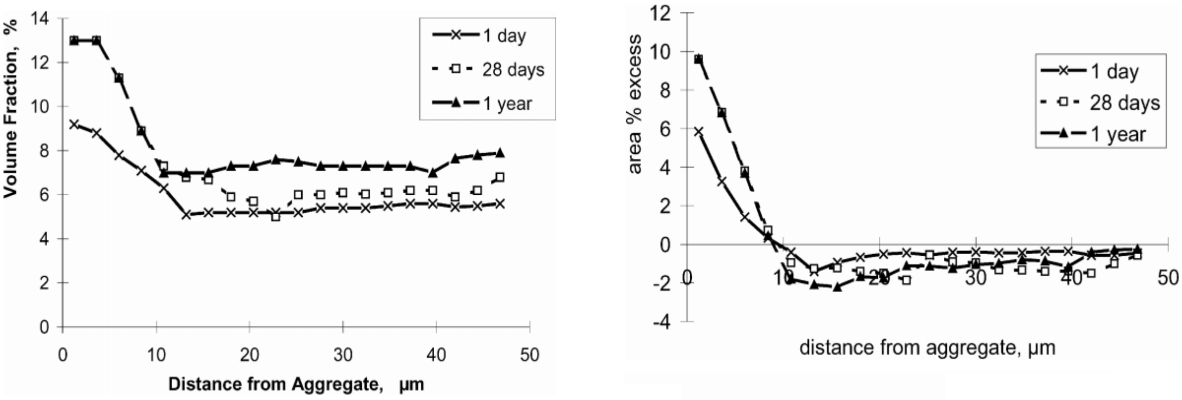

Fig. 2.10 Average distribution of calcium hydroxide (on the left) and its redistribution in the ITZ (on the right). The area of excess is the % area above that which would have been formed from the local reaction of anhydrous material [24].

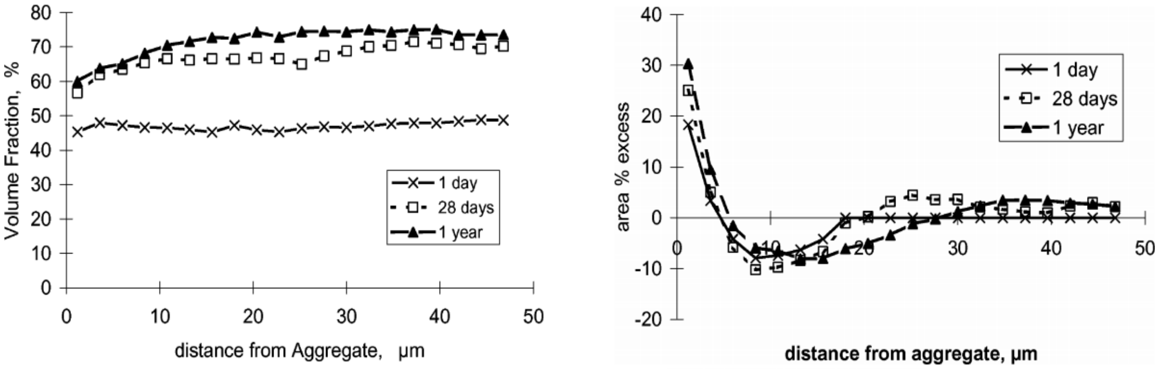

Fig. 2.11 Average distribution of C-S-H (on the left) and its redistribution in the ITZ (on the right) [24].

The quantification of the porosity in the ITZ may be performed by means of two main techniques: scanning electron microscopy (SEM) and mercury intrusion porosimetry (MIP) [28]. SEM backscattered electron studies of polished sections in conjunction with computerized image analysis allow to study porosity as a function of the distance from the aggregate surface as shown in Fig. 2.12 .By this figure it is important to notice that the ITZ has a maximum porosity that is about 3 times higher than the matrix paste and that the presence of the ITZ affects the matrix paste by reducing its porosity compared with the nominal average porosity. Moreover it is possible to notice by Table 2.4. [29] a significant reduction of the ITZ porosity with a continuation of the hydration.

Assuming that the two components have the same degree of hydration, this suggests that the matrix paste has gained cement at the expense of the ITZ and thus has a reduced water/cement ratio.

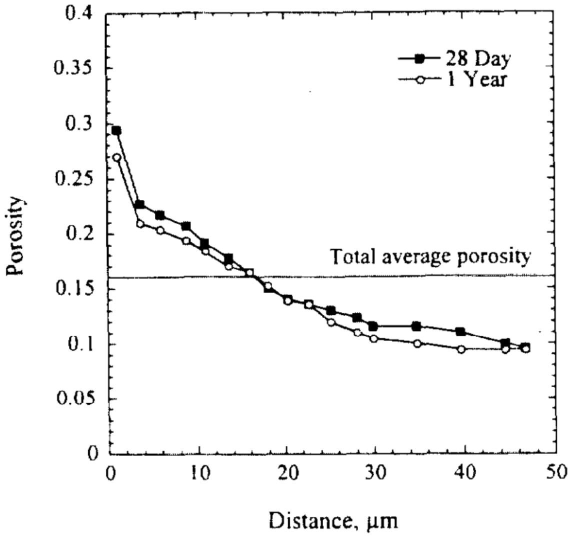

Fig. 2.12 Average porosity in the ITZ, as a function of distance from the aggregate surface for a concrete with w/c = 0.4 [28].

Table 2.4 Evolution of the ITZ porosity with hydration [29].

Time [months]	Porosity of the bulk paste (%)	Porosity of the ITZ (%)	Ratio
1	22±1	46±1	2.1±0.1
3	22±1	37±1	1.7±0.1
6	22±1	34±1	1.5±0.1
12	22±1	30±1	1.4±0.1

As regards MIP, it measures the overall porosity and approximates the pore-size distribution of a material, injecting mercury under pressure into an evacuated sample. A defect of this technique is that internal pore pressure will be attributed to the pore-neck diameters that connect them to the surface. Therefore, in mortars where the ITZ is not percolated through the sample (low volume fractions of sand), the volume of the ITZ pores will be wrongly assigned to pores of the matrix paste. However once the ITZ is percolated through the sample, the ITZ and matrix paste pores can be differentiated.

So this zone is characterized by a layered structure and has a lower density than the bulk matrix.

As regards the permeability, the significance of the interface zone remains uncertain; in fact for some author this zone contributes significantly to the permeability, for others it doesn’t seem to contribute to the flow.

For Massazza [30], the higher porosity (determined on composite concrete specimens consisting of a single cylindrical piece of limestone or quartz surrounded by a ring of cement paste) in the interfacial zone is associated with a greater permeability; indeed this higher permeability, compared with the cement paste, is confirmed by comparing the permeability coefficient of neat paste and limestone discs with the coefficients of discs formed by a cylindrical inclusion of limestone surrounded by paste.

In the work of Katz and Thomson [31] is reported the considerable increase in permeability when aggregates are added to a paste or mortar. Theoretically the addition of low permeability aggregates to cement paste should reduce overall permeability because they interrupt the pores continuity in the cement paste matrix; the results obtained by Katz and Thomson instead indicate that the opposite is true.

Mehta [32] analysed these tests and attributed the permeability increase in the ITZ to the presence of microcracks in this transition zone (these cracks become more severe in presence of aggregates of greater size).

On the contrary Larbi [33] found that, despite the higher porosity of the ITZ the permeability of concrete is controlled by the bulk of the cement paste, which is the only continuous phase in concrete. The permeability of hardened cement paste is not lower than that of concrete made with a similar cement paste.

Dhir et al [34] found no significant difference in air permeabilities of concrete made from aggregates of different size. There is a slight increase in the ITZ when using 40mm aggregates is considered; this is due to the lower quality of the transition zone.

Additionally, due to its complex structure, the ITZ appears to be the weakest region of the composite material when exposed to external loads [35]. In continuum mechanics, concrete is often schematised as a material showing a softening behaviour. Experimental studies have shown that if we zoom in on the material, we can explain why we have a softening behaviour; a zone of microcracks is formed and crack bridging, branching and friction effects all have a contribution to the toughness of concrete. The microstructure of the material has a large influence on the crack pattern; being the ITZ the weakest link in concrete the cracks follow this zone.

Experiments have demonstrated that the elastic modulus of concrete is strictly related to the elastic modulus and volume fraction of the ITZ regions.

In the work of Hashin et al. [36], since the elastic moduli of the cement paste and aggregate are often known but no experimental data exist on the elastic modulus of the ITZ, is reported an efficient methodology to estimate the values of the transition zone from experimental data on Portland cement mortar samples cast with varying amounts of sand concentration. This model predicts that the Young and shear's moduli of ITZ are ~50% of those of the bulk cement paste, where calculations are based upon experimental tests by Wang te al. In this paper concrete is modelled as a composite consisting of a matrix in which are embedded spherical particles, each of them surrounded by a concentric spherical shell. The phases are considered elastic isotropic and the entire composite is assumed to be homogeneous and isotropic.

In the work of Simenov and Ahmad [37], the influence of the transition zone on the elastic modulus is studied and the theoretical bounds of Hashin –Shtrikman (HS) for the modulus of elasticity of two-phase composite material are used as a criteria in the analysis. It is noticed a notable influence of the ITZ on the elastic behaviour of the composite; in fact is detected a divergence of the experimental data from the trend of the HS bounds with the increase of the aggregate volume. The influence of the transition zone it is strongly related to the water-cement ratio:

- for higher W/C the ITZ is with lower equivalent elasticity than that of the matrix and in a thicker layer and in bigger relative volume to a unit interface surface; so the result is a significant reduction of the Young modulus of the composite material if compared to the expected value obtained with HS bounds;

- for lower W/C the ITZ is thinner and its equivalent elastic properties are probably very close to that of the matrix or even higher; so the result is a notable relative increase of the Young modulus of the composite material if compared to the expected value obtained with HS bounds.

2.3 Mesoscale modelling in NEWCON3D

For the numerical simulations at the meso level (see Chapter 5) in this thesis have been adopted mesoscopic continuum models; the novelty here is that each single composite constituent itself can be approached as a multi-phase material, fully described and characterized via the coupled thermo-hydro-mechanical model described in Chapter 3.

As regards the 3D and 2D models (see the meshes reported in Fig. 2.5) the coarse aggregates occupy the 40-50% of concrete volume, have angular shapes of different sizes (for the bi-dimensional case also rounded shape are taken into account), are distributed randomly in the concrete sample and have an elastic behaviour (the do not creep and do not damage). They are assumed homogeneous and characterized by a higher elastic modulus if compared to the other two phases in the composite material, a very small permeability and an higher thermal conductivity.

The mortar matrix is a homogeneous material, comprehensive of the cement paste and of the fine aggregates; if compared to the coarse aggregates it has a smaller Young modulus, a smaller thermal conductivity and a higher permeability.

The interfacial transition zone is assumed to be homogeneous and with a thickness which is strictly linked to the diameter of each aggregate (thicker for larger diameters); it has a smaller Young modulus if compared to the cement paste (it is assumed that is $\sim$50% of the cement paste Young modulus) and a higher permeability.

For the mortar matrix and the ITZ it is not assumed an elastic behaviour; these two phases are subjected to creep (to characterize the creep features is adopted Model B3, by Bažant and Baweja) and damage behaviour (it is considered the non-local Mazars' damage law).

REFERENCES

[1] Roelfstra P.E., Sadouki H., Wittmann F.H. (1985), Le béton numerique, Mater Struct, 18, pp.309-317.

[2] Willam K.J,, Rhee I. and Xi J. (2005), Thermal degradation of heterogeneous concrete materials, Journal of Materials in Civil Engineering, ASCE, 17, No. 3, pp. 276-285.

[3] Sadouki H. and Wittmann (2001), Damage in a composite material under combined mechanical and hygral load, Continuous and Discontinuous Modelling of Cohesive-Frictional Materials, Edited by P.A. Vermeer, S. Diebels, W. Ehlers, H.J. Herrmann, S. Luding, E. Ramm, Lecture Notes in Physics, vol. 568.

[4] Wittmann F.H., Roelfstra P.E. and Kamp C.L. (1988), Drying of concrete: an application of the 3L-approach, Nucl. Eng. Des., 105, pp. 185-198

[5] Carol I., Lopéz C.M. and Roa O. (2001), Micromechanical analysis of quasi-brittle materials using fracture-based interface elements, Intern. J. Numer. Methods Engrg, 15, pp. 120- 133.

[6] Wriggers P. and Moftah S.O. (2006), Mesoscale models for concrete: Homogenisation and damage behaviour, Finite El An Des 2006, 42, pp. 623-636.

[7] Bazant Z.P., Tabbara M.R., Kazemi M.T. and Pijaudier-Cabot G. (1990), Random particle model for fracture of aggregate or fiber composites, J. Engrg. Mech., 116(8), pp. 1686-1705.

[8] Schlangen E and van Mier J.G.M (1992), Simple lattice model for numerical simulation of fracture of concrete materials and structures, Materials and Structures, 25(153), pp. 534-542.

[9] Schlangen E., (1993), Experimental and numerical analysis of fracture process in concrete, PhD Thesis, Delft University of Technology, Delft, The Netherlands.

[10] Schlangen E. (1995), Computational aspects of fracture simulations with lattice models, Fracture Mechanics of Concrete Structures, F.H. Wittmann ed., pp. 913-928.

[11] van Mier J.G.M., Vervuurt A. and Schlangen E. (1994), Boundary and size effects in uniaxial tensile tests: A numerical and experimental study, Fracture and damage in quasi brittle structures, Z.P. Bazant, Z. Bittnar, M. Jirasek and J. Mazars eds., E&F Spon, London.

[12] Lilliu G. and van Mier J.G.M. (2003), 3D lattice type fracture model for concrete, Engineering Fracture Mechanics, 70, pp. 927-941.

[13] Bolander J.E. and Saito S. (1998), Fracture analysis using spring networks with random geometry, Engineering Fracture Mechanics, 61, pp. 569-591.

[14] Bolander J.E., Yoshitake K. and Thomure J. (1999), Stress analysis using elastically uniform rigid-body-spring networks, Journal of Structural Mechanics and Earthquake Engineering, JSCE, No. 633/I-49, pp. 25-32.

[15] Bolander J.E., Hong G.S. and Yoshitake K. (2000), Structural concrete analysis using rigid-body-spring networks, Computer-Aided Civil and Infrastructure Engineering, 15, pp. 120-133.

[16] Cusatis G., Pelessone D., Mencarelli A. and Baylot J.T. (2011), Lattice Discrete Particle Model (LDPM): Formulation, Calibration, and Validation.

[17] Scrivener K.L. (1989), The microstructure of concrete, Material science of concrete, Skalny J., Ed., American Ceramic Society: Westerville (OH), 1, pp. 127–162.

[18] Scrivener K.L. and Pratt P.L. (1996), Characterization of interfacial microstructure, Interfacial transition zone in concrete, Maso J.C., Ed., RILEM Report 11, E&FN Spon: London, UK, pp. 3–17.

[19] Scrivener K.L. (1999), Characterization of the ITZ and its quantification by test methods, Engineering and transport properties of the interfacial transition zone in cementitious composites, Alexander M.G., Arliguie G., Ballivy G., Bentur A., Marchand J., Eds., RILEM Report 20, RILEM Publications S.A.R.L.: France, pp. 3–15.

[20] Scrivener K.L. and Nemati K.M. (1996), The percolation of pore space in the cement paste/aggregate interfacial zone of concrete, Cem Conc Res, 26(1), pp. 35–40.

[21] Bentz D.P., Garboczi E.J. and Stutzman P.E. (1993), Computer modeling of the interfacial transition zone in concrete, Interfaces in cementitious composites, Maso J.C., Ed., E&FN Spon: London, UK, Part I, Chapter 6, Section 3, pp. 259–268.

[22] Bentz D.P., Stutzman P.A. and Garboczi E.J. (1992), Experimental and simulation studies of the interfacial zone in concrete, Cem Conc Res., 22(5), pp. 891–902.

[23] Neville A.M. (2006), Properties of concrete, Fouth and Final Edition.

[24] Scrivener K.L., Crumbie A.K. and Laugesen P. (2004), The interfacial transition zone between cement paste and aggregate in concrete, Interface Science, 12, pp. 411-421.

[25] Bažant Z.P. and Kaplan M.F. (1996), Concrete at High temperatures: Materials properties ans mathematical models, Longman.

[26] Zoldners N.F. (1971), Thermal properties of concrete under sustained elevated temperatures, Temperature and Concrete, ACI Special Publication n° 25, Detroit.

[27] Blundell R., Diamond C. and Browne R.G. (1976), The properties of concrete subjected to elevated temperatures, Technical note n°9, CIRIA Underwater engineering group, London.

[28] Garboczi E. J., Bentz, D. P., Shane, J. D., Mason T. O and Jennings H.M. (2000), Effect of the interfacial transition zone on the conductivity of Portland cement mortars, Journal of the American Ceramic Society, 83(5), pp. 1137-1144.

[29] Marchand J. and Delagrave A. (1999), Influence of ITZ on ionic diffusion and leaching, in Engineering and Transport Properties of the Interfacial Transition Zone in Cementitious Composites, RILEM Report 20, pp. 157-171.

[30] Massazza F. (1996), Action of environmental conditions, Interfacial Transition Zone in Concrete, Ed. J.C. Maso, pp.132-149.

[31] Katz A.J. and Thomsom A.H. (1986), A quantitative prediction of permeability in porous rocks, Physical Reviews B, 24, pp. 8179-8181.

[32] Mehta P.K. (1986), Concrete: Structure, Properties and Materials, Prentice Hall, NJ.

[33] Larbi L.A. (1993), Microstructure of the interfacial zone around aggregate particles in concrete, Heron, 38.

[34] Dhir R.K., Hewlett P.C. and Chan Y.N. (1989), Near surface characteristics of concrete: intrinsic permeability, Magazine of Concrete Research, 41, n°147, pp. 87-97.

[35] Brandt A.M. (1995), Cement-based composites: materials, mechanical properties and performance, E&FN Spon: London, UK.

[36] Hashin Z. and Monteiro P.J.M. (2002), An inverse method to determine the elastic properties of the interphase betweenthe aggregate and the cement paste, Cement and Concrete Research, 32, pp. 1291-1300.

[37] Simeonov P. and Ahmad S. (1995), Effect of transition zone on the elastic behaviour of cement-based composites, Cem Conc Res, 25(1), pp. 165–176.

3 THE MATHEMATICAL MODEL

3.1 Introduction

For the numerical modelling of concrete, at the macro and meso-scale levels, has been adopted a 3D fully coupled thermo-hydro-mechanical model of heated concrete developed at Padua University. The generated F.E. code is named NEWCON3D and it represents an updated version of DAMVIS, VISCO and DAMAGE codes (see Refs. [1]-[4]).

In this code concrete is treated as a multiphase system where the voids of the skeleton are partly filled with liquid and partly with a gas phase (see [5],[6]). The liquid phase consists of bound water (or adsorbed water), which is present in the whole range of water contents of the medium, and capillary water (or free water), which appears when water content exceeds so-called solid saturation point Sssp [7], i.e. the upper limit of the hygroscopic region of moisture content. The gas phase, i.e. moist air, is a mixture of dry air (non-condensable constituent) and water vapour (condensable gas), and is assumed to behave as an ideal gas.

As regards the mechanical field, NEWCON3D couples creep and shrinkage, thermo-mechanical damage and plasticity effects under medium and high temperature level conditions.

The approach here is to start from a phenomenological model ([1], [8] and [9]), originally developed by Bažant and co-authors, e.g. [10]-[13], in which mass diffusion and heat convection-conduction equations are written in terms of relative humidity, to an upgraded version in which its non-linear diffusive nature is maintained as well as the substitution of the linear momentum balance equations of the fluids with a constitutive equation for fluxes, but new calculations of thermodynamic properties for humid gases are implemented too to take into account different phases as well as high ranges of both pressure and temperature. Additionally, Darcy's law is modified when describing gas flow through concrete. The proposed model couples non-linear material relations with experimental relations; to enhance its predictive capabilities, a predictor-corrector procedure is supplemented to check the exactness of the solution.

3.2 Heat and mass flow

3.2.1 Introduction

It is here presented the calculation method adopted for the determination of the hygrothermal fields of concrete during shrinkage.

Bažant and Najjar [14] have analysed the moisture loss in concrete using a nonlinear diffusion theory. The authors assumed diffusivity dependent by the humidity in the pores, through a highly nonlinear relation. Roelfstra and Wittmann [15] have numerically simulated drying and shrinkage of aerated concrete, using a finite element approach. The authors have developed an axisymmetric finite element to determine stresses and strains, which take place in a cylinder, for the humidity diffusion. The same approach has been used by Wittmann to describe drying and shrinkage of hardened cement paste [16].

Comini and Lewis [17] have simulated, with a finite element model, the coupled equations which govern the mass and heat fluxes in an unsaturated porous medium, to study the drying processes in ceramic materials. In this work the diffusion equation is function of the vapour content (i.e. mass vapour per unit volume). Majorana [18] has applied a formulation of the diffusion law in terms of the relative humidity, coupled with the equilibrium equations and the heat conduction, to the study of shrinkage of a three dimensional concrete model.

Sih, Michopoulos, and Chou [19] have analysed the stress field of elastic bodies subjected to the thermal and humidity fields, focusing on the properties of the materials, in the specific case resins.

Assuming that the various phases of water in each pore (vapour, absorbed and capillary water) are in thermodynamic equilibrium with each other (see Ref. [14]) and with the solid skeleton; the relation between the relative humidity and the moisture content , considering the temperature and hydration effects, can be written as:

$$\mathrm{d}h = K\mathrm{d}w + k\mathrm{d}T + \mathrm{d}h_s - \chi \mathbf{m}^T \mathrm{d}\boldsymbol{\varepsilon} \tag{3.1}$$

where $K = \left.\left(\dfrac{\partial h}{\partial w}\right)\right|_T$ is the cotangent of the slope of the isotherm $w = w(h)$, $k = \left.\left(\dfrac{\partial h}{\partial T}\right)\right|_{w,\varepsilon}$ is the hygrothermal coefficient representing the change in h due to one-degree change of T at constant w, $\boldsymbol{\varepsilon}$ and a fixed degree of saturation, $\mathrm{d}h_s$ is the self-desiccation and $\chi = \left.\left(\dfrac{\partial h}{\partial \boldsymbol{\varepsilon}_V}\right)\right|_{T,w}$ equals the change in h due to unit change of volumetric strain $\boldsymbol{\varepsilon}_V$ at constant w, constant T and given degree of saturation. The last term at the right hand side of eq. [3.1]represents the coupling term for connecting hygro-thermal and mechanical responses [8].

The relative humidity connects the equilibrium water vapour pressure to the saturation pressure through the Kelvin equation (see Ref. [20]):

$$p_{gw} = p_{gws}(T) \cdot h \tag{3.2}$$

where p_{gws} can be calculated e.g. from [21] or [22].

As said before, the diffusion equation governing moisture movement in concrete is known to be highly non-linear, due principally to diffusivity being strongly dependent on relative humidity [14]. Loss of moisture must therefore be treated as a non-linear diffusion problem, and since humidity change really depends on the free energy of water, a basic equation is:

$$\mathbf{J} = C \cdot \mathrm{grad}\mu_w \qquad [3.3]$$

where μ_w is the free energy of water and C is the diffusivity that can be expressed as:

$$C = a \cdot K$$

in which a is the permeability, that is a function of h and of the temperature T.

Additionally, the relation between the rate of change of the mass of water per unit volume and the flux field is defined by:

$$\frac{\partial w}{\partial t} = -\ \mathrm{div}\mathbf{J} \qquad [3.4]$$

Bažant and Najjar [14], used the following expression for :

$$C(h) = C_1 \left[\alpha_0 + \frac{1-\alpha_0}{1+\left(\frac{1-h}{1-h_c}\right)^n} \right] \qquad [3.5]$$

in which h_c = 0.75, 6 ≤ n ≤ 16, 0.025 ≤ α_0 ≤ 0.10, and C_1 is given by

$$C_1 = C_{10}\left(1 + \frac{10}{t_e}\right) \qquad (t_e \text{ in days}) \qquad [3.6]$$

where C_{10} is a material constant and t_e is an equivalent time.

In Ref. [23] is suggested the following expression for :

$$C_1(T,t_e) = C_0\left[0.3 + \sqrt{\frac{13}{t_e}}\right]\frac{T}{T_0}e^{\frac{Q}{R}\left(\frac{1}{T_0}-\frac{1}{T}\right)} \qquad [3.7]$$

in which C_0 is the diffusivity at 28 days and temperature T_0 (= 293K), R is the constant of perfect gases and Q is the activation energy of the diffusion process ($Q/R \approx$ 4700 K). In Fig. 3.1 is represented the variation of the diffusion coefficient with relative humidity (eqs. [3.5]-[3.7]).

Hence, the flux of humidity may be written as:

$$\mathbf{J} = -a \cdot \mathrm{grad}h \qquad [3.8]$$

The Soret flux (thermal moisture flux) is already included in eq. [3.8]; this is because:

$$\mathrm{grad}h = \mathrm{grad}\frac{p_{gw}}{p_{gws}} = \frac{1}{p_{gws}}\left[\left(\frac{\partial w}{\partial p_{gw}}\right)\mathrm{grad}p_{gw} + \left(\frac{\partial w}{\partial T}\right)\mathrm{grad}\mathrm{T}\right] \qquad [3.9]$$

which follows by differentiating the sorption relation $w = w(p,T)$.

The continuity equation for non-isothermal flow is finally obtained as (refs. [1], [2], [3], [8] and [9]):

$$\frac{\partial h}{\partial t} - \nabla^T \mathbf{C}\nabla h - \frac{\partial h_s}{\partial t} - k\frac{\partial T}{\partial t} + \chi \mathbf{m}^T \frac{\partial \boldsymbol{\varepsilon}}{\partial t} = 0 \qquad [3.10]$$

where $\mathbf{C}$ is the diffusivity diagonal matrix.

The heat balance requires that

$$\rho C_q \frac{\partial T}{\partial t} - C_a \frac{\partial w}{\partial t} - C_w \mathbf{J}\cdot\nabla T = -div\mathbf{q} \qquad [3.11]$$

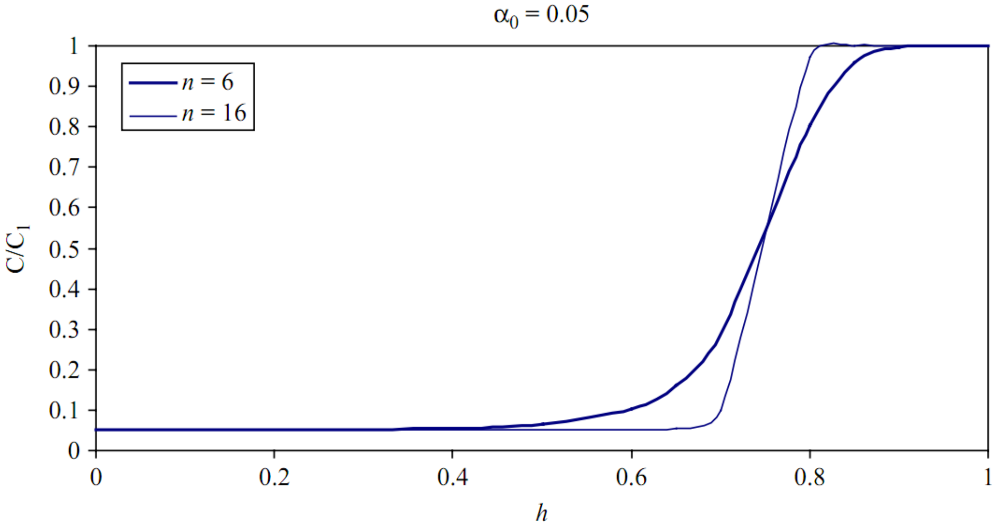

Fig. 3.1 Variation of the diffusion coefficient with relative humidity (redrawn from Bažant and Najjar).

in which ρ is the mass density of concrete, C_q the isobaric heat capacity of concrete (per kilogram of concrete) including chemically bound water but excluding free water, C_a the heat of sorption of free water (per kilogram of free water); C_w is the isobaric heat capacity of bulk (liquid) water; $C_w \mathbf{J}\cdot\nabla T$ is the rate of heat supply due to convection by moving water and $\boldsymbol{q}$ is the heat flux. Usually, the term of heat convection is negligible, but in rapid heating it might not be so. The heat of vaporization of water does not figure explicitly, but it may be included within the second term of the left hand side expression (see Ref. [12]).

The heat flux **q** is due to temperature gradient (governed by Fourier's law) and to the moisture concentration gradient (Dufour's flux)

$$\mathbf{q} = -a_{Tw} \nabla w - a_{TT} \nabla T \qquad [3.12]$$

where the coefficients a_{Tw} and a_{TT} depend on w and T respectively.

Due to the negligible contribution of the moisture flux, eq. [3.12] may be re-written as

$$\mathbf{q} = -a_{TT} \nabla T \qquad [3.13]$$

and a_{TT} is the heat conductivity.

3.2.2 Numerical formulation of heat and moisture transfer equations

The numerical formulation of the eqs. [3.10] and [3.11], together with the corresponding initial and boundary conditions, is an application of the classical finite elements theory.

Approximating temperatures and humidities with their nodal values, respectively **T** and **h**, through the shape functions **N** it is possible to obtain the following system of equations:

$$\mathbf{H} \cdot \mathbf{h} + \mathbf{S} \frac{d\mathbf{h}}{dt} + \mathbf{TH} \frac{d\mathbf{T}}{dt} + \mathbf{HR} \cdot \mathbf{T} = \frac{\partial \mathbf{HG}}{\partial t} \qquad [3.14]$$

$$\mathbf{TR} \cdot \mathbf{T} + \mathbf{TS} \frac{d\mathbf{T}}{dt} + \mathbf{HT} \frac{d\mathbf{h}}{dt} = -\frac{\partial \mathbf{TG}}{\partial t} \qquad [3.15]$$

in which:

- $\mathbf{H} = \int_{(S)} (\nabla \mathbf{N})^T \ \mathbf{C} \ (\nabla \mathbf{N}) \ dV$: is the matrix of humidity diffusion;

  where $\mathbf{C}$ is the diagonal matrix of diffusivity

- $\mathbf{S} = \int_{(S)} \mathbf{N}^T \ \rho c_m \ \mathbf{N} \ dV$: is matrix of humidity capacity;

  where ρc_m is the mass capacity

- $\mathbf{TH} = \int_{(S)} \mathbf{N}^T \ K \ \mathbf{N} \ dV$: is the coupling matrix representing the influence of temperature in the equation of humidity diffusion;

  where K is the hygrothermal coefficient

- $\mathbf{HR} = \int_{(S)} \nabla \mathbf{N}^T \ (\mathbf{C}\delta) \ \nabla \mathbf{N} \ dV$: is the coupling matrix representing the influence of temperature in the equation of humidity diffusion;

  where δ is the coefficient of the thermal diffusion gradient

- $\mathbf{HG} = \int_{(S)} \mathbf{N}^T \ h_s \ dV$: where $\frac{\partial \mathbf{HG}}{\partial t}$ represents the variation in humidity due to auto-drying;

  where h_s is the humidity at the end of the hydration process in a body waterproofed on the surface and initially h = 1

- $\mathbf{TR} = \int_{(S)} (\nabla \mathbf{N})^T \ \mathbf{\Lambda} \ (\nabla \mathbf{N}) \ dV$: is the matrix of thermal transmission;

  where $\mathbf{\Lambda}$ is the diagonal matrix of the thermal conductivity

- $\mathbf{TS} = \int_{(S)} \mathbf{N}^T \ (\rho c_q) \ \mathbf{N} \ dV$: is the matrix of heat capacity;

  where ρc_q is the heat capacity

- $\mathbf{HT} = \int_{(S)} \mathbf{N}^T \ (\varepsilon \lambda \rho c_m) \ \mathbf{N} \ dV$: is the coupling matrix representing the influence of humidity in the equation of heat transfer;

  where ε is the ratio between the vapour diffusion coefficient and the total fluid diffusion coefficient and λ is the latent heat of vaporization

- $\mathbf{TG} = \int_{(S)} \mathbf{N}^T \ Q_h \ \mathbf{N} \ dV - \int_{(c)} \mathbf{N}^T \ q_h \ d\Gamma$: where $\frac{\partial \mathbf{TG}}{\partial t}$ represents the variation in heat flux.

  where Q_h is the flow generated per unit volume and q_h is the flow generated per unit surface.

3.3 Creep and shrinkage modelling

3.3.1 Concrete as an aging viscoelastic material

The total strain of a uniaxial loaded concrete specimen at age t, can be represented in this additive form:

$$\begin{aligned}\varepsilon(t)&=\varepsilon_E(t)+\varepsilon_C(t)+\varepsilon_S(t)+\varepsilon_T(t)=\varepsilon_E(t)+\varepsilon''(t)=\varepsilon_E(t)+\varepsilon_C(t)+\varepsilon^0(t)\\&=\varepsilon_\sigma(t)+\varepsilon^0(t)\end{aligned} \qquad [3.16]$$

where $\varepsilon_E(t)$ is the instantaneous strain, which is elastic if the stress is sufficiently smaller than the yield stress in a uniaxial regime (immediately recoverable after the moment of loading, even if, with the passing of time, it is irreversible due to ageing caused by hydration), $\varepsilon_C(t)$ is the creep strain, $\varepsilon_S(t)$ is the shrinkage, $\varepsilon_T(t)$ is the thermal expansion, $\varepsilon^0(t)$ is the inelastic strain (stress-independent), $\varepsilon''(t)$ is the elastic strain (stress-dependent) and $\varepsilon^\sigma(t)$ is the stress produced strain.

Creep measurements, generally, require two identical specimens, with the same stress history; one specimen being loaded and the other being load free. The difference between the strains of these two specimens defines the mechanical strain, consisting of creep strain plus the instantaneous one.

Here are considered only creep strains produced by constant stresses. By measuring strains of test specimens loaded to different stress levels, and representing the creep isochrones (stress-strain curves for fixed load durations (Fig. 3.2)), one finds that for stresses less than 0.4 of the strength (within the so called service stress range) these curves are approximately linear.

Thus:

$$\varepsilon(t)=\sigma J(t,t')+\varepsilon^0(t) \qquad [3.17]$$

where σ is the uniaxial stress, ε is the uniaxial strain, t is the time (normally chosen to represent the age of concrete) and $J(t,t')$ is the compliance function that represents the creep plus the elastic strain at time t, produced by a unit constant uniaxial stress applied by the time t'.

Within the linear range, the creep strain produced by a uniaxial stress, is entirely characterized by function $J(t,t')$ (the typical shape is sketched in Fig. 3.3).

The compliance function is often expressed as a sum of an elastic part $1/E(t,t')$ and the creep compliance $C(t,t')$ (also called *specific creep*):

$$J(t,t')=\frac{1}{E(t')}+C(t,t')=\frac{1+\phi(t,t')}{E(t,t')} \qquad [3.18]$$

in which $E(t')$ is the elastic modulus characterizing the instantaneous strain at time t' and $\phi(t,t')=E(t')\cdot J(t,t')-1$ is the creep coefficient (i.e. the ratio of the creep strain to the initial elastic one). Typical values of $\phi(t,t')$ are included between 2 and 5 (2 for a concrete remained in a moist environment or in sealed conditions and 5 for a poor concrete exposed to intense drying).

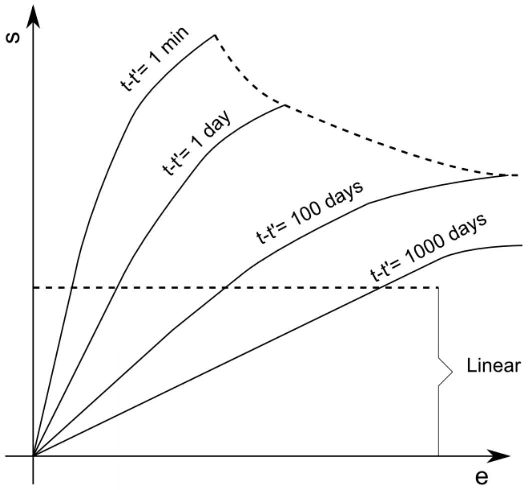

Fig. 3.2 Creep isochrones.

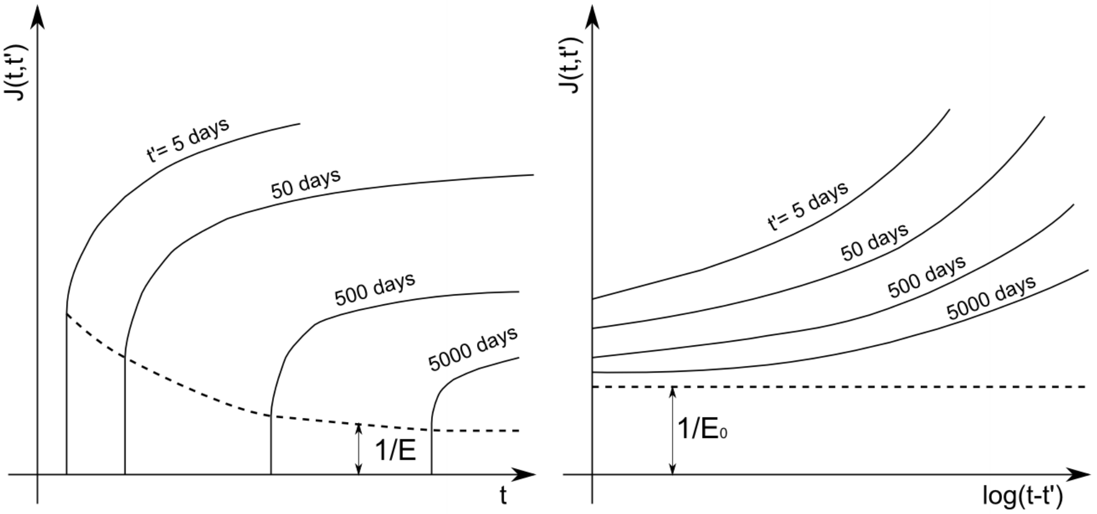

Fig. 3.3 Compliance curves for various age at loading t'.

The values of the compliance function and shrinkage are influenced by many factors, distinguishable into *intrinsic* and *extrinsic*. The intrinsic factors are those that become fixed when concrete is cast (concrete mix parameters such as the cement content, the water-cement ratio, the aggregate fraction, etc...) instead the extrinsic ones are those that can be modified after the casting of concrete (temperature, the degree of hydration, etc…). The mathematical expressions for the compliance function will be discussed later.

As a consequence of creep and shrinkage, the stress in redundant structures usually varies with time even if the load is constant. The calculation of creep caused by variable stress is greatly simplified by the *principle of superposition*; applicable for stress values within the service stress range. The principle of superposition, equivalent to the hypothesis of linearity of the constitutive equation, states that the answer of two stress (or strain) histories is the sum of the responses to each of them taken separately; thus the strain caused by stress history $\sigma(t)$ can be obtained decomposing the history into small increments $d\sigma(t')$ applied at times t', and integrating on the basis of eq. [3.17]:

$$\varepsilon(t)=\int_0^t J(t,t')d\sigma(t')+\varepsilon^0(t) \qquad [3.19]$$

This equation is a general uniaxial constitutive relation defining concrete as an ageing viscoelastic material. The integral in eq. [3.19] has to be intended as the Stieltjes integral, applicable also for discontinuous stress histories. If it is intended as an ordinary integral (Reimann integral) for every instantaneous variation $\Delta\sigma(t_j)$ at the time t_j it is necessary to add the term $J(t,t_j)\cdot\Delta\sigma(t_j)$.

The principle of superposition (eq. [3.19]) leads to accurate predictions only under the following conditions:

1. the stresses are within the service stress range, i.e. less than about 0.4 of the strength;
2. unloading, i.e. strain of decreasing magnitude, does not take place;
3. there is no significant change in the distribution of moisture during creep;
4. there is no large sudden stress increase after the initial loading.
5. In practice this principle is often applied even if the conditions 2 and 4 are violated; then obviously the obtained results will be approximated.

The principle of superposition may be equivalently expressed in terms of the relaxation function $R(t,t')$ (also called the relaxation modulus):

$$\sigma(t)=\int_0^t R(t,t')\cdot\left[d\varepsilon(t')-d\varepsilon^0(t')\right] \qquad [3.20]$$

In the eq. [3.20] the shrinkage (and thermal expansion) increments $d\varepsilon^0(t')$ are subtracted from the total strain increments $d\varepsilon(t')$ since they don't produce stress.

The relaxation function $R(t,t')$ represents the uniaxial stress at time t caused by unit constant axial strain imposed at time t'.

When the strain history is given, eq. [3.19] represents a Volterra integral equation for $\sigma(t)$. By solving this equation for the strain history specified as a step function from the time t', it is possible to calculate the stress histories for various t' (relaxation curves) and thus obtain the relaxation function. Inversely eq. [3.20] represents a Volterra integral equation for $\varepsilon(t)$ and solving this equation for the stress history in the form of a step function from the time t', it is possible to obtain the creep function starting from the relaxation one. Therefore, the only $R(t,t')$ or the only $J(t,t')$ completely define the uniaxial viscoelastic behaviour of a sample of concrete. The use of the one or of the other function is not completely equivalent since the creep function is more easy to determine from experimental tests (it requires the measurement of the strains; an easier process if compared with the measurement of the stresses), while the relaxation function allows to write more convenient relations from a computational point of view. The relaxation function is therefore preferred in the numerical formulation here reported.

Multiaxial generalization of the previous relations is obtained easily, since the material has an essentially isotropic behaviour. Based on the hypothesis of linearity, the eq. [3.19] can be generalized as:

$$\boldsymbol{\varepsilon}(t)=\int_0^t \mathbf{B}\cdot J(t,t')d\boldsymbol{\sigma}(t')+\boldsymbol{\varepsilon}^0(t) \qquad [3.21]$$

where:

$$\begin{aligned}\boldsymbol{\sigma}&=(\sigma_{11},\sigma_{22},\sigma_{33},\sigma_{12},\sigma_{23},\sigma_{31})^T\\ \boldsymbol{\varepsilon}&=(\varepsilon_{11},\varepsilon_{22},\varepsilon_{33},\varepsilon_{12},\varepsilon_{23},\varepsilon_{31})^T\\ \boldsymbol{\varepsilon}^0&=(\varepsilon^0,\varepsilon^0,\varepsilon^0,0,0,0)^T\end{aligned} \qquad [3.22]$$

$$\mathbf{B}=\begin{bmatrix}1 & -\nu & -\nu & 0 & 0 & 0\\ & 1 & -\nu & 0 & 0 & 0\\ & & 1 & 0 & 0 & 0\\ & & & 2(1+\nu) & 0 & 0\\ & & & & 2(1+\nu) & 0\\ & & & & & 2(1+\nu)\end{bmatrix} \qquad [3.23]$$

The subscriptions of σ and ε denote the components of the stress and strain tensors in Cartesian coordinates $x_i\left(i=1,2,3\right)$ and ν is the Poisson ratio generalized for viscoelastic behaviour.

Similarly, the generalization of eq. [3.20] leads to:

$$\boldsymbol{\sigma}(t)=\int_0^t \mathbf{B}^{-1}\cdot R(t,t')\left[d\boldsymbol{\varepsilon}(t')-d\boldsymbol{\varepsilon}^0(t')\right] \qquad [3.24]$$

3.3.2 Rate-type constitutive relations and the rheological models

The numerical solution of the eqs. [3.19] and [3.20] requires, for general creep and relaxation functions, the storage of the complete history of the stress or strain in the structure. This may be facilitated if the integral-type constitutive equations are converted to a rate-type form consisting of a system of first-order ordinary differential equations in time. The form of rate-type creep law can always be visualized by a spring-dashpot model. Although there are many possible arrangements of springs and dashpots, it has been shown that the most general creep behaviour can be described by the Maxwell chain or the Kelvin chain; described later in this subchapter.

The most general form of these rate-type equations can be written as:

$$J(t,t')=\sum_{\mu=1}^{N}\frac{1}{C_\mu(t')}\left\{1-\exp\left[y_\mu(t')-y_\mu(t)\right]\right\} \qquad [3.25]$$

$$R(t,t')=\sum_{\mu=1}^{N}E_\mu(t')\left\{\exp\left[y_\mu(t')-y_\mu(t)\right]\right\} \qquad [3.26]$$

in which $y_\mu(t)$ are the reduction times and may be considered as:

$$y_\mu(t)=\left(t/\tau_\mu\right)^{q_\mu} \qquad (\mu=1,2,\ldots,N) \qquad [3.27]$$

where q_μ are positive numbers ≤ 1, τ_μ are constants called retardation times (if referred to eq. [3.25]), or relaxation times (if referred to eq. [3.26]).

The expansion in eqs. [3.25] and [3.26] represents a series of real exponentials, called the Dirichlet series. The q_μ values can be chosen equal to unity, even if different choices can lead to good expansions with a smaller number of terms (see Refs. [24] and [13]).

Each individual term of the series has a trend in a semi-log scale similar to that of a step function; therefore the Dirichlet series expansion can be interpreted as a subdivision of the original function in horizontal stripes (see Fig. 3.4).

It follows that this expansion is not unique and different choices of τ_μ values, corresponding to different subdivisions in stripes, can provide equally good approximations of the starting function. Trying to determine τ_μ from test data is known to lead an ill-conditioned equation system. Therefore τ_μ must be properly chosen and a suitable choice is a uniform distribution in the logarithmic scale as reported in Ref. [25]. The value of C_μ and E_μ, corresponding to the chosen τ_μ, can be typically determined by least squares methods when analytical expressions for the compliance function are available.

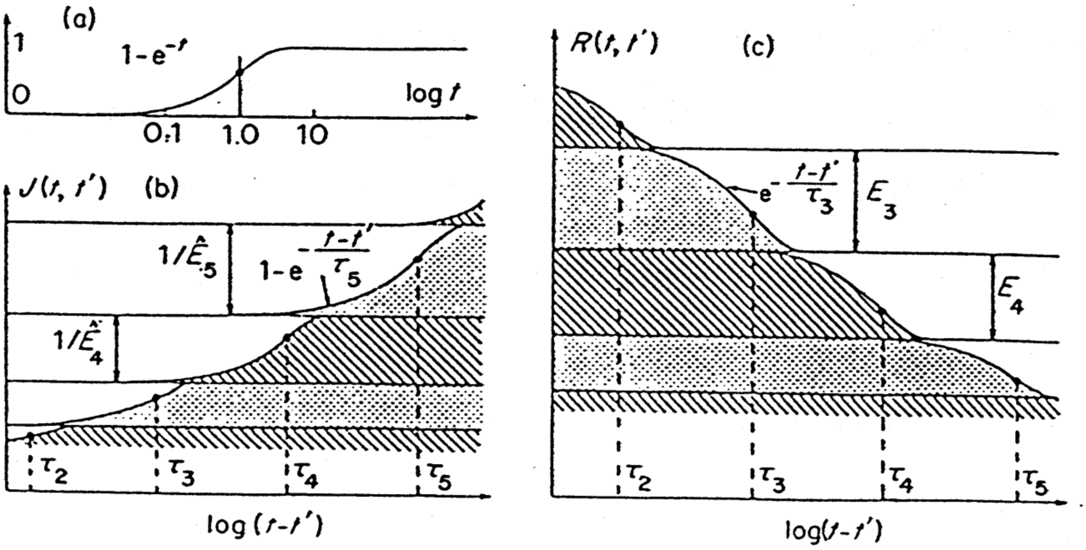

Fig. 3.4 Approximation of compliance or relaxation function curve at fixed age t' at loading by a sum of exponentials.

Consider now the above-named Maxwell and Kelvin spring-dashpot models. As already mentioned, the purpose of the Dirichlet series expansion is to convert a constitutive equation of an integral type to one of a differential type and this conversion is simpler when the relaxation function is used.

Eq. [3.20] with $R(t,t')$ given by eq. [3.26], may be rewritten as:

$$\boldsymbol{\sigma}(t)=\sum_{\mu=1}^{N}\boldsymbol{\sigma}_\mu(t) \qquad [3.28]$$

in which:

$$\boldsymbol{\sigma}_\mu(t)=e^{-y_\mu(t)}\int_0^t e^{y_\mu(t')}\mathbf{B}^{-1}E_\mu(t')\left[d\boldsymbol{\varepsilon}(t')-d\boldsymbol{\varepsilon}^0(t')\right] \qquad [3.29]$$

Expressing the derivative $d\boldsymbol{\sigma}_\mu/dy_\mu$ it is possible to verify that the column vectors $\boldsymbol{\sigma}_\mu$, satisfy the differential equations:

$$\dot{\boldsymbol{\sigma}}_\mu+\dot{y}_\mu(t)\boldsymbol{\sigma}_\mu=\mathbf{B}^{-1}E_\mu(t)\left(\dot{\boldsymbol{\varepsilon}}-\dot{\boldsymbol{\varepsilon}}^0\right) \qquad [3.30]$$

As regards the well-known Maxwell chain model (see Fig. 3.5), $\boldsymbol{\sigma}_\mu$ is interpreted as the stress in the μ-th Maxwell unit. The strain rate in the ageing spring is $\dot{\sigma}_\mu / E_\mu(t)$ and that in the dashpot is $\sigma_\mu / \eta_\mu(t)$, where η_μ represents the age-dependent viscosity of the μ-th dashpot. Summing the strain rates, we get:

$$\dot{\boldsymbol{\sigma}}_\mu + \frac{E_\mu(t)}{\eta_\mu(t)}\boldsymbol{\sigma}_\mu = \mathbf{B}^{-1} E_\mu(t)\left(\dot{\boldsymbol{\varepsilon}} - \dot{\boldsymbol{\varepsilon}}^0\right) \tag{3.31}$$

Comparing the coefficient of eq. [3.31] with eq. [3.29] we see that the spring moduli $E_\mu(t)$ of the Maxwell chain are identical to the functions $E_\mu(t)$ used in the Dirichlet series expansion (eq. [3.26]) and that η_μ is equal to:

$$\eta_\mu(t) = E_\mu(t) / \dot{y}_\mu(t) \tag{3.32}$$

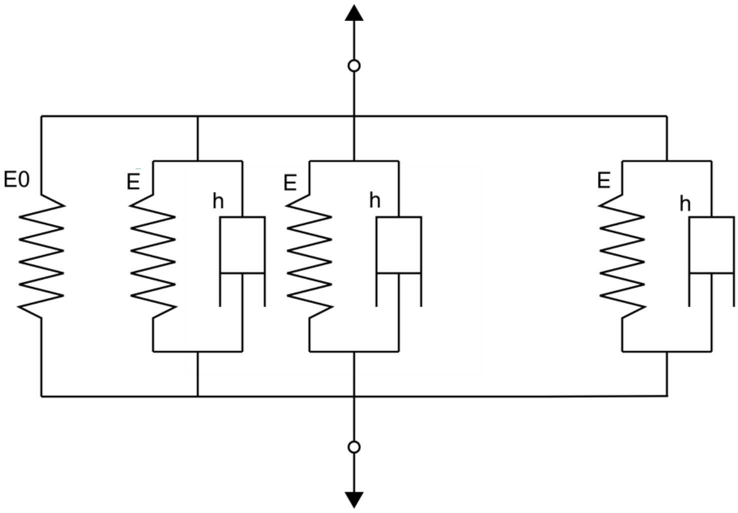

Fig. 3.5 Maxwell chain model.

An analogous conversion to a differential-type form may be determined for the Dirichlet series expansion of the compliance function (see eq. [3.25]).

Then, the constitutive law may be written as:

$$\boldsymbol{\varepsilon}(t) = \sum_{\mu=1}^{N} \boldsymbol{\varepsilon}_\mu(t) + \boldsymbol{\varepsilon}^0(t) \tag{3.33}$$

$$\ddot{\boldsymbol{\varepsilon}}_\mu + \frac{E_\mu(t) + \dot{\eta}_\mu(t)}{\eta_\mu(t)}\dot{\boldsymbol{\varepsilon}}_\mu = \mathbf{B}\frac{\dot{\boldsymbol{\sigma}}}{\eta_\mu(t)} \tag{3.34}$$

$$\eta_\mu(t)=\frac{C_\mu(t)}{\dot{y}_\mu(t)}; \qquad E_\mu(t)=C_\mu(t)-\frac{C_\mu(t)}{\dot{y}_\mu(t)} \qquad [3.35]$$

These three equations may be recognized as the differential-type constitutive equation based on the Kelvin or Kelvin-Voigt chain model, reported in Fig. 3.6. Then, the rate of stress in the μ-th spring is $E_\mu(t)\dot{\varepsilon}_\mu$, while the rate of stress in the μ-th dashpot is $\eta_\mu(t)\dot{\varepsilon}_\mu$. Setting the sum of these two rates equal to $\dot{\boldsymbol{\sigma}}$, we obtain the eq. [3.34].

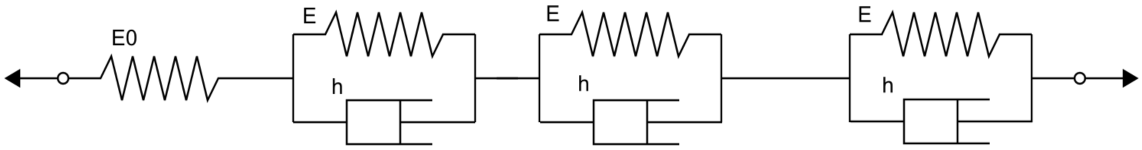

Fig. 3.6 Kelvin chain model.

Although in classical viscoelasticity it is proved that any material can be described with any desired accuracy either by a Kelvin chain or by a Maxwell chain, the Kelvin one has two disadvantages compared to a differential formulation based on Maxwell chain.

The first disadvantage is that the differential equation for Kelvin chain is of the second order (see eq. [3.34]), while for a non-aging material it is of the first order; the second one is that, due to the presence of the minus sign, eq. [3.35] can yield a negative spring modulus E_μ and this, of course, may create problems.

3.3.3 Humidity and temperature effects on creep behaviour

The humidity and temperature effects on the mechanical behaviour of a viscoelastic material, and therefore on the relations (see eqs. [3.21] and [3.24]) between stresses and strains, are essentially of three types (see Refs. [13], [26] and [27]):

1. direct effect on the hygrothermal strains;
2. effect on the hydration reactions, and thus on the aging of the material;
3. direct effect on the creep velocity.

Hygrothermal strains

Firstly are considered the strains due to loss of moisture. In what follows we will consider the shrinkage as a function of pore humidity h because the changes of h produced by hydration (only a few per cent) are very small while the changes of the evaporable water content are large. The shrinkage, as constitutive property, corresponds to the volumetric strain on a material element, of small dimensions, at zero stress and variable humidity. Unfortunately, it cannot be measured directly because it is impossible to obtain a specimen with no residual stresses. This is because of the extremely slow process of drying at normal temperatures. To measure the true shrinkage it is necessary to use a thin-walled specimen and vary the environmental humidity slowly, to maintain a nearly uniform pore humidity distribution throughout the wall of the specimen.

Shrinkage, as a material property, can be better described incrementally [28]:

$$\mathrm{d}\boldsymbol{\varepsilon}_s = \mathbf{k}\mathrm{d}h \qquad [3.36]$$

where:

$\mathrm{d}\boldsymbol{\varepsilon}_s$ is the strain increment due to shrinkage;

$\mathbf{k} = \left[k_{11}, k_{22}, k_{33}, k_{12}, k_{23}, k_{31}\right]^T$ is the vector of the shrinkage coefficients;

and $\mathrm{d}h$ is the humidity variation.

The shrinkage coefficients depends by the age of concrete, the humidity and the stress level according to the following relation:

$$k_{ij} = k^0\left(\delta_{ij} + r\sigma_{ij}\mathrm{sign}\left(\dot{H}\right)\right) \qquad [3.37]$$

in which r is a coefficient of the material, normally between $0.1/f'_t$ and $0.6/f'_t$ (being f'_t the ultimate stress limit in tension, in a uniaxial regime); $\dot{H} = \dot{h} + c\dot{T}$, where c is a parameter; T is the temperature and k^0 is defined by:

$$k^0 = \varepsilon_s{}^0\psi, \qquad \psi = g_s\left(t_e\right)\frac{\mathrm{d}f_s\left(h\right)}{\mathrm{d}h} \qquad [3.38]$$

where $\varepsilon_s{}^0$ is the unrestrained shrinkage, defined as shrinkage at zero stress, due to an instantaneous variation of humidity at time t_0 from 99% to 0%; $g_s\left(t_e\right) = E\left(t_0\right)/E\left(t_e\right)$ takes into account approximately the aging, which reduces shrinkage and t_e is the equivalent age (see eq. [3.41]).

As regards the functions , were introduced various formulations (see Refs. [28], [29], [30]) for different fields of application.

As regards the thermal strains, an analogous relation to eq. [3.36] is:

$$\mathrm{d}\boldsymbol{\varepsilon}_T = \boldsymbol{\alpha}\mathrm{d}T \qquad [3.39]$$

where:

$\boldsymbol{\alpha} = \left[\alpha_{11}, \alpha_{22}, \alpha_{33}, \alpha_{12}, \alpha_{23}, \alpha_{31}\right]^T$ is the vector with the linear thermal dilation coefficients:

$$\alpha_{ij} = \alpha^0 \left(\delta_{ij} + \rho\sigma_{ij}\mathrm{sign}\left(\dot{H}\right)\right) \tag{3.40}$$

in which:

α^0 is the linear thermal dilation coefficient near the point, at zero stress;

δ_{ij} is the Kronecker delta function;

$\rho \cong 2.5/f_t^{'}$ is a characteristic measure of the material;

$f_t^{'}$ is the ultimate limit stress in tension;

$\dot{H} = \dot{h} + c\dot{T}$ where c is a positive parameter.

Humidity and temperature effects on the aging of the material

Humidity and temperature act on the rate of hydration of the reagent components with water and thus on the “age” of the hydrated product. The rate of hydration strongly decreases as h decreases; at h =0.3 the hydration rate is almost zero, and then there is no ageing. Similarly, an increase of temperature accelerates the hydration until it reaches 100°C.

These effects can be considered as an alteration of the time scale; so that all the parameters, dependent by the aging, are function of the equivalent hydration period defined as:

$$t_e = \int_0^t \beta_T \beta_h \mathrm{d}t \tag{3.41}$$

in which:

$$\beta_T = \exp\left[\frac{U_h}{R}\left(\frac{1}{T_0} - \frac{1}{T}\right)\right] \tag{3.42}$$

$$\beta_h = \left[1 + \alpha\left(1 - h\right)^4\right]^{-1} \tag{3.43}$$

where:

U_h is the activation energy of hydration,

T is the absolute temperature (in kelvins),

T_0 is the reference absolute temperature (in kelvins),

R is the universal constant of gases,

U_h/R is equal to 2500K, or to 2700K, or to $4600 \cdot \left[30/(T-263)\right]^{0.39}$.

Humidity and temperature effects on creep velocity

Bažant, Asghari and Schmidt (see Ref. [31]) have observed that an increase of temperature causes an acceleration of creep, while the viscous strain rate is lower for lower moistures. This would seem to contradict the common experience that shows an increase of creep in specimens subjected to drying; but this apparent increase of deformation is mainly due to the dependence of the shrinkage strains by stresses and to the uneven distribution of these latest inside the specimen and the consequent microcracking (see Ref. [28]).

The humidity and temperature effects on creep velocity can be modelled replacing in the eqs. [3.25] or [3.26] $y_\mu(t)$ with $y_\mu(t_v)$, where t_v is defined by:

$$t_v = \int_0^t \varphi_T \varphi_h \mathrm{d}t \qquad [3.44]$$

This is equivalent to the dependence of creep ,of the μ -th damper, by the Maxwell chain by humidity and temperature according to (see Ref. [28]):

$$\frac{1}{\eta_\mu(t_e)} = \frac{\varphi_T \varphi_h}{\tau_\mu E_\mu(t_e)}, \qquad (\mu = 1,2,\dots,N) \qquad [3.45]$$

The coefficients φ_T and φ_h can be expressed as (see Ref. [28]):

$$\varphi_T = \exp\left[\frac{U_c}{R}\left(\frac{1}{T_0} - \frac{1}{T}\right)\right] \qquad [3.46]$$

$$\varphi_h = \alpha_h + (1-\alpha_h)h^2 \qquad [3.47]$$

in which U_c is the activation energy of creep, T is the absolute temperature (in kelvins), T_0 is the reference absolute temperature (in kelvins), R is the universal constant of gases.

3.3.4 Bažant–Baweja B3 Model

The Bažant–Baweja B3 Model (see Refs. [32], [33], [34] and [35]) represents the third major update of the earlier BP and BP-KX models (see Refs. [29] and [36]), previously developed at Northwestern University.

This model has been implemented in the F.E. code for the following reasons: it is simpler than the previous versions, gives good agreement with available test data (is calibrated by a computerized data bank comprising practically all the relevant test data obtained in various laboratories throughout the world) and is better justified theoretically on the basis of an understanding of the mechanism of creep and shrinkage (it incorporates the theoretical advances during the last three decades).

This model uses the compliance function, which reduces the risk of errors due to inaccurate values of the elastic modulus. Moreover this model separates basic creep (time-dependent deformations where no moisture exchanges with the environment occur) and drying creep (additional creep strain accounting for drying).

The prediction of the material parameters of the B3 model, from strength and composition, is restricted to Portland cement concrete with the following parameter ranges:

- water cement ratio by weight: $0.35 \leq w/c \leq 0.85$;
- aggregate cement ratio by weight: $2.5 \leq a/c \leq 13.5$;
- 28-day standard cylinder compression strength of concrete: $17 \leq f_{cm28} \leq 70$ MPa;
- cement content: $160 \leq c \leq 720$ kg/m^3.

The Bažant–Baweja B3 Model is restricted to the service stress range (up to 0.45 f_{cm28}), for which creep is assumed to be dependent linearly on stress. This means that, for constant stress applied at age t':

$$\varepsilon(t) = J(t,t')\sigma + \varepsilon_{sh}(t) + \alpha\Delta T(t) \qquad [3.48]$$

where $J(t,t')$ is the compliance function (strain at time t, caused by a unit uniaxial constant stress applied at time t'), σ is the uniaxial stress, ε is the strain, ε_{sh} is the shrinkage strain, $\Delta T(t)$ is the temperature change from reference temperature at time t and α is the thermal expansion coefficient.

The parameters required for this model are:

- age of concrete when drying starts (in days);
- age of concrete at loading (in days);
- aggregate content in concrete (in kg/m^3);
- cement content in concrete (in kg/m^3);
- water content in concrete (in kg/m^3);
- cement type;
- concrete mean compressive strength at 28 days (in MPa);
- modulus of elasticity of concrete at 28 days (in MPa);
- curing condition;
- relative humidity expressed as decimal;

- shape of specimen;
- volume-surface ratio or effective cross-section thickness (in mm).

The compliance function , may be decomposed as:

$$J(t,t')=q_1+C_0(t,t')+C_d(t,t',t_0) \qquad [3.49]$$

in which q_1 is the instantaneous strain due to unit stress, $C_0(t,t')$ is the compliance function for basic creep, $C_d(t,t',t_0)$ is the drying creep and t_0 is the age when drying begins, in days (only $t_0 \leq t'$ is considered).

The instantaneous strain, which is the same as in previous models BP and BP-KX, may be written as $q_1 = 1/E_0$ where E_0 is called the asymptotic modulus. The use of E_0 instead of the conventional static modulus E is convenient because concrete exhibits pronounced creep even for very short load durations, even shorter than 10^{-4} s. E_0 should not be regarded as a real elastic modulus but merely as an empirical parameter that can be considered as age-independent. As a rough estimate $E_0 \approx 1.5E$.

Bažant recommends to use as q_1 :

$$q_1 = 0.6/E_{cm28} \qquad [3.50]$$

where E_{cm28} is the mean modulus of elasticity of concrete at 28 days. So, it is possible to determine E_{cm28} as

$$E_{cm28} = 4734\sqrt{f_{cm28}} \qquad [3.51]$$

in which f_{cm28} is the concrete mean compressive strength.

As regards the basic creep, it is composed of three terms: an aging viscoelastic term, a non-aging viscoelastic term and an aging flow term

$$C_0(t,t')=q_2\cdot Q(t,t')+q_3\cdot\ln\left[1+(t-t')^n\right]+q_4\cdot\ln\left(\frac{t}{t'}\right) \qquad [3.52]$$

where q_2, q_3 and q_4 are empirical constitutive parameters and $Q(t,t')$ is a binomial integral which cannot be expressed analytically .

Indeed, predicting the creep and shrinkage properties of concrete from the composition of the concrete mix and the strength of the concrete is an extremely difficult problem for which no good theory has yet been developed. So Bažant has furnished, for q_2, q_3 and q_4 (and also for the parameter of the drying creep q_5), formulae which are partly empirical and partly reflects trends deduced theoretically from an understanding of the physical mechanisms; that were calibrated by statistical analysis of the data in a computerized data bank.

Therefore the parameter q_2, which appear in the aging viscoelastic compliance term $q_2 \cdot Q(t,t')$, is equal to:

$$q_2 = 185.4 \times 10^{-6} c^{0.5} f_{cm28}{}^{-0.9} \qquad [3.53]$$

in which c is the cement content.

As regards the binomial integral $Q(t,t')$ it is given a table (see Table 3.1) and it can also be obtained from the following approximate formula (derived by Bažant and Prasannan, Ref. [25]) which is valid also for m and n values different from 0.5 and 0.1 (values for all normal concretes).

$$Q(t,t') = Q_f(t')\left[1 + \left(\frac{Q_f(t')}{Z(t,t')}\right)^{r(t')}\right]^{-1/r(t')} \qquad [A.1]$$

in which:

$$Q(t,t') = Q_f(t')\left[1 + \left(\frac{Q_f(t')}{Z(t,t')}\right)^{r(t')}\right]^{-1/r(t')} \qquad [3.55]$$

in which:

$$Q_f(t') = \left[0.086(t')^{2/9} + 1.21(t')^{4/9}\right]^{-1} \qquad [3.56]$$

$$r(t') = 1.7(t')^{0.12}; \qquad Z(t,t') = (t')^{-m} \ln\left[1 + (t - t')^n\right] \qquad [3.57]$$

The non-aging viscoelastic compliance parameter q_3 is equal to:

$$q_3 = 0.29(w/c)^4 q_2 \qquad [3.58]$$

where w/c is the water cement ratio

The aging flow compliance parameter q_4 is expressed as

$$q_4 = 20.3 \times 10^{-6} (a/c)^{-0.7} \qquad [3.59]$$

in which a/c is the aggregate cement ratio

Table 3.1 Values of function $Q(t,t')$ for m=0.5 and n=0.1.

	log t'								
log (t-t')	**0.0**	**0.5**	**1.0**	**1.5**	**2.0**	**2.5**	**3.0**	**3.5**	**4.0**
-2.0	0.4890	0.2750	0.1547	0.08677	0.04892	0.02751	0.01547	0.008699	0.004892
-1.5	0.5347	0.3009	0.1693	0.09519	0.05353	0.03010	0.01693	0.009519	0.005353
-1.0	0.5586	0.3284	0.1848	0.1040	0.05846	0.03288	0.01849	0.01040	0.005846
-0.5	0.6309	0.3571	0.2013	0.1133	0.06372	0.03583	0.02015	0.01133	0.006372
00.0	0.6754	0.3860	0.2185	0.1231	0.06929	0.03897	0.02192	0.01233	0.006931
0.5	0.7108	0.4125	0.2357	0.1334	0.07516	0.04229	0.02379	0.01338	0.007524
1.0	0.7352	0.4335	0.2514	0.1436	0.08123	0.04578	0.02576	0.01449	0.008149
1.5	0.7505	0.4480	0.2638	0.1529	0.08727	0.04897	0.02782	0.01566	0.008806
2.0	0.7597	0.4570	0.2724	0.1602	0.09276	0.05239	0.02994	0.01687	0.009494
2.5	0.7652	0.4624	0.2777	0.1652	0.09708	0.05616	0.03284	0.01812	0.01021
3.0	0.7684	0.4656	0.2808	0.1683	0.1000	0.05869	0.03393	0.01935	0.01094
3.5	0.7703	0.4675	0.2827	0.1702	0.1018	0.06041	0.03541	0.02045	0.01166
4.0	0.7714	0.4686	0.2838	0.1713	0.1029	0.06147	0.03641	0.02131	0.01230
4.5	0.7720	0.4692	0.2844	0.1719	0.1036	0.06210	0.03702	0.02190	0.01280
5.0	0.7724	0.4696	0.2848	0.1723	0.1038	0.06247	0.03739	0.02225	0.01314

The compliance function for drying creep is defined by eq. [3.60]. The equation accounts for the drying before loading (note that drying before loading is considered only for drying creep).

$$C_d\left(t,t',t_0\right)=q_5\left\{\exp\left[-8H\left(t\right)\right]-\exp\left[-8H\left(t'\right)\right]\right\}^{0.5} \tag*{[3.60]}$$

in which q_5 is the drying creep compliance parameter, equal to:

$$q_5=0.757f_{cm28}{}^{-1}\left[\varepsilon_{sh\infty}\times10^6\right]^{-0.6} \tag*{[3.61]}$$

is function of the mean compressive strength at 28 days f_{cm28} and of the ultimate shrinkage strain $\varepsilon_{sh\infty}$, given by:

$$\varepsilon_{sh\infty}\left(t,t_0\right)=-\varepsilon_{s\infty}\frac{E_{cm607}}{E_{cm}\left(t_0+\tau_{sh}\right)} \tag*{[3.62]}$$

in which $\varepsilon_{s\infty}$ is equal to

$$\varepsilon_{s\infty}=-\alpha_1\alpha_2\left[0.019w^{2.1}f_{cm28}{}^{-0.28}+270\right]\times10^{-6} \tag*{[3.63]}$$

and $E_{cm607}/E_{cm}\left(t_0+\tau_{sh}\right)$ is a factor to account for the time dependence of ultimate shrinkage

$$E_{cmt}=E_{cm28}\left(\frac{1}{4+0.85t}\right)^{0.5} \tag*{[3.64]}$$

where w is the water content and α_1, α_2 are constants related to the cement type and curing condition (see Table 3.2 and Table 3.3).

Table 3.2 Constant α_1, related to the cement type.

Type of cement	**α₁**
Type I	1.00
Type II	0.85
Type III	1.10

Table 3.3 Constant α_2, related to the curing conditions.

Curing method	**α₂**
Steam cured	0.75
Cured in water or at 100% relative humidity	1.00
Sealed during curing or normal curing in air with initial protection against drying	1.20

The functions $H(t)$ and $H(t')$ in the case that more complex models (such as the hygro-mechanical ones where the humidity is computed as a variable of the problem[1]) are not considered, can be obtained by formulas derived from experimental data.

Bažant proposed the following expressions:

$$H(t)=1-(1-h)S(t-t_0) \qquad [3.65]$$

$$H(t')=1-(1-h)S(t'-t_0) \qquad [3.66]$$

where $S(t-t_0)$ and $S(t'-t_0)$ are time function for shrinkage calculated at the age of concrete t and the age of concrete at loading t'.

The time function for shrinkage $S(t-t_0)$ is equal to:

$$S(t-t_0)=\tanh\sqrt{\frac{(t-t_0)}{\tau_{sh}}} \qquad [3.67]$$

where τ_{sh} is the shrinkage half-time:

---

[1] this is the case of NEWCON3D, a 3D fully coupled thermo-hygro-mechanical F.E. code.

$$\tau_{sh} = 0.085 t_0^{-0.08} f_{cm28}^{-0.25} \left[2k_s \left(V/S \right) \right]^2 \qquad [3.68]$$

where k_s is the cross section shape-correction factor (Table 3.4) and V/S is the ratio between the volume of the concrete element and the surface exposed to the environmental humidity.

Table 3.4 k_s as cross section shape.

Cross section shape	k_s
Infinite slab	1.00
Infinite cube	1.15
Infinite square prism	1.25
Sphere	1.30
Cube	1.55

For example, considering a concrete element with a ratio V/S = 100mm, subjected to an environmental relative humidity equal to 70%, loaded at t'=14 days, while the drying starts at t_0 =7 days; then the variation of the relative humidity, according to model B3, is shown in Fig. 3.7. This formulation assumes that all the concerned section in the V/S ratio has the same relative humidity and vary instantaneously in the same way.

Then finally, the creep coefficient $\phi(t,t')$ is so calculated from the compliance function:

$$\phi(t,t') = E(t') J(t,t') - 1 \qquad [3.69]$$

where $E(t')$ is the modulus of elasticity at loading age t'.

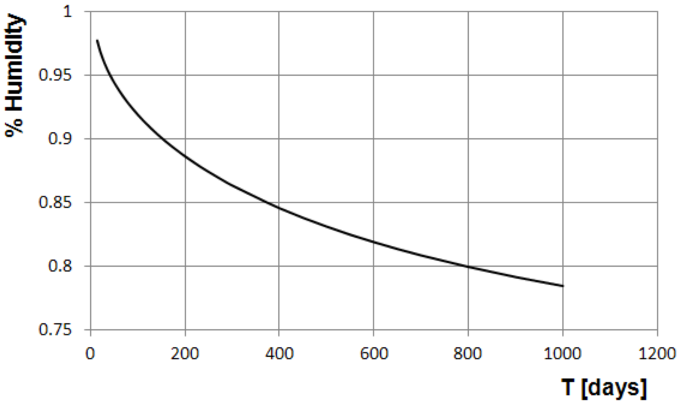

Fig. 3.7 Example of the evolution of relative humidity according to model B3.

3.3.5 Double Power Law

Before B3 model, in the F.E. code NEWCON3D, was implemented only the Double Power Law (see Refs. [29] and [37]). This is a simple law but, if compared to model B3, is less detailed and accurate, it doesn't consider drying creep and cannot be well characterized if concrete is considered as a composite material (e.g. the compliance function of Model B3 is function of the aggregate content in concrete, cement content in concrete , cement type…). Moreover, as reported in [38], this model can exhibit the phenomenon of divergence of creep curves for short time periods. In any case this problem is nevertheless not serious for normal applications.

The compliance function of Double Power Law is here reported:

$$J(t,t')=\frac{1}{E_0}+\frac{\phi_1}{E_0}\left(t'^{-m}+\alpha\right)\cdot\left(t-t'\right)^n \qquad [3.69]$$

where, approximately, if the age of concrete t and the age at loading t' are in days, the values of the parameters of eq. [3.69] are:

$$n\cong\frac{1}{8}; \qquad \alpha\cong 0.05; \qquad m\cong\frac{1}{3}; \qquad \phi_1\cong 3\div 6$$

and E_0 is the asymptotic modulus, estimable roughly as $E_0\cong 1.5E_{cm28}$.

These coefficients can be determined, easily, with experimental tests.

3.3.6 Creep of concrete if considered as a composite material

If concrete is considered as a composite material made of aggregates, cement paste and ITZ, many experiments in literature have shown the source of creep in concrete is the hardened cement paste (and therefore also the ITZ). The aggregates, typically do not creep in the range of stresses encountered in service (see Refs. [13], [39] and [40]).

It is therefore reasonable to consider concrete as a composite formed by one aging viscoelastic phase (cement paste) and one elastic phase (aggregate). The mortar matrix is characterized by an aging viscoelastic compliance function $J(t,t')$ and a Poisson's ratio ν that is constant in time; instead the aggregate is considered to be elastic, characterized by its elastic modulus and its Poisson's ratio. The compliance function for the mortar matrix may be represented by Model B3, described in Section 3.3.4: although this model was developed for concrete, the physical basis of the assumptions used in its derivation is also valid for cement paste.

3.3.7 Numerical Implementation in NEWCON3D

In this subchapter is reported the numerical implementation of B3 Model in NEWCON3D.

Indeed, in this F.E. code, all the equations reported in Section 3.3.4 have been implemented with a difference: the spatial averages of pore relative humidity $H(t)$ and $H(t')$ (see eqs. [3.65] and [3.66]), used to determine the compliance function for drying creep, have been replaced by the current humidity values at each time step, being relative humidity one of the main variables in the code, so being unnecessary to evaluate it via approximate expressions.

This is really important, especially for modelling of concrete at the meso-level, characterized by different components with different properties. In fact, it clearly appears by eqs. [3.67] and [3.68], where S mainly depends on characteristics related to the geometry of the studied model but not on the permeability of the different component materials, a property of the material that controls the humidity and so the drying creep evolution.

Therefore in the Box 1-7, all the subroutines and functions implemented in NEWCON3D for the computation of creep using the Model B3 (see Section 3.3.4) or the Double Power Law (see Section 3.3.5) are reported.

```
module cCreepModel
implicit none

  type, public :: dpl                  ! Double Power Law
    real*8   ::  E0                    ! E0 – asymptotic modulus
    real*8   ::  phi1                  ! φ1
    real*8   ::  alfa                  ! α
    real*8   ::  emme                  ! m
    real*8   ::  enne                  ! n
  end type
  type, public :: b3                   ! Model B3
    real*8   ::  E0                    ! E0 – asymptotic modulus
    real*8   ::  fc                    ! fc – concrete mean compressive strength
    real*8   ::  Ecm28                 ! Ecm28- mean modulus of elasticity of concrete at 28 days
    real*8   ::  wcr                   ! w/c – water cement ratio
    real*8   ::  c                     ! c – cement content
    real*8   ::  acr                   ! a/c – aggregate cement ratio
    real*8   ::  vs                    ! v/s – volume surface ratio
    real*8   ::  ks                    ! ks – cross section shape correction factor
    real*8   ::  t0                    ! t0 – age when drying begins
    real*8   ::  rh                    ! rh – relative humidity
    real*8   ::  m                     ! m
    real*8   ::  n                     ! n
  end type
!
  type, public :: tCreepModel
    integer                                     :: modelType
    integer                                     :: indexMat
    type(dpl), dimension(:), allocatable        :: dplParam
    type(b3),  dimension(:), allocatable        :: b3Param
  end type
!
contains
!
! costructor
```

```
!
   subroutine tCreepModel_(modelType, creepModel)
   implicit none
   integer                                      :: modelType
   type(tCreepModel)                            :: creepModel
      creepModel%modelType   = modelType
      creepModel%indexMat    = 0
      select case (modelType)
      case (1)

         allocate(creepModel%dplParam(1))
         allocate(creepModel%b3Param(0))
         call dpl_(creepModel%dplParam(1))
      case(2)
         allocate(creepModel%dplParam(0))
         allocate(creepModel%b3Param(1))
         call b3_(creepModel%b3Param(1))
      end select
   return
   end subroutine tCreepModel_
!
! initialization parameters
!
   subroutine dpl_(valueDpl)              ! Double Power Law
   implicit none
   type(dpl)  :: valueDpl
      valueDpl%E0            = 0.d0
      valueDpl%phi1          = 0.d0
      valueDpl%alfa          = 0.d0
      valueDpl%emme          = 0.d0
      valueDpl%enne          = 0.d0
   return
   end subroutine dpl_
!
   subroutine b3_(valueB3)                ! Model B3
   implicit none
   type(b3)  :: valueB3
      valueB3%E0             = 0.d0
      valueB3%fc             = 0.d0
      valueB3%Ecm28          = 0.d0
      valueB3%wcr            = 0.d0
      valueB3%c              = 0.d0
      valueB3%acr            = 0.d0
      valueB3%vs             = 0.d0
      valueB3%ks             = 0.d0
      valueB3%t0             = 0.d0
      valueB3%rh             = 0.d0
      valueB3%m              = 0.d0
      valueB3%n              = 0.d0
   return
   end subroutine b3_
!
end module cCreepModel
```

Box. 1 Costructor of cCreepModel module.

```
!
! reading and writing parameters of Double Power Law and Model B3
!
subroutine readCreepModel (unitInput,unitOutput,creepModel,nMat)
```

```
implicit none
integer                                    :: unitInput
integer                                    :: unitOutput
integer                                    :: nMat
type(tCreepModel), dimension(nMat)         :: creepModel
! internal variables
character*80                               :: st
integer                                    :: i

  i = 1
  read(unitInput,*) st
  readLoop: do while (st.ne.'end')
  if (st == 'dpl') then
    creepModel(i)%modelType = 1
    write(unitOutput, *) st
  else if (st == 'b3') then
    creepModel(i)%modelType = 2
    write(unitOutput, *) st
  else
    write(*,*)  'error creep model in input file'
    stop
  end if
  call tCreepModel_(creepModel(i)%modelType, creepModel(i))
  read(unitInput,*) creepModel(i)%indexMat
  write(unitOutput,*) creepModel(i)%indexMat
  select case(creepModel(i)%modelType)

! reading and writing  parameters Double Power Law
  case (1)
    read(unitInput,*) creepModel(i)%dplParam(1)%E0,             &
                creepModel(i)%dplParam(1)%phi1,                 &
                creepModel(i)%dplParam(1)%alfa,                 &
                creepModel(i)%dplParam(1)%emme,                 &
                creepModel(i)%dplParam(1)%enne
    write(unitOutput,*) creepModel(i)%dplParam(1)%E0,           &
                creepModel(i)%dplParam(1)%phi1,                 &
                creepModel(i)%dplParam(1)%alfa,                 &
                creepModel(i)%dplParam(1)%emme,                 &
                creepModel(i)%dplParam(1)%enne
! reading and writing  parameters Model B3
  case (2)
    read(unitInput,*) creepModel(i)%b3Param(1)%E0,              &
                creepModel(i)%b3Param(1)%fc,                    &
                creepModel(i)%b3Param(1)%Ecm28,                 &
                creepModel(i)%b3Param(1)%wcr,                   &
                creepModel(i)%b3Param(1)%c,                     &
                creepModel(i)%b3Param(1)%acr,                   &
                creepModel(i)%b3Param(1)%vs,                    &
                creepModel(i)%b3Param(1)%ks,                    &
                creepModel(i)%b3Param(1)%t0,                    &
                creepModel(i)%b3Param(1)%rh,                    &
                creepModel(i)%b3Param(1)%m,                     &
                creepModel(i)%b3Param(1)%n
    write(unitOutput,*) creepModel(i)%b3Param(1)%E0,            &
                creepModel(i)%b3Param(1)%fc,                    &
                creepModel(i)%b3Param(1)%Ecm28,                 &
                creepModel(i)%b3Param(1)%wcr,                   &
                creepModel(i)%b3Param(1)%c,                     &
                creepModel(i)%b3Param(1)%acr,                   &
                creepModel(i)%b3Param(1)%vs,                    &
                creepModel(i)%b3Param(1)%ks,                    &
                creepModel(i)%b3Param(1)%t0,                    &
                creepModel(i)%b3Param(1)%rh,                    &
```

```
                    creepModel(i)%b3Param(1)%m,                    &
                    creepModel(i)%b3Param(1)%n
  end select

  read(unitInput,*) st
  i = i+1
  end do readLoop

return
end subroutine readCreepModel
```

Box. 2 Subroutine readCreepModel.

```
subroutine setCreepModel(creepModel)
implicit none
type(tCreepModel), dimension(:), pointer              :: creepModel
type(tCreepModel), dimension(:), allocatable          :: creepModel_Copy
! internal variables
integer                                               :: i

  if (size(creepModel) <= 0) then
    allocate(creepModel(1))
  else
    allocate(creepModel_Copy(size(creepModel)))
    creepModel_Copy = creepModel
    deallocate(creepModel)
    allocate(creepModel(size(creepModel_Copy)+1))
    do i = 1,size(creepModel_Copy)
      creepModel(i) = creepModel_Copy(i)
    end do
    deallocate(creepModel_Copy)
  end if

return
end subroutine setCreepModel
```

Box. 3 Subroutine setCreepModel.

```
!
!  run Model B3
!
subroutine runCreepModel(NMAT,MAT,durataCarico,etaCarico,CREEPV,creepModel,                    &
           IGS,MDF1,MP,GASHT,P,NSIZE2,NCN,IGJG,ME,NOP,NEL,ICONVG,UmidIniz)
implicit none
integer                                    :: NMAT
integer                                    :: MAT
integer                                    :: IGS
integer                                    :: MDF1
integer                                    :: MP
integer                                    :: IGJG
integer                                    :: NSIZE2
integer                                    :: NCN
integer                                    :: ME
integer                                    :: NEL
integer                                    :: ICONVG
real*8                                     :: durataCarico
real*8                                     :: etaCarico
```

```
real*8                                          :: CREEPV
real*8,  dimension (IGS,MDF1,MP)                :: GASHT
real*8,  dimension (NSIZE2)                     :: P
integer, dimension (ME,20)                      :: NOP
real*8, dimension(MP)                           :: UmidIniz
type(tCreepModel), dimension(nMat)              :: creepModel

   if ((creepModel(MAT)%modelType) == 2) then
      call creepB3vef (NMAT,MAT,durataCarico,etaCarico,CREEPV,creepModel,NHT)                     ! Basic creep
      call creepB3Ddrying (NMAT,MAT,durataCarico,etaCarico,CREEPV,creepModel,           &          ! Drying creep
            IGS,MDF1,MP,GASHT,P,NSIZE2,NCN,IGJG,ME,NOP,NEL,ICONVG,UmidIniz)
   else
      write(*,*)'error, creep model not implemented'
   end if

return
end subroutine runCreepModel
```

Box. 4 Subroutine runCreepModel.

```
!
! creep computation - Double Power Law
!
subroutine creepDPLaw(NMAT,MAT,durataCarico,etaCarico,CREEPV,creepModel)
implicit none
integer                                 :: NMAT
integer                                 :: MAT
real*8                                  :: durataCarico
real*8                                  :: etaCarico
real*8                                  :: CREEPV
type(tCreepModel), dimension(nMat)      :: creepModel

! J= 1/E0 + ( φ1/E0 ) ( ((t’)^-m) + α ) ( t - t’ )^n
   CREEPV = 1.0d0/(creepModel(MAT)%dplParam(1)%E0) + (creepModel(MAT)%dplParam(1)%phi1)/                          &
                 (creepModel(MAT)%dplParam(1)%E0)*(etaCarico ** (-(creepModel(MAT)%dplParam(1)%emme))  +          &
              (creepModel(MAT)%dplParam(1)%alfa)) * durataCarico ** (creepModel(MAT)%dplParam(1)%enne)

return
end subroutine creepDPLaw
```

Box. 5 Subroutine creepDPLaw, for the computation of creep following the Double Power Law.

```
!
! computation of instantaneous strain + basic creep - Model B3
!
subroutine creepB3vef (NMAT,MAT,durataCarico,etaCarico,CREEPV,creepModel)
implicit none
integer                                         :: NMAT
integer                                         :: MAT
real*8                                          :: durataCarico
real*8                                          :: etaCarico
real*8                                          :: CREEPV
type(tCreepModel), dimension(nMat)              :: creepModel
! internal variables
real*8                                          :: q1
real*8                                          :: q2
real*8                                          :: q3
real*8                                          :: m
```

```
real*8                                        :: n
integer                                       :: lambda0
real*8                                        :: psi
real*8                                        :: r
real*8                                        :: Z1
real*8                                        :: Z2
real*8                                        :: Z
real*8                                        :: exp1
real*8                                        :: exp2
real*8                                        :: exp3
real*8                                        :: Qf
real*8                                        :: Q
real*8                                        :: C0ve1
real*8                                        :: C0ve
real*8                                        :: Q2bis

! eta carico = t', age at loading [d]
! durata carico = t - t'  [d]
! *** ***  instantaneous strain q1

  q1        = (0.6D0/(creepModel(MAT)%b3Param(1)%Ecm28))                        ! q1 [1/MPa]

! *** *** Basic Creep =  q2 · Q + q3 · ln[ 1 + ( t – t' )^n ] + q4 /  ln (  t / t' )
  q2    = (185.4D0*((creepModel(MAT)%b3Param(1)%c)**(0.5D0))*      &
          ((creepModel(MAT)%b3Param(1)%fc)**(-0.9D0)))*(10**(-6.D0))            ! q2 [1/MPa]
  q3    = 0.29D0*((creepModel(MAT)%b3Param(1)%wcr)**4.D0)*q2                    ! q3 [1/MPa]
  q4    = (20.3d0*(((creepModel(MAT)%b3Param(1)%acr))**(-0.7D0)))*(10**(-6.D0)) ! q4 [1/MPa]
  m     = creepModel(MAT)%b3Param(1)%m                                          ! m
  n     =  creepModel(MAT)%b3Param(1)%n                                         ! n
  lambda0 = 1.D0                                                                ! λ0
  psi   = (durataCarico)/(lambda0)                                              ! ( t - t' ) / λ0
  r     = 1.7D0*((etaCarico)**(0.12D0))+8.D0                                    ! r
  Z1    = ((durataCarico)**(n))
  Z2    = log (1 + Z1)
  Z     = ((etaCarico)**(-m))* Z2                                               ! Z
  exp1   = 2.D0/9.D0
  exp2   = 4.D0/9.D0
  Qf    = (0.086D0*((etaCarico)**(exp1)) + 1.21D0*((etaCarico)**(exp2)))**(-1.D0)  ! Qf
  exp3   = -1.D0/r
  Q     = Qf*(1+((Qf/Z)**(r)))**(exp3)                                          ! Q
  C0ve1  = q3*log(1.D0+(psi)**n)                                                ! q3 · ln[ 1 + ( t – t' )^n ]
  C0ve   = q2*Q + C0ve1                                                         ! q2 · Q + q3 · ln[ 1 + ( t – t' )^n ]
  C0f    = q4*log((durataCarico + etaCarico)/etaCarico)                         ! q4 /  ln (  t / t' )

! *** ***  instantaneous strain + Basic Creep =  q1 + q2 · Q + q3 · ln[ 1 + ( t – t' )^n ] + q4 /  ln (  t / t' )
  CREEPV= q1 + C0ve + C0f

return
end subroutine creepB3vef
```

Box. 6 Subroutine creepB3vef for the computation of the instantaneous strain and basic creep of Model B3.

```
!
! computation of drying creep - Model B3
!
subroutine creepB3Ddrying (NMAT,MAT,durataCarico,etaCarico,CREEPV,               &
                           creepModel,IGS,MDF1,MP,GASHT,P,NSIZE2,                &
                           NCN,IGJG,ME,NOP,NEL,ICONVG,UmidIniz)
implicit none
```

```
integer                                        :: NMAT
integer                                        :: MAT
integer                                        :: IGS
integer                                        :: MDF1
integer                                        :: MP
integer                                        :: IGJG
integer                                        :: NSIZE2
integer                                        :: NCN
integer                                        :: ME
integer                                        :: NEL
integer                                        :: ICONVG
real*8                                         :: durataCarico
real*8                                         :: etaCarico
real*8                                         :: CREEPV
integer, dimension (ME,20)                     :: NOP
real*8,  dimension (IGS,MDF1,MP)               :: GASHT
real*8,  dimension (NSIZE2)                    :: P
real*8, dimension(MP)                          :: UmidIniz
type(tCreepModel), dimension(nMat)             :: creepModel
! internal variables
real*8                                         :: coeff1
real*8                                         :: coeff2
real*8                                         :: coeff3
real*8                                         :: taush
real*8                                         :: coeff4
real*8                                         :: coeff5
real*8                                         :: coeff6
real*8                                         :: epsinf
real*8                                         :: coeff7
real*8                                         :: Ecm607
real*8                                         :: coeff8
real*8                                         :: Ecmt0taush
real*8                                         :: RappEcm
real*8                                         :: epshinf
real*8                                         :: coeff9
real*8                                         :: q5
real*8                                         :: H1
real*8                                         :: S2
real*8                                         :: H2
real*8                                         :: Cd1
real*8                                         :: Cd2
real*8                                         :: Cd
real*8                                         :: CREEPVbis

! *** *** Drying Creep = q5 { exp [ -8H (t) ] – exp [ -8H (t’) ] } ^0.5
   coeff1     = (creepModel(MAT)%b3Param(1)%t0)**(-0.08D0)
   coeff2     = (creepModel(MAT)%b3Param(1)%fc)**(-0.25D0)
   coeff3     =  0.085D0 *coeff1 * coeff2
   taush      =  coeff3*((2.D0*(creepModel(MAT)%b3Param(1)%ks)*                &
                 (creepModel(MAT)%b3Param(1)%vs))**(2.D0))                                    ! sh
   coeff4     = ((creepModel(MAT)%b3Param(1)%wcr)*(creepModel(MAT)%b3Param(1)%c))**(2.1D0)
   coeff5     = (creepModel(MAT)%b3Param(1)%fc)**(-0.28D0)
   coeff6     =  0.019D0 * coeff4 * coeff5 +270.D0
   epsinf     =  coeff6 *(10**(-6.D0))                                                        ! ε∞
   coeff7     =  607.D0/(4+(0.85D0*607.D0))
   Ecm607 = (creepModel(MAT)%b3Param(1)%Ecm28)*((coeff7)**(0.5D0))                            ! Ecm607
   coeff8     = ((creepModel(MAT)%b3Param(1)%t0)+taush)/(4+                      &
                (0.85D0*((creepModel(MAT)%b3Param(1)%t0)+taush)))
   Ecmt0taush  = (creepModel(MAT)%b3Param(1)%Ecm28)*((coeff8)**(0.5D0))
   RappEcm       =  Ecm607/Ecmt0taush                                                         ! Ecm607/Ecm▯sh
   epshinf  = abs(-epsinf * RappEcm)                                                          ! εsh∞
   coeff9    = ((creepModel(MAT)% b3Param(1)%fc)**(-1.d0))
   q5          = 0.757D0 * coeff9 *((epshinf*(10**6.d0))**(-0.6d0))                           ! q5
```

```
   H1         = UmidRelGauss(IGS,MDF1,MP,IGJG,GASHT,NSIZE2,P,NCN,ME,NOP,NEL,ICONVG)             ! H1 = current r.h.
   H2         = UmidInizGauss(IGS,MDF1,MP,IGJG,UmidIniz,NSIZE2,P,NCN,ME,NOP,NEL,ICONVG)         ! H2 = initial r.h.
   Cd1        = exp(-8*H1)                                                                      ! exp ( -8H1)
   Cd2        = exp(-8*H2)                                                                      ! exp ( -8H2)
   Cd         = q5*((Cd1 - Cd2)**(0.5D0))                                                       ! Cd
   CREEPVbis = Cd
! J = q1 + C0 + Cd
   CREEPV               = CREEPV + CREEPVbis

return
end subroutine creepB3Ddrying
```

Box. 7 Subroutine creepB3Ddrying for the computation of the drying creep of Model B3.

3.4 Numerical solution of integral equation

3.4.1 Formulation without the history memorization

The numerical integration of eq. [3.24] or its dual form requires the knowledge of the whole strain or stress history. This leads to remarkable imitations in practical analyses due to the huge memory requirements.

Such requirements may be dramatically reduced if relaxation or creep functions are written in degenerate form and suitable analytical developments are carried out.

As regards the relaxation function:

$$R(t,t')=\sum_{\mu=1}^{N} E_{\mu}(t_e')\left\{\exp\left[y_{\mu}(t_v')-y_{\mu}(t_v)\right]\right\} \qquad [3.70]$$

with $y_{\mu}(t_v)=t_v/\tau_{\mu}$ and τ_{μ} relaxation times of the μ -th Maxwell unit.

If eq. [3.70] is substituted in the [3.24] one obtains:

$$\boldsymbol{\sigma}(t)=\int_0^t \mathbf{B}^{-1}\sum_{\mu=1}^{N} E_{\mu}(t_e')e^{y_{\mu}(t_v')-y_{\mu}(t_v)}\left[d\boldsymbol{\varepsilon}(t)-d\boldsymbol{\varepsilon}^0(t)\right] \qquad [3.71]$$

3.4.2 Numerical solution

The calculation procedure based on the approximation of the superposition integral by a summation and a subsequent elimination of the strain history, using recursive formulas, was developed for relaxation functions by Lewis, Shrinatha and Thomas [41] and the application to a tridimensional case was studied by Majorana [42].

Taking as reference [27]; assuming a continuous strain history it can be posed that:

$$\mathrm{d}\varepsilon(t)-\mathrm{d}\varepsilon^0(t)=\frac{\mathrm{d}\left(\boldsymbol{\varepsilon}(t)-\boldsymbol{\varepsilon}^0(t)\right)}{\mathrm{d}t'}\mathrm{d}t' \qquad [3.72]$$

and the equation [3.24] may be integrated by parts as follows:

$$\boldsymbol{\sigma}(t)=\mathbf{B}^{-1}R(t,t')\left[\boldsymbol{\varepsilon}(t)-\boldsymbol{\varepsilon}^0(t)\right]-\int_0^t \mathbf{B}^{-1}\frac{\partial R(t,t')}{\partial t'}\left[\boldsymbol{\varepsilon}(t')-\boldsymbol{\varepsilon}^0(t')\right]\mathrm{d}t' \qquad [3.73]$$

in which $\mathbf{B}^{-1}R(t,t')$ represents stress at time t due to a unit strain imposed at the same time instant, i.e. $\mathbf{B}^{-1}E(t)$ with $E(t)$ instantaneous elastic modulus at time t.

Performing time integration of eq. [3.73] by means of a finite difference technique implies the following operations. Time variable t must be subdivided in n time intervals whose length is $\Delta t = t_{i+1} - t_i$, with $t_1 = 0$ and $t_{n+1} = t$. After applying the sum property of integrals, eq. [3.73] becomes:

$$\begin{aligned} \boldsymbol{\sigma}\left(t_{n+1}\right) &= \mathbf{B}^{-1} R\left(t_{n+1}, t_{n+1}\right) \boldsymbol{\varepsilon}\left(t_{n+1}\right) - \mathbf{B}^{-1} R\left(t_{n+1}, t_{n+1}\right) \boldsymbol{\varepsilon}^{0}\left(t_{n+1}\right) + \\ & -\sum_{i=1}^{n} \int_{t_i}^{t_{i+1}} \mathbf{B}^{-1} \frac{\partial R\left(t_{n+1}, t'\right)}{\partial t'} \boldsymbol{\varepsilon}\left(t'\right) \mathrm{d}t' + \sum_{i=1}^{n} \int_{t_i}^{t_{i+1}} \mathbf{B}^{-1} \frac{\partial R\left(t_{n+1}, t'\right)}{\partial t'} \boldsymbol{\varepsilon}^{0}\left(t'\right) \mathrm{d}t' \end{aligned} \qquad [3.74]$$

Each integral contained in the first sum at the r.h.s. of eq. [3.74] may be approximated as

$$\begin{aligned} \int_{t_i}^{t_{i+1}} \mathbf{B}^{-1} \frac{\partial R\left(t_{n+1}, t'\right)}{\partial t'} \boldsymbol{\varepsilon}\left(t'\right) \mathrm{d}t' &\cong \int_{t_i}^{t_{i+1}} \mathbf{B}^{-1} \frac{\partial R\left(t_{n+1}, t'\right)}{\partial t'} \mathrm{d}t' \frac{1}{2}\left[\boldsymbol{\varepsilon}\left(t_{i+1}\right) + \boldsymbol{\varepsilon}\left(t_i\right)\right] = \\ &= \mathbf{B}^{-1}\left[R\left(t_{n+1}, t_{i+1}'\right) - R\left(t_{n+1}, t_i'\right)\right] \frac{1}{2}\left[\boldsymbol{\varepsilon}\left(t_{i+1}\right) + \boldsymbol{\varepsilon}\left(t_i\right)\right] \end{aligned} \qquad [3.75]$$

The first sum, is so well approximated:

$$\begin{aligned} \sum 1 &= \sum_{i=1}^{n} \int_{t_i}^{t_{i+1}} \mathbf{B}^{-1} \frac{\partial R\left(t_{n+1}, t'\right)}{\partial t'} \boldsymbol{\varepsilon}\left(t'\right) \mathrm{d}t' \cong \\ &\cong \frac{1}{2} \mathbf{B}^{-1} \sum_{i=1}^{n} \left[\boldsymbol{\varepsilon}\left(t_{i+1}\right) + \boldsymbol{\varepsilon}\left(t_i\right)\right]\left[R\left(t_{n+1}, t'_{i+1}\right) - R\left(t_{n+1}, t'_{i}\right)\right] \end{aligned} \qquad [3.76]$$

explaining the last term of the summation, we obtain:

$$\begin{aligned} \sum 1 &= \frac{1}{2} \mathbf{B}^{-1} \boldsymbol{\varepsilon}\left(t_{n+1}\right)\left[R\left(t_{n+1}, t'_{n+1}\right) - R\left(t_{n+1}, t'_{n}\right)\right] + \\ &+ \frac{1}{2} \mathbf{B}^{-1} \boldsymbol{\varepsilon}\left(t_{n}\right)\left[R\left(t_{n+1}, t'_{n+1}\right) - R\left(t_{n+1}, t'_{n}\right)\right] + \\ &+ \frac{1}{2} \mathbf{B}^{-1} \sum_{i=1}^{n-1} \left[\boldsymbol{\varepsilon}\left(t_{i+1}\right) + \boldsymbol{\varepsilon}\left(t_i\right)\right]\left[R\left(t_{n+1}, t'_{i+1}\right) - R\left(t_{n+1}, t'_{i}\right)\right] \end{aligned} \qquad [3.77]$$

Examining the second summation at the r.h.s. of eq. [3.74], which the generic term can still be approximated in a similar manner to those used to derive eq. [3.75]:

$$\begin{aligned} \int_{t_i}^{t_{i+1}} \mathbf{B}^{-1} \frac{\partial R\left(t_{n+1}, t'\right)}{\partial t'} \boldsymbol{\varepsilon}^{0}\left(t'\right) \mathrm{d}t' &\cong \int_{t_i}^{t_{i+1}} \mathbf{B}^{-1} \frac{\partial R\left(t_{n+1}, t'\right)}{\partial t'} \mathrm{d}t' \frac{1}{2}\left[\boldsymbol{\varepsilon}^{0}\left(t_{i+1}\right) + \boldsymbol{\varepsilon}^{0}\left(t_i\right)\right] = \\ &= \mathbf{B}^{-1}\left[R\left(t_{n+1}, t_{i+1}'\right) - R\left(t_{n+1}, t_i'\right)\right] \frac{1}{2}\left[\boldsymbol{\varepsilon}^{0}\left(t_{i+1}\right) + \boldsymbol{\varepsilon}^{0}\left(t_i\right)\right] \end{aligned} \qquad [3.78]$$

The second sum, is so well approximated:

$$\begin{aligned}\sum 2 &= \sum_{i=1}^{n} \int_{t_i}^{t_{i+1}} \mathbf{B}^{-1} \frac{\partial R\left(t_{n+1},t'\right)}{\partial t'} \boldsymbol{\varepsilon}^0\left(t'\right)\mathrm{d}t' \cong \\ &\cong \frac{1}{2}\mathbf{B}^{-1}\sum_{i=1}^{n}\left[\boldsymbol{\varepsilon}^0\left(t_{i+1}\right)+\boldsymbol{\varepsilon}^0\left(t_i\right)\right]\left[R\left(t_{n+1},t'_{i+1}\right)-R\left(t_{n+1},t'_{i}\right)\right]\end{aligned} \qquad [3.79]$$

Assigning $R\left(t,t'\right)$ as a degenerate kernel (see eq. [3.70]), posing $\mathbf{D}_\mu\left(t_e\right)=\mathbf{B}^{-1}E_\mu\left(t_e\right)$ and taking into account eq. [3.77], enables to write eq. [3.74] as follows:

$$\begin{aligned}\boldsymbol{\sigma}\left(t_{n+1}\right) &= \sum_{\mu=1}^{N}\mathbf{D}_\mu\left(t_{e_{n+1}}\right)\boldsymbol{\varepsilon}\left(t_{n+1}\right)-\sum_{\mu=1}^{N}\mathbf{D}_\mu\left(t_{e_{n+1}}\right)\boldsymbol{\varepsilon}^0\left(t_{n+1}\right)+ \\ &-\frac{1}{2}\sum_{\mu=1}^{N}\left\{\mathbf{D}_\mu\left(t_{e_{n+1}}\right)-\mathbf{D}_\mu\left(t_{e_n}\right)\exp\left[-\left(t_{v_{n+1}}-t_{v_n}\right)/\tau_\mu\right]\right\}\boldsymbol{\varepsilon}\left(t_{n+1}\right)+ \\ &-\frac{1}{2}\sum_{\mu=1}^{N}\left\{\mathbf{D}_\mu\left(t_{e_{n+1}}\right)-\mathbf{D}_\mu\left(t_{e_n}\right)\exp\left[-\left(t_{v_{n+1}}-t_{v_n}\right)/\tau_\mu\right]\right\}\boldsymbol{\varepsilon}\left(t_{n}\right)+ \\ &-\sum 1B+\sum 2\end{aligned} \qquad [3.80]$$

in which:

$$\begin{aligned}\sum 1B &= \frac{1}{2}\sum_{i=1}^{n-1}\sum_{\mu=1}^{N}\left\{\mathbf{D}_\mu\left(t_{e_{i+1}}\right)\exp\left[-\left(t_{v_{n+1}}-t_{v_{i+1}}\right)/\tau_\mu\right]-\mathbf{D}_\mu\left(t_{e_i}\right)\exp\left[-\left(t_{v_{n+1}}-t_{v_i}\right)/\tau_\mu\right]\right\}\cdot \\ &\cdot\left[\boldsymbol{\varepsilon}\left(t_{i+1}\right)+\boldsymbol{\varepsilon}\left(t_i\right)\right]\end{aligned} \qquad [3.81]$$

Reversing the order of the summation:

$$\begin{aligned}\sum 1B &= \sum_{\mu=1}^{N}\frac{1}{2}\sum_{i=1}^{n-1}\left\{\mathbf{D}_\mu\left(t_{e_{i+1}}\right)\exp\left[-\left(t_{v_{n+1}}-t_{v_{i+1}}\right)/\tau_\mu\right]-\mathbf{D}_\mu\left(t_{e_i}\right)\exp\left[-\left(t_{v_{n+1}}-t_{v_i}\right)/\tau_\mu\right]\right\}\cdot \\ &\cdot\left[\boldsymbol{\varepsilon}\left(t_{i+1}\right)+\boldsymbol{\varepsilon}\left(t_i\right)\right]=\sum_{\mu=1}^{N}\frac{1}{2}\cdot\mathbf{Q}_{\mu,n+1}\end{aligned} \qquad [3.82]$$

where it is placed:

$$\begin{aligned}\mathbf{Q}_{\mu,n+1} &= \sum_{i=1}^{n-1}\left\{\mathbf{D}_\mu\left(t_{e_{i+1}}\right)\exp\left[-\left(t_{v_{n+1}}-t_{v_{i+1}}\right)/\tau_\mu\right]-\mathbf{D}_\mu\left(t_{e_i}\right)\exp\left[-\left(t_{v_{n+1}}-t_{v_i}\right)/\tau_\mu\right]\right\}\cdot \\ &\cdot\left[\boldsymbol{\varepsilon}\left(t_{i+1}\right)+\boldsymbol{\varepsilon}\left(t_i\right)\right]\end{aligned} \qquad [3.83]$$

Collecting the term $\exp\left[-\left(t_{v_{n+1}}-t_{v_{i+1}}\right)/\tau_\mu\right]$, we obtain:

$$\begin{aligned}\mathbf{Q}_{\mu,n+1} &= \sum_{i=1}^{n-1}\exp\left[-\left(t_{v_{n+1}}-t_{v_{i+1}}\right)/\tau_\mu\right]\cdot\left\{\mathbf{D}_\mu\left(t_{e_{i+1}}\right)-\mathbf{D}_\mu\left(t_{e_i}\right)\exp\left[-\left(t_{v_{i+1}}-t_{v_i}\right)/\tau_\mu\right]\right\}\cdot \\ &\cdot\left[\boldsymbol{\varepsilon}\left(t_{i+1}\right)+\boldsymbol{\varepsilon}\left(t_i\right)\right]\end{aligned} \qquad [3.84]$$

Explaining the last term of the summation:

$$\begin{aligned}\mathbf{Q}_{\mu,n+1} = {}& \exp\left[-\left(t_{v_{n+1}}-t_{v_n}\right)/\tau_\mu\right]\left\{\mathbf{D}_\mu\left(t_{e_n}\right)-\mathbf{D}_\mu\left(t_{e_{n-1}}\right)\exp\left[-\left(t_{v_n}-t_{v_{n-1}}\right)/\tau_\mu\right]\right\}\cdot \\ & \cdot\left[\boldsymbol{\varepsilon}\left(t_n\right)+\boldsymbol{\varepsilon}\left(t_{n-1}\right)\right]+\sum_{i=1}^{n-2}\exp\left[-\left(t_{v_{n+1}}-t_{v_{i+1}}\right)/\tau_\mu\right]\cdot \\ & \cdot\left\{\mathbf{D}_\mu\left(t_{e_{i+1}}\right)-\mathbf{D}_\mu\left(t_{e_i}\right)\exp\left[-\left(t_{v_{i+1}}-t_{v_i}\right)/\tau_\mu\right]\right\}\cdot\left[\boldsymbol{\varepsilon}\left(t_{i+1}\right)+\boldsymbol{\varepsilon}\left(t_i\right)\right]\end{aligned} \qquad [3.85]$$

Collecting the term $\exp\left[-\left(t_{v_{n+1}}-t_{v_n}\right)/\tau_\mu\right]$ in the summation at the r.h.s. of eq. [3.85], we obtain:

$$\begin{aligned}\mathbf{Q}_{\mu,n+1} = {}& \exp\left[-\left(t_{v_{n+1}}-t_{v_n}\right)/\tau_\mu\right]\left\{\mathbf{D}_\mu\left(t_{e_n}\right)-\mathbf{D}_\mu\left(t_{e_{n-1}}\right)\exp\left[-\left(t_{v_n}-t_{v_{n-1}}\right)/\tau_\mu\right]\right\}\cdot \\ & \cdot\left[\boldsymbol{\varepsilon}\left(t_n\right)+\boldsymbol{\varepsilon}\left(t_{n-1}\right)\right]+\exp\left[-\left(t_{v_{n+1}}-t_{v_n}\right)/\tau_\mu\right]\cdot\sum_{i=1}^{n-2}\exp\left[-\left(t_{v_n}-t_{v_{i+1}}\right)/\tau_\mu\right]\cdot \\ & \cdot\left\{\mathbf{D}_\mu\left(t_{e_{i+1}}\right)-\mathbf{D}_\mu\left(t_{e_i}\right)\exp\left[-\left(t_{v_{i+1}}-t_{v_i}\right)/\tau_\mu\right]\right\}\cdot\left[\boldsymbol{\varepsilon}\left(t_{i+1}\right)+\boldsymbol{\varepsilon}\left(t_i\right)\right]\end{aligned} \qquad [3.86]$$

Collecting the common term $\exp\left[-\left(t_{v_{n+1}}-t_{v_n}\right)/\tau_\mu\right]$:

$$\begin{aligned}\mathbf{Q}_{\mu,n+1} = {}& \exp\left[-\left(t_{v_{n+1}}-t_{v_n}\right)/\tau_\mu\right]\left\{\left\{\mathbf{D}_\mu\left(t_{e_n}\right)-\mathbf{D}_\mu\left(t_{e_{n-1}}\right)\exp\left[-\left(t_{v_n}-t_{v_{n-1}}\right)/\tau_\mu\right]\right\}\cdot\right. \\ & \left.\cdot\left[\boldsymbol{\varepsilon}\left(t_n\right)+\boldsymbol{\varepsilon}\left(t_{n-1}\right)\right]+\mathbf{Q}_{\mu,n}\right\}\end{aligned} \qquad [3.87]$$

with:

$$\begin{aligned}\mathbf{Q}_{\mu,n} = {}& \sum_{i=1}^{n-2}\exp\left[-\left(t_{v_n}-t_{v_{i+1}}\right)/\tau_\mu\right]\cdot\left\{\mathbf{D}_\mu\left(t_{e_{i+1}}\right)-\mathbf{D}_\mu\left(t_{e_i}\right)\exp\left[-\left(t_{v_{i+1}}-t_{v_i}\right)/\tau_\mu\right]\right\}\cdot \\ & \cdot\left[\boldsymbol{\varepsilon}\left(t_{i+1}\right)+\boldsymbol{\varepsilon}\left(t_i\right)\right]\end{aligned} \qquad [3.88]$$

For $\sum 2$, it is possible to obtain a similar expansion:

$$\begin{aligned}\sum 2 = {}& \sum_{\mu=1}^{N}\frac{1}{2}\sum_{i=1}^{n}\left\{\mathbf{D}_\mu\left(t_{e_{i+1}}\right)\exp\left[-\left(t_{v_{n+1}}-t_{v_{i+1}}\right)/\tau_\mu\right]-\mathbf{D}_\mu\left(t_{e_i}\right)\exp\left[-\left(t_{v_{n+1}}-t_{v_i}\right)/\tau_\mu\right]\right\}\cdot \\ & \cdot\left[\boldsymbol{\varepsilon}^0\left(t_{i+1}\right)+\boldsymbol{\varepsilon}^0\left(t_i\right)\right]=\sum_{\mu=1}^{N}\frac{1}{2}\cdot\mathbf{R}_{\mu,n+1}\end{aligned} \qquad [3.89]$$

in which;

$$\begin{aligned}\mathbf{R}_{\mu,n+1} = {}& \sum_{i=1}^{n-1}\left\{\mathbf{D}_\mu\left(t_{e_{i+1}}\right)\exp\left[-\left(t_{v_{n+1}}-t_{v_{i+1}}\right)/\tau_\mu\right]-\mathbf{D}_\mu\left(t_{e_i}\right)\exp\left[-\left(t_{v_{n+1}}-t_{v_i}\right)/\tau_\mu\right]\right\}\cdot \\ & \cdot\left[\boldsymbol{\varepsilon}^0\left(t_{i+1}\right)+\boldsymbol{\varepsilon}^0\left(t_i\right)\right]\end{aligned} \qquad [3.90]$$

Collecting the term $\exp\left[-\left(t_{v_{n+1}}-t_{v_{i+1}}\right)/\tau_\mu\right]$, we obtain:

$$\begin{aligned}\mathbf{R}_{\mu,n+1}=&\sum_{i=1}^{n-1}\exp\left[-\left(t_{v_{n+1}}-t_{v_{i+1}}\right)/\tau_\mu\right]\left\{\mathbf{D}_\mu\left(t_{e_{i+1}}\right)-\mathbf{D}_\mu\left(t_{e_i}\right)\exp\left[-\left(t_{v_{i+1}}-t_{v_i}\right)/\tau_\mu\right]\right\}\\&\cdot\left[\boldsymbol{\varepsilon}^0\left(t_{i+1}\right)+\boldsymbol{\varepsilon}^0\left(t_i\right)\right]\end{aligned}\qquad[3.91]$$

and explaining the last term of the summation:

$$\begin{aligned}\mathbf{R}_{\mu,n+1}=&\exp\left[-\left(t_{v_{n+1}}-t_{v_{n+1}}\right)/\tau_\mu\right]\left\{\mathbf{D}_\mu\left(t_{e_{n+1}}\right)-\mathbf{D}_\mu\left(t_{e_n}\right)\exp\left[-\left(t_{v_{n+1}}-t_{v_n}\right)/\tau_\mu\right]\cdot\right.\\&\cdot\left[\boldsymbol{\varepsilon}^0\left(t_{n+1}\right)+\boldsymbol{\varepsilon}^0\left(t_n\right)\right]+\sum_{i=1}^{n-1}\exp\left[-\left(t_{v_{n+1}}-t_{v_{i+1}}\right)/\tau_\mu\right]\left\{\mathbf{D}_\mu\left(t_{e_{i+1}}\right)-\mathbf{D}_\mu\left(t_{e_i}\right)\cdot\right.\\&\left.\cdot\exp\left[-\left(t_{v_{i+1}}-t_{v_i}\right)/\tau_\mu\right]\right\}\cdot\left[\boldsymbol{\varepsilon}^0\left(t_{i+1}\right)+\boldsymbol{\varepsilon}^0\left(t_i\right)\right]\end{aligned}\qquad[3.92]$$

Reminding that $\exp(0)=1$ and collecting $\exp\left[-\left(t_{v_{n+1}}-t_{v_n}\right)/\tau_\mu\right]$ in the summation:

$$\begin{aligned}\mathbf{R}_{\mu,n+1}=&\left\{\mathbf{D}_\mu\left(t_{e_{n+1}}\right)-\mathbf{D}_\mu\left(t_{e_n}\right)\exp\left[-\left(t_{v_{n+1}}-t_{v_n}\right)/\tau_\mu\right]\right\}\cdot\left[\boldsymbol{\varepsilon}^0\left(t_{n+1}\right)+\boldsymbol{\varepsilon}^0\left(t_n\right)\right]+\\&+\exp\left[-\left(t_{v_{n+1}}-t_{v_{i+1}}\right)/\tau_\mu\right]\cdot\mathbf{R}_{\mu,n}\end{aligned}\qquad[3.93]$$

in which

$$\begin{aligned}\mathbf{R}_{\mu,n}=&\sum_{i=1}^{n-1}\exp\left[-\left(t_{v_n}-t_{v_{i+1}}\right)/\tau_\mu\right]\cdot\left\{\mathbf{D}_\mu\left(t_{e_{i+1}}\right)-\mathbf{D}_\mu\left(t_{e_i}\right)\exp\left[-\left(t_{v_{i+1}}-t_{v_i}\right)/\tau_\mu\right]\right\}\cdot\\&\cdot\left[\boldsymbol{\varepsilon}^0\left(t_{i+1}\right)+\boldsymbol{\varepsilon}^0\left(t_i\right)\right]\end{aligned}\qquad[3.94]$$

Taking into account the above developments, the stress-strain relationship (eq. [3.80]) can be written in this form:

$$\begin{aligned}\boldsymbol{\sigma}\left(t_{n+1}\right)=&\sum_{\mu=1}^{N}\mathbf{D}_\mu\left(t_{e_{n+1}}\right)\boldsymbol{\varepsilon}\left(t_{n+1}\right)-\sum_{\mu=1}^{N}\mathbf{D}_\mu\left(t_{e_{n+1}}\right)\boldsymbol{\varepsilon}^0\left(t_{n+1}\right)+\\&-\frac{1}{2}\sum_{\mu=1}^{N}\left\{\mathbf{D}_\mu\left(t_{e_{n+1}}\right)-\mathbf{D}_\mu\left(t_{e_n}\right)\exp\left[-\left(t_{v_{n+1}}-t_{v_n}\right)/\tau_\mu\right]\right\}\boldsymbol{\varepsilon}\left(t_{n+1}\right)+\\&-\frac{1}{2}\sum_{\mu=1}^{N}\left\{\mathbf{D}_\mu\left(t_{e_{n+1}}\right)-\mathbf{D}_\mu\left(t_{e_n}\right)\exp\left[-\left(t_{v_{n+1}}-t_{v_n}\right)/\tau_\mu\right]\right\}\boldsymbol{\varepsilon}\left(t_n\right)-\\&-\sum_{\mu=1}^{N}\frac{1}{2}\ \mathbf{Q}_{\mu,n+1}+\sum_{\mu=1}^{N}\frac{1}{2}\ \mathbf{R}_{\mu,n+1}\end{aligned}\qquad[3.95]$$

where $\mathbf{Q}_{\mu,n+1}$ and $\mathbf{R}_{\mu,n+1}$ are defined by the eqs. [3.87] and [3.93].

Substituting eq. [3.95] in the equilibrium equation at time t_{n+1} obtained by means of virtual work theorem:

$$\int_{(s)} \delta\boldsymbol{\varepsilon}^T \boldsymbol{\sigma}(t_{n+1})\mathrm{d}V = \delta\mathbf{u}^T\mathbf{F}(t_{n+1}) \tag{3.96}$$

one obtains

$$\begin{aligned}
&\int_{(s)} \delta\boldsymbol{\varepsilon}^T \sum_{\mu=1}^{N} \mathbf{D}_\mu\left(t_{e_{n+1}}\right)\boldsymbol{\varepsilon}(t_{n+1})\mathrm{d}V - \frac{1}{2}\int_{(s)} \delta\boldsymbol{\varepsilon}^T \sum_{\mu=1}^{N}\Big\{\mathbf{D}_\mu\left(t_{e_{n+1}}\right) - \\
&-\mathbf{D}_\mu\left(t_{e_n}\right)\exp\left[-\left(t_{v_{n+1}} - t_{v_n}\right)/\tau_\mu\right]\Big\}\cdot\boldsymbol{\varepsilon}(t_{n+1})\mathrm{d}V = \\
&= \int_{(s)} \delta\boldsymbol{\varepsilon}^T \sum_{\mu=1}^{N} \mathbf{D}_\mu\left(t_{e_{n+1}}\right)\boldsymbol{\varepsilon}^0(t_{n+1})\mathrm{d}V + \frac{1}{2}\int_{(s)} \delta\boldsymbol{\varepsilon}^T \Bigg\{\sum_{\mu=1}^{N}\mathbf{D}_\mu\left(t_{e_{n+1}}\right) - \mathbf{D}_\mu\left(t_{e_n}\right)\cdot \\
&\cdot\exp\left[-\left(t_{v_{n+1}} - t_{v_n}\right)/\tau_\mu\right]\boldsymbol{\varepsilon}(t_n) + \sum_{\mu=1}^{N}\mathbf{Q}_{\mu,n+1}\Bigg\}\mathrm{d}V - \frac{1}{2}\int_{(s)} \delta\boldsymbol{\varepsilon}^T \sum_{\mu=1}^{N}\mathbf{R}_{\mu,n+1}\mathrm{d}V + \delta\mathbf{u}^T\mathbf{F}(t_{n+1})
\end{aligned} \tag{3.97}$$

The introduction of spatial finite element approximation allows to obtain the following relationship:

$$(\mathbf{K}_1 - \mathbf{K}_2)\mathbf{u}(t_{n+1}) = \mathbf{F}(t_{n+1}) + \mathbf{F}_{ML} + \mathbf{F}_{TH} + \mathbf{F}_{MTH} \tag{3.98}$$

where

$$\mathbf{K}_1 = \int_{(s)} \mathbf{B}^T \sum_{\mu=1}^{N} \mathbf{D}_\mu\left(t_{e_{n+1}}\right)\mathbf{B}\,\mathrm{d}V \tag{3.99}$$

$$\mathbf{K}_1 = \frac{1}{2}\int_{(s)} \mathbf{B}^T \sum_{\mu=1}^{N}\Big\{\mathbf{D}_\mu\left(t_{e_{n+1}}\right) - \mathbf{D}_\mu\left(t_{e_n}\right)\exp\left[-\left(t_{v_{n+1}} - t_{v_n}\right)/\tau_\mu\right]\Big\}\mathbf{B}\,\mathrm{d}V \tag{3.100}$$

$$\mathbf{F}_{ML} = \frac{1}{2}\int_{(s)} \mathbf{B}^T \left\{\sum_{\mu=1}^{N}\Big\{\mathbf{D}_\mu\left(t_{e_{n+1}}\right) - \mathbf{D}_\mu\left(t_{e_n}\right)\exp\left[-\left(t_{v_{n+1}} - t_{v_n}\right)/\tau_\mu\right]\Big\}\boldsymbol{\varepsilon}(t_n) + \sum_{\mu=1}^{N}\mathbf{Q}_{\mu,n+1}\right\}\mathrm{d}V \tag{3.101}$$

$$\mathbf{F}_{TH} = \int_{(s)} \mathbf{B}^T \sum_{\mu=1}^{N} \mathbf{D}_\mu\left(t_{e_{n+1}}\right)\boldsymbol{\varepsilon}^0(t_{n+1})\,\mathrm{d}V \tag{3.102}$$

$$\mathbf{F}_{MTH} = -\frac{1}{2}\int_{(s)} \mathbf{B}^T \sum_{\mu=1}^{N} \mathbf{R}_{\mu,n+1}\,\mathrm{d}V \tag{3.103}$$

and $\mathbf{u}(t_{n+1})$ is the unknown displacement vector.

After solving the system of equations [3.98], strains at time t_{n+1} are calculated as usually:

$$\boldsymbol{\varepsilon}(t_{n+1}) = \mathbf{B}\cdot\mathbf{u}(t_{n+1}) \tag{3.104}$$

while the stresses are obtained by eq. [3.95].

The following procedure can be applied. At the first step $\left(i=1,\ n+1=1\right)$ it must be set $\boldsymbol{\varepsilon}\left(t_0\right)=\boldsymbol{\varepsilon}^0\left(t_0\right)=\mathbf{Q}_{\mu,1}=\mathbf{R}_{\mu,1}=0$, hence, if $\boldsymbol{\varepsilon}^0\left(t_1\right)$ is known (it is obtained solving heat and moisture transfer equations which allow to find ΔT and Δh), eq. [3.98] can be solved.

Subsequently strains, stresses, $\mathbf{Q}_{\mu,2}$ and $\mathbf{R}_{\mu,2}$ terms are calculated and the iteration cycle is repeated solving eq. [3.98] at time t_2. The assumed continuity of strain history implies that any instantaneous variation of hygrothermal and mechanical loads can be applied with the corresponding time interval tending to zero.

3.5 Damage modelling

3.5.1 Damage mechanics

The damage process corresponds to the localization and accumulation of strain and it is irreversible. Indeed defects that occur in materials, and generally in structures, lead to cracks and thus to possible phenomena of collapse, but also cause a progressive deterioration of the material, measured in terms of reduction of stiffness, strength, stability and remaining life.

Before presenting the damage model used in the F.E. code NEWCON3D, let's introduce some useful definition for the following developments, in particular the measure of the damage, initially defined through a scalar variable indicated by the symbol D.

Definition of damage

As limit state of a damage process, we refer to the state at which it is formed, in general, a macro crack. In the fracture mechanics, the beginning of a macro crack supposes the presence of a gap enough large if compared with the microscopic heterogeneities, eg. grains and microcracks. It is assumed that the macro crack grows along the surface interface of more grains.

Measurement of damage

There are different types of indirect measurements of the degree of damage that affects a given material:

- *Measurement of the remaining life* of the material: it is a method that has led to the linear rule of Miner and is used for materials subjected to fatigue phenomena;
- *Measurement of microscopic defects* such as intergranular cavities in viscous phenomena, surface microcracks in fatigue phenomena and size of the cavities in ductile fracture;
- *Measurement of damage through physical quantities and introduction of the concept of the effective stress.* The influence of damage on the macroscopical properties of the material under exam can be measured and used to define the variables contained in the damage law. Therefore it is measured the variation of density, of the acoustic emission, of the fatigue limit and also the change of mechanical properties.

The last method has been more developed, especially as regards the measurements of the variations of the mechanical properties of the material. Consequently it has been introduced the concept of the effective stress , according to which:

"An element volume made of damaged material and subjected to a given stress σ, has the same strain of the same element volume made of undamaged material and subjected to an effective stress $\tilde{\sigma}$."

This definition, can be expressed in the following form:

- for the undamaged material: $\varepsilon = f(\sigma)$;
- for the damaged material or the equivalent undamaged: $\varepsilon = f(\tilde{\sigma})$.

If the damage D represents the reduction of the resistant area due to the onset and propagation of the micro crack, then it is possible to write:

$$\tilde{\sigma} = \sigma \frac{S}{\tilde{S}} = \frac{\sigma}{1-D} \qquad [3.105]$$

in which S is the resistant area of the undamaged material and $\tilde{S}$ is the resistant area of the damaged material.

In the case of ductile fracture, it is possible to gauge the variation of the elastic modulus. In fact, by the known relations applied to the damaged material and to the undamaged one:

$$\tilde{\sigma} = \tilde{E} \cdot \varepsilon_e; \qquad \sigma = E \cdot \varepsilon_e \qquad [3.106]$$

it is obtained:

$$\tilde{\sigma} = \frac{E}{\tilde{E}} \sigma = \frac{\sigma}{1-D} \qquad \Rightarrow \qquad D = 1 - \frac{\tilde{E}}{E} \qquad [3.107]$$

where E is the elastic modulus of the undamaged material and $\tilde{E}$ is the elastic modulus of the damaged material.

Thanks to the introduction of the concept of the effective stress $\tilde{\boldsymbol{\sigma}}$ it is possible to define the value of the critical damage *D_c* and the value for which there is the break of the material for decohesion.

If in fact $\tilde{\sigma}_u$ is the uniaxial ultimate stress for decohesion and σ_u is the classical ultimate stress., we have:

$$\tilde{\sigma}_u = \frac{\sigma_u}{1-D_c} > \sigma_u \qquad [3.108]$$

therefore:

$$D_c = 1 - \frac{\sigma_u}{\tilde{\sigma}_u} \qquad [3.109]$$

As $\tilde{\sigma}_u$ varies from $E/50$ to E/20 instead σ_u varies from $E/100$ to E/250, it is possible to deduce that D_c has a value between 0.5 and 0.9.

3.5.2 The thermodynamic applied to the damage theories

The behaviour of a material as concrete, at constant temperature, can be described through the following variables:

$\boldsymbol{\varepsilon}^e$ = elastic strain tensor,

D = scalar damage variable,

$\boldsymbol{\varepsilon}^p$ = plastic strain tensor.

Every equilibrium state is characterized by the value of the thermodynamic potential $\rho\psi$, function of the previous variables (ρ is the density of the material).

To satisfy the first principle of thermodynamic, it is chosen a quadratic form of (see Ref. [43]). Furthermore it is assumed that only the elastic properties of the material are affected by damage.

The potential $\rho\psi$ can be described as reported here:

$$\rho\psi = \rho\psi^e + \rho\psi^p \tag{3.110}$$

in which the terms on the right are respectively functions of the elastic and plastic strain.

The stress $\boldsymbol{\sigma}$ is obtained from above as follows:

$$\boldsymbol{\sigma} = \frac{\partial\left(\rho\psi^e\right)}{\partial\boldsymbol{\varepsilon}^e} \tag{3.111}$$

The permanent strains, as damage, are irreversible processes that lead to a decrease of mechanical energy with partial conversion into heat.

To satisfy the Clausius-Duhem inequality, in analytic terms:

$$\dot{\phi} = \boldsymbol{\sigma} : \dot{\boldsymbol{\varepsilon}} - \rho\dot{\psi} \geq 0 \tag{3.112}$$

It is useful, in the following, to distinguish the portion of dissipated energy due to damage by the other portion related to the plastic strains:

$$\dot{\phi}_d = \boldsymbol{\sigma} : \dot{\boldsymbol{\varepsilon}}_e - \rho\dot{\psi}_e; \qquad \dot{\phi}_p = \boldsymbol{\sigma} : \dot{\boldsymbol{\varepsilon}}_p - \rho\dot{\psi}_p \tag{3.113}$$

A sufficient condition because the inequality is respected (see eq. [3.112]) is that contemporaneously $\dot{\phi}_d \geq 0$ and $\dot{\phi}_p \geq 0$.

For the elastic potential, it is assumed the following expression:

$$\rho\dot{\phi}^e = \frac{1}{2}\boldsymbol{\Lambda}(D):\boldsymbol{\varepsilon}^e:\boldsymbol{\varepsilon}^e \qquad [3.114]$$

in which $\boldsymbol{\Lambda}(D)$ can be interpreted as the secant stiffness matrix of the material and is function of the damage D.

Considering the first in [3.113], it is obtained:

$$\dot{\phi}_d = -\left(\frac{1}{2}\frac{\partial(\boldsymbol{\Lambda}(D))}{\partial D}:\boldsymbol{\varepsilon}^e:\boldsymbol{\varepsilon}^e\right)\dot{D} \geq 0 \qquad [3.115]$$

Since the stiffness of the material, or the elastic modulus, decreases with the increasing of damage:

$$\frac{\partial(\boldsymbol{\Lambda}(D))}{\partial D} < 0 \qquad [3.116]$$

follows that, a sufficient condition because the equation is satisfied is that $\dot{D} \geq 0$ (or that the damage of the material never decreases). In fact, as already stated, since the changes induced by the damage on the material structure are irreversible, during a damage process appears an increase of entropy.

The function of damage that satisfies this property describes a surface of equation $f(\boldsymbol{\varepsilon},\boldsymbol{\Lambda},K_0)=0$, where K_0 is the initial threshold of damage. The uniqueness of this function for a given state of stress, is guaranteed if f is chosen as function of strains and not as function of stresses (in fact, because of the relation, two strain tensors may correspond to the same stress value).

To respect the loading conditions, the evolution of damage is defined as follows:

$$\dot{D} = 0 \quad if \quad (f<0) \quad or \quad (f=0 \;\; and \;\; \dot{f}<0) \qquad [3.117]$$

$$\dot{D} = \mathbb{F}(\boldsymbol{\varepsilon}) \quad if \quad f=0 \;\; and \;\; \dot{f}=0 \qquad [3.118]$$

in which $\mathbb{F}(\boldsymbol{\varepsilon})$ is a positive function of strains, experimentally determined.

3.5.3 Damage models

Introduction

In the past mathematical models based on elasticity, plasticity and viscoelasticity formulations were used to describe the nonlinearity in concrete. In the 1970s models based on nonlinear fracture and continuum damage mechanics were developed to simulate the crack propagation and the progressive degradation of stiffness in concrete.

In the 1970's models, concrete is not considered as an heterogeneous material but as an homogenised one; therefore they are not so capable to characterize the entire fracture process from the initialization, propagation to the formation of macro cracks in concrete and they don't allow a comprehensive understanding of the fracture process, as they don't consider the randomness of the properties in the concrete at the mesoscale.

Therefore in recent years, different models for the simulation of the fracture process in concrete at the mesoscale were developed (see Ref. [44]): Bažant et al. [45] presented a random particle model for fracture of brittle aggregate composite material, in which the matrix material is described by a softening stress-strain relation corresponding to a prescribed microscopic interparticle fracture energy; in the lattice model of Schlangen and Garboczi [46] and Schlangen and van Mier [47] the tensile strengths are given to the lattice elements to simulate the fracture process in heterogeneous such as concrete (an extension to 3D was developed by Lilliu and van Mier [48]); Eckardt et al. [49] described the fracture behaviour of the matrix and the aggregates trough the smeared crack concept.

The continuum models assume that the local damage in the material can be averaged and represented in the form of damage variables, which are related to the tangential stiffness tensor of the material. Krajcinonovic [50] as well as Mazars and Pijaudier-Cabot [51] used a scalar damage variable to model isotropic damage based on an experimental stress-strain curve of concrete under uniaxial tension.

In this work the non-local scalar damage model of Mazars is used in order to model the mechanical behaviour of concrete at the meso level due to its simplicity; in fact this material model is only applied to the cement paste and the ITZ whereas the aggregates are assumed to behave linearly elastic. In fact, for normal weight concrete the aggregates generally, as already said, have an higher stiffness and strength as the matrix. Therewith cracks arise in the mortar matrix and in the interface zone and propagate into the matrix around the aggregates.

Scalar isotropic damage model

In this model, the material is assumed elastic, homogeneous and isotropic. This approach has been extensively used in the literature and the cause is more for reasons of simplicity than the attempt to describe accurately the behaviour of concrete. In fact damage is developed in the body always according to a more precise direction, e.g. perpendicular to the load in the case of uniaxial tension and parallel to the load in the case of uniaxial compression.

It has proved that the scalar damage model of Mazars (see Refs. [51], [52]-[54]) describes accurately the response of non-reinforced concrete beams, carved and subjected to bending; as well as the fracture of specimens studied in the laboratory. The constitutive laws, which derive from this model, are very simple, especially in view of the implementation of the algorithms for nonlinear codes.

Mazars' damage law

The scalar isotropic damage model of Mazars ([51], [52]-[54]) allows to model the strain-softening behaviour of concrete with the damage mechanics.

The fundamental concept on which is founded this theory is that of the effective stress $\tilde{\boldsymbol{\sigma}}$ (eq. [3.105]). According to this definition the stress-strain law assumes the following form:

$$\boldsymbol{\sigma} = \boldsymbol{\Lambda}_0 \left(1 - D\right) : \boldsymbol{\varepsilon}_e \qquad [3.119]$$

in which $\boldsymbol{\sigma}$ and $\boldsymbol{\varepsilon}_e$ are, respectively, the stress and strain tensors, D is the damage parameter and $\boldsymbol{\Lambda}_0$ is the initial stiffness matrix of the material. It is supposed that concrete remains isotropic also when it damages. For this reason $\boldsymbol{\Lambda}_0$ depends by the Young's Modulus E and by the Poisson's ration ν of the undamaged material. According to eq. [3.119], at the unloading phase do not correspond permanent strains.

The damage parameter D varies from 0 (undamaged material) to 1 (totally damaged material). It is also assumed that the extensional strains are responsible for the propagation of the crack.

The response of the material is related to the application of loading functions which satisfy the principle of maximum De Saint-Venant's strain:

$$f\left(\boldsymbol{\varepsilon}, \boldsymbol{\Lambda}, K_0\right) = \tilde{\varepsilon} - K\left(D\right) \qquad [3.120]$$

where $\tilde{\varepsilon}$ is the equivalent strain and is defined as follows:

$$\tilde{\varepsilon} = \sqrt{\sum \left(\left\langle \boldsymbol{\varepsilon}_i \right\rangle_+\right)^2}; \qquad \left(\left\langle x \right\rangle_+ = \frac{|x| + x}{2}\right) \qquad [3.121]$$

and $\boldsymbol{\varepsilon}_i$ are the principal strains.

The evolution of damage D is obtained by the following expressions, considering eqs. [3.117] and [3.118], and assuming:

$$F = \int_0^{\varepsilon_M} \mathbb{F}(\tilde{\varepsilon})\, d\tilde{\varepsilon} \qquad [3.122]$$

where ε_M is the maximum value reached by $\tilde{\varepsilon}$.

If $f(\tilde{\varepsilon}) = 0$ and $\dot{f}(\tilde{\varepsilon}) = 0$ then:

$$D = F(\tilde{\varepsilon}) \qquad \text{(loading phase)} \qquad [3.123]$$

instead, if $f(\tilde{\varepsilon}) < 0$ or $f(\tilde{\varepsilon}) = 0$ and $\dot{f}(\tilde{\varepsilon}) < 0$ then:

$$\dot{D} = 0 \qquad \text{(unloading phase)} \qquad [3.124]$$

The eq. [3.122] defines the damage surface.

$K(D)$ is an hardening/softening parameter, initially equal to K_0, that assumes the higher value reached by the equivalent strain $\tilde{\varepsilon}$ during the loading history of the material, in the point in question.

By the results of experimental tests, it is known that the damage mechanism is different for a test of uniaxial tension (micro cracks are opened by the components of transversal dilation, directly connected to the load) by a compression one (micro cracks are opened by the effect of transversal dilation, related to the Poisson's ratio). This observation suggests the need of a decomposition of damage in two parts: the damage due to tension D_t and the damage due to compression D_c. So the total damage is a weighted sum of the previous components of damage. Therefore the evolution law $f(\tilde{\varepsilon})$, in the eqs. [3.123] and [3.124], is described through the two damage parameters D_t and D_c (see Ref. [53]):

$$D = \alpha_t D_t + \alpha_c D_c, \qquad D_t = F_t(\tilde{\varepsilon}), \qquad and \qquad D_c = F_c(\tilde{\varepsilon}) \qquad [3.125]$$

$$F_i(\tilde{\varepsilon}) = 1 - \frac{(1 - A_i) K_0}{\tilde{\varepsilon}} - \frac{A_i}{\exp\left[B_i(\tilde{\varepsilon} - K_0)\right]} \qquad (i = t, c) \qquad [3.126]$$

the weighting coefficients α_t and α_c are assigned, so that:

in pure tension: $\alpha_t = 1, \quad \alpha_c = 0, \quad and \quad D = D_t$

in pure compression: $\alpha_t = 0, \quad \alpha_c = 1, \quad and \quad D = D_c$

The weights α_t and α_c are defined as dimensionless functions of the principal values of the strains.

Let's introduce the notation [53]:

$$\langle\varepsilon_i\rangle=\varepsilon_{ci}+\varepsilon_{ti} \qquad [3.127]$$

in which ε_{ti} is the positive dilation (of tension) due to positive stresses (of tension) and ε_{ci} is a positive strain due to negative stresses or (of compression, Poisson's effect).

The coefficients α_t and α_c are defined by the following expressions:

$$\alpha_t=\sum_{i=1}^{3}\left(\frac{\varepsilon_{ti}\left(\varepsilon_{ti}+\varepsilon_{ci}\right)}{\tilde{\varepsilon}^2}\right) \qquad [3.128]$$

$$\alpha_c=\sum_{i=1}^{3}\left(\frac{\varepsilon_{ci}\left(\varepsilon_{ti}+\varepsilon_{ci}\right)}{\tilde{\varepsilon}^2}\right) \qquad [3.129]$$

If all the stress components have the same sign, we obtain $\alpha_t=1,\ \alpha_c=0$ or $\alpha_c=1,\ \alpha_t=0$.

Modified Mazars' damage law

In the previous paragraph the coefficients α_t and α_c, defined by eqs. [3.128] and [3.129], were introduced. It was proposed a modification to take into account the following circumstance (see Ref. [55]):

- the coefficients α_t and α_c are less than one if the stress is tensile combined to compression, i.e. shear stress.

Consequently the modification is the following:

$$\alpha_t=\sum_{i=1}^{3}\left(\frac{\varepsilon_{ti}\left(\varepsilon_{ti}+\varepsilon_{ci}\right)}{\tilde{\varepsilon}^2}\right)^{\beta} \qquad [3.130]$$

$$\alpha_c=\sum_{i=1}^{3}\left(\frac{\varepsilon_{ci}\left(\varepsilon_{ti}+\varepsilon_{ci}\right)}{\tilde{\varepsilon}^2}\right)^{\beta} \qquad [3.131]$$

The main difference compared to the previous expressions of α_t and α_c is that the sum of the two coefficients is no more equal to one if the exponent β is different from the unity. To justify the introduction of this new parameter, it is consider a state of pure shear stress:

$$\sigma=\begin{bmatrix}0 & \tau & \tau\\ \tau & 0 & \tau\\ \tau & \tau & 0\end{bmatrix} \qquad [3.132]$$

The eq. [3.119] gives $\tau = \frac{E(1-D)}{1-\nu}\varepsilon_{12}$ (where ε_{12} is the shear strain), the eq. [3.121] provides $\tilde{\varepsilon} = \varepsilon_{12}$. The eqs. [3.130] and [3.131] become:

$$\alpha_t = \left(\frac{1}{1+\nu}\right)^{\beta} \qquad [3.133]$$

$$\alpha_c = \left(\frac{\nu}{1+\nu}\right)^{\beta} \qquad [3.134]$$

For large values of ε_{12}, we have that $D_t \cong D_c \cong 1$ and, by the eqs. [3.117] and [3.118]:

$$D = \left(\frac{1}{1+\nu}\right)^{\beta} + \left(\frac{\nu}{1+\nu}\right)^{\beta} \qquad [3.135]$$

If β =1, being $D \cong 1$, the material cannot tolerate any tension. In fact, due to internal friction and the mutual constraint exercised by the aggregates, an additional residual stress remains; consequently, the behaviour subjected to a uniform shear stress corresponds more to a plastic model than to a damage one.

The damage influences the shear behaviour of concrete, through the shear retention factor. In the same way, the β exponent, introduced in this formulation, reduces the damage influence on the shear stiffness since $\alpha_t + \alpha_c < 0$. The introduction of β is an artifice; it must be related to the fact that it is considered an isotropic damage model and should be applied only in this case.

In Fig. 3.8 it is reported the response of the model to a pure shear stress for different values of β.

So, considering the modified Mazars' damage model there are eight model parameters. Young's modulus and Poisson's ratio are measured from a uniaxial compression test. A direct tensile test or three-point bend test can provide the damage parameters in tension (k_0, A_t, B_t). The parameters (A_c, B_c) are fitted from the response of the material to uniaxial compression. As regards the way to perform experimental tests for the determination of β we proceed as follows. It would seem logical to use shear tests, but they are not common and it is difficult to perform them properly. An alternative way would be pull-out tests. Table 3.5 presents the standard intervals for the model parameters in the case of concrete (see Refs. [44] and [58]).

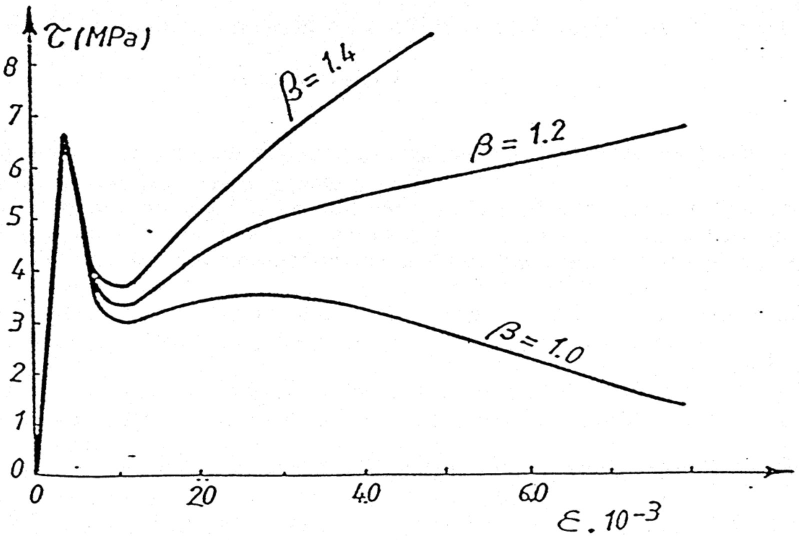

Fig. 3.8 Response of the model to a pure shear stress for different values of β.

Table 3.5 Standard model parameters.

Parameters of isotropic damage model
$k_0 \approx 1\times10^{-4}$
$0.7 \le A_t \le 1.2$
$1\times10^{-4} \le B_t \le 5\times10^{-4}$
$1.0 \le A_c \le 1.5$
$1\times10^{3} \le B_c \le 2\times10^{3}$
$1.0 \le \beta \le 1.05$

Non-local damage model

For the numerical analysis of the collapse of heterogeneous materials, as concrete, it is developed the theory of non-local damage. An important feature of the non-local formulation is that the solution of the elastic equilibrium problem doesn't change with the variation of the adopted discretization.

The non-local model is based on the computation of a strain variable, defined as:

$$\bar{\varepsilon}(\mathbf{x})=\frac{1}{V_r(\mathbf{x})}\int_V \tilde{\varepsilon}(\mathbf{s})\alpha(\mathbf{s}-\mathbf{x})dv \qquad [3.136]$$

in which:

- $\tilde{\varepsilon}$ is the equivalent strain defined by the eq. [3.121];
- $\mathbf{x}$ is the coordinate of the current Gauss point;
- $\mathbf{s}$ is the coordinate of the generic Gauss point;
- α is a weight function, so defined:

$$\alpha(\mathbf{s}-\mathbf{x}) = \exp\left(\frac{k|\mathbf{s}-\mathbf{x}|}{l}\right)^2 \qquad [3.137]$$

- V_r is the characteristic volume, defined by the integral:

$$V_r = \int_V \alpha(\mathbf{s}-\mathbf{x})\,dv \qquad [3.138]$$

The parameter k, in two-dimensional problems, assumes a value equal to 2 and l is the characteristic length. By experimental tests (see Ref. [56]) $l = 2.8 \cdot d_a$ in which d_a is the maximum size of the aggregate in concrete.

V_r has the same meaning of the representative volume introduced in the statistical theory of heterogeneous materials of Kroner. An important feature of this approach is that only one variable is computed in a non-local way, the one that controls the strain-softening in the $\sigma-\varepsilon$ curve; all the other variables are computed in a local manner.

In Ref. [57] is reported the case of samples subjected to pure tension, studied numerically and experimentally. By Fig. 3.9 and Fig. 3.10 it is possible to observe:

- the diagram is almost equal for the 2 discretization in the non-local continuum case, instead the strain-softening part undergoes an evident change in the local continuum one;
- the two types of calculations give the same result only for not refined discretization, such as those consisting of few elements.

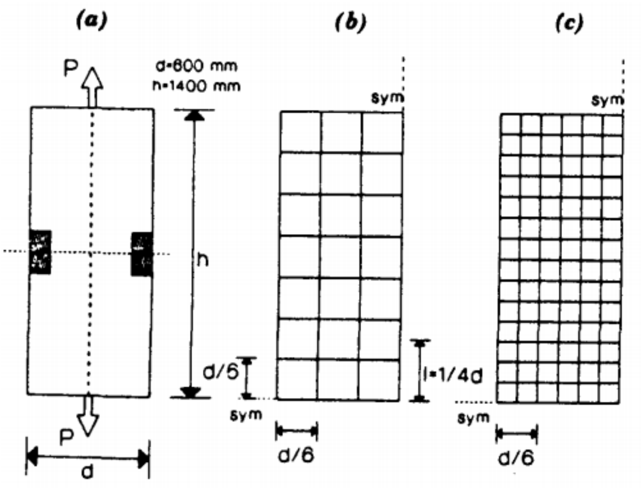

Fig. 3.9 Specimen subjected to pure tension and two different finite element meshes (***(b)*** mesh of 21 elements and ***(c)*** mesh of 84 elements).

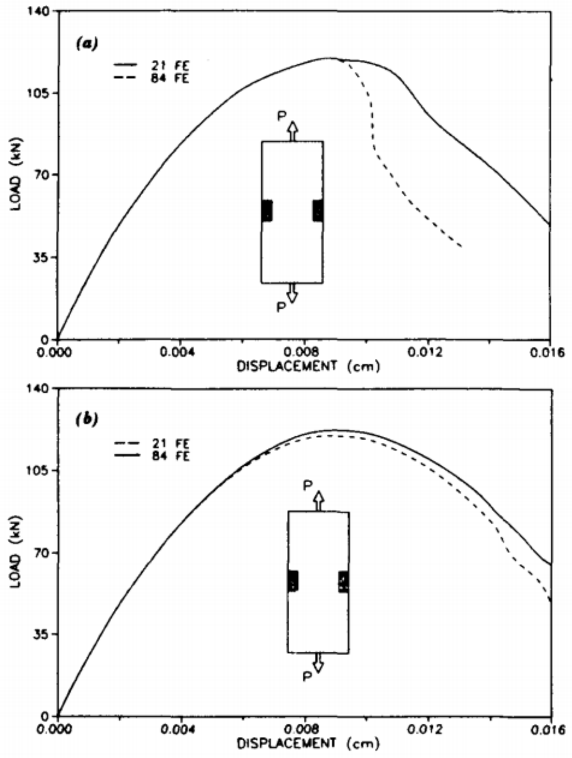

Fig. 3.10 Load-displacement curves obtained with meshes shown in Fig. 3.9: ***(a)*** local continuum, ***(b)*** non-local continuum.

REFERENCES

[1] Majorana C.E., Salomoni V.A. and Schrefler B.A. (1998), Hygrothermal and mechanical model of concrete at high temperature, Mat Struc, 31(210), pp. 378-386.

[2] Majorana C.E. and Salomoni V.A. (2004), Parametric analyses of diffusion of activated sources in disposal forms, J Haz Mat, A113, pp. 45-56.

[2] Salomoni V.A., Mazzucco G. and Majorana C.E. (2007), Mechanical and durability behaviour of growing concrete structures, Eng Comp, 24(5), pp. 536-561.

[3] Salomoni V.A., Majorana C.E., Giannuzzi G.M. and Miliozzi A. (2008), Thermal-fluid flow within innovative heat storage concrete systems for solar power plants, Int J Num Meth Heat Fluid Flow, 18, pp. 969-999.

[4] Salomoni, V.A., Majorana C.E., Mazzucco G., Xotta G. and Khoury G.A. (2009), Multiscale modelling of Concrete as a Fully Coupled Porous Medium, Concrete Materials: Properties, Performance and Applications, Ch. 3, NOVA Science Publishers, pp. 171-231.

[5] Gawin D., Majorana C.E. and Schrefler B.A. (1999), Numerical analysis of hygro-thermal behaviour and damage of concrete at high temperature, Mech Coh Frict Mat, 4, pp. 37-74.

[6] Baggio P., Majorana C.E. and Schrefler B.A. (1995), Thermo-hygro-mechanical analysis of concrete, Int J Num Meth Fluids, 20, pp. 573-595.

[7] Couture F., Jomaa W. and Ruiggali J.R. (1996), Relative permeability relations: a key factor for a drying model, Tran Por Media, 23, pp. 303-335.

[8] Schrefler B.A., Simoni L. and Majorana C.E. (1989), A general model for the mechanics of saturated-unsaturated porous materials, Mat Str, 22, pp. 323-334.

[9] Majorana C.E., Salomoni V. and Secchi S. (1997), Effects of mass growing on mechanical and hygrothermic response of three-dimensional bodies, J Mat Proc Tech, PROO64/1-3, pp. 277-286.

[10] Bažant Z.P. (1975), Pore pressure, uplift, and failure analysis of concrete dams, Int. Commission on Large Dams, Swansea, UK.

[11] Bažant Z.P. and Thonguthai W. (1978), Pore pressure and drying of concrete at high temperature, J Eng Mat Div, ASME, 104, pp. 1058-1080.

[12] Bažant Z.P. and Thonguthai W. (1979), Pore pressure in heated concrete walls: theoretical predictions, Mag Con Res, 31(107), pp. 67-76.

[13] Bažant Z.P. (1988), Mathematical Modelling of creep and shrinkage of concrete, J. Wiley & Sons: NY, USA.

[14] Bažant Z.P. and Najjar L.N. (1972), Nonlinear water diffusion in non-saturated concrete, Mat Str, 5(25), pp. 3-21.

[15] Roelfstra P.E. and Wittmann F.H., Numerical analysis of drying and shrinkage, in Autoclave aerated concrete, moisture content and properties, Elsevier, The Netherlands.

[16] Wittmann F.H. (1985), Deformation of concrete at variable moisture content, Mechanics of Geomaterials, Rock, Concrete, Soils, ed by Z.P. Bažant, Wiley.

[17] Comini and Lewis R.W. (1976), A numerical solution of two dimensional problems involving heat and mass transfer, Int J. Heat Mass Transfer, 19, pp. 1387-1392.

[18] Majorana C.E. (1985), Numerical simulation of drying and shrinkage of concrete with a multiphase inhomogeneous material model, Istituto di Scienza e Tecnica delle Costruzioni, Università di Padova.

[19] Sih G.C., Michopoulos J.G. and Chou S.C. (1986), Higrothermoelasticity, Martinus Nijhoff Publishers.

[20] Gregg S.J. and Sing K.S.W. (1982), Adsorption, Surface Area and Porosity, Academic Press, London.

[21] Hyland R.W. and Wexler A. (1983), Formulation for the thermodynamic properties of dry air from 173.15K to 473.15K, and of saturated moist air from 173.15K to 372.15K, at pressures to 5MPa, ASHRAE Trans. A, 89(2), pp. 520-535.

[22] ASHRAE (1997), Handbook of Fundamentals. American Soc. of Heating, Refrigerating and Air Conditioning Engineers Inc.: Atlanta, USA.

[23] Bažant Z.P. (1986), Material models for structural creep analysis, in Creep and Shrinkage of Concrete: Mathematical Modeling, Bažant Z.P. Ed., Northwestern University, Evanston, IL, USA, Ch. 2.

[24] Bažant Z.P. and Wittmann F.H. (1982), Creep and shrinkage in concrete structures, John Wiley & Sons, London.

[25] Bažant Z.P. and Prasannan J. (1989), Soldiification theory for concrete creep. I: Formulation and II: Verification and application, Journal of Engineering Mechanics, 115, N. 8, pp. 1691-1703, 1704-1725.

[26] Shrinatha H.R. and Lewis R.W., A finite element method for termoviscoelastic analysis of plane problems, University College of Swansea, UK, Internal report

[27] Majorana C.E. and Vitaliani R. (1990), Numerical modelling of creep and shrinkage of concrete by finite element method, 2nd Int. Conf. on Computer Aided Design in Concrete Structures, Zell-Am-See (Austria), pp. 773-784.

[28] Bažant Z.P. (1986), Material models for structural analysis, Cap. 2 in Preprint fourth RILEM international symposium on creep and shrinkage of concrete: material modeling, ed. by Z.P. Bažant.

[29] Bažant Z.P. and Panula L. (1978-1979), Practical prediction of time-dependent deformation for concrete, Materials and Structures, (RILEM, Paris). Part I and II , 11, N. 65, (1978), pp. 302-327; Part III and IV, 11, N. 66, (1978), pp. 415-434; Part V and VI, 12, N. 69, (1979), pp. 169-183.

[30] Roelfstra P.E. and Wittmann F.H. (1985), Deformation of concrete at variable moisture content, Mechanics of Geomaterials, Rock, Concrete, Soils, ed. by Z.P. Bažant.

[31] Bažant Z.P., Asghari A.A. and Schmidt J, (1976), Experimental study of creep of hardened Portland cement paste at variable water content, Materials and Structures, 9, n° 52, pp. 279-290.

[32] Bažant Z.P. and Baweja S. (1995), Creep and shrinkage prediction model for analysis and design of concrete structures - Model B3, Materials and Structures, 28, pp. 357-365, 415-430, 488-495.

[33] Bažant Z.P. and Baweja S. (1995), Creep and shrinkage prediction model for analysis and design of concrete structures: Model B3, The Adam Neville Symposium: Creep and Shrinkage Structural Design Effects, SP-194, A. Al-Manaseer, ed., American Concrete Institute, Farmington Hills, MI, pp. 1-83.

[34] ACI Committee 209 (2008), Guide for Modeling and Calculating Shrinkage and Creep in Hardened Concrete, ACI Report 209, 2R-08, Farmington Hills.

[35] Bažant Z.P., Yu Q., Li G.-H., Klein G.J. and Kristek V. (2010), Excessive deflections of record-span prestressed box-girder. Lessons learned from the collapse of the Koror-Babeldaob bridge in Palau, ACI Concrete International, 32(6), pp. 44-52.

[36] Bažant Z.P., Kim Joong-Koo and Panula L. (1991-1992), Improved prediction model for time dependent deformations of concrete, Materials and Structures, Part I and II , 24, (1991), pp. 327-345, 409-442; Part III, IV and IV, 25, (1992), pp. 21-28, 84-94, 163-169.

[37] Bažant Z.P. and Osman E. (1976), Double power law for basic creep of concrete, Materials and Structures, 9, N. 49.

[38] Bažant Z.P. and Baweja S. (2000), Creep and shrinkage prediction model for analysis and design of concrete structures: Model B3-short form, Adam Neville Symposium: Creep and Shrinkage-Structural Design Effects, ACISP-194, A. AL-Manaseer ed., Am Concrete Institute, Farmington Hills, Michigan.

[39] Granger L. and Bažant Z.P. (1995), Effect of composition on basic creep of concrete and cement paste, Journal of engineering mechanics, 121.

[40] Baweja S., Dvorak G.J. and Bažant Z.P. (1998), Triaxial composite model for basic creep of concrete, Journal of Engineering Mechanics, pp. 959-965.

[41] Lewis R.W., Shrinatha H.R. and Thomas H.R. (1984), A finite element study of the drying stresses in timber using viscoelastic and elasto-viscoplastic rheological models, Cap. 5 in Numerical methods in coupled systems, ed. R.W. Lewis, P. Bettess, E. Hinton, John Wiley and Sons, pp. 147-190.

[42] Majorana C.E., Soluzione numerica di equazioni integrali di Volterra per la analisi del comportamento meccanico di corpi viscoelastici tridimensionali mediante il metodo degli elementi finiti, Istituto di Scienza e Tecnica delle Costruzioni, Università di Padova.

[43] Lemaitre J. and Caboche J.L. (1978), Aspect phenomenologique de la rupture par endommagement, J. de Mech. Appl., 2, pp. 317–365.

[44] Wriggers P. and Moftah S.O., Mesoscale models for concrete: Homogenisation and damage behaviour, Finite Elements in Analysis and design, 42, pp. 623-636.

[45] Bažant Z.P., Tabbara M.R., Kazemi M.T. and Pijaudier-Cabot J., Random particle model for fracture of aggregate or fiber composite, J. Engng. Mech, 117 (8), pp. 1686-1705.

[46] Schlangen E. and Garboczi E.J. (1997), Fracture simulations of concrete using lattice models: computational aspects, Eng. Fract. Mech., 57, pp. 319-332.

[47] Schlangen E. and van Mier J.G.M. (1992), Simple lattice model for numerical simulation of fracture of concrete materials and structures, Mater. Struct., 25, pp. 534-542.

[48] Lilliu G. and van Mier J.G.M. (2003), 3D lattice type fracture model for concrete, Eng. Fract. Mech., 70, pp. 927-941.

[49] Eckardt S, Hafner S. and Konke C. (2004), Simulation of the fracture behaviour of concrete using continuum damage models at the mesoscale, Proceedings of ECCOMAS 2004.

[50] Krajcinovic D. (1979), Distributed damage theory of beams in pure bending, ASME Journal of Applied Mechanics, 46, pp. 592-596.

[51] Mazars J. and Pijaudier–Cabot J. (1989), Continuum Damage Theory – Application to Concrete, J Engrg Mech, ASCE, 115, pp. 345-365.

[52] Mazars J. (1984), Application de la mecanique de l'endommagement au comportament non lineaire et la rupture du beton de structure, Thèse de Doctorat d' Etat, L.M.T., Universitè de Paris, France.

[53] Mazars J. (1986), A description of micro and macroscale damage of concrete structures, Engng. Fract. Mech., 25, N°5-6, pp. 729-737.

[54] Mazars J. (1989), Description of the behaviour of composite concretes under complex loadings through continuum damage mechanics, Proc. 10th U.S. National Congress of Applied Mech., Lamb J.P., Ed., ASME.

[55] Mazars J., Pijaudier-Cabot G. and Pulikowski J. (1989), Steel concrete bond analysis with nonlocal continuos damage, Rapport Interne N°96.

[56] Bažant Z.P. and Pijaudier-Cabot G. (1989), Measurement of characteristic length of nonlocal continuum, Report No. 87-12/498m, Northwestern University, Evanston USA.

[57] Bažant Z.P. and Ozbolt J. (1990), Nonlocal Microplane Model for Fracture, Damage, and Size Effect in Structures, J. Eng. Mech., 116, pp. 2485-2505.

[58] Lemaitre j. (2001), Handbook of material behaviour models: Failures of materials, vol. 2, Academic Press, San Diego.

4 CONCRETE AT HIGH TEMPERATURE

4.1 Introduction

Although concrete is a well-understood construction material, in the last years the attention has focused on the performance of concrete in the fire safety assessment of the buildings and tunnels. In fact the exposure of concrete to high temperatures can lead to a decline of load bearing capacity and a significantly impair the structural integrity, especially during a rapid and/or prolonged increase of ambient temperature, like during a fire or a nuclear accident. Fire represents possibly one of the most severe conditions encountered during the lifetime of a structure and, when all other measures for contained a fire have failed, structural integrity represents the last defence (see Ref. [1]).

Thus the provision of appropriate safety measures is one of the most important requirements in modern structural design and for that it is necessary that the designer is provided with all the required information on behaviour of concrete exposed to elevated temperatures.

Although concrete compares well to other construction materials such in fire performance when comparing combustion and thermal diffusivity; the exposure to elevated temperatures results in degradation of its mechanical properties and reduction of cross-section area through spalling. Comparing the experiences of spalling obtained from buildings and from tunnels, the key differences are the heating rate and moisture which are greater in tunnels. Added to these there are normally higher strengths and lower permeabilities in tunnel concrete linings than in buildings. These, and other factors, in combination renders tunnel concrete more susceptible to damage by spalling.

Spalling ranges from superficial damage of surface layers to explosive events which lead to an extensive removal of concrete and exposure of the core of the section and the reinforcing steel or tendons. As regards the explosive spalling, it has featured prominently in the news recently after the damage caused by the fire in the Danish Great Belt tunnel in 1994 and the fire in the Channel Tunnel in 1996. As regards the Danish fire up to 75% of the concrete liner thickness was lost after multiple spalling (see Fig. 4.1). Multiple spalling was less evident in the Channel tunnel fire despite higher estimated temperatures (1000°C in 10 hours) (see Refs. [2], [3] and [4]).

So in this chapter the first section will regard the influence of high ranges of temperatures on the concrete constituents at the meso level (i.e. cement paste and aggregates) and their properties, the second one will treat a description of the different types of spalling and its mechanisms and finally, in the third one, will be presented the modifications introduced in the numerical F.E. code NEWCON3D to study concrete behaviour under high temperature conditions.

Fig. 4.1 The Great tunnel severe spalling and steel damage after the 1994 fire.

4.2 Temperature effects on concrete mesostructure

As already explained at the mesoscale level concrete is a complex composite material made of aggregates bounded together by a softer matrix of hardened cement paste surrounding the aggregates in a weak interfacial transition zone.

Therefore concrete properties and concrete response to temperature, depend on the properties of the concrete constituents, which can be significantly altered when exposed to high temperatures. Moreover, the compatibility between the cement paste and the different types of aggregates at ambient temperatures is distorted when exposed to high temperatures (see Refs. [5]-[8]).

Generally it can be said that concrete has good properties with respect to fire resistance; however the high temperature gradients and the hygral conditions introduced during fire conditions, can result in concrete spalling , discussed in detail in Section 4.3. Consequently, the reduction of cross-section area results in reduced load-carrying capacity and potentially structural failure.

In fact heating concrete induces physical and chemical changes throughout the temperature from ambient up to melting thus influencing its thermal, hydral and mechanical properties. So, the first part of this section, will treat the changes, during heating, to the microstructure of the cement paste and the aggregates; instead the second part will describe the changes in their properties, in order to better understand the concrete behaviour under high temperature conditions.

4.2.1 Cement paste

Before presenting the cement paste behaviour at high temperatures, it is important to distinguish between the "unsealed" cement paste (allowed to dry during heating), such as in fire and the "sealed" one (permanently saturated), such as that found in nuclear reactors. In this work the first type of cement paste is considered (see [5]-[7]).

During a fire, in the cement paste, the mobility of water and the moisture diffusivity is increased; this accelerates drying and the loss of, firstly, free water, then physically bound water and followed by chemically bound water. The most important microstructural changes of cement paste during heating, are associated with the loss of physically and chemically bound water (this is evident for temperatures up to 800°C, within which the cement paste is held together by hydraulic bonds). Added to these physical effects is the chemical process of accelerated hydration. Other components of cement paste experience transformations are measured by DTA (differential thermal analysis, which measures endo- and exo- thermic reactions), GTA (thermogravimetric analysis that measures processes that results in weight loss), dilatation tests etc…

At about 80°C starts the decomposition of the cement gel (C-S-H) and the loss of chemically bound water, and the chemical conversion of the gel continues non linearly until is 70% and 100% converted (respectively at 500°C and 850°C). By Fig. 4.2 it is possible to notice that the rate of conversion reaches a peak at 150°C, decreases until 650°C and reaches a second lower peak at about 720°C (CSH tobermorite gel decomposes into β-C_2S (β-dicalcium silicate), βCS (β-wollastonite) and water). The loss of chemically bound water causes an increase in porosity and a creation of additional pore space, thus contributing to a strength reduction.

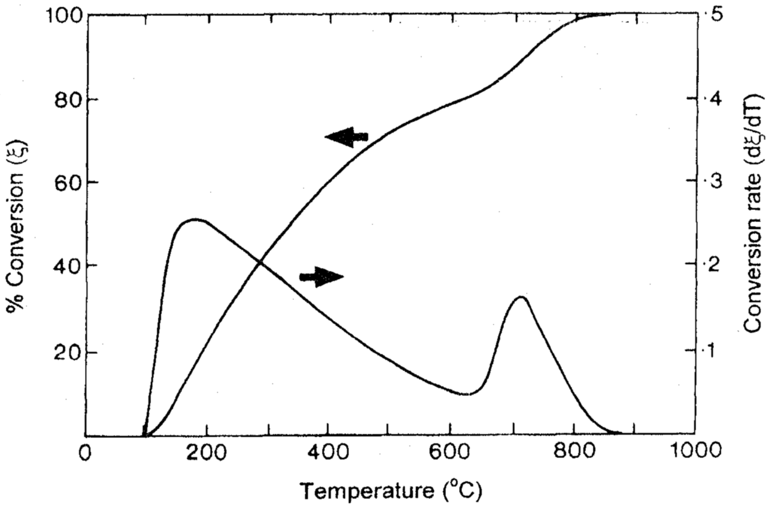

Fig. 4.2 Degree and rate of conversion of C-S-H in an idealized heated cement paste [5].

Simultaneously occurs the dissociation of CA(OH_2) into lime CA0 and water H_20; as regards this dehydration process, the rate of decomposition is zero at about 400°C, increases reaching a peak at 500°C and declines to zero at 600°C.

The total porosity of cement paste is an important feature that influences the permeability; it increases non-linearly with temperature due to the breakdown of the gel C-S-H as dehydration proceeds. Generally the increase in total pore volume after heating from 20 to 300°C is smaller than expected from weight loss measurements, instead from 300 to 600 °C is greater than one would expect from the additional loss of weight. In fact scanning electron microscopy indicates that microcracking increases significantly beyond 300°C.

The differential thermal analysis indicates that the transformations in the cement paste are largely endothermic (see Fig. 4.3): the first peak at above 100°C is due to the dehydration of various phases in hydrated cement and to the loss of evaporable water; the second peak at about 500°C is caused by the endothermic dissociation of the crystalline $Ca(OH_2)$ and the third peak may be attributed to the dissociation of $CaCO_3$, into free lime CaO and carbon dioxide $C0_2$.

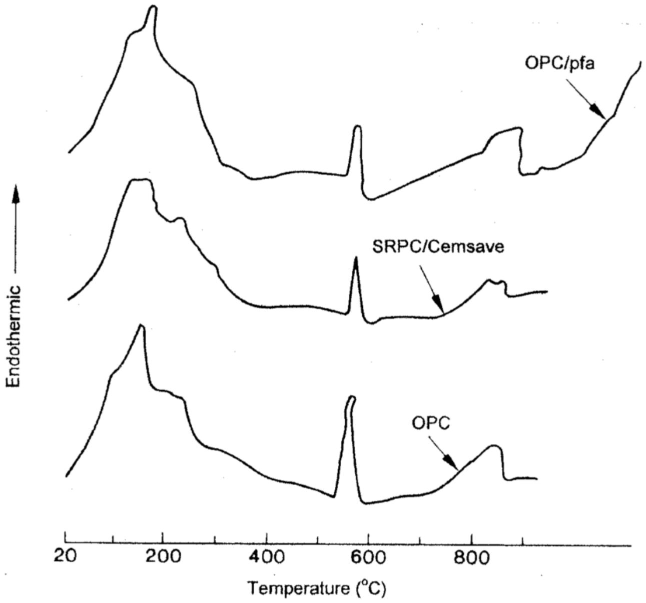

Fig. 4.3 Differential thermal analysis (DTA) of various cement pastes heated at 10°C/min in nitrogen. OPC=ordinary Portland cement; Cemsave=granulated blast furnace slag; SRPC=sulphate resisting Portland cement; pfa=pulverished fuel ash [5].

The DTA curves are not able to do a distinction between a dissociation and a phase change; this is enabled by the thermo gravimetric analysis, responding only to dissociations and transformations involving change in weight. In Fig. 4.4 are reported the curves for similar mixes as those used for DTA tests. By this figure it is possible to notice that the peaks at around 100°C and 500°C are due to the dissociation, since an increase of weight loss is detected.

Heating materials increases molecular thermal agitation and reduces surface energy; this effect which becomes significant at temperatures above about 550-600°C, corresponds to a strength reduction and leads ultimately to melting.

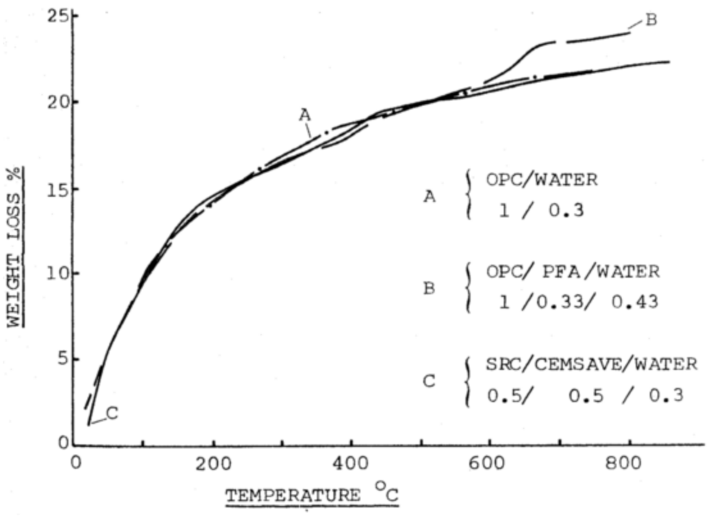

Fig. 4.4 Thermogravimetric analysis (TGA) of various cement pastes heated at 15°C/min [7].

At about 800°C, in cement paste, ceramic binding takes place and at this temperature all chemically bound water is lost; this will cause an increase in residual strength once cooled. Ultimately, cement paste starts to melt at temperatures higher than 1100°C depending upon its chemical composition (generally Portland cement paste starts to melt at 1350°C).

4.2.2 Aggregates

Aggregates, as mentioned in Chapter 2, occupy a large volume of concrete, around 60-80%; this is one of the reasons because they play a crucial role in concrete behaviour exposed to high temperatures. Another reason is that variations in their properties can have a significant effect on the performance of concrete al elevated temperature (e.g. thermal strain and thermal conductivity of concrete are governed by those of the aggregates, as anticipated in Chapter 2).

Moreover there are many types of aggregates that can be used in concrete mix design and, depending on the type, physical-chemical changes occur in the aggregates. But aggregates differ greatly in their response to heat. Therefore the choice of the aggregate is probably the most important factor in determining the thermal properties and thermal stability of the concrete in fire [5].

For example, as said by Bailey and Khoury in [6], the thermal stability of different aggregates increases in the following order: flint, Thames river gravel, limestone, siliceous, basalt, granite and gabro.

Thermal stability of aggregates is measured by thermogravimetric analysis (TGA), differential thermal analysis (DTA) and dilatometry. Aggregates that are thermally stable up to a given temperature show no weight loss, no thermic reactions and negligible residual strain.

As regards the DTA analysis, since thermally induced transformations in the aggregate (dissociation or phase change) influence the concrete behaviour on heating, a number of aggregates and sands were tested (see Fig. 4.5 and [7]).

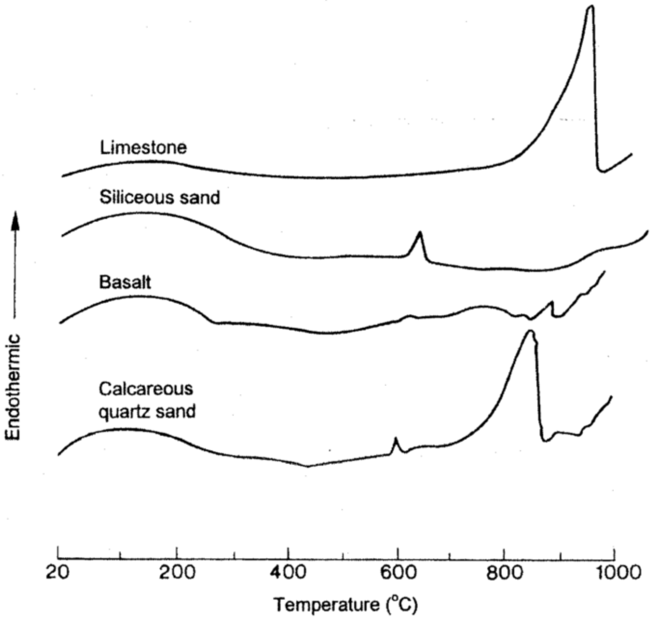

Fig. 4.5 DTA curves of various aggregates and sands, heated at 10°C/min in nitrogen [5].

In Fig. 4.5 there are essentially two endothermic peaks of interest; the first occurs at about 600°C both for the siliceous and the calcareous quartz sands instead the second one occurs at above 800°C and is the predominant feature of the limestone aggregate and the calcareous quartz sand.

As regards the first peak, it is due to the reversible endothermic crystalline α-β transformation of quartz (SIO_2) which occurs at 575°C, accompanied by a sudden volumetric expansion of about 5.7%; instead the second peak occurs at when the calcium carbonate ($CaCO_3$) starts to decompose into free lime (CaO) and carbon dioxide (CO_2). This process expels a considerable amount of CO_2 and reaches a peak at about 800°C.

By Fig. 4.5 it is also possible to notice that basalt aggregate, which contains smaller proportions of silica and lime, exhibits a relative thermal stability on heating .

The results obtained by the TGA analyses on the aggregates confirm the peaks found with DTA analysis. Indeed in Fig. 4.6 there is no weight loss in correspondence of the first peak; a large increase in weight loss occurs at about 700°C where the second peak appeared. This indicates that no dissociation takes place within the temperature range up to at least 800°C.

Finally, as seen previously for the cement paste, also the aggregates start to melt when is reached a certain temperature; depending on the type of the aggregate, the melting temperatures vary greatly (e.g. basalt 1060°C, quartzite 1700°C, pure CaO 2570°C, etc…).

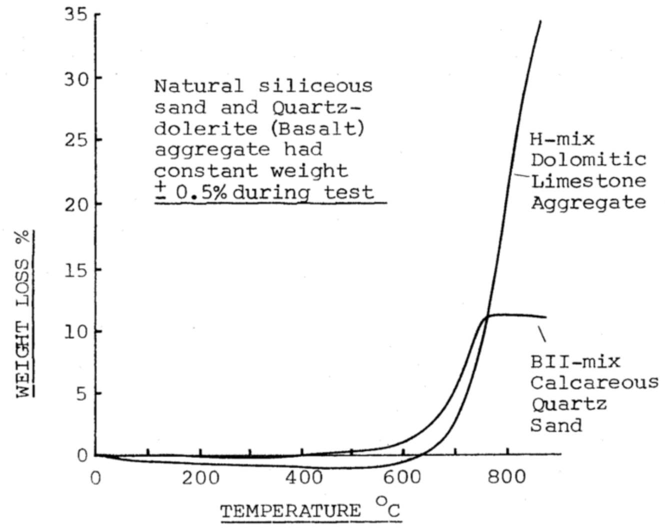

Fig. 4.6 TGA curves of aggregates heated at rate of 1.5°C/min in high purity nitrogen [7].

All the global physico-chemical processes, described separately before for cement paste and aggregates, in Portland concrete during heating are summarized in Fig. 4.7.

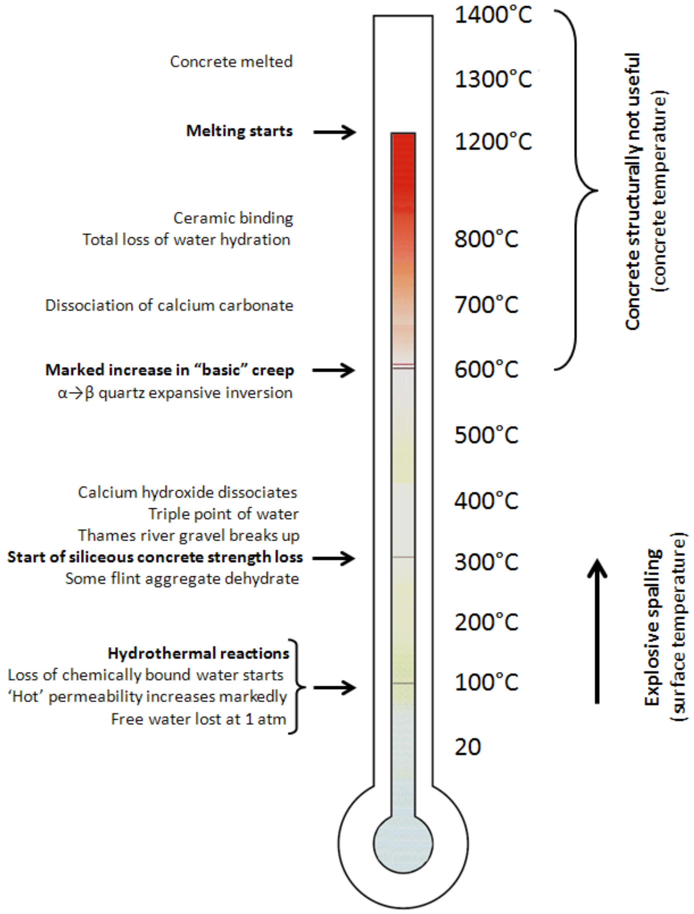

Fig. 4.7 Simplified global presentation of physico chemical processes in concrete during heating [6].

4.2.3 Properties

Compressive strength

This is a really important property because it gives an overall impression of the quality of concrete. Most concretes exhibit a strength reduction above 300°C but this is dependent by the type of the aggregate (see Fig. 4.8) and by the cement used. However, at about 550-600°C in the cement paste and concrete occur a marked increase in the basic creep; thus indicates that the temperature is critical and above this temperature concrete is not structurally useful [6].

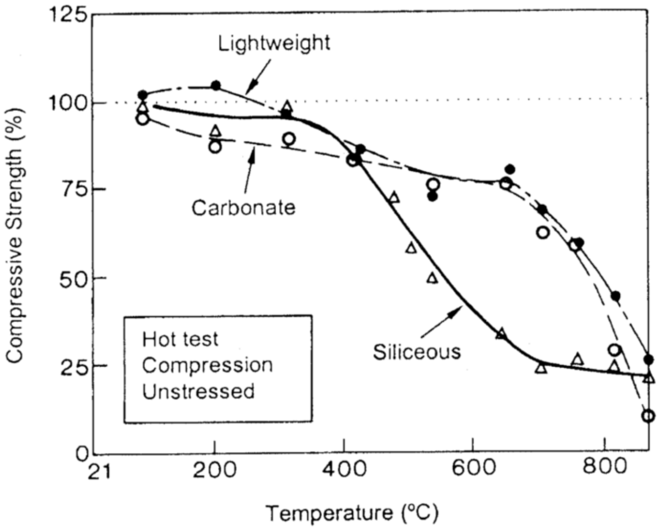

Fig. 4.8 Influence of aggregate type upon the compressive strength of concrete [5].

Elastic Modulus

The behaviour of the Young modulus during heating depends largely by the load condition [6]; indeed if we compare the results obtained for two heated concretes, with and without load applied, it is possible to notice that compressive load has a more important effect on the decline of the elastic modulus with increase in temperature (see Fig. 4.9).

The elastic modulus is also influenced by the moisture condition; considering an unsealed condition, the elastic modulus decreases for temperatures up to 80°C (minimum) and this is due to the dilation of water which reduces physical forces in the C-S-H phases. Then, for higher temperatures, water is driven off and the elastic modulus increases reaching a maximum at about 100-200°C. Compressive strength presents a similar trend.

Another influence is given by the aggregate used in concrete mix design; depending on the type there is a wide variation in the percentage reduction of the elastic modulus up to 80°C. Moreover due to thermal incompatibility with the cement paste, concretes which contain aggregates of low thermal expansion experience a greater reduction of elastic modulus than those with a higher thermal expansion.

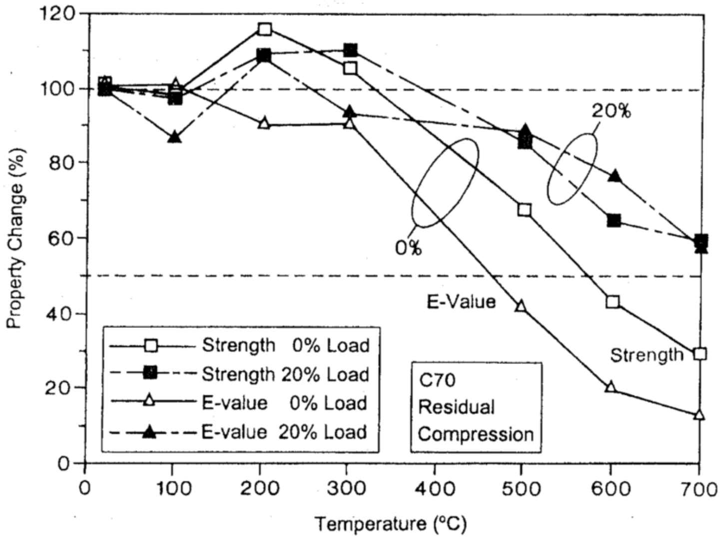

Fig. 4.9 Relative reduction of residual strength and E value for heated concrete C70 with and without load [5].

As regards the cement paste Young modulus, Harmathy and Berndt observed a decrease of elastic modulus and the curve obtained is reported in Fig. 4.10; in this figure it is possible to notice that this decline is more important after 400°C. In this paper is also investigated the change of ultimate strength of cement paste at elevate temperatures, that decreases as temperature increases. Also the Young modulus of aggregates decreases at elevated temperatures [9].

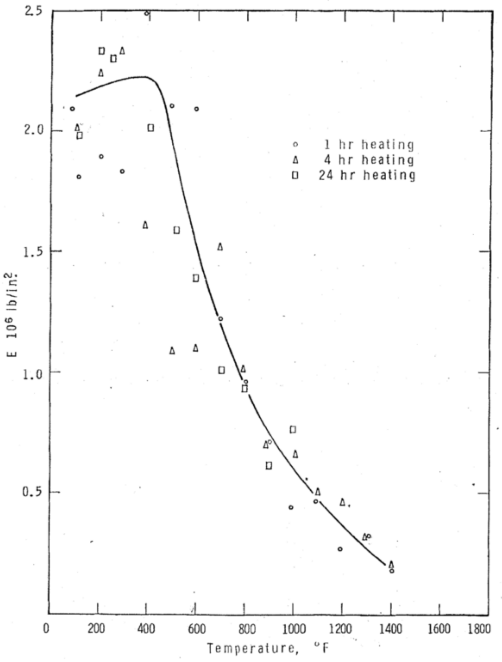

Fig. 4.9 Modulus of elasticity of Portland cement at elevated temperatures [9].

Specific heat

This thermal property is the amount of heat per unit mass required to increase the temperature of the material by 1°C.

At elevated temperatures, Harmathy [10] estimated the specific heat of idealized Portland cement pastes from theoretical considerations coupled with experimental data. It is seen that, owing to the absorption of heat in the dehydration reactions (dehydration occurs from 100°C and 850°C), the effective value of the specific heat may be several times higher than the "sensible heat capacity", which is approximately the value measurable by drop calorimetry.

Harmathy also calculated the specific heat of four types of aggregate; therefore the specific heat versus temperature relation for the anorthosite and the expanded shales yields a smooth curve because these aggregates are stable until 1000°C. Instead the specific heat of quartz aggregate shows a peak value at 575°C, when a transformation from α-quartz to β-quartz occurs.

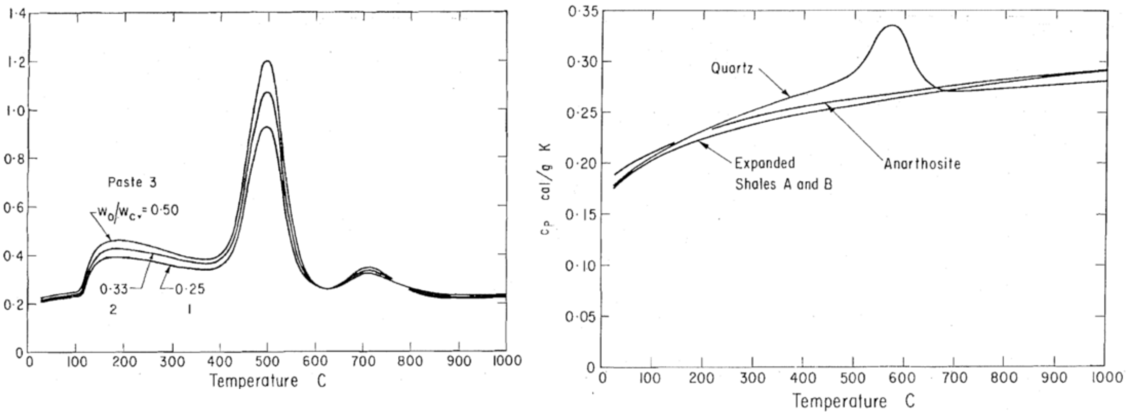

Fig. 4.10 Specific heat of cement pastes on the left and of four aggregates on the right [10].

Thermal conductivity

At normal temperatures, as already said in Section 2.2, the thermal conductivity of concrete is predominantly affected by the aggregate type and the moisture content. On average, for ordinary concrete it ranges between 1.4 and 3.6 W/m°C.

At elevated temperatures [10], for oven-dried hardened cement paste, the thermal conductivity, up to 1000°C, is not subjected to large variations (see Fig. 4.12).

Since the thermal conductivity of the cement paste doesn't vary so much, is the conductivity of the aggregates that determines the insulating quality of the concrete. Therefore, concrete aggregates such as quartzite (which have a relatively high thermal conductivity at normal temperature) have a thermal conductivity that decreases as the temperature increases [10]. Instead, for basalts and dolerites (which have a low thermal conductivity at normal temperature), with increased temperature, Kingery and McQuarrie [11] noted a slight increase in thermal conductivity (see Fig. 4.12).

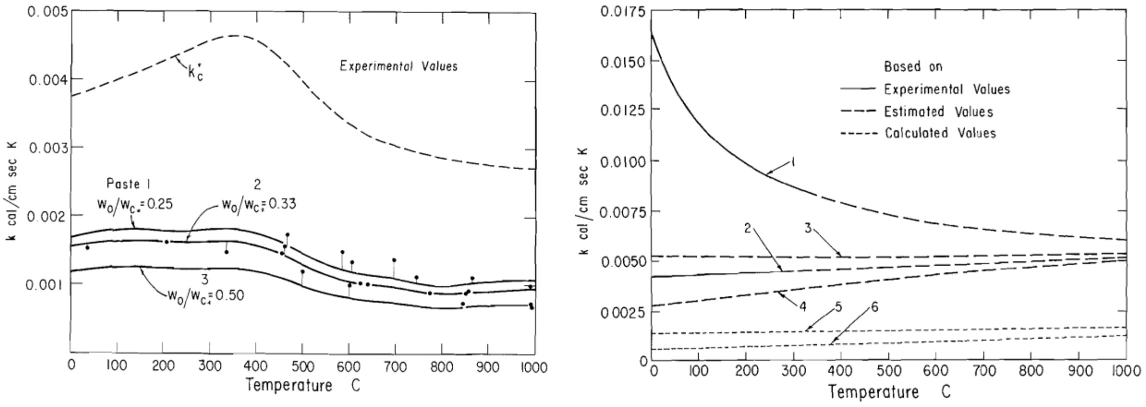

Fig. 4.11 Thermal conductivity of cement pastes on the left and of aggregates on the right [10].

Thermal diffusivity

This property represents the rate at which temperature changes within a mass can take place. It determines the temperature gradient during transient heating problem and can be calculated by this expression:

$$D = k/c\rho \qquad [4.1]$$

where k is the thermal conductivity, ρ is the density and c is the specific heat.

It shows approximately the same trend at elevated temperatures as thermal conductivity.

Thermal expansion

It is also called thermal strain or thermal dilation and represents the volume change of a material due to temperature change. This is expressed as change in length per degree of temperature change. Being typically non uniform throughout the structure, because of temperature non uniformity, stresses arise. This often leads to cracking and large spalling.

This type of expansion depends by the composition of the concrete mix (differences between the thermal expansions of aggregate and cement paste are important) and by the hygral state at the time of the temperature change.

Considering the results obtained by Khoury [7]; as regards the cement paste, during first heating it initially expands (while free water escapes), but above 70-100°C significantly shrinks (as physically and chemically bounded water escapes) and reaches a plateau between 500 and 800°C or continues to expands depending by the proportion of unhydrated cement grains present in the paste (see Fig. 4.13). It is interesting to notice that, even if all the three tested pastes show similar trends, the strain magnitude are significantly different. Moreover on first cooling all the pastes have a residual contraction. This behaviour is really different in a subsequent heating and cooling [7].

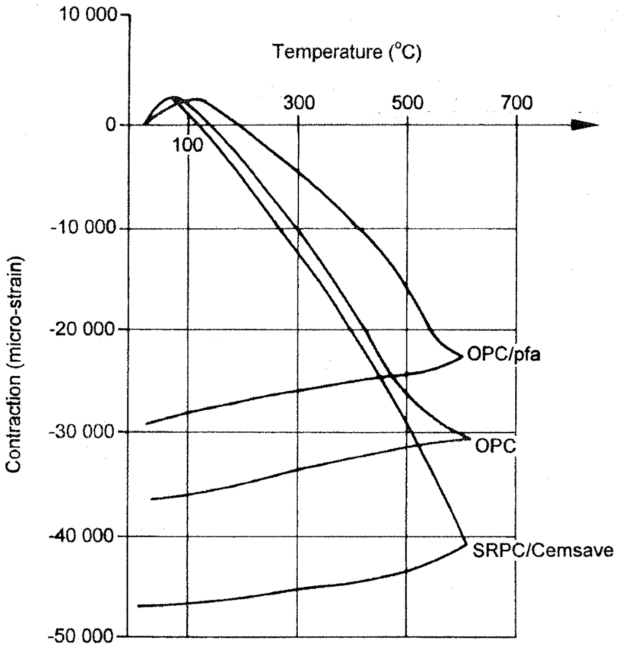

Fig. 4.12 Thermal strains of three cement pastes during first heating at 2°C/min and during subsequent cooling [5].

As regards the aggregates, they expand non linearly with increase in temperature as reported in Fig. 4.14. On first cooling from 650°C the limestone and basalt aggregates have a residual strain; this is significantly larger in the limestone one (initial heating of the limestone aggregate to that temperature results in significant damage) [7]. Gravel aggregate presents a totally different behaviour; it expands and considerably breaks up at about 350°C because of thermal incompatibility within the aggregate itself and possibly due to the dehydration of any chemically combined moisture present. The concrete made with this aggregate also disintegrates.

Considering the tests of Cruz and Guillen [12]; they report the results of thermal expansion of concrete, as well as its individual constituents: cement paste, mortar and dolomite rock aggregate (Dolomite rock). In their tests, temperature ranges between 27 and 871°C.

As regards the Portland cement paste, it expands until 149°C and then contracts from 149 to 871°C. In contrast, between 93 and 871ºC, dolomite rocks expand slightly from 27 to 93°C and expand almost linearly from 93 to 871°C. All mortars and concretes expand (see Fig. 4.15).

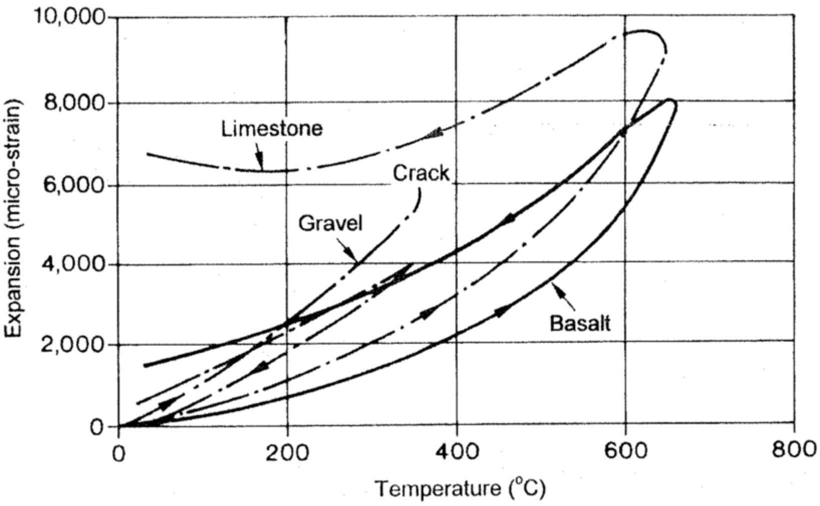

Fig. 4.13 Thermal expansion of aggregates during first heating and during subsequent cooling [5].

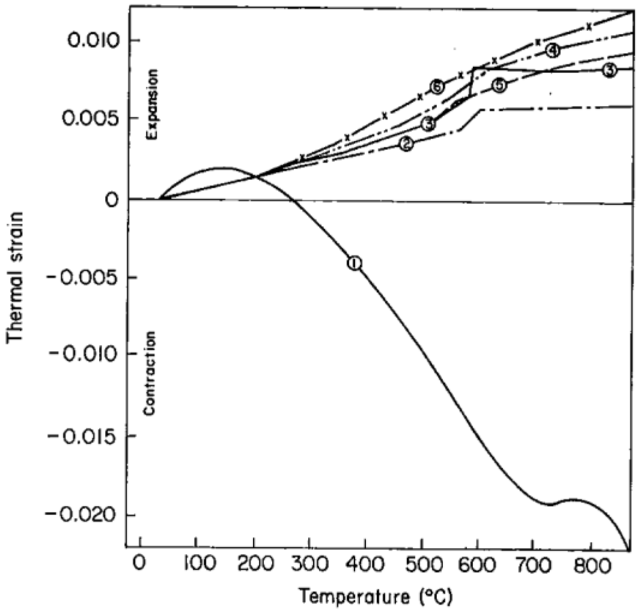

Fig. 4.14 Thermal strains evolutions of: 1, Portland cement paste; 2, Elgin sand mortar; 3, Ottawa sand mortar; 4, Elgin sand mortar and gravel concrete; 5, Elgin sand and crushed dolomite concrete; 6, dolomite rock [12].

Density

The changes in density are related to the weight changes, thermal dilation and changes in porosity. In fact these variations reflect the influences of physico chemical transformations such as the dilation up to 80°C, the loss of free and physically bound water at 100°C, the loss of chemically bound water for temperatures above 100°C, the dissociation of calcium hydroxide at 400-500°C and the de-carbonation over 600°C.

The role of aggregate is important in terms of thermal dilation and the dissociation of some aggregates such as carbonate aggregates.

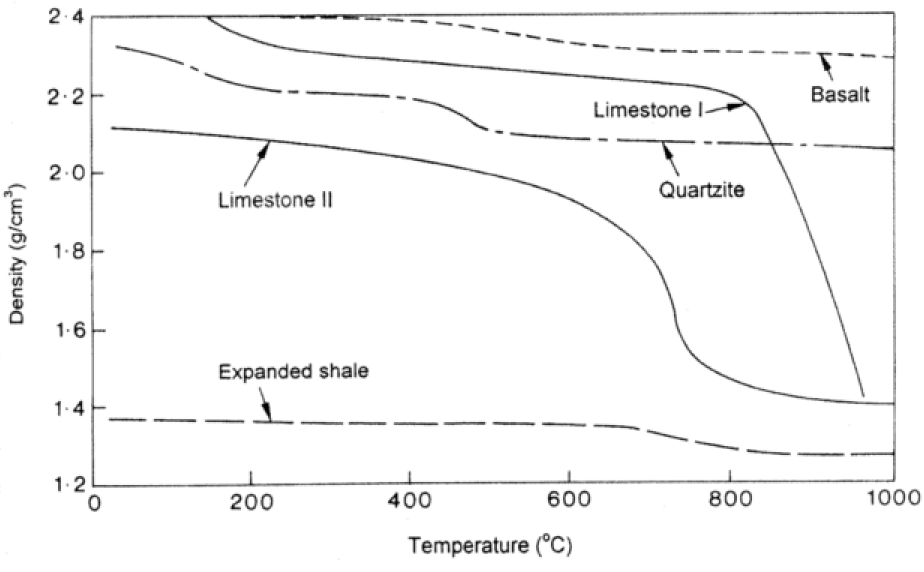

Fig. 4.15 Density of concretes with four different types of aggregates[5].

4.3 Spalling

4.3.1 Introduction

Spalling (see refs. [4] and [13]) is the separation (violent or not-violent) of pieces of concrete from the surface of a structural element when it is exposed to high and rapidly rising temperatures, as in fires. It is stochastic in nature; in fact for specimens from the same batch, and under identical conditions, some could spall while others do not. Furthermore, contradictions between the results from different authors are quite common. All this is partly due to the different experimental conditions and materials tested, the incomplete understanding of processes that contribute to spalling and the stochastic nature of spalling. Scientists have been trying to describe the different forms of spalling by the basic mechanisms which cause them. In some cases one mechanism dominates and in other cases another mechanism dominates; because of this complexity, there is no a real demarcation between one type and another type of spalling.

The division of spalling in different types will be presented in the next section.

The most dangerous type is the explosive one, because it is sudden and capable to result in a general collapse of the structure. Explosive spalling in fact is a violent form of spalling characterized by the forcible separation of pieces of concrete, accompanied by a typically loud explosive noise. It normally occurs within the first 30-40 minutes of exposure to fire and it can occur as a single explosion or a series of explosions, each removing a thin layer of concrete ranging from 100 mm to 300 mm in length and 15 mm to 20 mm in depth, capable of causing physical damage on impact.

4.3.2 Types of spalling

The division of spalling in different types can be classified as follows [3]:

- **aggregate spalling** (splitting of aggregates, popping sound);
- **corner spalling** (i.e. corners of columns or beams fall off, non-violent);
- **surface spalling** (surface layers of concrete fall out or burst out of the structural element, violent and cracking sound);
- **explosive spalling** (violent burst-out of concrete pieces characterized by sudden release of energy, violent and loud bang);
- **sloughing-off spalling** (or progressive gradual spalling, where pieces of concrete fall out of the structural elements, non-violent);
- **post-cooling spalling** (occurs after the fire is over, after cooling down or maybe even during extinguish, non-violent).

A summary of the characteristics of these different forms of spalling is reported in Table 4.1.

Table 4.1 Characteristics of the different forms of spalling (see Ref. [3]); A = aggregate thermal expansion, AT = aggregate type, D= aggregate thermal diffusivity, F_s= shear strength of concrete, F_t= tensile strength of concrete, G = age of concrete, H = heating rate, L = loading/restraint, O = heating profile, P = permeability, Q= section shape, R = reinforcement, S = aggregate size, T= max temperature, W= moisture content, W1 = moisture absorption and Z= section size.

Spalling	Probabilistic Time of Occurence	Nature	Sound	Influence	Main Influences
Aggregate	7-30 mins	Splitting	Popping	Superficial	H, A, S, D, W
Corner	30-90 mins	Non-violent	None	Can be serious	T, A F_t, R
Surface	7-30 mins	Violent	Cracking	Can be serious	H, W, P, F_t
Explosive	7-30 mins	Violent	Loud bang	Serious	H, A, S, F_s, G, L, O, P, Q, R, S, W, Z
Sloughing-off	when concrete weakens	Non-violent	None	Can be serious	T, F_s, F_t, L, Q, R
Post-cooling	During & after cooling upon absorption of moisture	Non-violent	None	Can be serious	T, F_s, F_t, L, Q, R, W1, AT

As reported in Table 4.1 many factors influence explosive spalling in concrete, such as heating rate and heating profile, temperature level reached during the explosion, section size and shape, moisture content, water curing, pore pressure, permeability of the material and mean pore radius, concrete age, concrete strength, mix and quality, type and size of aggregates etc… Their influence is extensively described in Ref. [14].

4.3.3 Significance of spalling in fire

As mentioned in the introduction and in the previous section; the extent, severity and nature of occurrence of spalling varies. In fact spalling may be insignificant in amount and consequence, such as when superficial damage occurs, or alternatively it can have a serious effect on the fire resistance of the structural element because of extensive removal of concrete which exposes the core of the section and the reinforcing steel or tendons. The consequences of spalling are very much affected by the applications for which concrete is being used.

Spalling may result in the loss of load-bearing capacity, through loss of section or loss of protection to steel reinforcement, or separating function of a concrete member and these are discussed below (see Refs. [3] and [4]):

Loss of section

In some cases, the occurrence of spalling may reduce the cross-sectional area of the concrete to such an extent that is no longer able to sustain the compressive stresses imposed upon it. The scope for such failure has been increased by current trends towards rationalisation in design and the increasing likelihood for larger design stresses.

Loss of protection to steel reinforcement

A second mechanism for load-bearing failure is that spalling of the concrete, which provides protective cover to the steel reinforcement, may result in the reinforcement reaching excessive temperatures. As the yield strength of steel is considerably reduced at elevate temperatures, spalling may hasten the steel towards yield, thus precipitating flexural failure of the concrete member. With tension in the extreme fibres governing the design of most concrete elements of structure, this form of spalling failure is quite commonly found in practice. The likelihood of flexural failure is increased by the fact that spalling and crumbling of concrete from around the reinforcement may cause loss of bond, and load-bearing failure could result from the loss of composite action. If the reinforcement becomes exposed as a result of spalling, it is heated quickly and the resistance of the section decreases at a rapid rate.

Separating function

Spalling can also affect the separating function of elements by causing holes to appear in slabs or panels thus enabling the fire to spread into other compartments. Thin slabs are particularly susceptible to such “integrity” failure.

4.3.4 Spalling Mechanism

As regards explosive spalling, there are two main mechanisms driving spalling: pore pressure spalling and thermal stress spalling. They act singly or in combination depending upon the section size, the material, and the moisture content (see Refs. [3], [4] and [13]).

Pore pressure spalling (as proposed by [15], [16] and [17]): has been predicted using a "moisture clog model" [15], "vapour drag forces model" [16] or an "idealized spherical pore model" [17]. The main factors which influence pore pressure spalling are the permeability of the concrete, the initial water saturation level, and the rate of heating. Pore pressure spalling may apply by itself only for small unloaded specimens. For larger specimens, the pore pressure will have to be considered together with both the thermal and applied load stresses before the likelihood of explosive spalling can be assessed.

Thermal stress spalling (as proposed by [18] and [19]): at sufficiently high heating rates, ceramics and dry concrete can experience explosive spalling. This is attributed to excessive thermal stresses generated by rapid heating and demonstrates that factors other than pore pressures may contribute to explosive spalling. Heating concrete generates temperature gradients that induce compressive stresses close to the heated surface (due to restrained thermal expansion) and tensile stresses in the cooler interior regions. Surface compression may be augmented by load or prestress, which are super-imposed upon the thermal stresses. However, very few concrete structures are loaded to levels where the necessary failure stress state is reached. This makes thermal stress spalling - by itself - a relatively rare (but not impossible) occurrence.

Combined thermal stress and pore pressures (as proposed by [20]): explosive spalling generally occurs under the combined action of pore pressure, compression in the exposed surface region, and internal cracking. Cracks develop parallel to the surface when the sum of the stresses exceeds the tensile strength of the material. This is accompanied by a sudden release of energy and a violent failure of the heated surface region.

The most effective methods to reduce the risk of explosive spalling include (see Ref. [21]): (a) the use of a thermal barrier, (b) employing polypropylene fibres, (c) employing an air-entraining agent, (d) using thicker sections, (e) use of low thermal expansion aggregate.

In addition, appropriate use of reinforcement could limit the extent of spalling, though not prevent the phenomenon itself. The risk of spalling is also reduced if the moisture content is low and the permeability of the concrete is high.

4.4 NEWCON3D modifications for high temperatures

The following changes to the program NEWCON3D are activated placing the parameter NHT=1 in the data file; for NHT=0 they are ignored.

4.4.1 Concrete Permeability

For temperatures exceeding 100°C , it was found, from experimental data, that permeability increases about two orders of magnitude.

This, according to Bažant (see Ref. [8]), can be explained as follows: due to the flattening of the pores surfaces to reduce the surface energy, the width of the necks, which governs the flow, increases of a factor equal to 1000 when T exceeds 100°C, allowing water to pass through the necks in a liquid or vapour state; at the same time, being negligible the volume of the necks in the total porosity, there is no a significant effect on the distribution of pores size at high temperature due to the considerable relative increase of the width of the necks.

In this way, while at room temperature the width of the neck must be related to the capillar porosity , at elevated temperatures this relation decays.

The fact that the necks should be of sub capillary sizes it is also suggested by the results of [22] that at room temperature the permeability decreases of about 20 times for a decrease of from 0.9 to 0.6. Indeed, the only reasonable explanation seems to be that the mechanism of moisture transport through the necks is the migration of water molecules in the layers of absorbed water which become thinner when the humidity decreases and therefore retain more strongly the water molecules in movement. In the light of this mechanism, it was previously proposed that below 100°C the permeability dependence from temperature was not governed by the viscosity of liquid water or steam but by the activation energy , for the migration of water molecules adsorbed along the walls of the necks.

As a result of this scheme, the permeability a can be introduced in the following form:

$$for \quad T \le 95°C: \qquad a = a_0 f_1(h) f_2(T) \qquad [4.2]$$

$$\begin{aligned} for \quad T > 95°C: \qquad & a = a_0^{'} f_3(T) \\ with: \qquad & a_0^{'} = a_0 f_2(95°C) \end{aligned} \qquad [4.3]$$

in which a_0 is the reference permeability at 25°C.

A temperature equal to 95°C it is chosen as the beginning of the transition. The function $f_1(h)$ reflects the moisture transfer in the layers of adsorbed water in the necks, and in agreement with [23]:

$$f_1(h) = \alpha + \frac{1-\alpha}{1+\left(\frac{1-h}{1-h_c}\right)^4}, \quad for \quad h \le 1 \qquad [4.4]$$

$$f_1(h)=1 \quad for \quad h>1 \qquad [4.5]$$

where $h \approx 0.75$ is the humidity transition and $\alpha \approx 1/20$ at 25°C.

If $T=95°C$, it is assumed that the necks are sufficiently large to allow the passage of water, both liquid and vapour. Therefore α is equal to 1 at 95°C, instead can be taken a linear interpolation of α if $25°C \le T \le 95°C$. In the case of an extent under 25°C, an appropriate relation is $1/\alpha = 1+19(95-T)/70$.

The permeability dependence by temperature if $T \le 95°C$ is given by an Arrhenius type equation:

$$f_2 = \exp\left[\frac{Q}{R}\left(\frac{1}{T_{0a}}-\frac{1}{T_a}\right)\right] \qquad [4.6]$$

in which T_a is the absolute temperature, Q is the activation energy for the migration along the multimolecular layers of adsorbed water into the necks and R is the gas constant. According to [23], $Q/R \approx 2700K$.

The function $f_3(T)$ must lead the leap of two orders of magnitude, between 95 °C and 105°C.

Let's imagine that this jump corresponds to the transition from the moisture transfer mechanism governed by the activation energy of adsorption to the mechanism governed by the viscosity of a water mixture of liquid and steam. If the transition is complete (around 105°C), the function $f_3(T)$ should follow the temperature dependence of the water viscosity and steam; above 105°C both vary nothing much and then, above 105°C, $f_3(T)$ should be almost constant.

All these properties can be described as:

$$f_3(T) = \exp\left(\frac{T-95}{0.881+0.214(T-95)}\right), \quad for \quad T>95°C \qquad [4.7]$$

where T is in Celsius .

Aside from the temperature and pressure effects in the pores, permeability is drastically influenced also by the hydration degree. In agreement with the available data it seems that this dependence can be well described as:

$$a_0 = a_1 10^{\sqrt{a_2/t_e}} \qquad [4.8]$$

in which t_e is the period of equivalent hydration, defined in eq. [3.41]. The values of $a_1 = 10^{-13}$ m/s, a_2 = 40 days agree with the data by Powers and Brownyard [24]. For an hardened cement paste, .the values of a_0 varies from 10^{-10}m/s to 10^{-14}m/s (see Refs. [25] and [26]).

The eqs. [4.4] and [4.5] indicate that permeability is continuous passing the saturation point $p_s(T)$; however for some types of concrete, as lean concrete used for dams, the permeability in terms of hydraulic overpressure at low temperatures can increase significantly in passing the saturation point [25].

Numerical Implementation

The eqs. [4.2] - [4.8] are introduced in the subroutine *SETD*[2] to consider the concrete permeability variation of two orders of magnitude around 100°C.

In Box. 8 are reported the modifications in the code NEWCON3D to take into account the variation of permeability at T>95°C.

```
!
! HIGH TEMPERATURE VERSION *******************************************
! ******  a=a0 · f2(95°C) · f3(T)
! ****** a0= a0 · 10√ a2 /te
!
      T25 = 25.d0+273.15d0
      T95 = 95.d0+273.15d0
      T0A    =   PROP(MAT,26) + 273.15d0
!
      FACHT1 = dEXP((TEMP-95.d0)/(0.881d0+0.214d0*(TEMP-95.D0)))          ! f3(T)
      FACHT2 = dEXP(2700.D0*(1.D0/T25-1.D0/T95))                           ! f2(95°C)
      FACHT =(0.3d0 + dSQRT(13.d0/TE)) * T95/T0A * FACHT1 * FACHT2         ! a0 · f2(95°C) · f3(T)
!
      D(1,1)  =   D(1,1) * FACHT
      D(2,2)  =   D(2,2) * FACHT
      D(3,3)  =   D(3,3) * FACHT
!
```

Box. 8 Modification of concrete permeability for T>95°C, in the subroutine SETD.

4.4.2 Creep

As is well known, the temperature effect on creep has two implications. First, at higher temperatures the hydration process, which it appears as maturation, grows more rapidly, and since for the applied loads, at older ages, the creep is smaller, this effect tends to reduce creep.

---

[2] in subroutine *SETD* the constitutive matrix for the current Gauss point is built.

Second, at higher temperatures, the velocity of breaking bonds which is responsible for creep and manifests itself in the creep parameters, it is higher. This effect tends to increase the creep and usually prevails over the first.

As already said in the effect of humidity and temperature on the rate of hydration can be considered as an alteration of the time scale, through the equivalent hydration period t_e:

$$t_e = \int_0^t \beta_T \beta_h \mathrm{d}t \tag{4.9}$$

The expression for β_T is reported in eq. [3.42] and is valid up to 100°C; above 100°C the hydration process does not advance, and above about 200°C the reverse process takes place. The dehydration, however, is not very significant below 400°C and in this field can be neglected.

As regards the compliance function for the Bažant-Baweja B3 model (see Section 3.3.4) , to consider the temperature influence it can be re-written as:

$$J(t,t') = q_1 + \phi_T \cdot f_w \cdot C_0(t,t') + C_d(t,t',t_0) \tag{4.10}$$

where ϕ_T is function of temperature:

$$\phi_T = \phi_0 \exp\left[\frac{U}{R}\left(\frac{1}{T_0} - \frac{1}{T}\right)\right] \tag{4.11}$$

in which ϕ_0 is a parameter for the given type of concrete [27] and U is the activation energy for creep velocity.

In fact the variation in viscosity due to temperature effect on creep is connected to the model of the theory of reaction velocity since the creep mechanism consists of broken links, in the solid microstructure, thermally activated. If below 100°C the dependence expressed by eq. [4.11] is obfuscated by the simultaneous effect of temperature on the hydration velocity; from 100°C to 400°C this dependence can be directly measured because the hydration effects are unimportant.

Numerical Implementation

It is considered the compliance function proposed in eq. [4.10]. So, the subroutine *CREEPB3vef*[3] was changed to consider the increase of the creep rate for higher temperature, through the coefficient ϕ_T (see Box. 9); so it has been eliminated the updating of the shifted time t_v of the strain evaluation, that played the same effect using φ_T, fixing φ_T =1 in the function *PHITI* (see Box. 10).

---

[3] in subroutine *CREEPB3vef* the compliance function of model B3 is computed, without drying part.

The inverse effect of temperature on creep of concrete that accelerates the aging, shifting the equivalent age of load, stops above 100°C s dehydration takes place; this suspension of hydration has been taken into account fixing β_T above 100°C in the function *BETATI*(see Box. 11).

```
! HIGH TEMPERATURE VERSION *******************************************
! ****** J(t,t') =q1 +ΦT ·fw . C0(t,t')
!
   FW = 0.5d0
!
   if (NHT .eq. 0) then
       CREEPV  = q1 + C0ve + C0f
   else
       if (TEMPER .ge. 100.d0) then
             FACHT = EXP (2000.d0 * (1.d0 / 373.d0 - 1.d0 / (TEMPER + 273.15d0)))
       else
                FACHT = 1.d0
       end if
       CREEPV  = q1 + FACHT*FW*(C0ve+C0f)
   end if
!
```

Box. 9 Increase of the creep rate for higher temperature in the subroutine CREEPvef, through the coefficient ϕ_T.

```
! HIGH TEMPERATURE VERSION *******************************************
!
   XA   =  X + 273.15D0
   YA   =  Y + 273.15D0
!
   if (NHT .eq. 0) then
      PHITI =  EXP(5000.D0 * (1.D0 / XA - 1.D0 / YA))
   else
      PHITI = 1.d0
   end if
!
```

Box. 10 Modification of φ_T expression if NHT=1 in the function PHITI.

```
! HIGH TEMPERATURE VERSION *******************************************
!
   XA   =  X + 273.15D0
   YA   =  Y + 273.15D0
!
   if ((NHT .EQ. 1) .AND. (Y .GT. 100.D0)) then
       BETATI = 6.77d0
   else
       BETATI =   EXP(2700.D0 * (1.D0 / XA - 1.D0 / YA))
   end if
!
```

Box. 11 Modification of β_T expression for T>100°C in the function BETATI.

4.4.3 Equation of state for pore water

For temperatures $T < 647.3K$ (critical point of water) we must distinguish between saturated and partially saturated concrete. A concrete saturation state can be referred to the value of the relative humidity h or to the degree of saturation, linked to h through the capillary pressure (Refs. [28] and [29]):

$$p_c = \frac{\rho_w RT}{M_w} \ln h \qquad [4.12]$$

in which M_w is the molecular weight of water and $\rho_w = \rho_w(p,T)$ is the liquid water density.

The liquid water density may be calculated through a linear relationship of temperature T and water pressure $p_w = p_g - p_c$ (see Refs. [31], [32] and [33]):

$$\rho_w = \rho_{w0}\left[1 - \beta_w\left(T - T_0\right) + \alpha_w\left(p_w - p_{atm}\right)\right] \qquad \left(if \quad T \geq T_{cr},\ T = T_{cr}\right) \qquad [4.13]$$

in which ρ_{w0} is the liquid water density at reference temperature T_0 and atmospheric pressure p_{atm}, β_w is the volumetric thermal expansion coefficient of water and α_w is the isothermal compression modulus of water.

Typical values of β_w are 0.68×10^{-4} K^{-1} if T = 273.15 K and 1.01×10^{-4} K^{-1} if T = 420 K; its relationship with temperature is non-linear, hence the present authors propose the following expression:

$$\beta_w\left(T\right) = 4 \times 10^{-7} e^{0.00184T} \qquad [4.14]$$

The water vapour pressure may be derived from the field of temperatures T and humidities h as follows:

$$p = h \cdot p_s\left(T\right) \qquad [4.15]$$

where $p_s\left(T\right)$ is the saturation pressure of the water vapour, that is function of temperature (see Ref. [30]).

The degree of saturation can be calculated as (see Refs. [34] and [35]):

$$S = \begin{cases} \left[\dfrac{\left(\dfrac{T_{cr} - T_0}{T_{cr} - T}\right)^N}{a^*} p_c\right]^{\frac{b}{b-1}} & T \leq T_{cr} \\ \dfrac{N}{z^{N+1}}\left(T_{cr} - T_0\right)^N T + \left(\dfrac{T_{cr} - T_0}{z}\right)^N \left[1 - \dfrac{N}{z}(T_{cr} - z)\right] & T > T_{cr} \end{cases} \qquad [4.16]$$

in which T_{cr} is the critical temperature of water, N an empirical parameter (= 1.2), z a parameter governing the transition through the critical temperature of water (0.5K), b a constant (= 2.2748) and a* is a parameter, function of temperature:

$$a^* = \begin{cases} Q_3 = 18.6237 \text{ MPa} & T \le 373.15K \\ Q_0 + Q_2 & \\ with\ Q_2 = 7 \text{ MPa}, Q_0 = (Q_3 - Q_2)\left[2\left(\frac{T-373.15}{T_{cr}-373.15}\right)^3 - 3\left(\frac{T-373.15}{T_{cr}-373.15}\right)^2 + 1\right] & T > 373.15K \end{cases} \qquad [4.17]$$

Another expression for the degree of saturation was proposed by Bažant:

$$S = h^{1/m(t)} \qquad [4.18]$$

in which the expression for $m(t)$ will be reported in eq. [4.20].

The expression in eq. [4.16] is a proposal for upgrading the Baroghel-Bouny's desorption isotherms to account for high temperature effects. Using such an approach it is possible to skip a problem arising when using Bažant's model, i.e. under the critical point of water, the water content is considered as liquid water (free water plus a small percentage of bound water), while when T overcomes the critical point, the residual water has to be considered as gas water or a monolayer of physically bound water. Differently, through this upgraded approach, it is possible to have a consistent amount of water also above critical temperature, representing the gas phase and the chemically bound water in this zone which are separately computed.

Partially saturated concrete

From experimental data it was seen that the following semi-empirical expression is acceptable:

$$\frac{w}{c} = \left(\frac{w_1}{c} h\right)^{\frac{1}{m(t)}} \qquad for\ h \le 0.96 \qquad [4.19]$$

in which

$$m(t) = 1.04 - \frac{t'}{22.34 + t'}, \qquad t' = \left(\frac{t+10}{t_0+10}\right)^2 \qquad [4.20]$$

with t expressed in °C, t_0 = 25°C, c is the (dried) cement mass per m^3 of concrete and w_1 is the saturation water content at $25^\circ C$.

Fully saturated concrete

In saturated states, the thermodynamic properties of water can be taken into account in terms of specific volume of water υ, as a function of T and p. In this way, the effect of porosity variation and of volumetric elastic expansion can be described by Powers and Brownyard formula [36]:

$$w = \frac{\left(1+3\varepsilon^{v}\right)\phi}{\upsilon} \qquad for\ h=1 \tag{4.21}$$

where

$$d\varepsilon^{v} = \frac{d\sigma^{v}}{3\bar{K}} + \alpha dt, \qquad \sigma^{v} = \phi p \tag{4.22}$$

in which φ is the porosity, ε^{v} is the volumetric strain of concrete due to the stress σ^{v}, $\bar{K}$ is the volumetric stiffness modulus, α is the coefficient of linear thermal expansion of concrete (typically equal to 12×10^{-6}°C^{-1}), and p is the pore water pressure (i.e. an average pressure of the mixture of fluids filling the voids), which takes the form

$$p = p_g - p_c - p_{atm} \tag{4.23}$$

where p_g is the moist air pressure and p_{atm} the atmospheric pressure.

A more interesting approach is presented in [29], following [37], according to which the linear strain associated with the pressure change within the pore fluid can be expressed as: $\varepsilon = \Delta pS\left[\frac{1}{3k_s} - \frac{1}{k_{ss}}\right]$

[4.24]

in which Δp is calculated by subtracting p_c calculated from eq. [4.12] prior to the temperature change from the p_c again calculated from eq. [4.12] after the temperature change, k_s is the bulk modulus of the porous solid, k_{ss} the bulk modulus of the solid skeleton of the material and S (there defined as *saturation factor*) is referable to the degree of saturation of eq. [4.16].

Numerical Implementation

The overpressure in the pores can be well approximated by the water vapour pressure (see eq. [4.15]), considering the water vapour as the dominant cause towards the entire gas phase present in the pores.

Of fundamental importance, in the analysis of stress states of elements subjected to thermal shock, will be the use of volume forces equal to the opposite of the overpressures gradient:

$$f_p = -\mathbf{grad} \quad p \qquad [4.25]$$

in which p is the water vapour pressure, given by eq. [4.15]

So, in the subroutine *STRLOA* (see Box.12) is performed the computation of the water vapour pressure, the capillary pressure, the degree of saturation (eq. [4.18]), the moist air pressure, the water pressure and the equivalent nodal forces f_p.

Moreover, in the subroutine *CALWSC* is computed the w/c reported in eq. [4.19]: at every step are summed the w/c values computed for every Gauss point multiplied by the respective volumes; dividing the summation by the total volume it is possible to obtain the mean w/c, weighted on the volume of the entire mesh (see Box. 13).

```
! HIGH TEMPERATURE VERSION *******************************************
!
  if (NHT .eq. 1) then
!
! *** OVERPRESSURES COMPUTATION(in MPa) IN THE NODES OF THE ELEMENTS
!
      PATM = 0.101325d0    !atmosferic pressure
!
! CPGR  = Constant of perfect gases [cm³*MPa/(K*mol)]
! MW      = Molecular weight of water [g/mol]
! RW0 for calculating variable water density with temperature [kg/m³]
!
      CPGR = 8.314472d0
      MW = 18.d0
      RW0 = 999.84d0
!
      do I = 1,NCN
         K = NOP(NEL,I)
         TEMPER = GASHT(1,5,K)*CU1
         UMIDIT = GASHT(1,4,K)*CURILL
         if (UMIDIT .LT. 0.d0) then
            UMIDIT = 0.d0
         end if
!
         TEMPERK = TEMPER + 273.15d0
!
! water density
!
         BETAW = 4.d0*10.d0**(-7.d0)*EXP(0.0184d0*TEMPERK)
         RW = RW0*(1.d0 - BETAW*(TEMPERK - 273.15d0))
         RW = RW*10.d0**(-3.d0)
!
! saturation pressure of the water vapour PSAT
!
         PSAT =   (TEMPER/100.d0)**4*PATM
         SPRESS(I) = UMIDIT * PSAT
!
! pressure of the water vapour GASPRS
!
         GASPRS(K) = SPRESS(I)
!
! capillary pressure [MPa]
!
         if (UMIDIT .GT. 0.d0 .AND. UMIDIT .LE. 1.d0) then
```

```
        CAPP1(I) = RW*CPGR*TEMPERK/MW*log(UMIDIT)
      end if
!
      if (UMIDIT .GT. 1.d0) then
        CAPP1(I) = 0.d0
      end if
      if (UMIDIT .EQ. 0.d0) then
        CAPP1(I) = -10.d0**10.d0
      end if
      CAPP(K) = CAPP1(I)
!
! calculation of saturation according to Bazant
! S = h**1/m(t)
! T' = ((t + 10)/(t0 +10))**2, t in °C and t0 = 25°C
! m(t) = 1.04 - T'/(22.34 + T')
!
      TPRIMO = ((TEMPER + 10.d0)/35.d0)**2.d0
      MT = 1.04d0 - TPRIMO/(22.34d0 + TPRIMO)
      SATURR(I) = UMIDIT**(1.D0/MT)
      SATUR(K) = SATURR(I)
!
! dry air density; air press [MPa]
!
      PAIR1(I) = 0.62198d0*PATM/(0.62198d0 + UMIDIT)
      PAIR(K) = PAIR1(I)
!
! moist air pressure PGG
! water pressure WATP
!
      PGG(K) = PAIR(K) + GASPRS(K)
      WATP(K) = PGG(K) - CAPP(K)
    end do
!
! computation of pressure gradient in the current Gauss point
!
    BIT = 0.d0
    BIT1 = 0.d0
    BIT2 = 0.d0
!
    do I = 1,KSIZE1
      J = (I+2)/3
      BIT = BIT + B(1,I)*SPRESS(J)
      BIT1 = BIT1 + B(2,I)*SPRESS(J)
      BIT2 = BIT2 + B(3,I)*SPRESS(J)
    end do
    GRADXP = BIT
    GRADYP = BIT1
    GRADZP = BIT2
!
! computation of the nodal forces equivalent to the pressure gradient
!
    do I = 1,KSIZE1-3,3
      PLOAD(I)     = 0.d0
      PLOAD(I+1) = 0.d0
      PLOAD(I)     = - P(I)*GRADXP*DAREA
      PLOAD(I+1) = - P(I)*GRADYP*DAREA
      PLOAD(I+2) = - P(I)*GRADZP*DAREA
    end do
!
  end if
```

Box. 12 Computation of saturation, moist air pressure, water pressure and equivalent nodal forces in the subroutine STRLOA.

4.4.4 Dehydration

The changes of the hydrated water content with temperature and the source term related to it:

$$\Delta\dot{m}_{dehydr} = \frac{\partial}{\partial t}\left(\Delta m_{dehydr}\left(T\right)\right) = \frac{\partial}{\partial T}\left(\Delta m_{dehydr}\right)\frac{\partial T}{\partial t} \qquad [4.26]$$

should be measured during laboratory tests.

For temperatures below the critical point of water, the dehydrated water content increases, when temperature increases, approximately following a step function where there is a sharp change between 200°C and 500°C.

For an ordinary concrete, if the hydration process stops around 105°C the dehydrated amount of water is small; only around 200°C this amount assumes significant values.

The expression for $\Delta m_{dehydr}\left(T\right)$ is here reported:

$$\Delta m_{dehydr} = f_s \cdot m \cdot f\left(T\right) \qquad [4.27]$$

in which f_s is stechiometric factor, *m* is ageing degree of concrete (between 0 and 1), *c* is the cement content and $f\left(T\right)$ is a function of temperature:

$$\begin{aligned} &if \quad T < 105°C \qquad && f\left(T\right) = 0 \\ &if \quad T > 105°C \qquad && f\left(T\right) = \frac{\left[1 + sin\left(3.1416/2\left(1 - 2\,exp\left(-0.004\left(T - 105\right)\right)\right)\right)\right]}{2} \end{aligned} \qquad [4.28]$$

Numerical Implementation

The eqs. [4.26]-[4.28], presented in the previous section, were implemented in the subroutine *CALWSC* for the computation of the weight loss (see Box. 13). As already mentioned in this subroutine the mean w/c is also determined, weighted on the volume of the entire mesh.

```
!
! HIGH TEMPERATURE VERSION ********************************************
!
   if (TIMA .EQ. TIN) then
      WFREE0 = 0.d0
   end if
!
   W1SUCI = 135.d0/227.d0                    ! w1/c
   WSUCIE = 0.d0                             ! w/c for element
   VOL    = 0.d0                             ! volume
!
   DUEPI  = 2.d0*piGreco
```

```
  WFREE   = 0.d0
  HYDWL   = 0.d0                          ! Δmdehydr
  WEIGHTL = 0.d0                          ! weight loss
!
  FINV = 0.65d0                           ! m
  FSTE = 0.39d0                           ! fs
  C1 = 450.d0*10.d0**(-9.d0)              ! cement content c, changed from kg/m3 to kg/mm3
!
! ***  loop over elements
!
  do M = 1,NE
     NEL = IONARY(M)
     MAT = IMAT(NEL)
!
     do J = 1,MGNG
        WSUCIG(J) = 0.d0                  ! w/c for gauss point
        HYDW2(J) = 0.d0                   ! Δmdehydr for gauss point
        DEHYDWT2(J) = 0.d0                ! d(Δmdehydr) for gauss point
     end do
!
! *** *** loop over nodes for each element
!
     do I = 1,NCN
        NODO = NOP(NEL,I)
        TEMPER = GASHT(1,5,NODO)
        UMIDIT = GASHT(1,4,NODO)
!
! calculation of f(t)
!
        if (TEMPER .LT. 105.d0) then
             FHY = 0.d0          ! f(T)
             DFHYT = 0.d0        ! df(T)/dT
        else
             FHY = (1.d0+sin(piGreco/2.d0*
    .         (1.d0-2.d0*exp(-0.004d0*(TEMPER-105.d0)))))/2.d0
              DFHYT =(piGreco*0.004d0/2.d0)*cos(piGreco/2.d0
    .         *(1.d0-2.d0*exp(-0.004d0*(TEMPER-105.d0)))) *
    .         exp(-0.004d0*(TEMPER-105.d0))
        end if
!
! calculation of Δmdehydr and d( Δmdehydr)
!
        HYDW    = FSTE * FINV * C1 * FHY
        DEHYDWT = FSTE * FINV * C1 * DFHYT
!
        HYDW1(I) = HYDW
        DEHYDWT1(I) = DEHYDWT
!
! Hydration energy =0.5 MJ/kg
!
        HYDREN = 0.5d0*10**6
!
! calculation of w/c
!
        if (UMIDIT .ge. 1.) then
             WSUCI(I) = W1SUCI
        else
             if (UMIDIT .LT. 0) then
               UMIDIT = 0.d0
             end if
           TPRIMO = ((TEMPER + 10.d0)/35.d0) ** 2                  ! T'=[(T+10)/(T0+10)]**2
           EMMETI = 1.04d0 - TPRIMO/(22.34d0+TPRIMO)              ! m(T)=1.04-(T'/(22.34+T'))
           WSUCI(I) = (W1SUCI * UMIDIT) ** (1.d0 / EMMETI)         ! w/c = (w1/c * h) **(1/m(T))
```

```
        end if
!
! *** *** *** contribute of each node at the Gauss Point J
!
        do J = 1,MGNG
           WSUCIG(J) = WSUCIG(J) + WSUCI(I) * PDUM(I,J)
!
! ------------- weight loss
!
           HYDW2(J) = HYDW2(J) + HYDW1(I)*PDUM(I,J)
           DEHYDWT2(J) = DEHYDWT2(J) + DEHYDWT1(I)*PDUM(I,J)
        end do
     end do
!
! *** *** end loop over nodes for each element
!
     do J = 1,MGNG
        WSUCIE = WSUCIE + WSUCIG(J) * DARDUM(J)
        HYDWL = HYDWL + HYDW2(J)*DARDUM(J)
!
        if (TIMA.EQ.TIN) then
!
! density from g/cm3 (see strloa) to kg/mm3
!
              WFREE0 = WFREE0 + DARDUM(J)*SATURR(J)*RW*0.1268d0*
   .       10.d0**(-9.d0)
        end if
!
        WFREE = WFREE + DAREAG*SATURR(J)*RW*0.1268d0*10.d0**(-9.d0)
!
        VOL    = VOL + DARDUM(J)
     end do
!
  end do
!
! *** end loop over elements
!
!
! calculation of  weight loss
!
   WEIGHTL = HYDWL + (WFREE0 - WFREE)
!
! calculation of the mean w/c , weighted on the volume of the entire mesh
!
   WSUCIM = WSUCIE / VOL
!
```

Box. 13 Computation of the mean w/c , weighted on the volume of the entire mesh and of the weight loss in SUBROUTINE CALWSC.

4.4.5 Damage

Until now in the F.E. code NEWCON3D the changes of concrete strength properties were expressed as functions of the mechanical damage and temperature, hence any information about the thermally induced material deterioration was not directly available.

So, similarly as done by Gerard [38] a parameter call thermo-chemical damage V has been introduced (see Ref. [2]) and it accounts for changes of material stiffness due to thermally induced micro-cracks and due to the decrease of concrete strength properties caused by the dehydration process.

The thermo-chemical damage parameter V is defined in terms of the experimentally determined evolution of Young's modulus of mechanically undamaged material E_0, expressed as function of temperature:

$$V = 1 - \frac{E_0(T)}{E_0(T_a)} \tag{4.29}$$

in which T_a is room temperature.

Material damage of concrete is considered following the scalar isotropic model by Mazars, as said in Section 3.5.2. Its Young's modulus at this temperature $E(T)$, can be obtained from the value of the mechanically undamaged material at the same temperature $E_0(T)$ and the mechanical damage parameter d as follows:

$$E = (1-d)E_0(T) \tag{4.30}$$

A total effect of the mechanical and thermo-chemical damages, to which the material is exposed at the same time, is multiplicative, i.e. the total damage parameter D is defined by:

$$D = 1 - \frac{E(T)}{E_0(T_a)} = 1 - \frac{E(T)}{E_0(T)}\frac{E_0(T)}{E_0(T_a)} = 1 - (1-d)(1-V) \tag{4.31}$$

as not just the sum of the two components of damage.

Therefore the classical effective stress concept is modified to take into account both the mechanical and thermo-chemical damage, so there is a further reduction of resistant section area due to thermo-chemical degradation:

$$\tilde{\boldsymbol{\sigma}} = \boldsymbol{\sigma}\frac{S}{\tilde{S}} = \frac{\boldsymbol{\sigma}}{(1-d)(1-V)} \tag{4.32}$$

where S and $\tilde{S}$ are the total and resistant area of the damaged material, $\boldsymbol{\sigma}$ is the tensor of nominal stress and $\tilde{\boldsymbol{\sigma}}$ is the tensor of "modified" effective stress.

Hence the stress-strain relationship is:

$$\boldsymbol{\sigma} = (1-d)(1-V)\boldsymbol{\Lambda}_0\boldsymbol{\varepsilon}^{\mathbf{e}} = (1-D)\boldsymbol{\Lambda}_0\boldsymbol{\varepsilon}^{\mathbf{e}} \tag{4.33}$$

REFERENCES

[1] Kukla Konrad K. (2010), Concrete at high temperatures: hygro-thermo-mechanical degradation of concrete, PhD Thesis, University of Glasgow.

[2] Corsi F., Schrefler B.A., Majorana C.E., Pesavento F. and Gawin D. (2006), UPTUN Upgrading of existing tunnels for fire safety – Work Package 4, Qualified and validated procedure for spalling evaluation.

[3] Fellinger J.H.H., Gambarova P., Khoury G., Santonicola F. and Majorana C. (2005), UPTUN Upgrading of existing tunnels for fire safety – Work Package 4, Damage to concrete in tunnels after fire exposure – Evaluation Report, Ed. Prof. Corsi F.

[4] Khoury G.A. and Anderberg Y. (2000), Concrete Spalling Review, Fire Safety Design.

[5] Fib Bulletin 38: Fire design of concrete structures – materials, structures and modelling (2007), State-of-art report prepared by Khoury G.A., Anderberg Y., Both K., Fellinger J., HØy N.P. and Majorana C.E.

[6] Bailey C.G. and Khoury G.A. (2011), Performance of concrete structures in fire, A cement and concrete industry publication.

[7] G. A. Khoury (1983), Transient thermal creep of nuclear reactor pressure vessel type concretes, Ph.D. Thesis, University of London.

[8] Bažant Z.P. and Kaplan M.F. (1996), Concrete at High temperatures: Materials properties ans mathematical models, Longman.

[9] Harmathy T.Z. and Berndt (1966), Hydrated Portland Cement and Lightweight Concrete at Elevated Temperatures, ACI, 63, pp. 93-112.

[10] Harmathy T.Z. (1970), Thermal properties of concrete at elevated temperatures, ASTM Journal of Materials, pp. 47-74.

[11] Kingery W.D. and McQuarrie M.C. (1954), Thermal conductivity: I, Concepts of measurement and factors affecting thermal conductivity of ceramic materials, J. Am. Ceramic Soc., 37, pp. 67-72.

[12] Cruz C. R. and Gillen M. (1980), Thermal expansion of Portland cement paste, mortar and concrete at high temperatures, Fire and materials, 4 nº2, pp. 66-70.

[13] Majorana C.E., Salomoni V.A., Mazzucco G. and Khoury G.A. (2010), An approach for modeling concrete spalling in finite strains, Mathematics and Computers in Simulation (Special Issue), 80(8), pp. 1694-1712.

[14] Khoury G.A. (2006), Spalling Review, UPTUN Project, Lausanne, (technical report).

[15] Shorter G.W. and Harmathy T.Z. (1965), Moisture Clog Spalling. Proc. Institution of Civil Engineers, 20, pp. 75-90.

[16] Meyer-Ottens, C. (1972), The question of spalling of concrete structural elements of standard concrete under fire loading, PhD Thesis, Technical University of Braunschweig, Germany.

[17] Akhtaruzzaman A.A. (1973), The effect of transient and steady state temperatures on concrete, PhD Thesis, Imperial College, London.

[18] Saito H. (1965), Explosive spalling of prestressed concrete in fire, Occasional Report n°22, Building Research Institute, Japan.

[19] Dougill J.W. (1972), Models of failure of concrete panels exposed to high temperatures, Magazine of Concrete Research, 24(79), pp.71-76.

[20] Zhukov V.V. (1975), Explosive failure of concrete during a fire, Translation n° DT 2124, Joint Fire Research Organisation, Borehamwood.

[21] Khoury, G.A. (2008), Passive fire protection of concrete structures, ICE Proceedings Structures & Buildings, Volume 161, Issue 3, pp. 135-145.

[22] Bažant Z.P. and Thonguthai W. (1978), Pore pressure and drying of concrete at high temperature, J Eng Mat Div 1978, ASME, 104, pp. 1058-1080.

[23] Bažant Z.P. and Najjar L.N. (1972), Nonlinear water diffusion in non-saturated concrete, Mat Str, 5(25), pp. 3-21.

[24] Powers T.C. and Brownyard T.L. (1947), Studies of the physical properties of hardened portland cement pastes, Proc. Am. Concr. Inst., ACI Journal, 41, pp. 845-880.

[25] Bažant Z. P. (1975), Pore pressure, uplift and failure analysis of dams, Internationa Commission on Large Dams, Swansee, England.

[26] Neville A.M. (1973), Properties of concretes, A Halsted Press Book, John Wiley and Sons, New York.

[27] Bažant Z.P. and Panula L. (1978-1979), Practical prediction of time-dependent deformation for concrete, Materials and Structures, (RILEM, Paris). Part I and II , 11, N. 65, (1978), pp. 302-327; Part III and IV, 11, N. 66, (1978), pp. 415-434; Part V and VI, 12, N. 69, (1979), pp. 169-183.

[28] Gawin D., Majorana C.E. and Schrefler B.A. (1999), Numerical analysis of hygro-thermal behaviour and damage of concrete at high temperature, Mech Coh Frict Mat, 4, pp. 37-74.

[29] Grasley Z.C. and Lange D.A. (2007), Thermal dilation and internal relative humidity of hardened cement paste, Mat Str 2007, 40, pp. 311-317.

[30] Cavallini A. and Mattarolo L. (1990), Termodinamica applicata, CLEUP, Padova.

[31] Reid R.C., Prausnitz J.M. and Bruce E.P. (1987), The properties of gases and liquids, Mc Graw-Hill, New York.

[32] Bear J. (1988), Dynamics of fluids in porous media, Dover, New York.

[33] Forsyth P.A. and Simpson R.B. (1991), A two-phase, two-component model for natural convection in a porous medium, International Journal for Numerical Methods in Fluids, 4, pp. 655-682.

[34] Baroghel-Bouny V., Mainguy M., Lassabatere T. and Coussy O. (1999), Characterization and identification of equilibrium and transfer moisture properties for ordinary and high-performance cementitious materials, Cem Con Res, 29, pp. 1225-1238.

[35] Majorana C.E. (2007), Tables of physical and thermodynamic properties of fluids - Tables of physical and thermodynamic properties common to all concretes, private communication.

[36] Powers T.C. and Brownyard T.L. (1947), Studies of the physical properties of hardened portland cement pastes, Proc. Am. Concr. Inst., ACI Journal, 41, pp. 845-880.

[37] Bažant Z.P., Chern J.C., Rosenberg A.M. and Gaidis J.M. (1988), Mathematical Model for Freeze-Thaw Durability of Concrete, J Am Cer Soc, 71(9), pp. 776-83.

[38] Gerard B., Pijaudier –Cabot J. and Laborderie C. (1998), Coupled Diffusion-Damage Modelling and the Implications on Failure due to Strain Localisation, Int. J. Solids Structures, 35, pp. 4107-4120.

5 NUMERICAL ANALYSES

In this chapter are reported numerous analyses at the macro and the meso scale level, in order to highlight the importance of the individual components of concrete in the global hygro-thermo mechanical behaviour.

This part will be so structured:

- a first part where is investigated the role of the ITZ on the hygro-thermal response of concrete at medium temperatures, comparing the results obtained at the meso scale level, with and without the presence of the ITZ;

- a second part where is investigated the visco-damaged behaviour of concrete at the meso level, in order to understand the influence of ITZ and aggregates on the overall mechanical behaviour at medium temperatures. In fact, these two components are crucial for defining a realistic structural response as well as damage scenarios that allows for defining an appropriate concrete mixture to withstand spalling. Particularly Model B3 and Mazars' damage law have been chosen and implemented in NEWCON3D when considering creep and damage respectively;

- and finally the study of concrete under high temperature conditions, in order to catch the "shape effect", comparing columns of different section at the macro level, and the crucial role of aggregates and the ITZ for spalling predictions at the mesolevel, one of the main objectives of this thesis.

5.1 Hygro-thermal response of concrete

These first tests allow for understanding the contribution of each component at the meso level to the whole hygro-thermal response. Therefore in this section will be presented two tests, one without ITZ and the other one with a more refined mesh and the presence of ITZ, in order to capture the fundamental role of the aggregates and the transitional zone.

As regards the analysis in absence of the ITZ, a cubic concrete sample of 100×100×100 mm3 has been considered, whose discretization is characterized by hexahedral elements; the adopted one is reported in Fig. 5.1. By this figure and by Fig. 5.2 it can be noticed that for these first studies has been adopted a symmetrical distribution of aggregates of three dimensions: 30 mm, 20 mm and 15 mm. This type of discretization has been chosen for sake of simplicity, being this one the first model realized at the mesolevel and analysed using NEWCON3D. Even if, as will be seen later, it already provides very promising results for the hygro-thermal fields and the role of the aggregates (and in the subsequent analysis of the ITZ) is evident; in the further analyses this will be modified in order to obtain a more realistic model, with a more refined mesh and a random aggregate distribution and dimension (see Section 2.1).

The main material data for both cement paste and aggregates are reported in Table 5.1; as can be seen, in this application we chose (taking in consideration the characterization of the different phases reported in Section 2.2) aggregates characterized by a higher Young modulus and a very low permeability if compared to the cement paste. Moreover they are assumed more thermally conductive and with a lower thermal expansion coefficient.

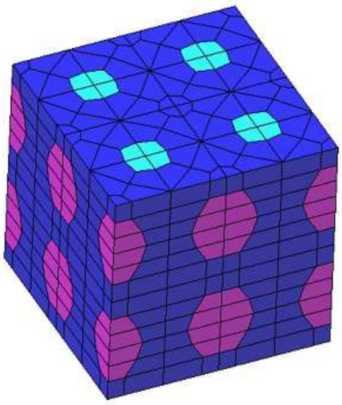

Fig. 5.1 Adopted discretization for the meso-scale analysis without ITZ.

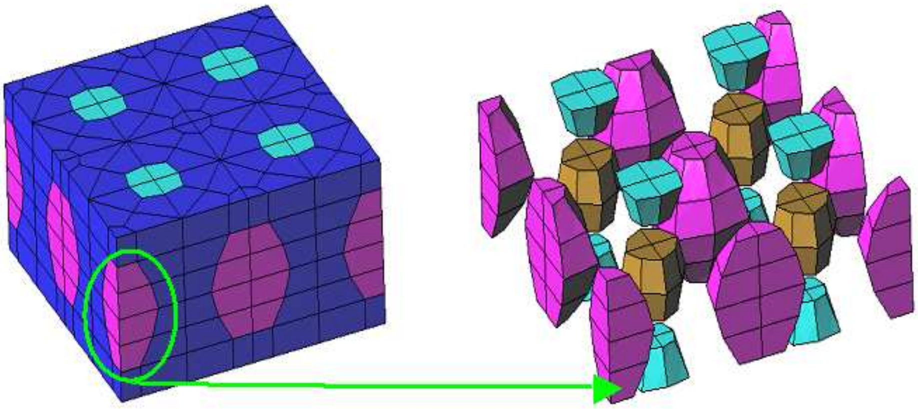

Fig. 5.2 Half sample and representation of the symmetric distribution of aggregates (different colours for different sizes).

Table 5.1 Material data for the meso-scale analysis without ITZ.

Components / Properties	Cement Paste	Aggregate
Elastic Modulus [MPa]	28000	50000
Poisson's Ratio	0.20	0.20
Reference diffusivity along x, y and z [mm^2/d]	40	0
Thermal capacity [N/(mm^{2}K)]	2	2
Heat conductivity along x, y and z [N/(d K)	110000	170000
Thermal expansion coefficient of solid	0.000012	0.000004

The sample has been supposed to be initially close to a saturated state, with (dry) aggregates fully surrounded by cement paste, and submitted to a temperature of 50°C on each external face.

As shown by Fig. 5.3 and Fig. 5.4 the sample appears to be completely heated just after 33’, but the major part of the volume is still in a partially saturated state even after 3 days.

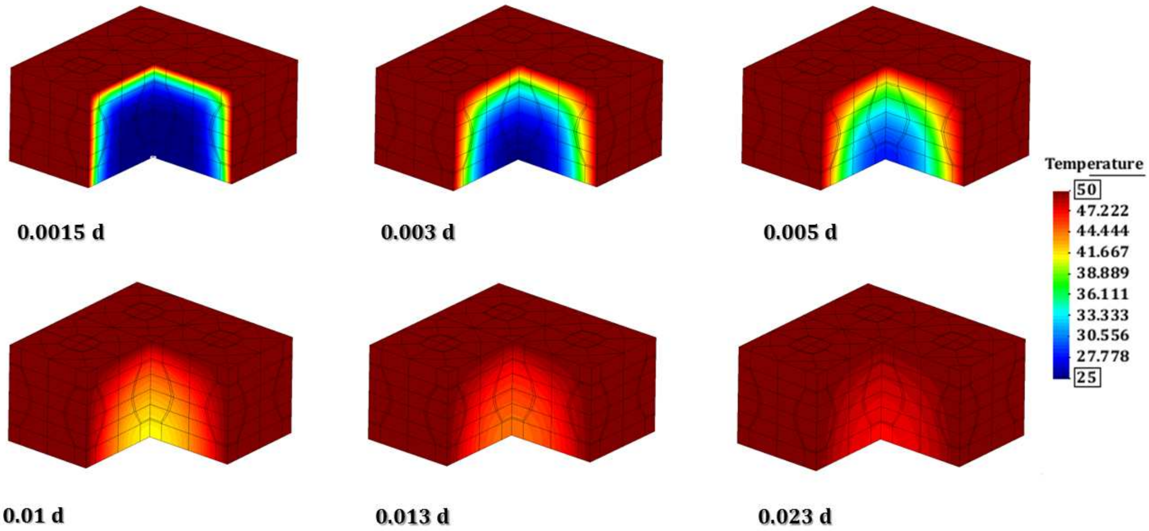

Fig. 5.3 Evolution of temperature on the meso-scale concrete sample (without ITZ; half sample).

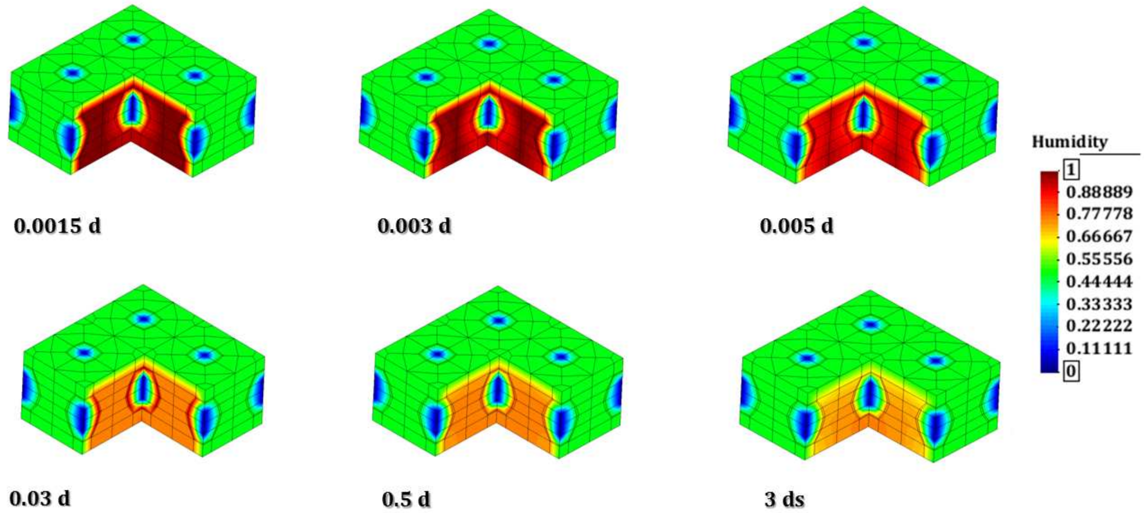

Fig. 5.4 Evolution of relative humidity on the meso-scale concrete sample (without ITZ; half sample).

Considering three representative nodes (one node inside the aggregate, one on the interface between cement paste and aggregate and the last one in the cement paste) of the sample and comparing their temperature distribution (see Fig. 5.5), it is possible to notice that the temperature increases slightly more rapidly in the aggregates, which have a higher thermal conductivity, inducing the interface to desaturate and causing thermo-diffusion of water vapour towards the colder zones.

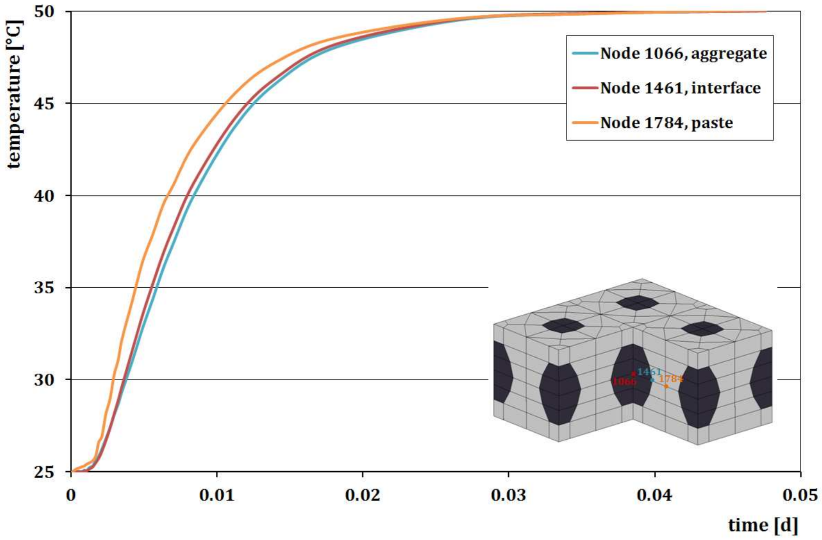

Fig. 5.5 Temperature distribution for three representative nodes of the sample.

On the other side, as regards the relative humidity behaviour, in correspondence of the interface there is a first evident increase in humidity, caused by the presence of aggregates that constitute a physical obstacle to humidity fluxes, accompanied by a decrease in the cement paste, due to thermal gradients. Then, before reaching equilibrium, the situation is reversed and humidity flows tend to become equally distributed between the aggregates surface and the cement paste (see Fig. 5.6).

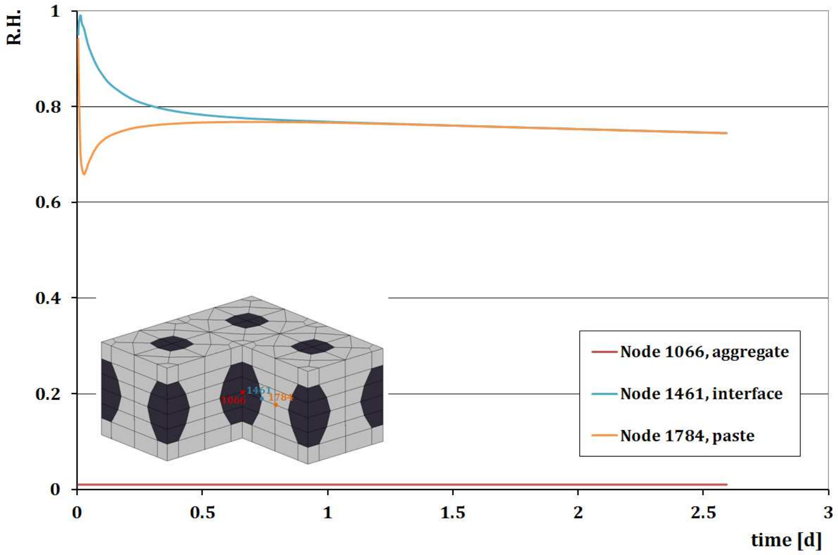

Fig. 5.6 R.H. distribution for three representative nodes of the sample.

The second numerical example deals with another cubic concrete sample of 100×100×100 mm^3 with a symmetric distribution of aggregates of three different sizes and a more refined mesh (928 hexahedral elements and 4625 nodes) and the presence of the Interfacial Transition Zone (the adopted discretization for half sample is represented in Fig. 5.7); the main material data for cement paste, ITZ and aggregates are reported in Table 5.2.

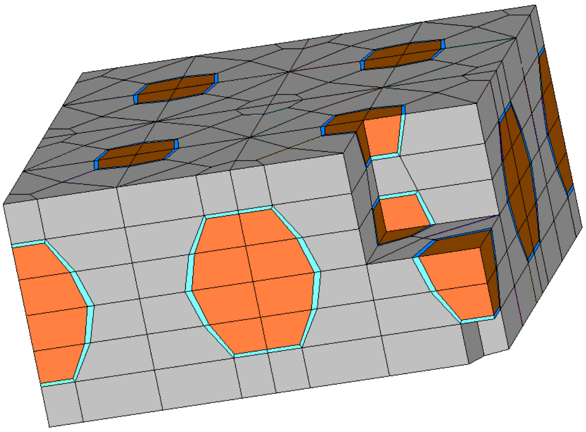

Fig. 5.7 Adopted discretization for the meso-scale analysis with ITZ (half sample).

Table 5.2 Material data for the meso-scale analysis with ITZ.

Components / Properties	Cement Paste	ITZ	Aggregate
Elastic Modulus [MPa]	20000	67000	50000
Poisson's Ratio	0.20	0.20	0.20
Reference diffusivity along x, y and z [mm^2/d]	40	80	0
Thermal capacity [N/(mm^{2}K)]	2	2	2
Heat conductivity along x, y and z [N/(d K)	110000	220000	170000
Thermal expansion coefficient of solid [1/K]	0.000012	0.000012	0.000004

Again, the sample has been supposed to be initially close to a saturated state and heated on the external surfaces up to 50°C, but differently from the previous example the (dry) aggregates are fully surrounded by an interfacial transition zone (ITZ). The presence of this zone influences the temperature and humidity fields because of its lower density and its higher porosity compared with that of the cement paste (see Table 5.2). Whereas the temperature evolution is very similar to the previous analysis, the effect of ITZ is particularly evident on the sample's hygral state; differently from what shown before, if we consider again three representative nodes in the sample (one node inside the aggregate, one in the ITZ and the last one in the cement paste), it is possible to notice that a higher diffusivity of the ITZ pushes water flows towards the cement paste, hence increasing its saturation level (see Fig. 5.8). For a better comprehension of this phenomenon, a comparison of the evolution of relative humidity along a reference line for the same sample, with or without ITZ is reported in Fig. 5.9.

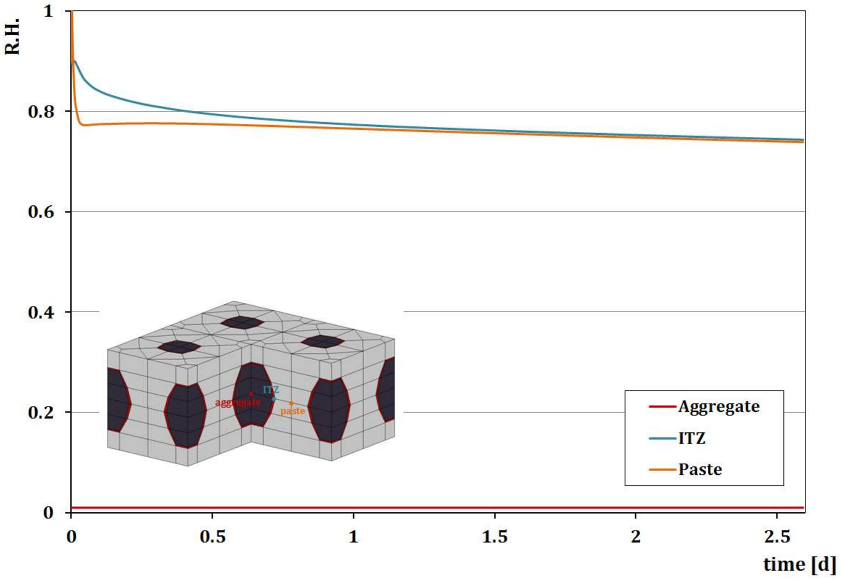

Fig. 5.8 R.H. distribution for three representative nodes of the sample, with ITZ.

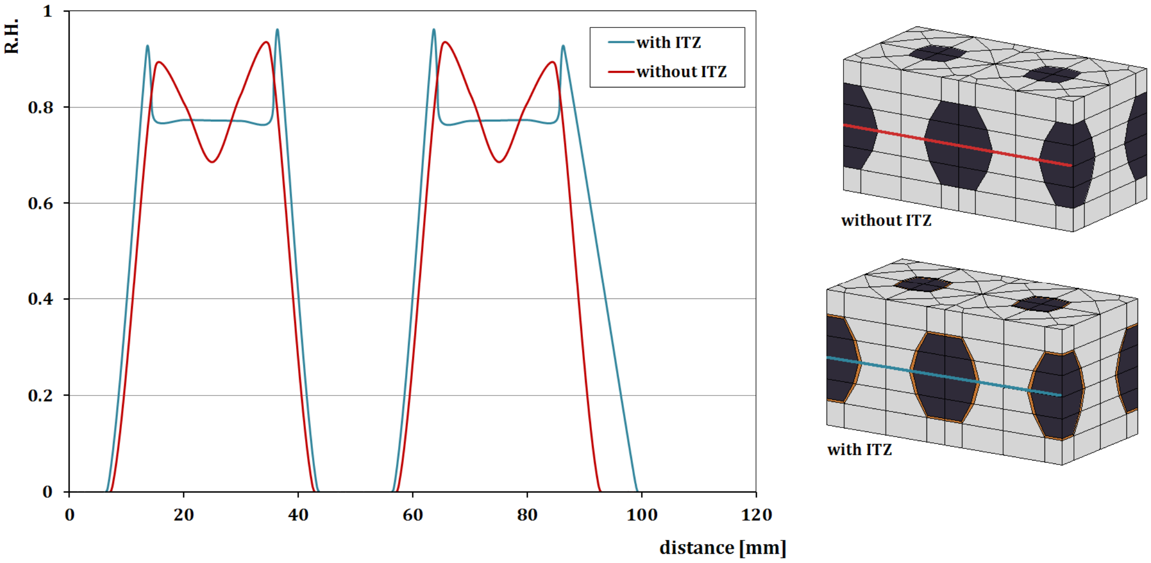

Fig. 5.9 Evolution of R.H. along a reference line for the 2 samples, with and without ITZ.

5.2 Thermo-hygro-mechanical response of concrete as viscoelastic damaged material

In the second part of the analyses, the visco-damaged behaviour of concrete at the meso level is studied, in order to understand the crucial role of aggregates and ITZ for defining a realistic structural response as well as damage scenarios. As regards creep, as already explained in Section 3.3.4, it has been upgraded in NEWCON3D, substituting the Double Power Law with Model B3, a new creep model developed by Bažant and Baweja in 1995.

Therefore this section will be so structured: a first part where is presented the validation of Model B3 within NEWCON3D to fit experimental tests at the macro-level; then two tests, one without and one with the presence of the ITZ, where this new creep model is adopted to perform predictive creep and shrinkage analyses at the meso-level. Additionally the last part is a study of the damaged behaviour of concrete at the meso-level in order to understand the influence of ITZ, the weakest region of the composite material, on the overall mechanical behaviour.

Model B3 calibration

To calibrate Model B3 in NEWCON3D, the tests by L'Hermite et al. (see Ref. [1]) have been taken as reference; particularly, a 7×7×28 cm3 concrete prism has been considered, with the same characteristics as reported in literature (see Ref. [2] (part III) and see Table 5.3). Moreover this specimen is firstly kept in water for 2 days (this means that during this period the sample is subjected to basic creep only) and then, from t0 = 2 days, is exposed to drying, i.e. to an environmental relative humidity of 50% and an environmental temperature equal to 20°C (therefore, by this time the specimen cured in water is subjected also to drying creep).

Table 5.3 Parameters for model calibration.

Elastic Modulus *E*[MPa]	28522.1
f_{cm28} [MPa]	36.3
Cement content *c* [kg/m^3]	350
Water content *w* [kg/m^3]	171.5
Aggregate-cement ratio *a/c*	4.82
Age at the start of drying t_0 [d]	2
Age of loading *t'* [d]	7 - 28 - 90
Axial compressive stress [MPa]	9.07
Environmental relative humidity	50%
Environmental temperature [°C]	20

The model assumes a homogeneous concrete sample, which is additionally loaded by an axial compressive stress of 9.07 MPa and three different loading times are considered: 7, 28 and 90 days. The mesh adopted, composed by 512 20-node brick elements and 2673 nodes, in NEWCON3D is reported in Fig. 5.10; as can be seen we studied only one eighth of the specimen, thanks to the symmetry of the prism. By this figure it is possible to notice the presence of elements of different colour on top and externally: the elements on top represent an infinitely rigid layer which allows to distribute uniformly the load applied; instead the external ones, are "fictitious" elements (i.e. with zero elastic modulus and with a very high diffusivity and thermal conductivity) that allow to apply the Dirichlet boundary condition so as not to generate oscillations due to the change in humidity from the inside to the outside of the specimen.

In Fig. 5.11 are reported the curves of the compliance function (including drying creep), numerically obtained via the code once Model B3 has been implemented. Three different loading times are considered (7, 28 and 90 days) and a comparison with the curves given by Bažant ([2] part III) is depicted, showing a good agreement between numerical and experimentally based results.

Additionally, having replaced the spatial averages of pore relative humidity $H(t)$ and $H(t')$ within drying creep with the current relative humidity obtained at each time step from the coupled **u**-**H**-**T** system of equations, it has been possible to effectively estimate the humidity variation contribution on the creep term: by Fig. 5.12 it is possible to notice how the result obtained using the spatial averaged humidity is a media of the other results; this gap can be clearly more important when bigger concrete samples are considered. Moreover it is important to keep in mind that we achieved these differences considering concrete as an homogeneous material; at the meso-level these deviations are much more important, being the different components characterized by different values of permeability.

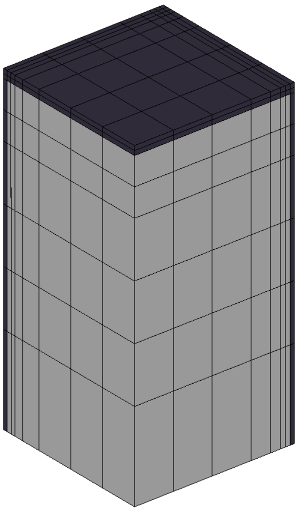

Fig. 5.10 Adopted discretization for the calibration of Model B3, an eighth of the entire sample for symmetry.

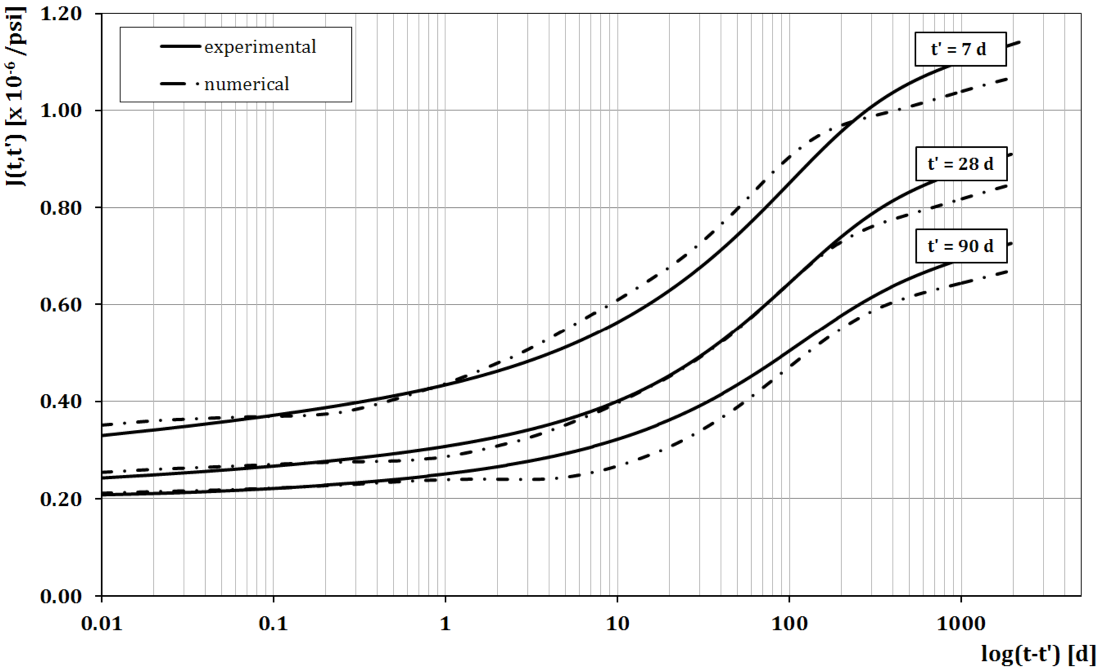

Fig. 5.11 Comparison between the experimental-based and the numerical results obtained via NEWCON3D (dashed lines).

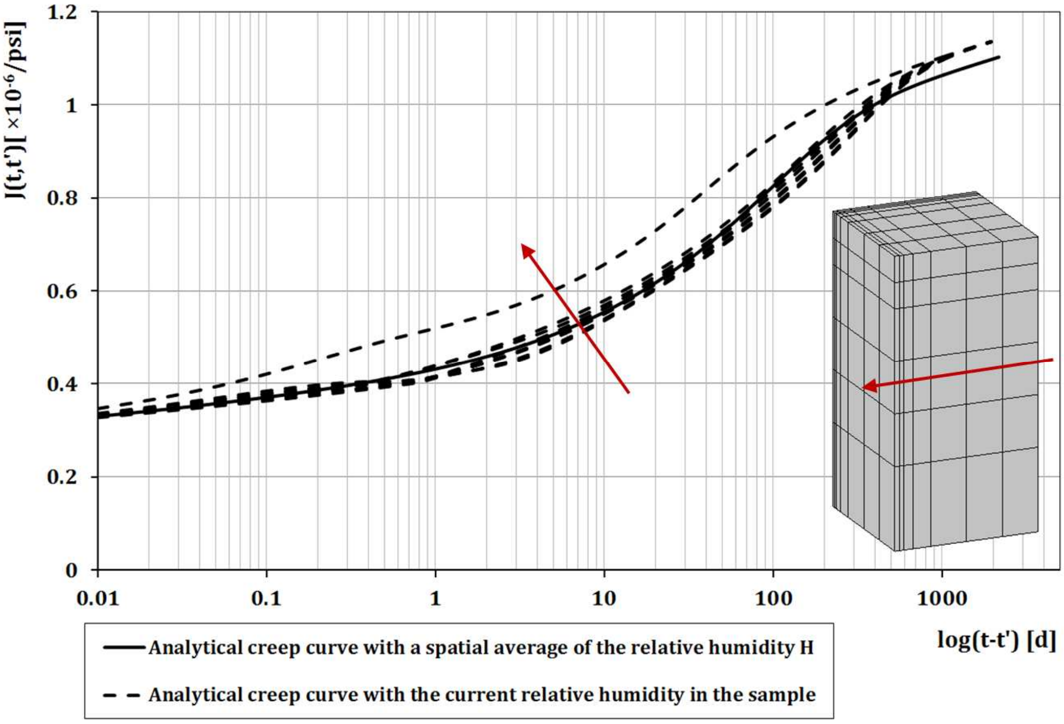

Fig. 5.12 Comparison between analytical creep curves obtained with the spatial average relative humidity (solid line) and with the current relative humidity (dashed lines).

Coupled THM and viscoelastic model validation

If concrete is considered as a composite material made of cement paste and aggregates, not including ITZ, the only phases subjected to creep is cement paste, whereas aggregates behave elastically, as reported in Section 3.3.6.

The adopted parameters in this analysis are listed in Table 5.4; as previously seen in the hygro-thermal analyses of concrete at the mesolevel, also here the cement paste is characterized by a lower Young modulus, a lower thermal conductivity and a higher permeability if compared to the aggregates.

Table 5.4 Material data for the meso-scale analysis without ITZ.

Components **Properties**	**Cement Paste**	**Aggregate**
Elastic Modulus [MPa]	20000	67000
Poisson's Ratio	0.20	0.20
Reference diffusivity along x, y and z [mm^2/d]	20	0
Thermal capacity [$N/(mm^2K)$]	2	2
Heat conductivity along x, y and z [N/(d K)	144288	220320
Thermal expansion coefficient of solid	0.000012	0.000004

For this analysis at the mesolevel (and also for the next one, where the transition zone is included) tests by L'Hermite et al. are again taken as reference; hence the sample is first subjected to basic creep only (specimen kept in water) and subsequently to drying creep (specimen cured in water; at t_0 = 2 days exposed to drying at 50% relative humidity and 20°C). The sample is additionally loaded by an axial compressive stress of 9.07 MPa at time t' = 7 days. Also in this analysis, for sake of simplicity we studied only one eighth of the specimen

The adopted discretization is reported in Fig. 5.13 **a**; this mesh, which includes also an infinitely rigid layer for a uniform distribution of the load applied on top, is characterized by 1275 hexahedral elements, 6250 nodes and a random aggregates distribution which occupies about the 50% of the total volume of the specimen.

If we study the evolution of the relative humidity along a line, indicated in Fig. 5.13 **b** (in which A indicates the side of the specimen exposed to the environmental conditions, instead B is the inner side; so the flux of humidity going from B to A), passing through an aggregate; it is possible to notice the physical barrier exerted by the aggregate towards the flux of humidity. Although some initial result in this direction was already found in the previous hygro-thermal analyses, this is more clear in Fig. 5.14, where is reported the humidity evolution of this line at different times. Indeed, being the aggregate an obstacle to the flux of humidity due to its very low permeability, in its proximity is visible an increase of the relative humidity level (this is more visible for longer times such as 24.3 days and 229.3 days).

Moreover, comparing the relative humidity evolutions along this line at the meso and at the macro-scale (for this comparison the mesh adopted at the macro level is the same of the mesoscale, but this time the material is only one) levels, some slight delay in drying can be noticed; as indicated in Fig. 5.15: in fact, the effect due to the inclusion of aggregates is not only local but has even repercussions on the global humidity distribution, as well as on its temporal variation. It's important to keep in mind that these hygral barriers due to the presence of aggregates can be seen only if we model at this level; so for these analyses a meso-scale approach is fundamental, being the macro-scale modelling not representative of the real behaviour of concrete.

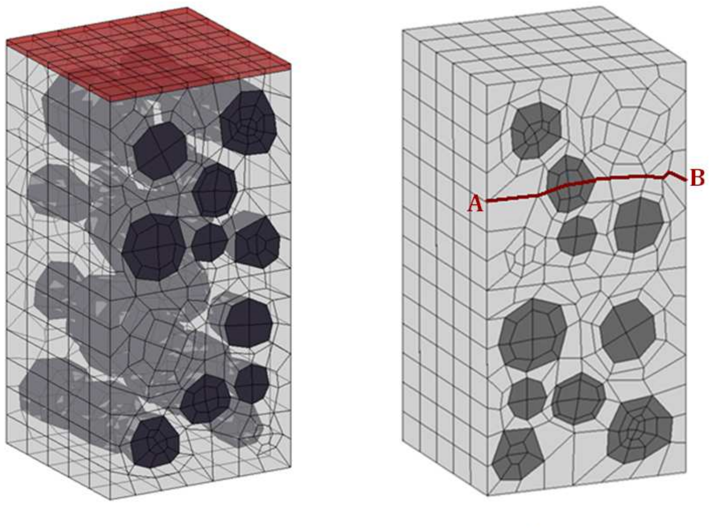

a. b.

Fig. 5.13 Adopted discretization for the meso-scale analysis without ITZ (**a**) and a particular of the line considered to study the relative humidity evolution (**b**).

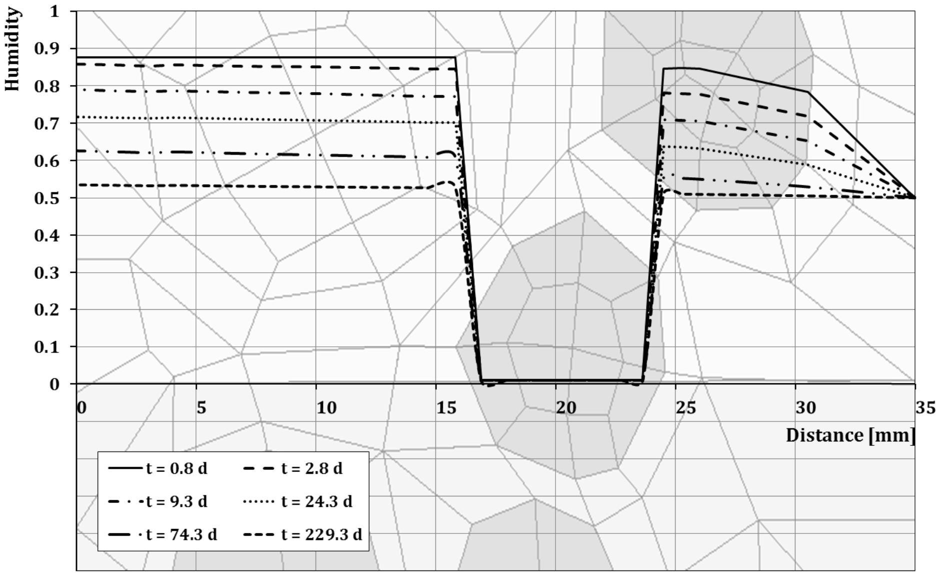

Fig. 5.14 Evolution of relative humidity in the sample along a reference line.

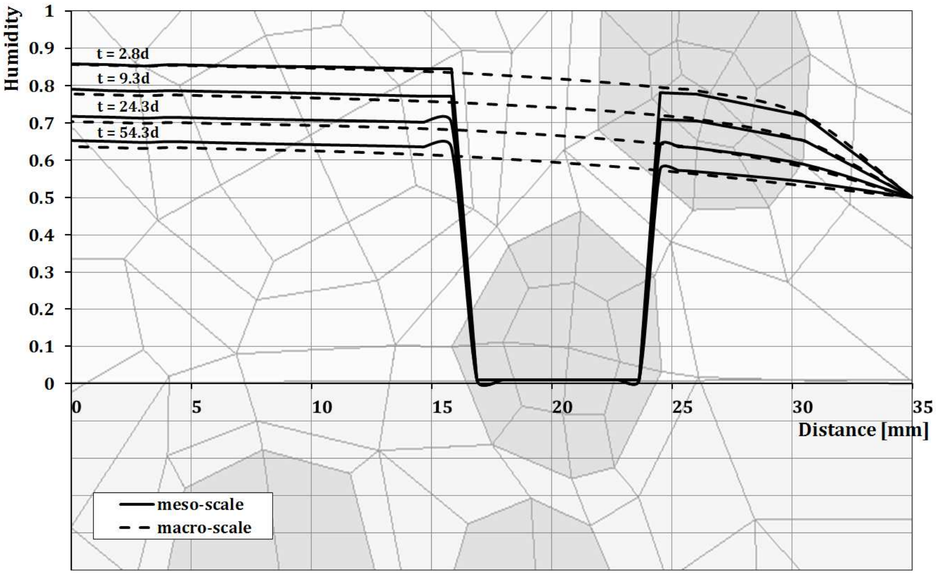

Fig. 5.15 Relative humidity evolutions, macro- vs. meso-scale results.

After having investigated the hygral behaviour of the sample, the vertical deformations of the specimen for a series of nodes in the cement paste moving away from an aggregate, are shown in Fig. 5.16; as expected, in proximity of the aggregate, these strains are reduced due to a “stiffening effect” coming from the aggregates themselves. Indeed, being the aggregates characterized by a higher Young modulus if compared to the cement paste, they go to stiffen the surrounding area.

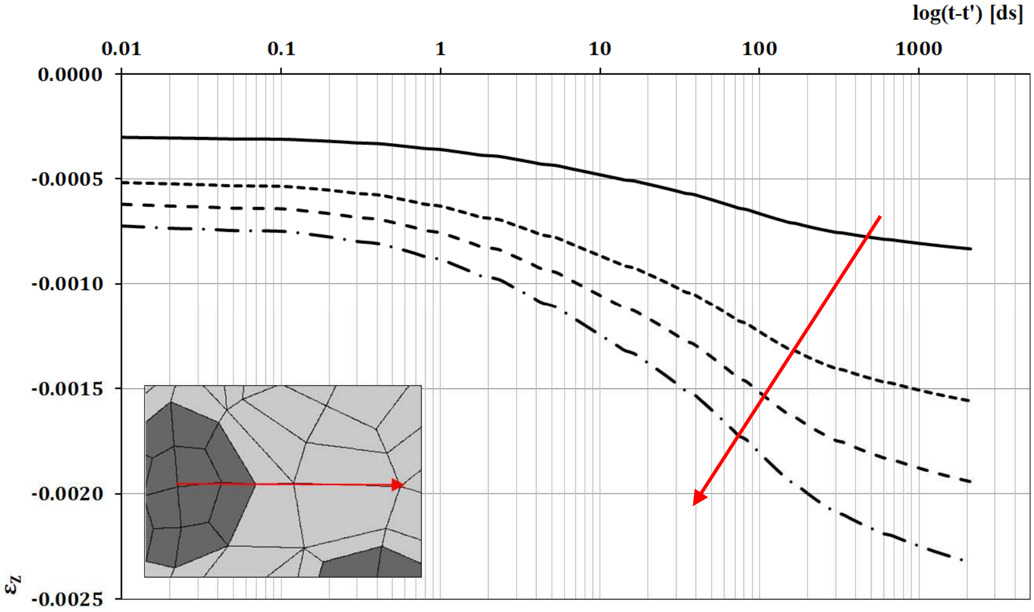

Fig. 5.16 Vertical deformations within cement paste, meso-scale analysis.

Evidently, such local effects do not affect the global response of the sample (Fig. 5.17), hence confirming the congruity of the chosen meso/macro material parameters.

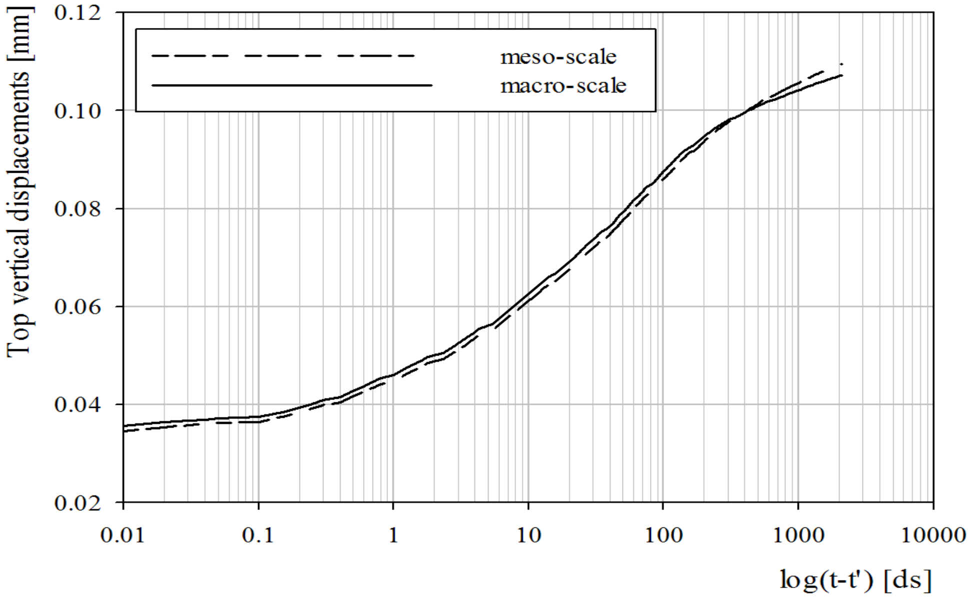

Fig. 5.17 Top vertical displacements evolutions, macro- vs. meso-scale results.

Finally, the same concrete sample investigated before, has been additionally studied by considering the inclusion of the transition zone, a thin layer of matrix material surrounding each inclusion and characterized by a lower density (hence higher permeability) and elastic modulus than cement paste (see the material data for the three components, reported in Table 5.5). In this analysis the ITZ is subjected to creep together with the cement paste, instead the aggregates are always supposed to behave elastically.

Table 5.5 Meso-scale analyses: parameters for cement paste, aggregates and ITZ.

Components / Properties	Cement Paste	ITZ	Aggregate
Elastic Modulus [MPa]	20000	10000	67000
Poisson's Ratio	0.20	0.20	0.20
Reference diffusivity along x, y and z [mm^2/d]	20	40	0
Thermal capacity [N/(mm^{2}K)]	2	2	2
Heat conductivity along x, y and z [N/(d K)	144288	144288	220320
Thermal expansion coefficient of solid	0.000012	0.000012	0.000004

The adopted discretization (see Fig. 5.18) is now characterised by 1955 hexahedral elements, 9284 nodes, a random distribution of aggregates which occupies about the 50% of the total volume of the specimen and an ITZ whose thickness is strictly linked to the diameter of each aggregate (thicker for larger diameters) and lower than 30 μm.

Reasonably, as can be seen in Fig. 5.19, the presence of ITZ does not change the overall spatial humidity distribution, but its contribution is concentrated around the aggregates: humidity gradients are now reduced as well as moisture concentrations (i.e. the small peaks reported in Fig. 5.14), with slightly sharpeless humidity curves.

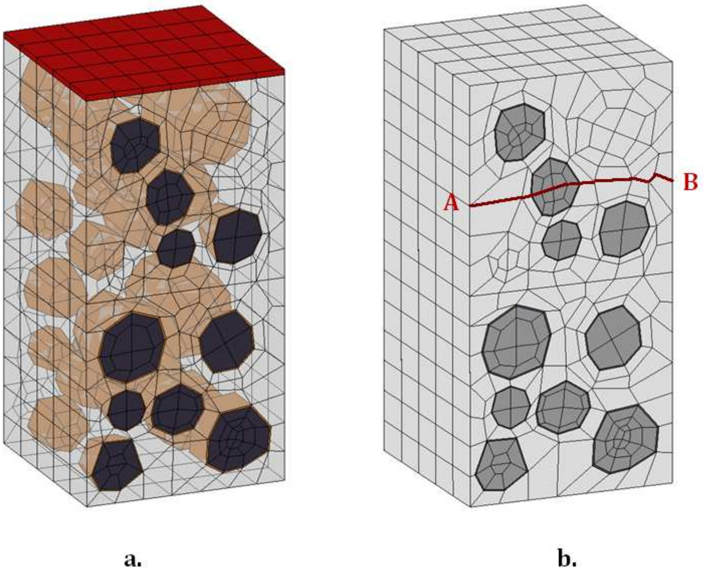

Fig. 5.18 Adopted discretization for the meso-scale analysis with ITZ (**a**) and a particular of the line considered to study the relative humidity evolution (**b**).

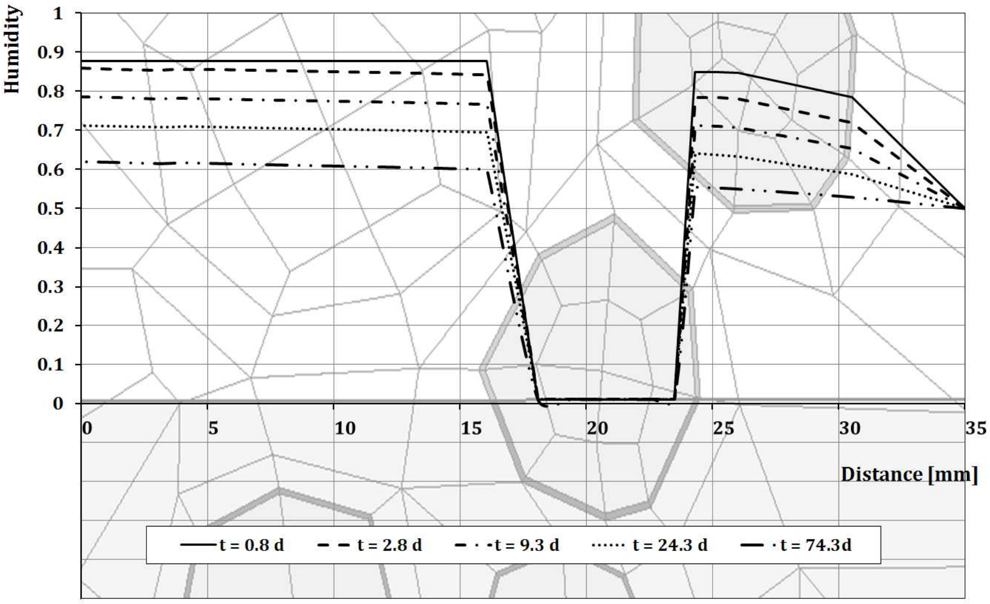

Fig. 5.19 Evolution of relative humidity in the sample along the reference line reported in Fig. 5.18 **b**.

If we investigate the creep behaviour of three nodes (see Fig. 5.20): one in the cement paste close to the side exposed to the environmental conditions (PASTE1), one in the ITZ and the third one in the cement paste behind the aggregate (PASTE2); it can be seen that the difference between the compliance functions of the two pastes is related to their different relative humidity values and so to a different drying creep. This result is once more the proof of the barrier effect exerted by the aggregate towards the flux of humidity. As regards the ITZ, this layer is characterized by a higher compliance function if compared to the cement pastes ones and this due to its relative humidity and to its lower Young modulus.

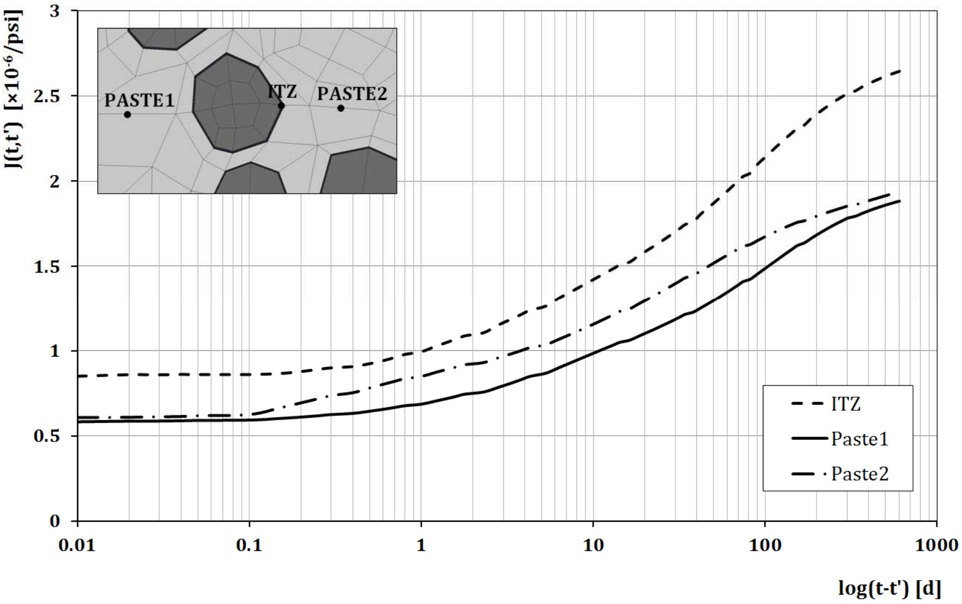

Fig. 5.20 Creep functions for three nodes; one within ITZ and two in cement paste.

Finally, considering the evolution of vertical strains in time for a series of nodes within ITZ and cement paste (see Fig. 5.21), it can be noticed that the general trend is similar to the one experienced without ITZ: close to aggregates the stiffening effect is still detectable, even if now reduced by the lower ITZ elastic modulus; in fact, as even demonstrated below, ITZ is known to be the weakest region of the composite material when exposed to external loads

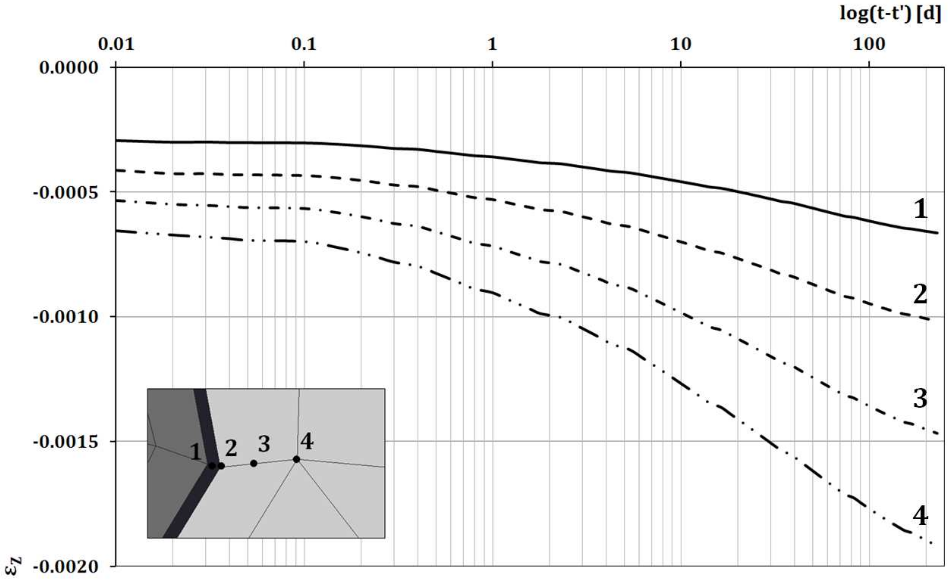

Fig. 5.21 Vertical deformations within ITZ and cement paste.

Damaged behaviour of concrete at the meso-level

In this section a prismatic concrete sample at the mesolevel, with the presence of the ITZ, has been considered (see the discretization reported in Fig. 5.18 **a**) and the damage behaviour of concrete at the meso-level is investigated, in order to understand the influence of ITZ, the weakest region of the composite material, on the overall mechanical behaviour and in view of defining an appropriate concrete mixture for e.g. responding to spalling under high temperature conditions.

The material data used for the three different phases are the same used previously (see Table 5.5), instead the parameters used for the Mazars' damage law are listed in Table 5.6. Damage parameters are valid only for the cement paste and the ITZ because the aggregates are supposed to behave elastically; therefore they are not subjected to damage.

Table 5.6 Parameters used for the isotropic Mazar's damage model (cement paste and ITZ).

$\mathbf{k_0}$	1×10^{-4}
$\mathbf{A_t}$	1.2
$\mathbf{B_t}$	5000
$\mathbf{A_c}$	1
$\mathbf{B_c}$	1000

The sample is a 3.5×3.5×7 cm^3 prism, discretized as in Fig. 5.18 **a**, but this time is constrained only at the base and is subjected to a compressive load, in displacements control so to simulate the non-linear material response in the softening regime.

The evolution of damage within the sample is investigated along the reference line reported; in particular in Fig. 5.22 are considered five different times and by these curves it can be noticed that the peaks (maximum damage) occur as expected in the ITZ (it corresponds to the zone comprised between the two red lines), being this phase the weakest zone of concrete when exposed to external loads.

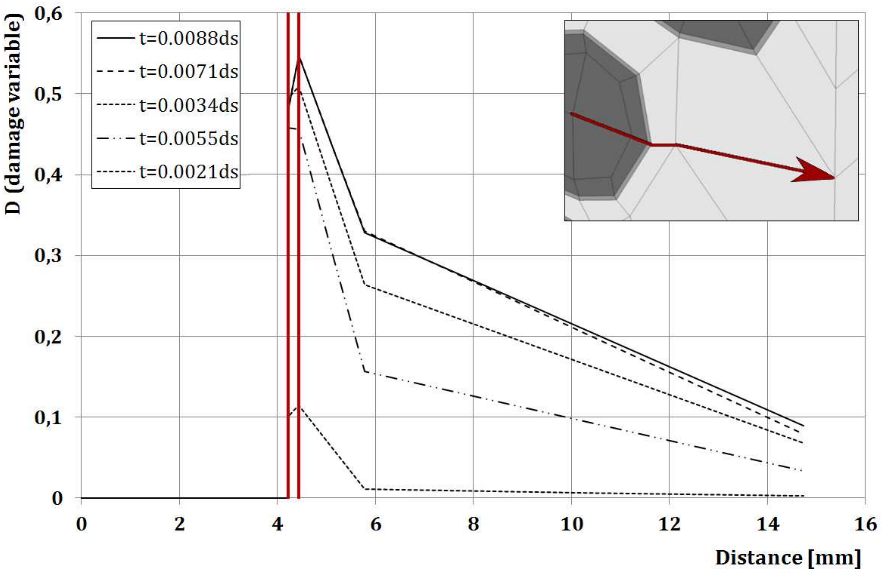

Fig. 5.22 Damage evolution along a reference line within the concrete sample.

5.3 Concrete under high temperature conditions

For spalling predictions the crucial role of the aggregates is largely recognized; so in this section of analyses spalling is investigated considering concrete as a homogeneous and a composite material made of cement paste, aggregates and ITZ.

As first is here presented a comparison between two concrete columns, at the macro-scale, of different section (circular and square) pointing out the “corner effect” in the square one; then the macro predictions are compared with the meso-scale results underlining the crucial role of the aggregates and the ITZ on the real evolution of cracking under high temperature conditions. Finally damage propagation in the individual components, is investigated in more detail through a more refined mesh and the chemo-thermo mechanical damage is presented.

Shape effect

As regards the analysis at the macro level, the discretization adopted for the two different sections (it has been studied only ¼ of the entire sections for the symmetry) is represented in Fig. 5.23**;** the circular mesh is characterized by 198 8-node plate elements and 641 nodes, instead the square one is characterized by 256 8-node plate elements and 833 nodes. Both specimens present an external layer of “fictitious” elements in order to avoid oscillations due to the application of a thermal ramp.

The size of the circular section is taken by an experimental study performed by Lee et al. (a test for cylindrical specimens representative of circular columns subjected to fire exposure), therefore it has a diameter of 100.16mm; instead the side of the square has been taken equivalent to 89.33mm, so that the area of this section is equal to the circular one.

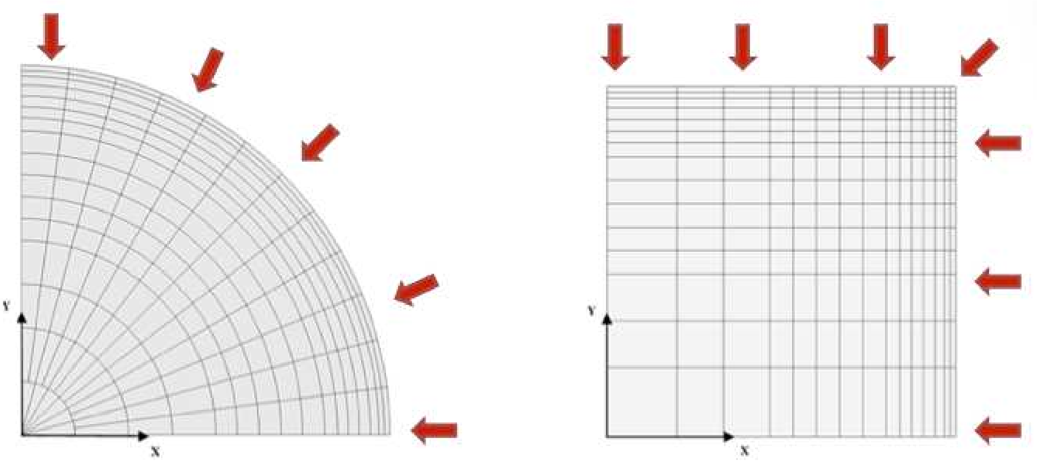

Fig. 5.23 Finite element meshes for the two sections (¼ due to symmetry).

The initial conditions correspond to a saturation of 90% and a temperature of 25°C while, as regards the boundary conditions, the two samples are heated externally with a thermal ramp of 100°C/min reaching a temperature of 345°C. The material data and the damage parameters are reported in Table 5.7.

Table 5.7 Material data and damage parameters adopted for the two samples.

Elastic Modulus [MPa]	35000
Poisson's Ratio	0.18
Reference diffusivity along x, y and z [mm^2/d]	10
Thermal capacity [$N/(mm^2K)$]	2
Heat conductivity along x, y and z [N/(d K)]	144288

k_0	1×10^{-4}
A_t	0.9
B_t	2000
A_c	2
B_c	2500

If we investigate the evolution of the relative humidity in time for a series of nodes going from the surface (A) to the centre (B) of the two different samples (see Fig. 5.24 and Fig. 5.25), the numerical results showed that there is no a big difference in the evolution and that the relative humidity for the internal nodes is still high at the end of the study.

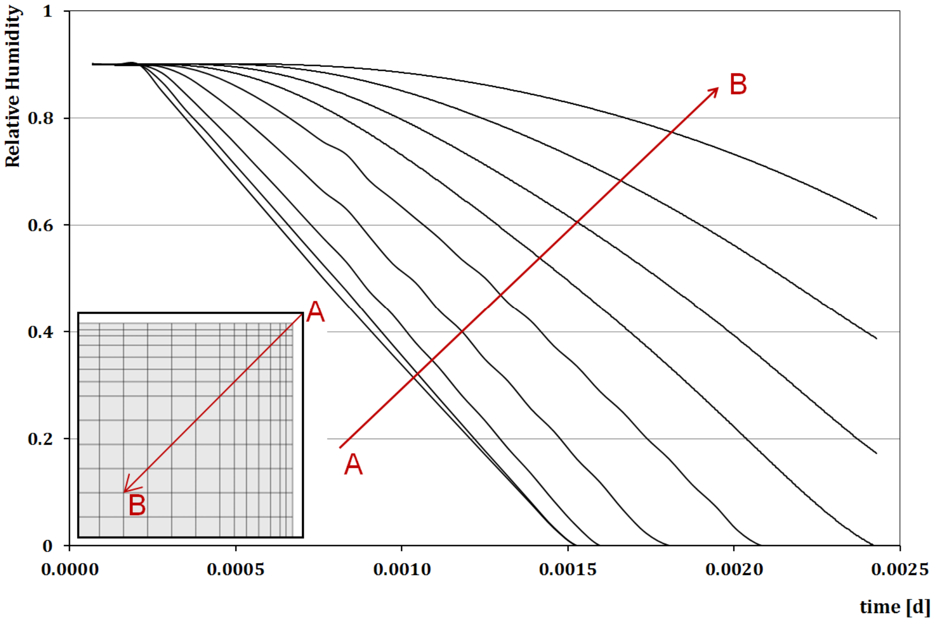

Fig. 5.24 Relative humidity evolution in time of the square specimen.

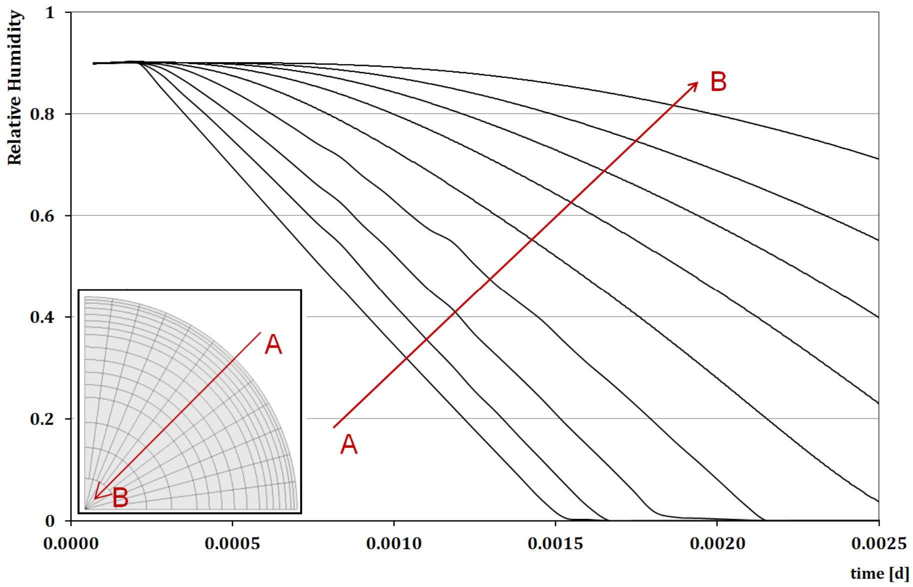

Fig. 5.25 Relative humidity evolution in time of the circular specimen.

Comparing the evolution of the total displacements in Fig. 5.26, it is possible to see how for the square specimen it changes more radically than in the cylinder from 125°C to 145°C; this is due to a loss of stiffness caused by damage under high temperatures. Instead, as regards the cylindrical column, the evolution of the displacements is totally different: the displacements are higher on the external boundary and they decrease going inside the sample.

This totally different behaviour seen analysing the total displacements is more evident studying the damage evolution. Fig. 5.27 illustrates the damage evolution in the two different specimen demonstrating clearly that the rate and the extent of damage is much faster and wide spread in the square specimen rather than in the circular section. In fact in the squared one the damage starts on the corner (T=145°C) and then affects the edges entering in the sample; on the contrary, in the cylinder sample the evolution of damage is really different; the “corner effect” is not present and the damage is confined to a narrow ring. So the so called “corner effect” is a very significant phenomenon when the difference of damage is compared in square vs. circular specimens under rapid heating and one may conclude that the evolution of damage in square or rectangular columns proceeds much faster than in circular columns.

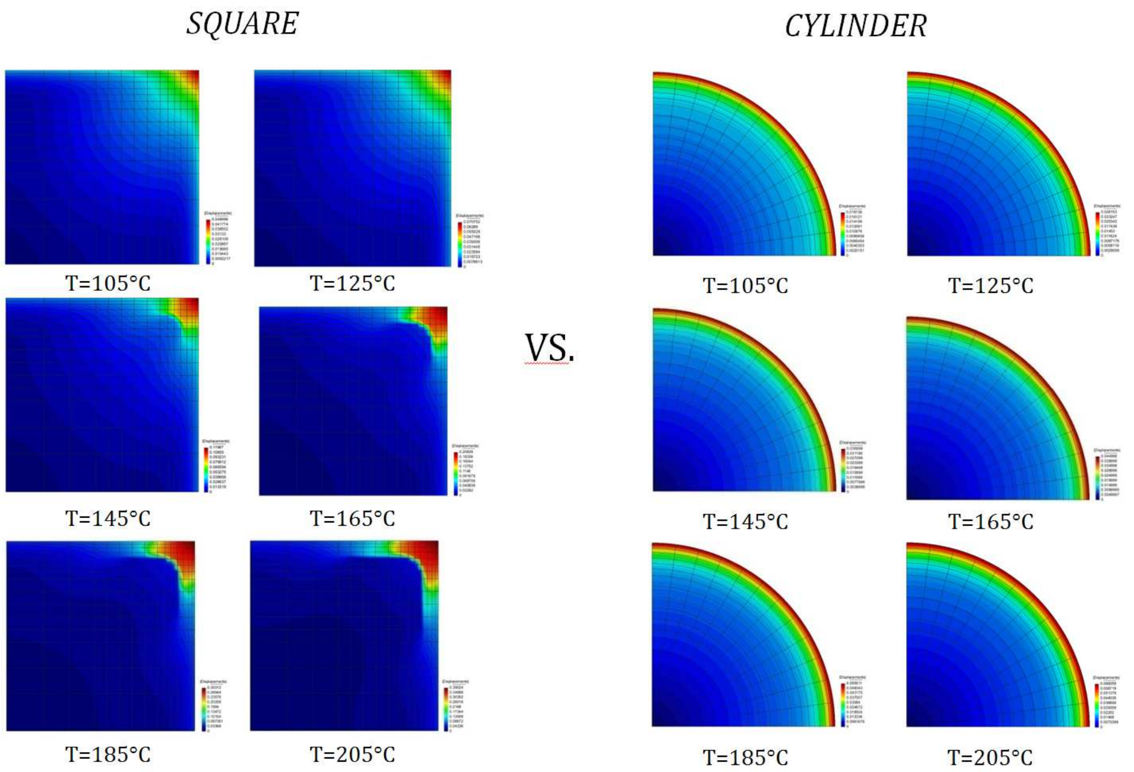

Fig. 5.26 Displacement evolution in square and circular sections.

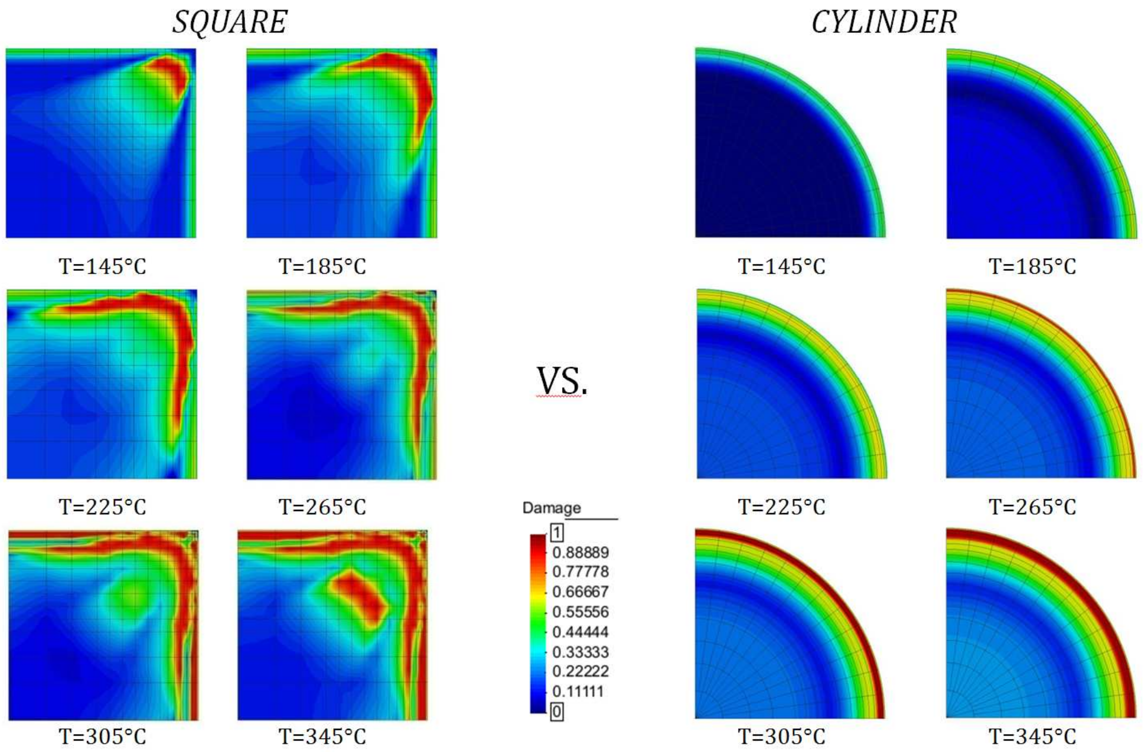

Fig. 5.27 Damage evolution in square and circular sections.

Macro vs. Mesoscopic concrete behaviour at elevated temperatures

The second numerical analysis is a comparison between two square columns under high temperature conditions, one modelled at the macro-scale and one modelled at the meso-scale (with the presence of ITZ) in order to catch the fundamental role of the aggregates on the real evolution of cracking under high temperature conditions. The initial conditions are the same of the first analysis and the two columns are heated externally with a thermal ramp of 100°C/min reaching a maximum temperature of 225°C. In Fig. 5.28 the two meshes are reported), while the material data and the damage parameters for the single components are summarized in Table 5.8 and Table 5.9 and the data for the homogenized material are the same reported in Table 5.7. As regards the mesh at the mesoscale level, it is formed by 1071 8-node plate elements and 3312 nodes, a random distribution of aggregates of different sizes which occupy about the 50% of the entire volume and the presence of a transition zone whose thickness is related to the diameter of the aggregate. Also in this analysis aggregates are assumed to behave elastically; therefore the damage parameters are valid only for the cement paste and the ITZ.

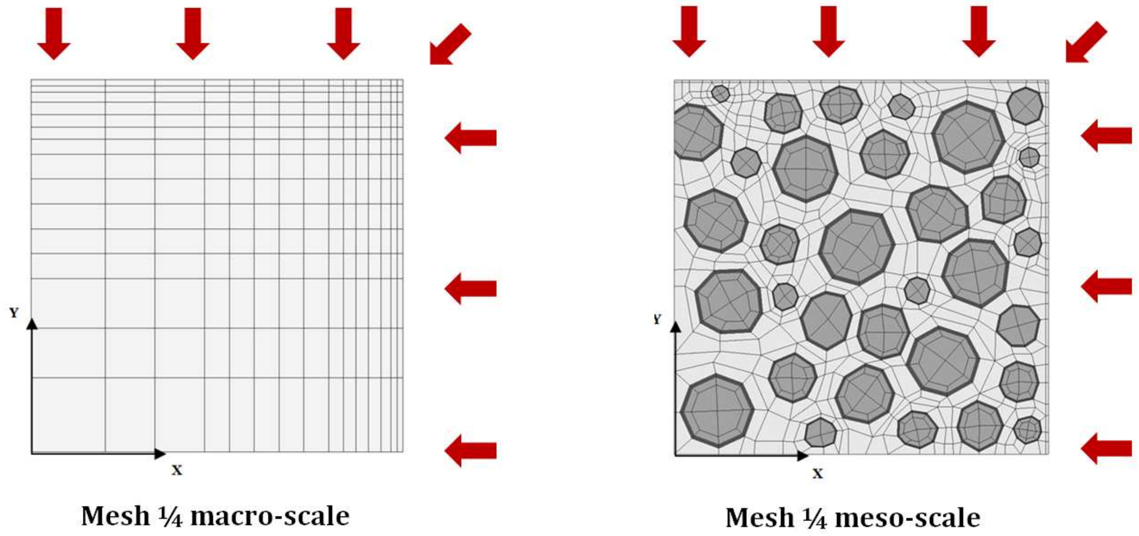

Fig. 5.28 Adopted discretization for the macro and meso-scale samples.

Table 5.8 Material data for the components at the meso-scale.

Components / Properties	Cement Paste	ITZ	Aggregate
Elastic Modulus [MPa]	30000	20000	70000
Poisson's Ratio	0.20	0.20	0.20
Reference diffusivity along x, y and z [mm²/d]	10	20	0
Thermal capacity [N/(mm²K)]	2	2	2
Heat conductivity along x, y and z [N/(d K)	144288	144288	220320

Table 5.9 Damage parameters for the cement paste and the interfacial transition zone.

k_0	1×10^{-4}
A_t	0.9
B_t	2000
A_c	2
B_c	2500

In Fig. 5.29 is reported the evolution of temperature in time for the 2 samples and it can be seen that the behaviour is similar.

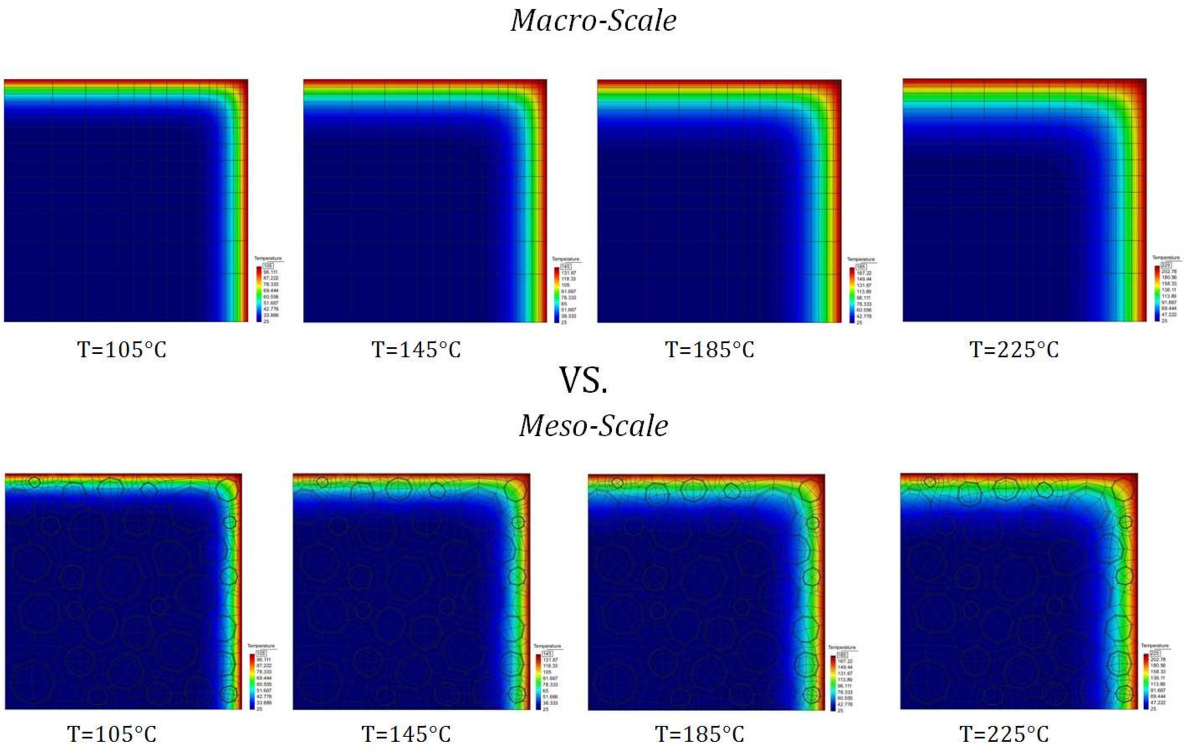

Fig. 5.29 Evolution in time of temperature at the macro and the meso scale levels.

The evolution of damage is reported in Fig. 5.30 and the results show a very interesting feature; indeed if at the macro-scale the "corner effect" is evident, at the meso-scale the damage starts also in the corner but its evolution is totally different and is driven by aggregates and the ITZ. This demonstrate that a study at the macro-scale of spalling is less representative and the real evolution of cracking is lost.

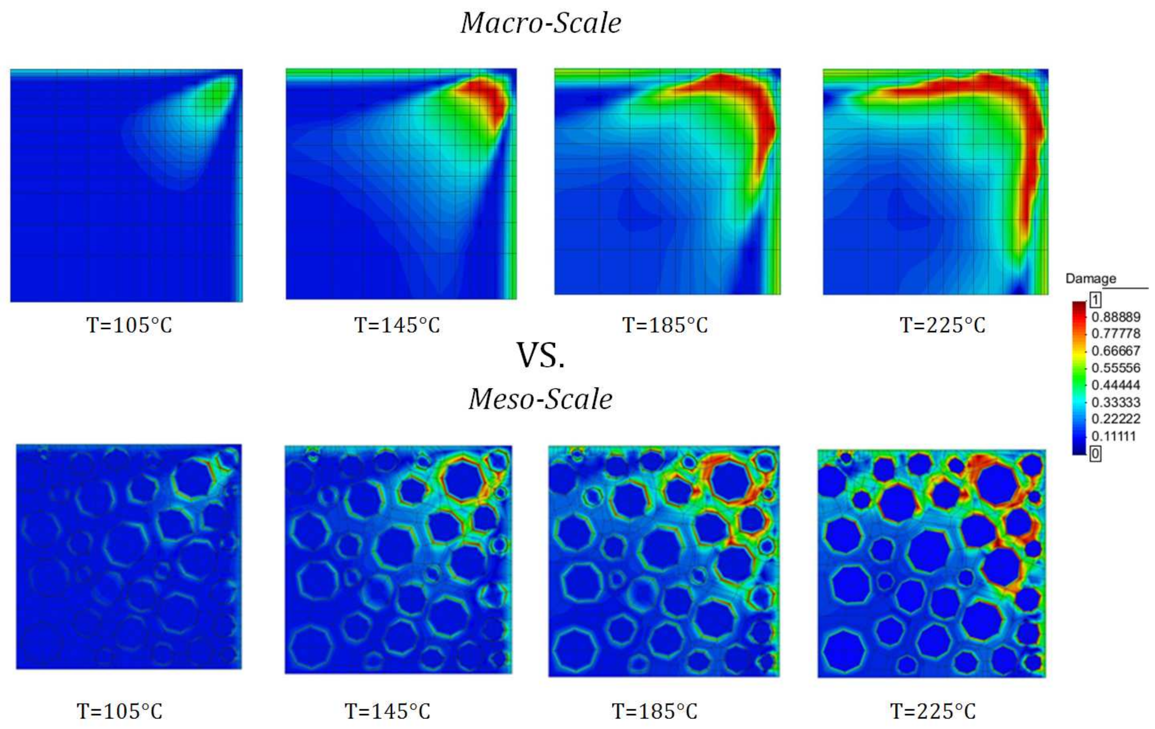

Fig. 5.30 Damage evolution in macro and meso-scale samples.

Damage characterization at the mesolevel

In order to obtain a deeper comprehension of the evolution of damage in the individual components of the material, several meso-scale models have been developed where the degree of discretization is increased and where the shape of the aggregate has been simplified with a rounded one in order to eliminate possible peak stress generated by the angularities of the aggregates with squared faces. Therefore the adopted mesh is shown in Fig. 5.31 and this discretization consists of 5364 8-node plate elements and 16293 nodes. Its dimensions are equivalent to the sample described in the 'previous analysis, maintaining the same percentage of aggregates, the same hygro-thermal mechanic characteristics for the different phases, shown in Table 5.8 and in Table 5.9 and the same boundary conditions.

The evolution of damage at different temperatures (from 100°C to 300°C) reported in Fig. 5.32 highlights very clearly that damage is driven by aggregates distribution and by ITZ; indeed, by these contours is possible to notice that initially it triggers in the ITZ (being this one the weakest zone for its properties), then spreads inside this layer and finally involves the cement paste.

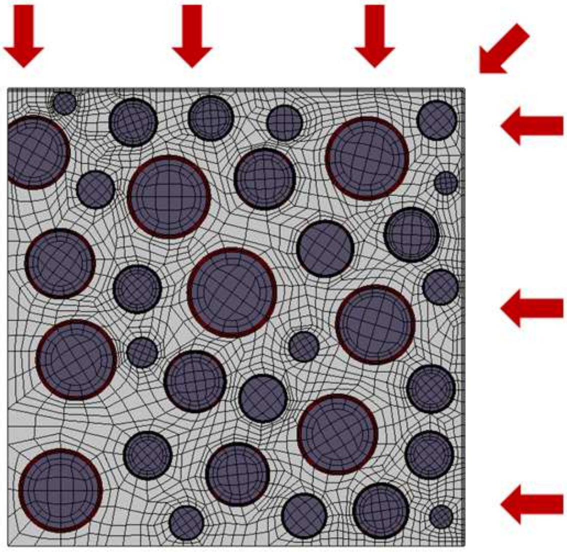

Fig. 5.31 Adopted discretization.

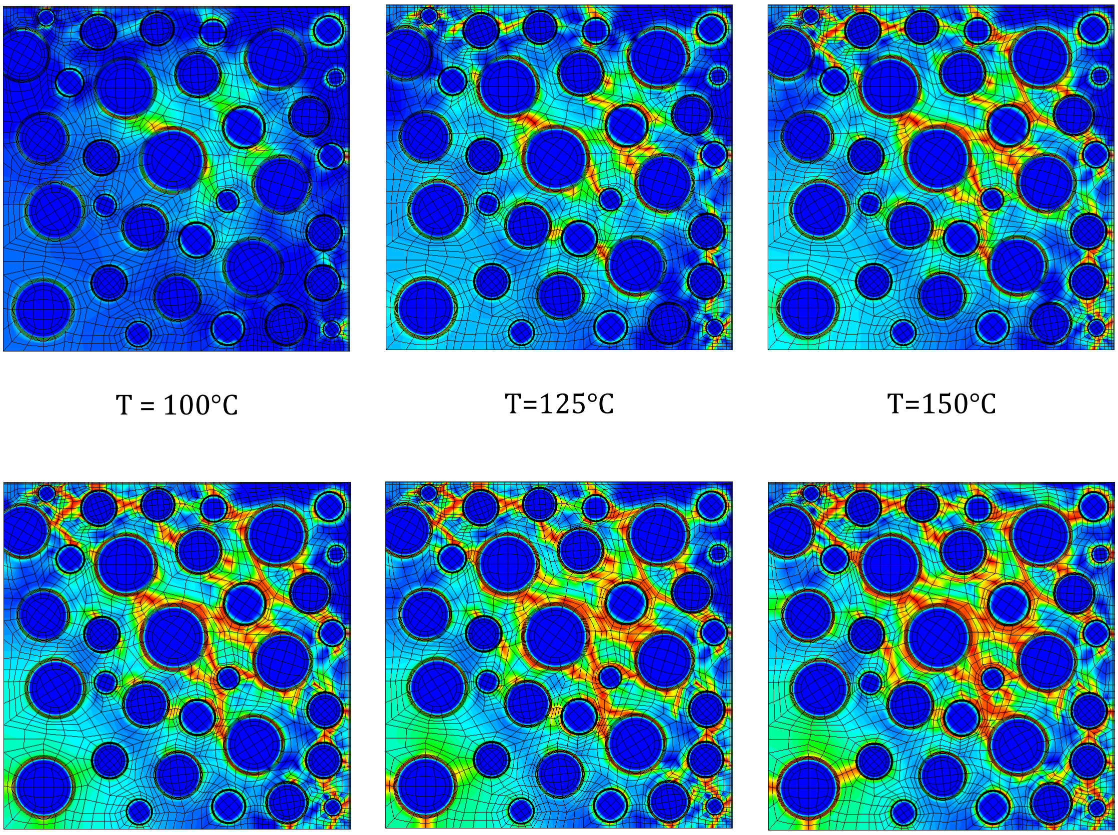

T = 100°C

T=125°C

T=150°C

T=175°C

T=200°C

T=225°C

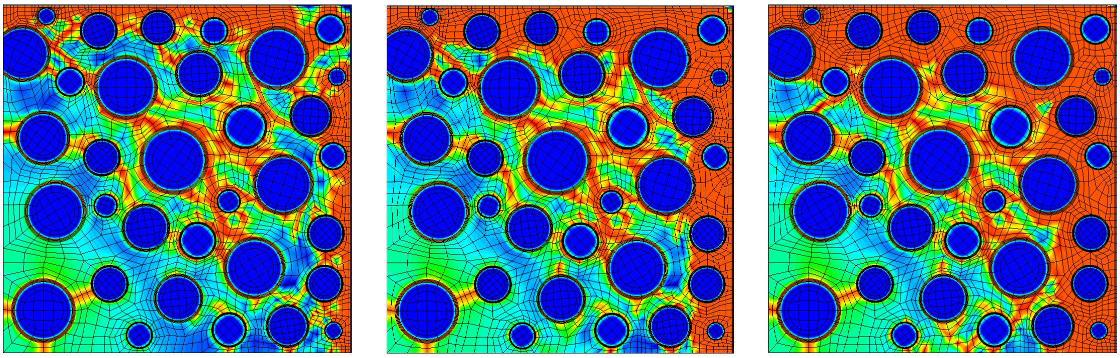

T = 250°C T = 275°C T = 300°C

Fig. 5.32 Damage evolution in time at the meso level; Blue: undamaged zone (damage variable D=0); Red: totally damaged zone (D=1).

To better understand as damage propagates, we have considered a small zone between two different aggregates (see Fig. 5.33); in particular we have analysed three points along the transition zone surrounding an aggregate (ITZ1, ITZ2 and ITZ3) and one point in the cement paste (PASTE) between the two aggregates.

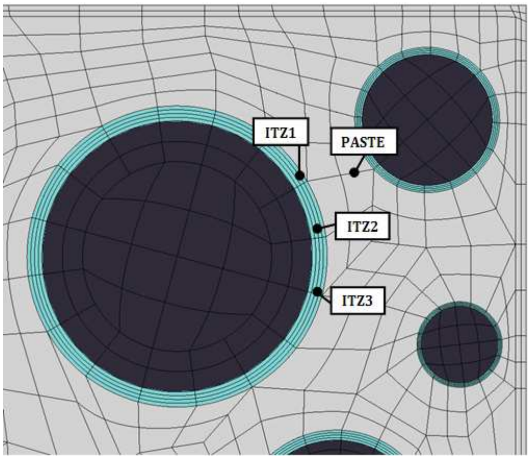

Fig. 5.33 Particular of the zone considered to study damage propagation.

The damage history during heating for these four representative points is shown in Fig. 5.34. By these curves can be seen that damage starts in the point ITZ1 at the temperature T=100°C (at about 0.0005 days) and grows rapidly until cracking (damage variable D=1). Subsequently, because of the stiffness variation occurred in ITZ1, there is a stress redistribution in the nearby area and for this reason damage starts also in the other three points (at about t=0.0007 days). This in reality doesn't happens simultaneously but the curves are delayed with respect to each other because, as damage increases in a point, the stiffness decreases and there is a new stress redistribution. This means that damage grows more slowly in the point considered and speeds up in the near points, characterized by an higher stiffness.

Indeed, if we consider for example the cement paste in Fig. 5.34; damage grows up to 40% in this point, then it stabilizes and increases in the other points ITZ2 and ITZ3 (being weaker because of their mechanical properties). Reached a certain level, the damage is stable for these two points, the cement paste is recharged and arrives to cracking. Finally, also the damage in the other two points grows until cracking. This damage sequence is clearly visible in Fig. 5.35.

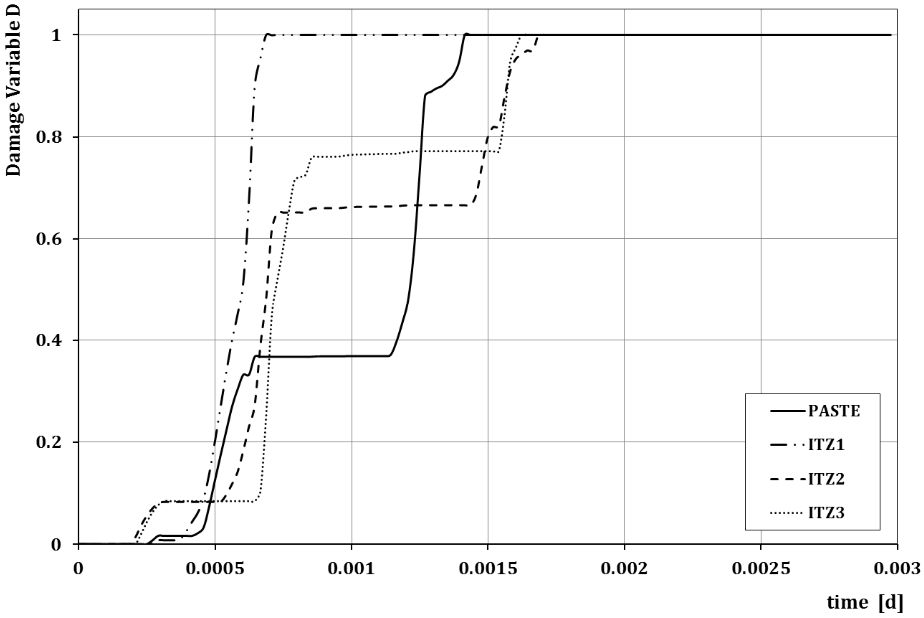

Fig. 5.34 Damage history for four points; one in the cement paste and three in the transition zone.

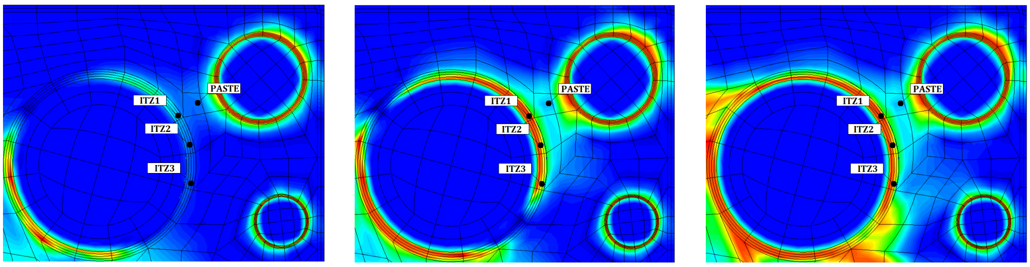

t=0.0005 ds (T=90°C)

t=0.0007 ds (T=120°C)

t=0.001 ds (T=165°C)

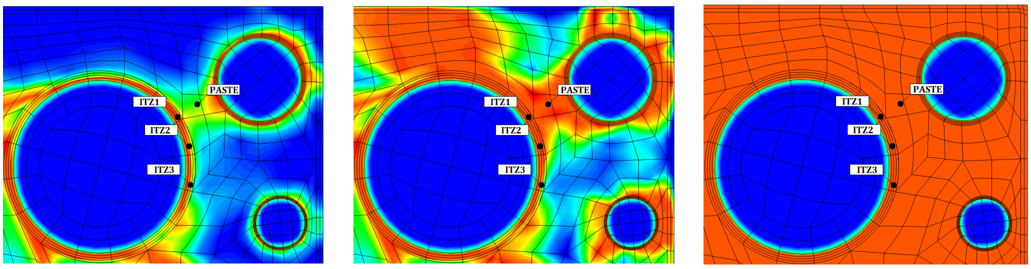

t=0.00125 ds (T=200°C)

t=0.0015 ds (T=235°C)

t=0.002 ds (T=305°C)

Fig. 5.35 Damage evolution for the four points indicated in Fig. 5.33; Blue: undamaged zone (damage variable D=0); Red: totally damaged zone (D=1).

Comparing the evolution of the total displacements at two different temperatures in Fig. 5.26**,** it is possible to see that at about 200°C the specimen is expanding, instead at 300°C is shrinking and this is due to the cement paste that is subjected to a small thermal expansion (up to 200 °C) and a larger shrinkage due to loss of humidity. If we go to consider the displacement along x of two nodes in the cement paste (see Fig. 5.37) these two effects are clearly visible.

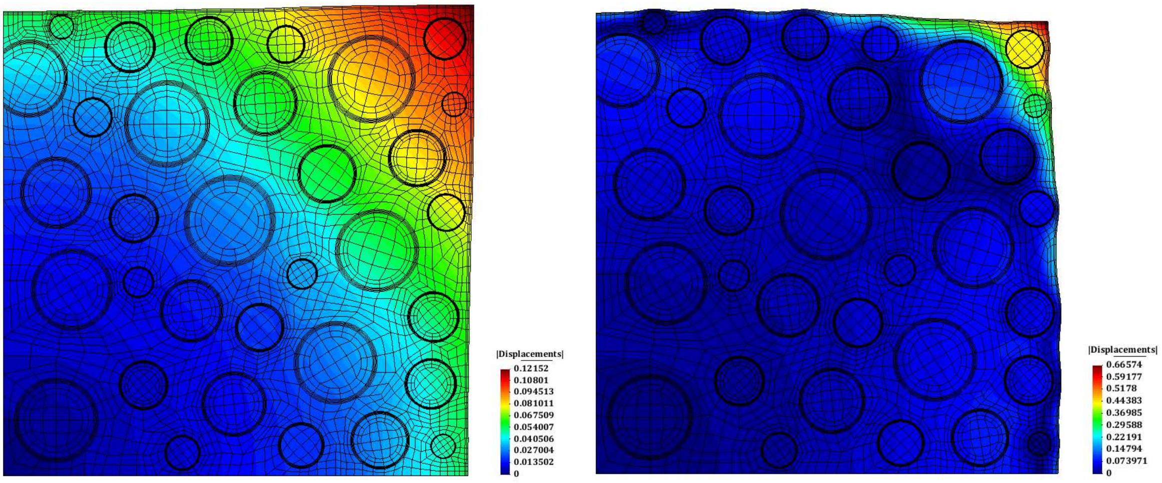

T = 200°C

T = 300°C

Fig. 5.36 Total displacements evolution at different temperatures.

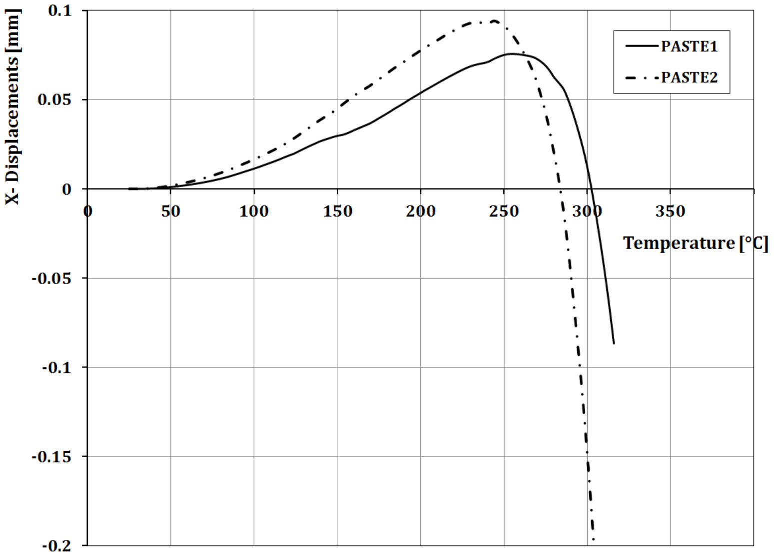

Fig. 5.37 X-Displacements evolution of two nodes in the cement paste.

Thermo-Mechanical damage at the mesolevel

In the previous analyses damage was a mechanical one and the damage parameter D was expressed through the non-local Mazars' damage law (see Section 3.5.3).

If we consider also a thermo-chemical damage in NEWCON3D, its parameter V is expressed as (see Section 4.4.5) $V=1-E_0(T)/E_0(T_a)$ where E_0 is the Young's modulus of mechanically undamaged material and T_a is room temperature.

As regards the temperature dependence of the elastic modulus for the different components at the mesolevel, we have adopted the expression proposed by Willam et al. [4]:

$$E(T)=E_0(T_a)\left[0.03921+e^{-0.002T}\right]$$

Assuming that the total effect of the mechanical and thermo-chemical damages is multiplicative, the total damage parameter D is defined by $D=1-(1-d)(1-V)$, where d is the mechanical damage parameter of Mazars.

Therefore, considering the previous analysis but taking into account a chemo-thermo mechanical damage, the evolution of the total damage parameter D is reported in Fig. 5.38. Comparing these contours with the ones of Fig. 5.32, can be seen that the propagation of damage in the ITZ and in the cement paste is similar even if in this case it triggers before due to the reduction of the elastic modulus of these two components under heating.

As regards the aggregates, while in Fig. 5.32 they don't damage as they are assumed to behave elastically; in Fig. 5.38 they are subjected to damage because their Young modulus decreases with temperature. A comparison between these two damage parameters for a node of an aggregate is reported in Fig. 5.39.

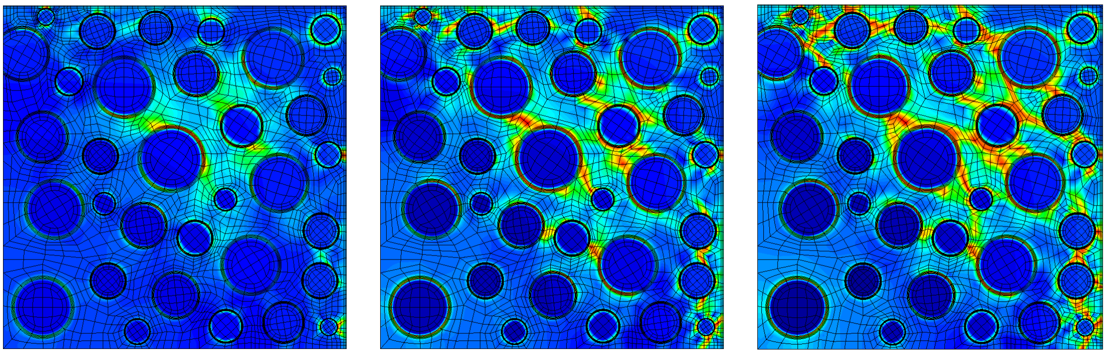

T = 100°C

T=125°C

T=150°C

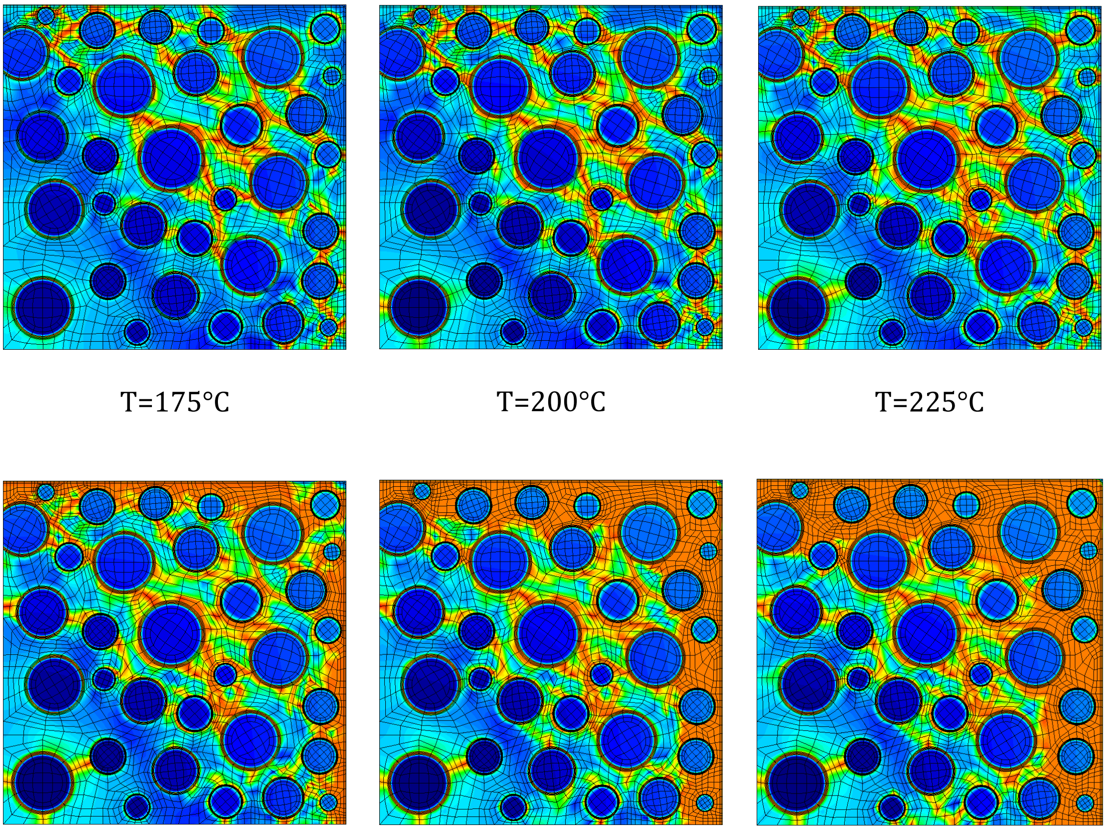

T=175°C T=200°C T=225°C

T = 250°C T = 275°C T = 300°C

Fig. 5.38 Damage (chemo-thermo mechanical damage) evolution in time at the meso level; Blue: undamaged zone (damage variable D=0); Red: totally damaged zone (D=1).

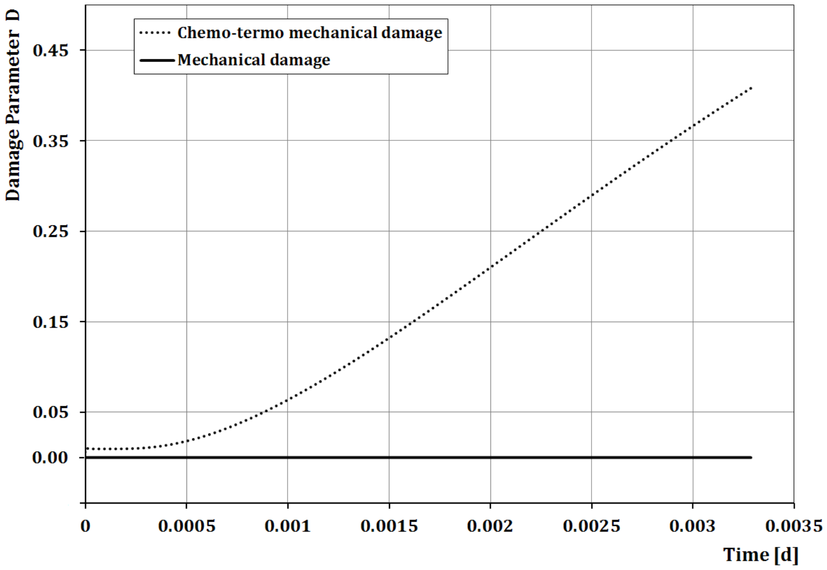

Fig. 5.39 Comparison between the mechanical and chemo-thermo mechanical damage for a node of an aggregate.

REFERENCES

[1] L'Hermite R., Mamillan M. and Lefèvre C. (1965), Nouveaux résultats de researches sur la déformation et la rupture du béton, Ann. Inst. Batiment Trav. Publics, 18, pp. 323-360.

[2] Bažant Z.P. and Kim J.(1992), Improved prediction model for time-dependent deformations of concrete: Part 1-7, Materials and Structures, 25.

[3] Lee, J. (2006), Experimental studies and theoretical modelling of concrete subjected to high temperatures, University of Colorado at Boulder, PhD Thesis.

[4] Willam K.J., Rhee I. and Xi J. (2005), Thermal degradation of heterogeneous concrete materials, Journal of Materials in Civil Engineering, ASCE, 17, No. 3, pp. 276-285.

6 CONCLUSIONS

In this work concrete has been investigated at the mesoscale level, i.e. as a composite material composed by aggregates, cement paste and the interfacial transition zone, in order to provide a deeper understanding of several concrete phenomena, such as creep, damage and spalling. Particularly model B3 and Mazars' law, have been chosen and implemented in the 3D, fully coupled thermo-hygro-mechanical model of heated concrete, FE code called NEWCON3D when considering creep and damage, respectively.

Thanks to the studies carried out at the meso-scale level it has been possible to observe the behavior of each component. In the case of long-term effects, creep of cement paste and ITZ, described by consolidated and complete models as the B3 one (carefully calibrated on the basis of well-known experimental results like the ones given by L'Hermite), allow to catch the complex nature of creep, which is not only given by fluid flow and pressure dissipation but it is the result of chemical-physical reactions. Again, the description of concrete as a composite material, in conjunction with fully coupled porous media analyses, allows for understanding the hygro-thermal and mechanical response of concrete, first of all in terms of hygral and thermal changes within a material where aggregate inclusions (encapsulated by ITZ concave volumes) appear with some statistical distribution (as originally described by Wittmann, even if without the ITZ effect (Wittman (1968)). Hygral barriers due to the presence of aggregates can be seen only at this modelling level. On the other side, thermal conductivity properties dominate the thermal conduction within the sample.

Moreover, from the mechanical viewpoint, it has been possible to notice the remarkable damage peak effect arising from the inclusion of ITZ, if compared with the less pronounced peak when ITZ is disregarded. This result allows for a first explanation of specific phenomena linked to spalling, e.g. the generation of cracks driven by aggregates and the possible explosion of aggregates themselves.

Spalling prediction of concrete under high temperature conditions and fire is largely recognized to be influenced by concrete aggregates; in fact comparing the different pattern of damage between an homogenous and a composite model, since it starts from the corner in both cases but the time evolution is totally different since it is driven by the aggregates and the ITZ. This demonstrates that a study at the macro-scale of spalling is less representative and the real evolution of cracking is lost.

Concrete is a mix of different components and each component has a different thermal expansion coefficient. At the meso-level scale, we have in the cement paste the two effects of a small thermal expansion (up to 200 °C) and a larger humidity shrinking due to evaporation. On the other side, aggregates expand only because in this case there is not loss of humidity. The whole dilation effect (of cement paste and aggregate, clearly distinguished at the meso-level scale) produce a mismatch, that is indeed a "thermohygrometric" mismatch and not only a "thermal" mismatch. The differences in thermal and hygral expansions therefore generate stresses in concrete, giving rise to damage and cracking.

From experimental tests it is possible to notice how concrete presents a small plastic behaviour, during an increasing load before failure. This can be simulated through a plasticity law; therefore in the latter part of the thesis the F.E. code upgrading is shown to innovatively couple creep, shrinkage and damage with plasticity. Several analyses have been exploited to verify the correct numerical implementation; further improvements will be the reproduction of a real case and then its application at the mesoscale.

APPENDIX

Implementation of the Subloading Surface elasto-plastic model in NEWCON3D

The elasto-plastic model

In the present paragraph the principal features of the elasto-plastic model, named Subloading Surface, will be shown. A first formal aspect that has to be highlighted is the difference between the already mentioned model and these classified as conventional (i.e. Drucker-Prager, Cam-Clay etc...).

The latter state that the yield surface encloses the pure elastic domain, where there is a perfect one-to-one linear correspondence between stress and strain and no permanent deformation can be produced inside this field. On the other hand whenever the stress goes outside the yield stress, plastic strains (i.e. permanent deformations) are induced. Material behaviour is then split into two part depending on the stress level in the stress space leading to a no smooth transition in the stress-strain evolution. In particular the results obtained in case of softening response of the material should be carefully considered.

Subloading surface model was proposed by Hashiguchi and Ueno [1] in order to describe the deformation mechanism of materials and to catch a more realistic smooth stress-strain transition. The reason why this theory has been considered as "unconventional" by Drucker [2] is due to the fact that plastic strains are produced for every change of the stress state without a clear distinction of plastic and elastic domains. The subloading surface model introduces a subloading surface inside the yield one which expands or contracts depending on whether the stress increase or decrease and keeps a similarity ratio to see yield surface. It is assumed that the plastic strain rate is induced gradually with an increasing ratio of the size of the subloading surface to that of the yield surface.

$$\mathbf{L} = \frac{\partial \mathbf{v}}{\partial \mathbf{x}} \qquad [A.1]$$

where $\mathbf{v}$ is the velocity vector, whereas $\mathbf{x}$ is the coordinate point. Using a property of the second-order tensor, as well known as the Cartesian decomposition, it is possible to split the velocity gradient tensor in two part: a symmetrical one $\boldsymbol{\varepsilon}$ (the strain rate) and the skew symmetric one $\mathbf{w}$ (the continuum spin). In detail:

$$\boldsymbol{\varepsilon} = \frac{1}{2}(\mathbf{L} + \mathbf{L}^T); \qquad \mathbf{w} = \frac{1}{2}(\mathbf{L} - \mathbf{L}^T) \qquad [A.2]$$

It is also assumed that the total strain rate $\boldsymbol{\varepsilon}$ can be additively decomposed into an elastic part $\mathbf{e}$ and into a plastic one $\mathbf{p}$, i.e. in a component:

$$\boldsymbol{\varepsilon}_{ij} = \mathbf{e}_{ij} + \mathbf{p}_{ij} \qquad [A.3]$$

It has to be noticed that the stress and strain used in the following equations shall be considered as rate despite it isn't used the conventional notation (i.e. $\overset{\bullet}{\boldsymbol{\sigma}}$, $\overset{\bullet}{\boldsymbol{\varepsilon}}$). The elastic contribution is given using the fourth-order elastic tensor as showed below:

$$\boldsymbol{\sigma}_{ij} = \mathbf{E}_{ijkl} \cdot \mathbf{e}_{kl} \qquad [A.4]$$

Finally, re-writing the previous relationship and including the additive property of the total strain rate, we obtain:

$$\boldsymbol{\sigma}_{ij} = \mathbf{E}_{ijkl}\left(\boldsymbol{\varepsilon}_{kl} - \mathbf{p}_{kl}\right) \qquad [A.5]$$

Conventional elasto-plastic equations

Starting from the previous preliminary hypothesis it is now possible to characterize the classical elasto-plastic model. First of all it is necessary to define an elastic domain, which allows to recognize points for which an increase in terms of stress will lead to a plastic response of the material. In other word a yield function form is needed to define the different material response in the stress space. It is given as follow:

$$f(\boldsymbol{\sigma}) - F(H) = 0 \qquad [A.6]$$

where the scalar H is the isotropic/softening variable, whereas *f* is a homogeneous function of degree one respect of the stress tensor. Using a time differentiation the consistency condition can be written as:

$$tr\left(\frac{\partial f(\boldsymbol{\sigma})}{\partial \boldsymbol{\sigma}} \overset{\circ}{\boldsymbol{\sigma}}\right) = F' \overset{\bullet}{H} \qquad [A.7]$$

where

$$F' \equiv \frac{dF}{dH} \qquad [A.8]$$

indicates the total derivate of function F respect of the isotropic/softening variable, tr is the trace, ($\overset{\circ}{\sigma}$) represents the co-rotational rate (becoming simply the time derivative under the hypothesis of small strain) and at last, the symbol ($\overset{\bullet}{}$) over the H stands for the time material derivative (i.e. $\frac{DH}{Dt} = \frac{\partial H}{\partial t} + \mathbf{v} \cdot \nabla H$). Once defined the yield function it has also to be specified a *flow rule* that governs the increments of plastic deformation. Depending on how this flow is obtained we can distinguish between associate and non-associate flow rule.

The former type is the most common and it is also used in this work; it is get deriving the expression of the yield function respect of the stress tensor for a certain point:

$$\mathbf{p} = \lambda \mathbf{N} \tag{A.9}$$

where λ is the positive proportional factor, whereas **N** is the normalized outward-normal of the yield function:

$$\mathbf{N} \equiv \frac{\partial f(\boldsymbol{\sigma})}{\partial \boldsymbol{\sigma}} \Bigg/ \left\| \frac{\partial f(\boldsymbol{\sigma})}{\partial \boldsymbol{\sigma}} \right\| \tag{A.10}$$

The latter type is obtained defining a further surface called potential plastic surface $g(\sigma) = g(\sigma_c)$ (σ_c stand for a specific point) from which again the derivative respect of the stress tensor in the point is taken:

$$\mathbf{p} = \lambda \mathbf{M} \tag{A.11}$$

$$\mathbf{M} \equiv \frac{\partial g(\boldsymbol{\sigma})}{\partial \boldsymbol{\sigma}} \Bigg/ \left\| \frac{\partial g(\boldsymbol{\sigma})}{\partial \boldsymbol{\sigma}} \right\| \tag{A.12}$$

Substituting the associate flow rule inside the consistency condition it is possible to write:

$$\lambda = \frac{tr(\mathbf{N}\overset{\circ}{\boldsymbol{\sigma}})}{M_p} \tag{A.13}$$

Where M_p term is the plastic modulus, which can be defined as well as:

$$M_p \equiv tr(\mathbf{N}\boldsymbol{\sigma}) \frac{F'}{F} h \tag{A.14}$$

As mentioned in the previous part of this chapter, we have chosen an *f* function such a homogeneous function of degree one respect of the stress tensor which means it is possible to apply the *Euler Theorem*:

$$\sum_{i=1}^{n} \frac{\partial f(x)}{\partial x_i} x_i = k\, f(x) \qquad \forall x \in A \tag{A.15}$$

Where k is the degree of homogeneity. Keeping in mind the previous equation it is possible to elaborate them, thanks to the property of the *f* function:

$$\frac{\partial f(\boldsymbol{\sigma})}{\partial \boldsymbol{\sigma}} = \left\| \frac{\partial f(\boldsymbol{\sigma})}{\partial \boldsymbol{\sigma}} \right\| \mathbf{N} = \frac{tr\left(\dfrac{\partial f(\boldsymbol{\sigma})}{\partial \boldsymbol{\sigma}} \boldsymbol{\sigma} \right)}{tr(\mathbf{N}\boldsymbol{\sigma})} \mathbf{N} \tag{A.16}$$

But we also know that:

$$tr\left(\frac{\partial f(\boldsymbol{\sigma})}{\partial \boldsymbol{\sigma}}\boldsymbol{\sigma}\right) = 1 \cdot f(\boldsymbol{\sigma}) \qquad [A.17]$$

So we can finally come to the following form:

$$\frac{\partial f(\boldsymbol{\sigma})}{\partial \boldsymbol{\sigma}} = \frac{f(\boldsymbol{\sigma})}{tr(\mathbf{N}\boldsymbol{\sigma})}\mathbf{N} = \frac{F(H)}{tr(\mathbf{N}\boldsymbol{\sigma})}\mathbf{N} \qquad [A.18]$$

In conclusion with some mathematical passages the direct and the inverse bond can be showed as reported below:

$$\boldsymbol{\varepsilon} = \mathbf{E}^{-1}\overset{\circ}{\boldsymbol{\sigma}} + \frac{tr(\mathbf{N}\overset{\circ}{\boldsymbol{\sigma}})}{M^p}\mathbf{M} \qquad [A.19]$$

$$\overset{\circ}{\boldsymbol{\sigma}} = \mathbf{E}\boldsymbol{\varepsilon} - \frac{tr(\mathbf{NE}\boldsymbol{\varepsilon})}{M^p + tr(\mathbf{NEM})}\mathbf{EM} \qquad [A.20]$$

$$\overset{\circ}{\boldsymbol{\sigma}} = \left\{\mathbf{E} - \frac{tr(\mathbf{NE}\boldsymbol{\varepsilon})}{M^p + tr(\mathbf{NEM})}(\mathbf{EM}) \otimes (\mathbf{NE})\right\}\boldsymbol{\varepsilon} \qquad [A.21]$$

The loading criteria, which is derived from the first of the direct bond equation, can be written as:

$$\begin{cases} \mathbf{p} \neq 0: & f(\boldsymbol{\sigma}) = F(H) \;\; and \;\; tr(\mathbf{NED}) > 0 \\ \mathbf{p} = 0: & otherwise \end{cases} \qquad [A.22]$$

The Subloading surface model

In the subloading surface model (Hashiguchi and Ueno [1]; Hashiguchi, [3], [4], [5]) the conventional yield surface is renamed *normal-yield surface* just to remark what already stated in the introduction of this chapter, which is that there is no longer separation between elastic and plastic domain but the yield surface became only a reference to draw the subloading once. This is such that always pass through the current stress point and keeps a similar shape and a similarity ratio in its arrangements to the normal-yield surface.

It is thus possible to list the following geometrical properties:

- All lines connecting an arbitrary point on or within the subloading surface and its conjugate point on or within the normal-yield surface connect to a unique point, called *similarity-centre*;

- All ratios of length of an arbitrary line-element connecting two points on or inside the subloading surface to that of an arbitrary conjugate line-element connecting two conjugate points on or inside the normal-yield surface are identical. The ratio is called the *similarity-ratio*, which coincides with the ratio of the size of these surfaces.

In detail the above mentioned similarity-ratio can assume every real value included between 0 and 1:

- $R = 0$ means that the stress state is zero, in the stress space the subloading surface degenerates into a point which lies at the origin of the axes;
- $0 < R < 1$ means that the stress state is included inside the normal-yield surface;
- $R = 1$ means that the subloading surface and the normal-yield surface perfectly overlap.

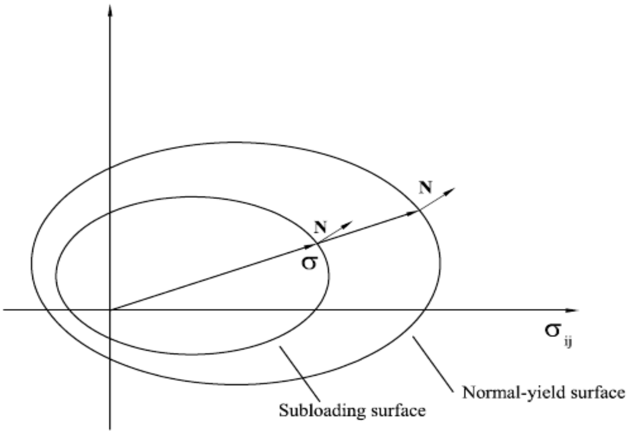

Fig. A.1 Normal-yield surface and subloading surface.

Once defined the similarity-ratio evolution and its field of existence it can be possible to obtain the analytical form for the subloading surface, which is quite similar of that of the yield surface in conventional elasto-plasticity:

$$f(\boldsymbol{\sigma}) - RF(H) = 0 \qquad [A.23]$$

Using time differentiation it is possible to get the consistency condition. It has to be noticed that functions product rule has to be used to arrive correctly at the following form:

$$tr\left(\frac{\partial f(\boldsymbol{\sigma})}{\partial \boldsymbol{\sigma}}\overset{\circ}{\boldsymbol{\sigma}}\right) = \overset{\bullet}{R}F + RF'\overset{\bullet}{H} \qquad [A.24]$$

Theoretically speaking if the stress shifts from a null state to a non-null one the R value consequently increases and the same does the subloading surface, which expands and comes near the normal-yield surface. It's so necessary to define an evolution law for the similarity ratio:

$$\overset{\bullet}{R} = U\|\mathbf{p}\| \quad per \quad \mathbf{p} \neq 0 \qquad [A.25]$$

Where U is a decreasing monotonic function of R that obeys to the following system of equations, in which small u it's a material parameter obtained experimentally.

$$U = -u\,ln(R) \qquad \begin{cases} U = +\infty & per \quad R = 0 \\ U = 0 & per \quad R = 1 \end{cases} \qquad (U < 0 \quad per \quad R > 1) \tag{A.26}$$

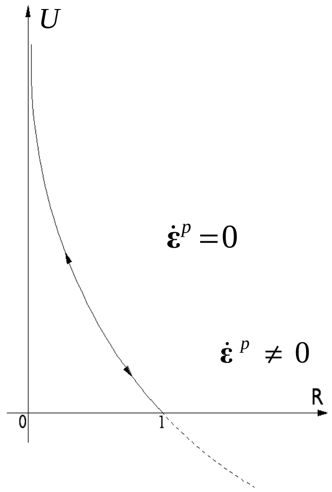

Fig. A.2 U dependence on similarity ratio.

Substituting the R evolution law inside the time differentiation of the subloading surface formula the extended consistence condition can be obtained as follows:

$$tr\left(\frac{\partial f(\boldsymbol{\sigma})}{\partial \boldsymbol{\sigma}}\overset{\circ}{\boldsymbol{\sigma}}\right) = U\|\,\mathbf{p}\,\|F + RF'\dot{H} \tag{A.27}$$

As already done in the previous paragraph, an associate flow rule is given:

$$\mathbf{p} = \bar{\lambda}\bar{\mathbf{N}} \tag{A.28}$$

Where $\bar{\lambda}$ once again is the positive proportional factor, whereas $\bar{\mathbf{N}}$ is the normalized outward-normal of the subloading surface (it's exactly the same vector seen before but now is applied to a different surface). Using the flow rule and introducing it in the extended consistency condition it is possible to obtain:

$$\bar{\lambda} = \frac{tr\,(\bar{\mathbf{N}}\overset{\circ}{\boldsymbol{\sigma}})}{\bar{M}^p} \tag{A.29}$$

Where

$$\bar{M}^p \equiv \left(\frac{F'}{F}\bar{h} + \frac{U}{R}\right) tr(\bar{\mathbf{N}}\boldsymbol{\sigma}) \tag{A.30}$$

$$\bar{h} \equiv \frac{\dot{H}}{\bar{\lambda}} \qquad \text{[A.31]}$$

It has to be noticed the simple form for the plastic modulus ($\overline{M}^p$), really close to the conventional one, with the only exception of the addition of the ratio between U and the similarity ratio. The function *f* in the subloading surface equation is such to be homogeneous function of degree one respect of the stress tensor which means that, as seen before, it is possible to apply the *Euler Theorem*, leading to:

$$\frac{\partial f(\boldsymbol{\sigma})}{\partial \boldsymbol{\sigma}} = \left\| \frac{\partial f(\boldsymbol{\sigma})}{\partial \boldsymbol{\sigma}} \right\| \overline{\mathbf{N}} = \frac{tr\left(\dfrac{\partial f(\boldsymbol{\sigma})}{\partial \boldsymbol{\sigma}} \boldsymbol{\sigma} \right)}{tr(\overline{\mathbf{N}}\boldsymbol{\sigma})} = \frac{RF}{tr(\overline{\mathbf{N}}\boldsymbol{\sigma})} \overline{\mathbf{N}} \qquad \text{[A.32]}$$

Finally the inverse and direct stress-strain relationship can be written after few mathematical passages:

$$\boldsymbol{\varepsilon} = \mathbf{E}^{-1} \overset{\circ}{\boldsymbol{\sigma}} + \frac{tr(\overline{\mathbf{N}} \overset{\circ}{\boldsymbol{\sigma}})}{\overline{M}^p} \overline{\mathbf{N}} \qquad \text{[A.33]}$$

$$\overset{\circ}{\boldsymbol{\sigma}} = \mathbf{ED} - \frac{tr(\overline{\mathbf{N}}\mathbf{ED})}{\overline{M}^p + tr(\overline{\mathbf{N}}\mathbf{E}\overline{\mathbf{N}})} \mathbf{E}\overline{\mathbf{N}} \qquad \text{[A.34]}$$

$$\overset{\circ}{\boldsymbol{\sigma}} = \left\{ \mathbf{E} - \frac{tr(\overline{\mathbf{N}}\mathbf{ED})}{\overline{M}^p + tr(\overline{\mathbf{N}}\mathbf{E}\overline{\mathbf{N}})} \left(\mathbf{E}\overline{\mathbf{N}} \right) \otimes \left(\overline{\mathbf{N}}\mathbf{E} \right) \right\} \mathbf{D} \qquad \text{[A.35]}$$

Where the terms contained inside brackets represent the elasto-plastic matrix in the subloading surface model. In conclusion the loading criteria just complete the theory establishing the conditions under which plastic deformations are induced.

$$\begin{cases} \mathbf{p} \neq 0: & tr(\overline{\mathbf{N}}\mathbf{ED}) > 0 \\ \mathbf{p} = 0: & tr(\overline{\mathbf{N}}\mathbf{ED}) \leq 0 \end{cases} \qquad \text{[A.36]}$$

Comparison between the two theories

A first main difference existing in these two models is the different form of the loading criteria. In the conventional elasto-plastic model it's necessary to satisfied two conditions for having permanent deformations, whereas in the unconventional theory the subloading surface is such that it always pass to the current stress point. This makes the consistency condition always valid so it is only necessary to observe if the stress increases or decreases to decide if plastic strains will be produced or not.

Moreover stress is automatically drawn back to the normal-yield surface even if it goes out from that surface because of similarity ratio evolution law analytical form:

$$\begin{cases} \dot{R} > 0 \quad per \quad R < 1 \quad \text{(sub - yield state)} \\ \dot{R} < 0 \quad per \quad R > 1 \quad \text{(over normal - yield state)} \end{cases} \tag{A.37}$$

This leads to a computational advantage that speeds up the calculation process. In fact it's no more necessary to use some pull-back algorithm for bringing the stress to lie on the yield-surface.

One another big difference is that the yield stress is not a characteristic of the material itself, but it depends on loading conditions. Vice versa in the classical plastic theory the yield surface is unique and depends only on the considered material, without pay any attention on how the load is applied.

In conclusion the adoption of an associate flow rule makes the stiffness matrix symmetric which simplified a lot the numerical implementation of the algorithm and its use.

The numerical procedure

The next few paragraphs will deal with the computational procedure to realize a visco-elasto procedure taking also into account permanent plastic deformations, computed thanks to an unconventional plasticity model (i.e. subloading surface model).

A first challenge to pursue this aim has been that of trying to merge together an incremental procedure such as the elasto-plastic one with the integral form of the visco-elastic theory. In order to do that, subloading surface model has to be properly included in the already existing F.E. algorithm of the code NEWCON3D for the displacement computation.

Visco-Elasto Plastic code

The 3D fully coupled F.E. research code NEWCON3D, as mentioned before, uses an integral form in the computations of the unknowns to take into account viscosity. This means that at every time step the algorithm starts from the beginning to compute the solution without remember of what happened in the previous steps.

Instead in conventional and also in unconventional elasto-plastic models, it is usual to adopt an incremental procedure for the evaluation of the displacements, strains and stresses because the elasto-plastic matrix strongly depends on the stress level reached and on the rate of stress (strain) subsequently applied. It is clear that to include a plastic algorithm in a total form is necessary to modify the structure of the code for simulating a plastic step.

The idea is that to subdivide the macro step time in a series of sub-steps creating a fake incremental plastic problem which is easy to solve. Once the correct plastic strain increment is computed, total plastic deformation are updated and added in the total visco-elastic and plastic problem. This is theoretically based on the fact that considering small strain hypothesis, plastic effect can be seen as a co-action of the viscous one, so the former can be computed separately and then included in the latter. The whole procedure requires a certain amount of memory to allow the sub-steps to store the intermediate vectors solution and to recall them back when necessary to compute the stress and strain rate.

Fig. A.3 graphically schematizes the different passages that will be explained in detail afterward.

Sub-step procedure

Each main time step has been divided in three sub-steps. For example, as it can be seen in the flow chart, a solution between main step 1 and 2 is computed for every sub-step in a different way: the first one is purely linear-elastic, the second is elasto-plastic and the last one in visco-elasto and plastic. In detail, supposing that main step 1 is the first of the analysis it will be shown how this algorithm works:

❶ *sub-step*: this sub-step computes the solution in terms of displacements, strains and stresses using a total integral form from the beginning of the analysis. It has to be highlighted that the solution is purely linear elastic. At this point, knowing the solution at the previous main time step, is it possible to compute the unknown increments (i.e. $\Delta\varepsilon^{e}$, ΔR1) which are needed in the second sub-step, and store them in ad hoc vectors.

Here, since time at step 1 is zero, the first sub-step can be also regarded as a sort of incremental step, so the rate of the variables are the variables themselves; but for sake of completeness its description has been given in general terms.

❷ *sub-step*: At this point from main step 2 we came back to main step 1 to perform the second sub-step computation. It's a pure incremental elasto plastic computation. ΔR1 is the incremental vector forces applied as boundary condition, thanks to $\Delta\varepsilon^{e}$ it is possible to set up the elasto-plastic matrix and find the solution of the system. In particular the permanent deformations can be estimated subtracting to the just computed $\Delta\varepsilon^{e,p}$, for the plastic sub-step, the one $\Delta\varepsilon^{e}$ stored at the previous elastic one, obtaining $\Delta\varepsilon^{p}$ vector.

This vector contains the plastic strains rate derived by means of subloading surface model for every Gauss point. Now it's necessary to store this contribute in a cumulative vector which allow us to have memory of the total plastic strain experienced by every of these Gauss points that have to be added in the next total sub-step as a co-action. The same thing is done for the $\Delta\sigma^{p}$ term, which is cumulated in an ad hoc vector (σ^{p}) for the next sub-step.

❸ *sub-step*: this third sub-step is the total visco-elastic and plastic one. Here we compute the visco-elastic solution in its integral form just applying as boundary condition the one that competes to the 1 main step. Recalling ε^p vector we introduce this term in an internal procedure which applies an additional fake external system of forces such to induce exactly this deformation. In this way the system of real forces is responsible for the visco-elastic part of the strains whereas the fake one for the plastic.

This can seem strange but it has to be noticed that we already exactly know the plastic contribute that compete to this main step and so, the setting up of this fake system of forces, it's just a numerical expedient to take it into account in the solution in the F.E.M. in a consistent way.

It also has to be pointed out that strains derived from the displacements are exactly the sum of the visco-elastic term and the plastic one. On the other hand the stresses are treated in a different way, because the fake system of forces doesn't contribute in stresses computation. Recalling σ^p vector, which contains the total plastic stress for the actual step, is possible to perform a stress redistribution modifying the $\sigma^{v.e.p}$ state of stress already estimated in the present sub-step. This is necessary because it's assumed that plasticity governs the equilibrium for the sample giving lower stress state in the material, otherwise we should consider a more high level of stress with higher plastic deformations which is unrealistic.

The procedure described above has to be repeated for every main step in the same way. For sake of completeness it has to be noticed that at the first sub-step of the second main step the strain rate $\Delta\varepsilon^e$ and the external load one ΔR1 can be calculate recalling the stored solution at the first sub-step of the previous main step as well clear in the flow chart. The loading procedure will be discussed in detail in the following paragraph.

Loading procedure

One of the most important point of the upgraded procedure is the setting up of the right terms of the resolving system. In fact, depending on the different loading history, the model behaves in a different way. The unconventional plastic model used in the analysis is not time dependent; this means that if we load the sample and let it deform both taking into account viscosity and plasticity and then we stop loading and just leave the load applied, only viscosity should contribute to the deformation.

The F.E. code is such that it divides permanent load and transient load terms. Only the latter should be used as right side of the system in the second pure incremental sub-step. This is why the algorithm has been changed according to the flow chart reported in Fig. A.4. RI-LOAD vector contains the permanent load, which affects only elasto-visco deformation part, whereas RLOAD is the transient load vector which is cumulated step by step in the total forces vector *R*.

If we start the analysis from step 1 the term ΔR1, mentioned above in the explanation of the sub-step procedure, coincides exactly with the transient load vector RLOAD①. Thus, this is the right hand term of the system that has to be applied in the second purely incremental plastic sub-step. At this point we have to store a vector, named R1M1 which contains the whole forces system applied passing through main step 1 to main step 2 (i.e. RI-LOAD + RLOAD①). This will allow us to correctly estimate the ΔR1 term that has to be used in the plastic sub-step of the second main step.

In other words the correct ΔR1 load vector in the second main step is exactly equal to RLOAD②, which can be obtained by subtracting from the total cumulative forces vector R1 (= RI-LOAD + RLOAD① + RLOAD②) the R1M1 vector stored before.

In this way we can guarantee that if transient load is null ($\text{RLOAD}^n = 0$), which means that we are not increasing the load on the sample but just maintaining it, R1 and R1M1 coincide and so also ΔR1 is null and plastic mechanism is not activated between two step.

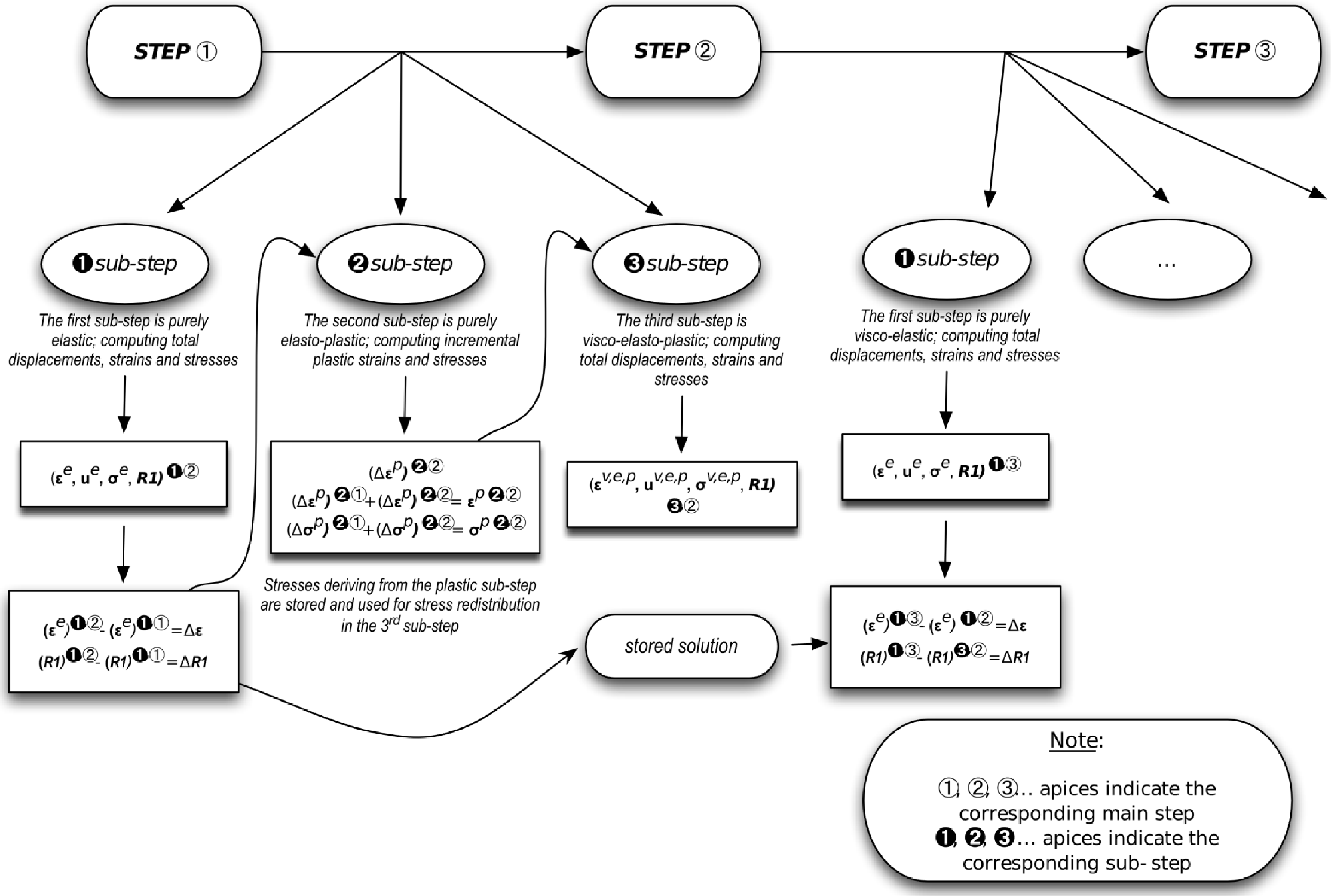

Fig. A.3 Visco-elasto plastic numerical procedure, implemented in the F.E. code NEWCON3D.

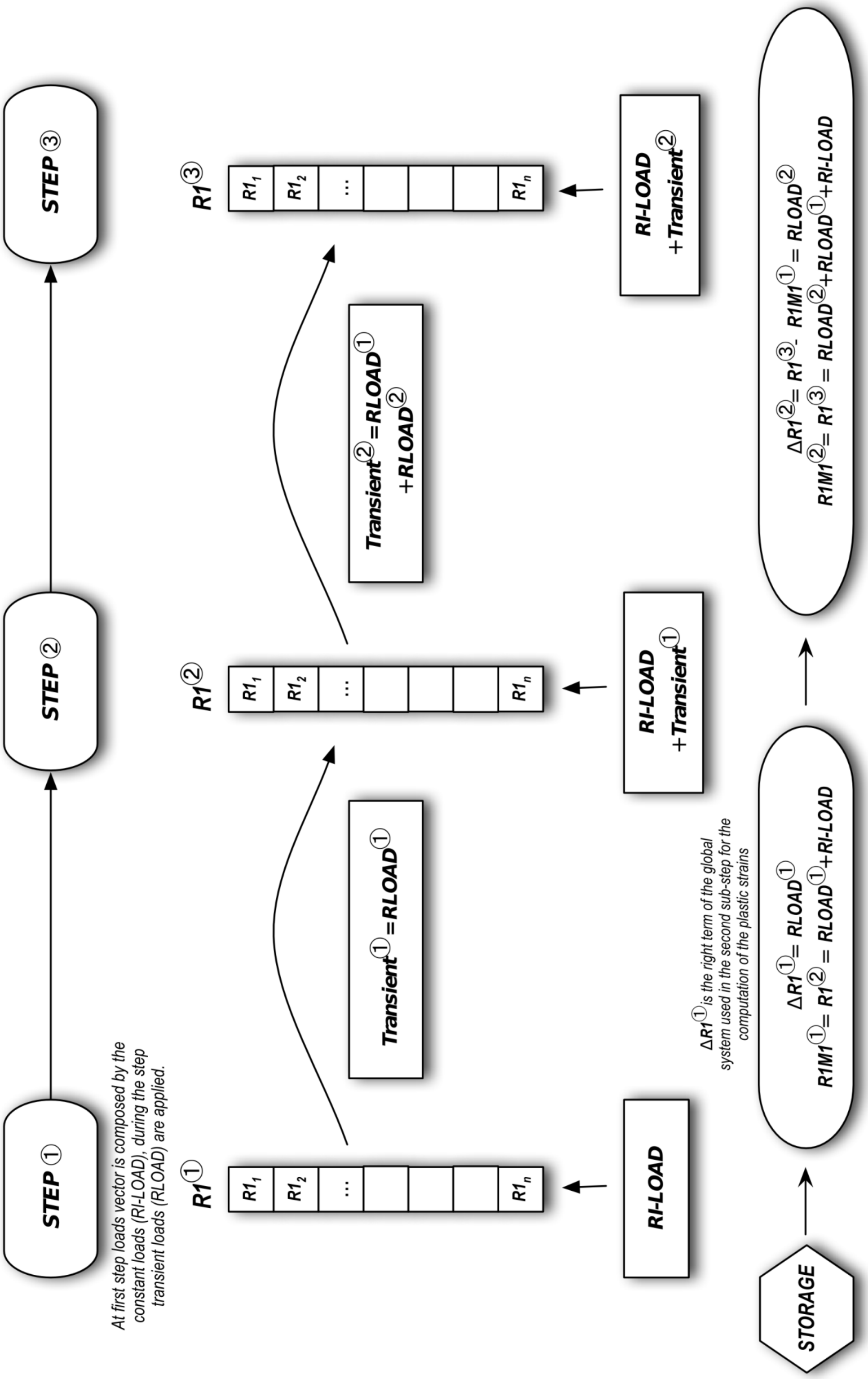

Fig. A.4 Loading procedure for the visco-elasto plastic code.

Numerical Analyses

The numerical analyses, here presented, for the visco-elasto and plastic algorithm are limited to simple cases because of the preliminary level of the actual study, which is still under development nowadays. This is also the reason why a small number of elements have been involved in the numerical simulation, together with the fact that the purpose of the work was to investigate the correct response of the algorithm, rather than the reproduction of a real case.

As it can be seen in Fig. A.5 the test sample is quite simple. It is composed by twelve 20-node brick elements, where the four on top represent a semi-infinite rigid layer which allow to distribute uniformly a concentrated load on top to the remaining elements below.

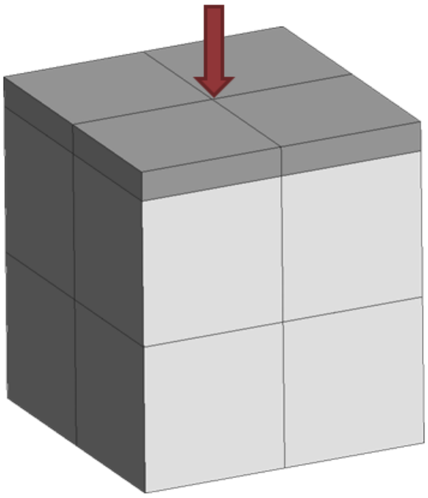

Fig. A.5 Adopted discretization for the 200×200×200 mm^3 cubic sample.

The block is constrained only at the base, whereas temperature and also relative humidity are free. In order to perform the first numerical controls, two different analyses, with different loading condition, have been carried out:

- ***Analysis 1***: the first type of loading procedure is that to apply a concentrate load on top from null value up to 400 kN. Different relationship existing between visco-elastic and plastic deformations has been investigated varying the time of application of the above mentioned load;
- ***Analysis 2***: the second loading procedure consists in rise the concentrated load on top up to 400 kN in a fix period of time (1 year), leave it constant for one year, and then increase its value, in the same way done before, from 400 kN to 800 kN. The purpose of this loading path is the test of the correct behaviour of the plastic sub-step which should not be activated when the load is keep constant.

For sake of completeness, the material parameters used in the two different analyses have been reported in Table A.1. While in Table A.2 are shown the six parameters required in the subloading surface model: F_0 is the initial value for F in the yield-surface, ρ and ϒ are respectively the constants prescribing the slopes of normal-consolidation and swelling lines, whereas m_c is the critical line slope, υ is the Poisson's ratio and *u* is a material constant governing the evolution of the similarity-ratio in the subloading surface problem. Finally in Table A. 3 are reported the creep parameters required for the Double Power Law (see Section 3.3.5).

Table A.1 Material parameters.

Size [mm³]	200×200×200
Elastic Modulus [MPa]	28522.1
Hydraulic Diffusivity [mm²/d]	20
Thermal Conductivity [W/m K]	1.67
Thermal Capacity [N/mm² K]	2.112

Table A.2 Subloading surface parameters.

υ	0.18
ρ'	0.10
γ	0.07
m_c	0.82
u	25
F_0 **[MPa]**	62000

Table A. 3 Creep parameters.

E_0 **[MPa]**	42783.16
φ_1	4.5
α	0.076
m	0.296
n	0.181

Analysis 1

As already mentioned in the previous paragraph, the first type of analysis has been carried out in order to evaluate the different relationship between the visco-elastic and the plastic strains using the same loading path but applying it in various time period.

In Fig. A.6 stress-strain evolutions in time for the same point are shown. It is quite clear that, due to the fact that the plastic algorithm is rate independent, the plastic response is exactly the same for all the lines; the difference is due to the contribute of the viscous deformation that increases in time.

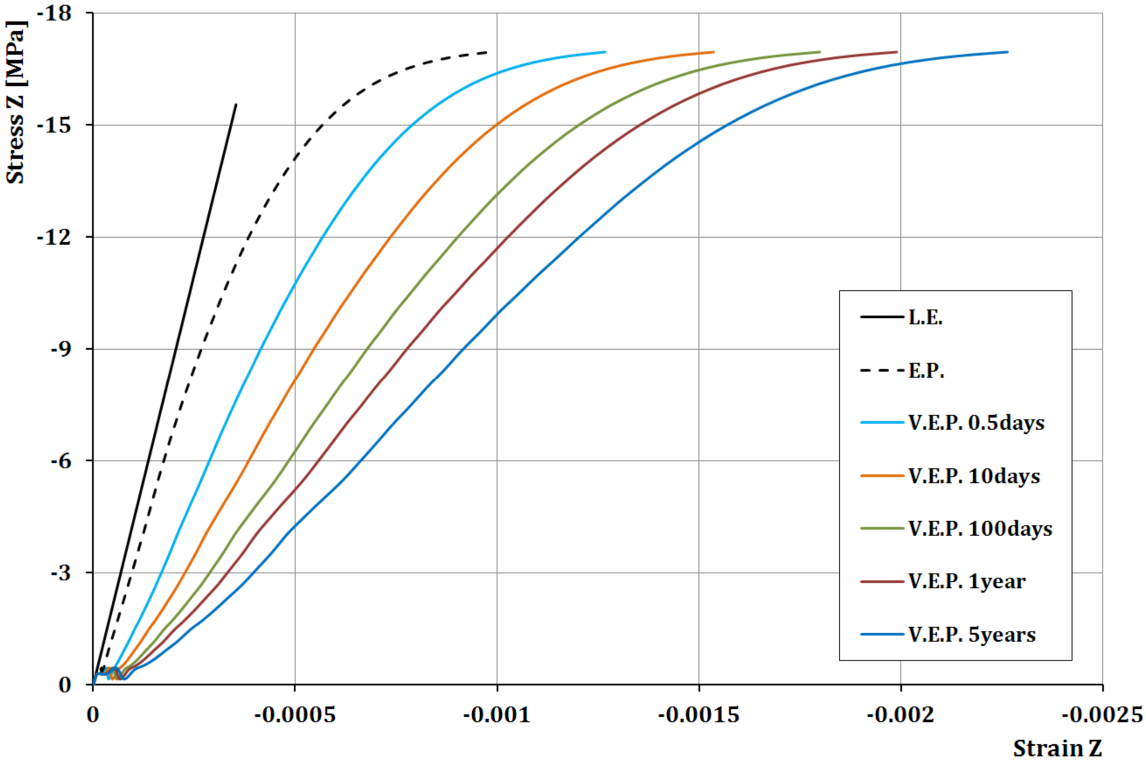

Fig. A.6 Stress vs. Strain evolution in time for the same load.

Two things must be pointed out. The former is that the stress level is governed by the plastic behaviour of the material, due to a stress re-distribution on the different Gauss point. The second is the decreasing magnitude of the visco-elastic deformation in time. The gap between two consecutive curves (only exception for the last one which is computed for a very long period time) decreases, whereas the time increases. This means that the viscous contribute is important in the short time period but its effects start to lose of importance over time, as both experimentally and theoretically expected.

If we analyse the strains evolution in time of two curves, the first one for a 10 days period and the second for 1 year period, we are able to appreciate the different contribute due to viscosity and plasticity. For shorter time the plastic strains are bigger than the viscous one, despite the fact that viscous effects are more relevant in the beginning of the analysis as written before. This can be easily noticed observing that the two lines intersect each other in Fig. A.7, where the plastic strain line crosses the visco elastic one.

On contrary in the graph of Fig. A.8 for longer period time, the two lines do not intersect each other and rather the visco-elastic one remains always below plastic contribute. These aspect can be better appreciate in Fig. A.9 and Fig. A.10. The first one is just the union of the previous two figures, whereas in the second one the strain evolution respect the time step is investigated. In detail, looking at the plastic deformation curves it can be noticed that there is a perfect overlap between the 10 days analysis and the 1 year one. This is because the plastic algorithm doesn't depend on time, but it's affected only by the loading path.

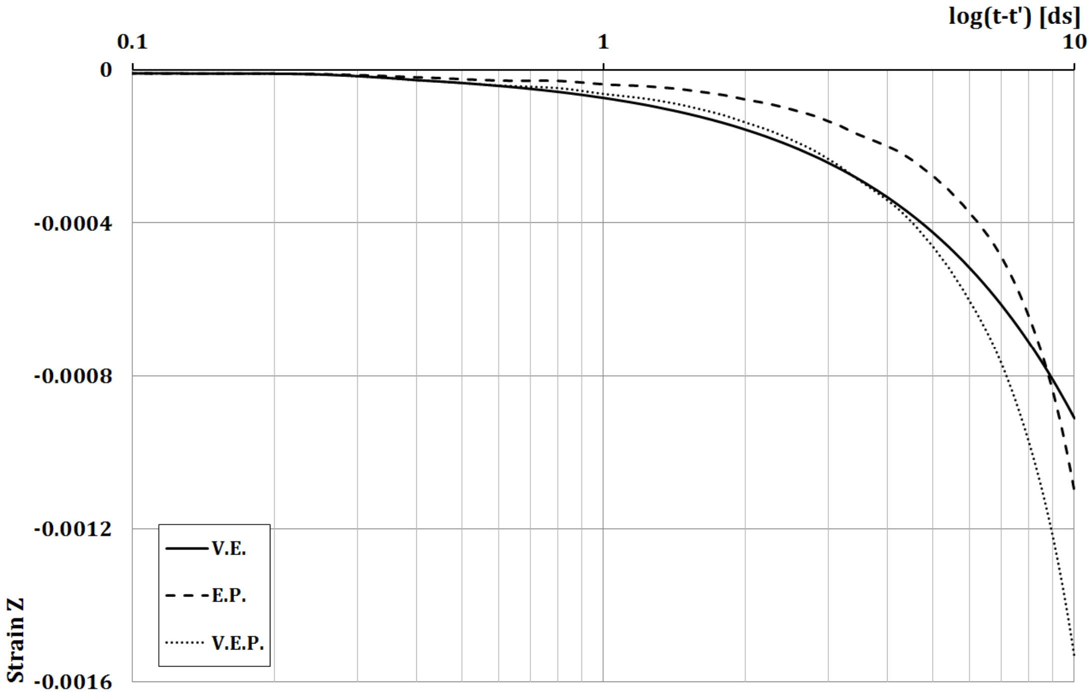

Fig. A.7 Strain vs. Time for a loading time equal to 10 days**.**

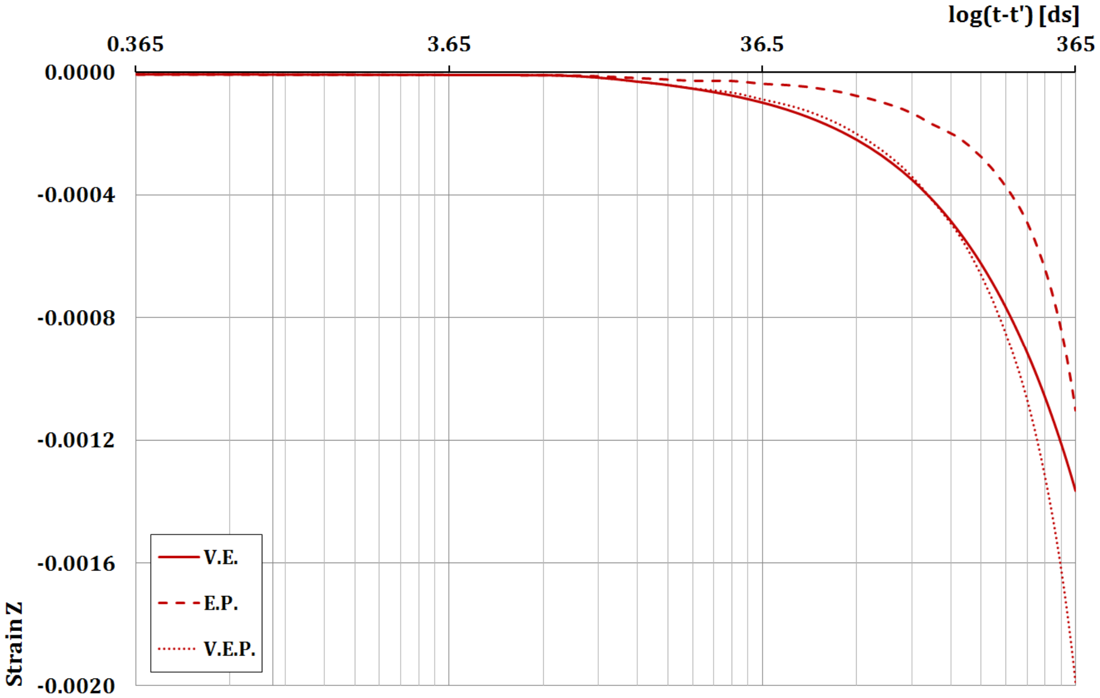

Fig. A.8 Strain vs. Time for a loading time equal to 1 year**.**

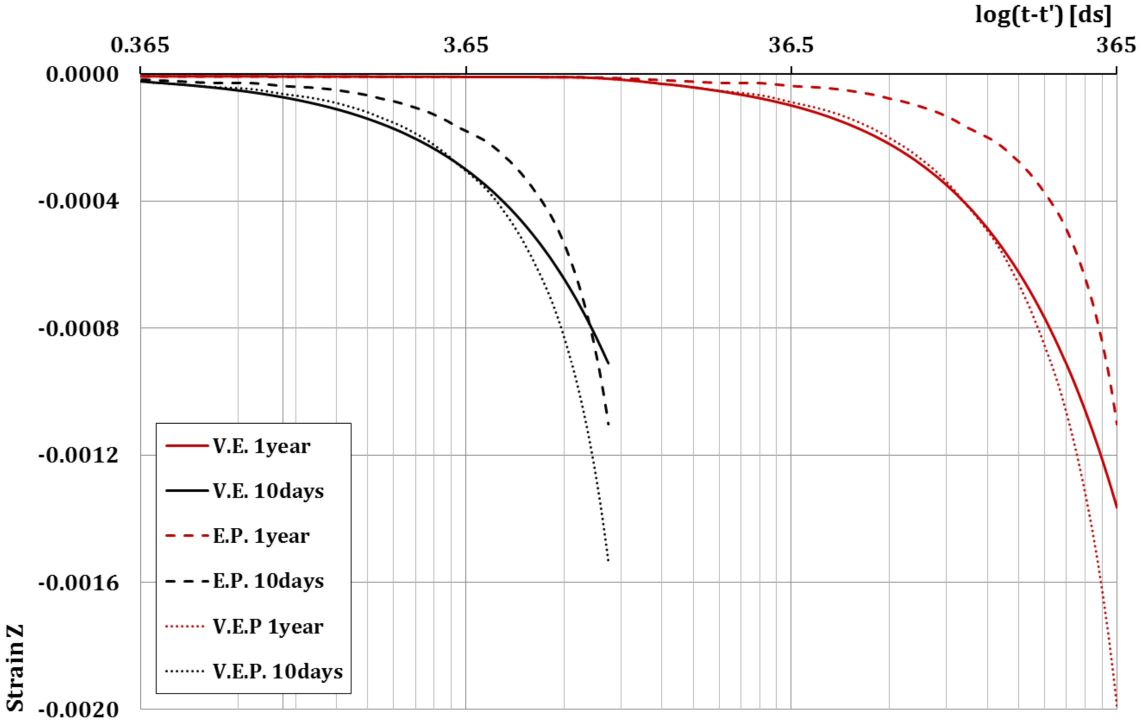

Fig. A.9 Strain vs. Time comparison for the previous two loading times (10 days and 1 year).

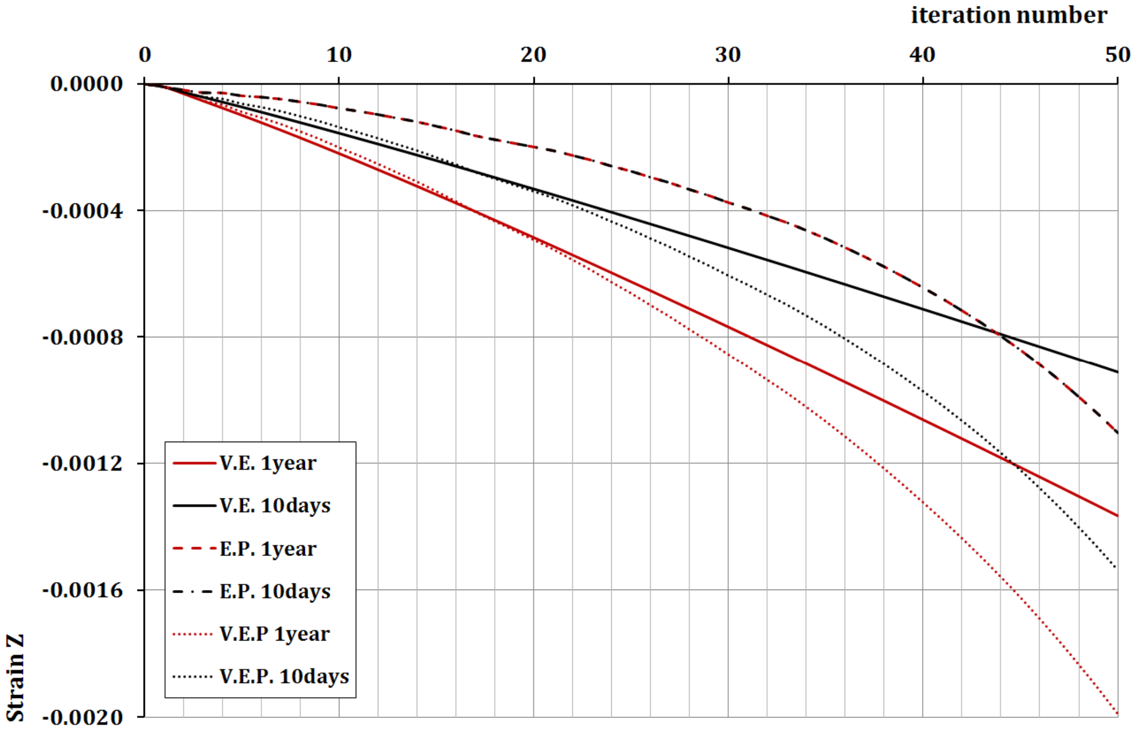

Fig. A.10 Strain vs. Iteration number comparison for two different loading times (10 days and 1 year).

Analysis 2

This second analysis differs from the previous one just because now the duration time is fixed and loading path is changed. It is an important test to verify the correct implementation of the three step procedure merging the total visco-elastic and incremental plastic rheology model. As it has been mentioned before and also in the *Loading procedure* paragraph it is important that plastic algorithm activates only if there is a change in the load applied, on the contrary if the external forces remain constant only visco elastic strains should be induced.

To check this important aspect the duration of the simulation has been subdivided in three parts. The first one runs one year simulation with an incrementing load from a null state up to 400kN, in which plastic deformations are produced in combination with visco-elastic ones. In the second one, the load of 400 kN magnitude is maintained at the top of the sample for one year. In this specific case what is expected is an increase in settlements but of minor entity because governed only by creep. In the last part of the analysis the load start to increasing again from 400 kN value up to 800 kN in one year in the same manner of the first part.

Result are briefly reported in Fig. A.11 and Fig. A.12. The former reports the strain evolution in time and as it can be seen the dashed line represent the plastic deformations evolution, which clearly shows an horizontal trend in the phase of constant load on top, verifying the correct implementation of the routine inside the code. As further validation the dotted line, which is the sum of the continue and dashed one (i.e. visco-elastic and plastic), presents an increment of strains in time during the second year simulation, which corresponds exactly to the creep contribute. In the third year of the analysis the stress state is such that plastic strains are more relevant then creep, in fact the dotted line shows more resemblance to the dashed curve.

The same behaviour can be observed in the stress-strain relationship reported in Fig. A.12. Clearly pure elasto-plastic curve and also the linear elastic one don't show any change during the second phase of the analysis, because the stress and the strain point doesn't change but keeps the same position in the graph. On the other hand both visco-elastic (i.e. dashed-dotted line) and the visco-elasto plastic (only dotted line) curves are affected by strains change proper of the creep model showing an horizontal increase of deformation with constant stress as was expected.

Conclusion

The two simple different analyses carried out so far verify the correct numerical implementation of the mixed visco-elastic and plastic algorithm but also represent a start point for a more complex study. The number of elements involved in the analyses, the loading and the boundary conditions have to be increased and adapted to reproduce a real case in order to validate better the model. For sake of completeness future improvements involve the possibility of check temperature effects as well as the possibility of apply hygrometric and not only mechanics loads on the sample.

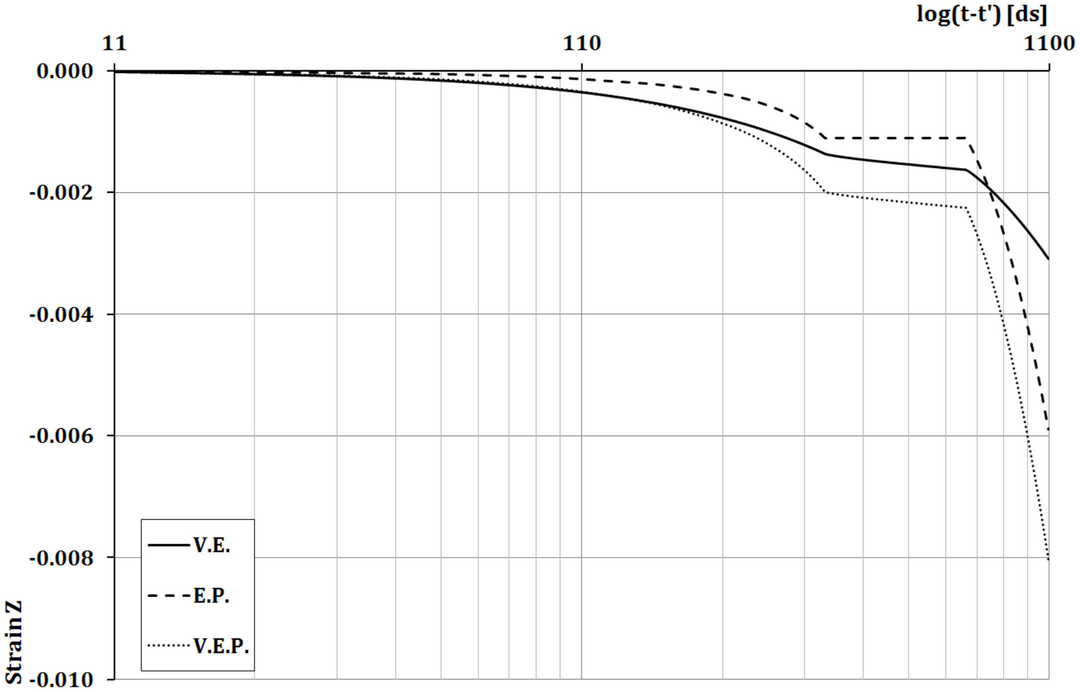

Fig. A.11 Strain vs. Time evolution, analysis 2.

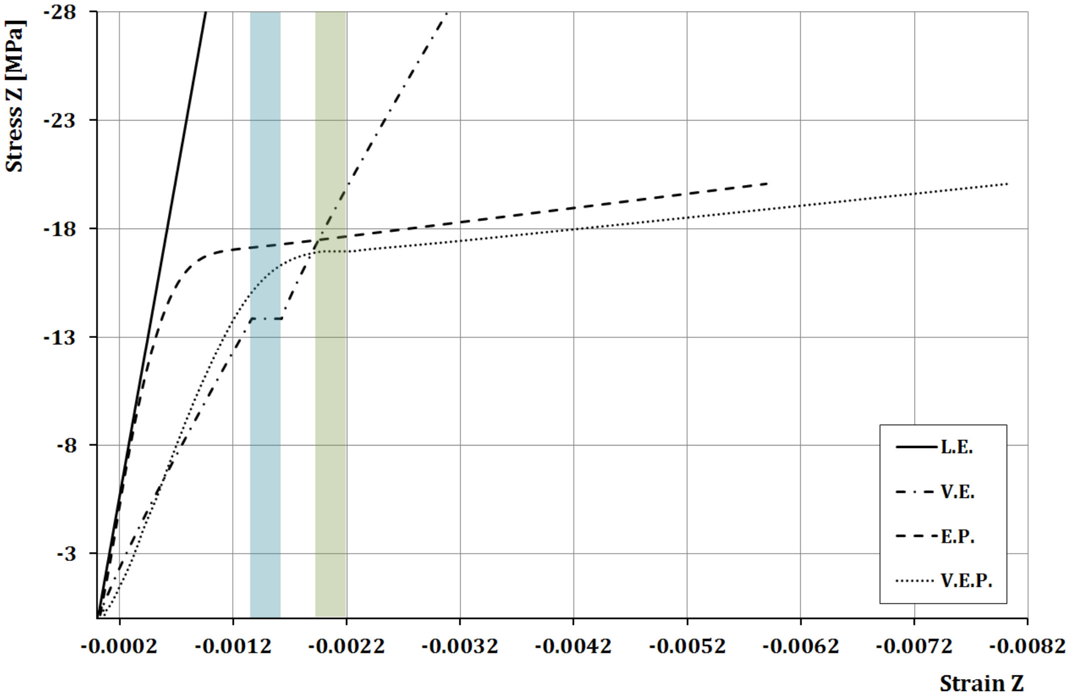

Fig. A.12 Stress vs. Strain evolution, analysis 2.

REFERENCES

[1] Hashiguchi K., Ueno M. (1977), Elastoplastic constitutive law of granular materials, Costitutive Equation of Soils, Murayama, S. Schifield, A.N. (eds.) Proc. 9th Int. Conf. Soil Mech. Found. Eng., Spec. Ses. 9 Tokyo, JSSMFE, pp.73-82.

[2] Drucker D.C. (1988), Conventional and unconventional plastic response and representation, Appl. Mech. Rev. (ASME) 41, pp.151-167.

[3] Hashiguchi K. (1978), Plastic constitutive equations of granular materials, Cowin S.C., Satake M. (eds.), Proc. US-Japan Seminar on Continuum Mech. Stast Appr. Mech. Granular Materials, Sendai, pp.321-329.

[4] Hashiguchi K. (1980), Constitutive equations of elastoplastic materials with elastic-plastic transition, J. Appl. Mech. (ASME), 47, pp.266-272.

[5] Hashiguchi K. (1989), Subloading surface model in unconventional plasticity, Int. J. Solids Structures, 25, pp. 917-945.

AKNOWLEDGEMENTS

First of all, I would like to thank my PhD advisors, Professor Carmelo Majorana and Dr. Ing. Valentina Salomoni, for supporting me during these years. Professor Majorana for his scientific advice and knowledge, Dr. Ing. Valentina Salomoni for her competence, her patient teachings and the many insightful discussions and suggestions. I enjoyed their interest in my research as well as the fruitful discussions.

My thanks to Professor Kaspar Willam for giving me the possibility of spending six months at Houston under his supervision, for his scientific competence and for his precious teachings. His enthusiasm and his love for research is wonderful.

My thanks to Gianluca and Riccardo for the support and friendship that I needed, even in difficult times, and all the working group do I belong.

Last but not least, I would like to thank my family and Filippo for their continuous encouragement and their precious support in these years.